Marc Martin Sommer

Mechanische Erzeugung von Nanopartikeln in Rührwerkskugelmühlen

Mechanical Production of Nanoparticles in Stirred Media Mills

Cuvillier Verlag Göttingen

Mechanische Erzeugung von Nanopartikeln in Rührwerkskugelmühlen

---

Mechanical Production of Nanoparticles in Stirred Media Mills

Der Technischen Fakultät der Universität Erlangen-Nürnberg zur
Erlangung des Grades

D O K T O R - I N G E N I E U R

vorgelegt von

Marc Martin Sommer

Erlangen - 2007

Als Dissertation genehmigt von der Technischen Fakultät der
Universität Erlangen-Nürnberg

Acknowledgments

Summary

Nanotechnology applications in the pharmaceutical, materials, and chemical industries has renewed interest in the use of wet grinding in stirred media mills for the production of nanoparticles with controlled microstructure. Quite recently it is possible to mill particles down to the size range of 10 nm [1, 2]. However, challenges arise in the production of sub-micron particles that are, in part, due to colloidal surface forces influencing slurry stability and rheology. In this work experiments are performed on a well characterized model system of monodisperse primary nanoparticles that are salt destabilized and aggregated under various milling conditions. Perikinetic and orthokinetic aggregation are measured, with the latter in a laminar shear flow as well as in a stirred media mill, to examine the effects of colloidal stability and flow on the aggregation process. The agglomeration kinetics are measured using dynamic light scattering (DLS) as a function of electrolyte concentrations. Further information on the agglomeration process and the structure of the agglomerates are also obtained from small angle neutron scattering (SANS) and rheo-optical light scattering (ROA) experiments both at rest and under flow. Theoretical predictions for the colloidal stability from independently measured particle and solution properties compare well with the experimental results. Orthokinetic aggregation is observed to result in faster aggregation and denser agglomerates.

Because of the high industrial demand for nanoparticles in organic media the study was extended to non-aqueous systems. Electrostatic stabilization requires a sufficiently high surface charge leading to a steeply decaying surface potential. These conditions can be met by solvents of medium dielectric constant (i.e. values larger than about 15-20), e.g. alcohols. In these media the particles may carry a high surface charge and the solubility of salts will be sufficient to enable a high repulsive barrier. It is shown that stable suspensions with high ζ-potentials can be achieved for alumina in ethanol with elecrostatic stabilization. Milling studies with electrostatic stabilization showed that the size of the primary particles is conspicuously smaller than the size of the particles milled under the same conditions in the aqueous phase. However, the media wear has a negative influence on the stability of the suspension since the ionic strengths in organic solvents are much lower.

Milling experiments with steric stabilization in organic solvents produced larger primary particle sizes than with electrostatic conditions. The polymer layer around the particles seems to adsorb part of the grinding energy during the impact of two grinding beads and cushions the comminution. However, media wear has in contrast to the electrostatic stabilized particles in organic solvents no influence on the stability of the suspension. An important question is whether the mechano-chemical activation which was observed in aqueous media is crucial to obtain nanoparticles. Differential Scanning Calorimetry (DSC) and X-ray diffraction (XRD) measurements showed no mechano-chemical changes during milling in ethanol and toluene. In the aqueous phase the stabilization

mechanism has no influence on the amount of hydroxide phase. A protecting polymer cover around the particles does not prevent the mechano-chemical changes.

Zusammenfassung

Die Anwendung der Nanotechnologie in der chemisch- pharmazeutischen, der keramischen und der mikroelektronischen Industrie hat das Interesse an der Nasszerkleinerung in Rührwerkskugelmühlen für die Herstellung von Kolloiden und Nanopartikeln verstärkt. Seit kurzem ist es möglich, Partikeln bis unter ca. 10 nm zu zerkleinern [1, 2]. Die Herausforderungen bei der Produktion von Nanopartikeln liegen im Wesentlichen in der Kontrolle von interpartikulären Wechselwirkungen, die das Verhalten von Suspensionen mit mittleren Partikelgrößen unterhalb von 1 μm maßgeblich beeinflussen. Mit abnehmender Partikelgröße dominieren die attraktiven van der Waals Wechselwirkungen, welche bei Kollision zu festen Agglomeraten und zu Änderung der rheologischen Eigenschaften der Produktsuspension führen können. Aufgrund der Reagglomerationserscheinungen stellt sich nach dem Erreichen einer bestimmten mittleren Partikelgröße ein Gleichgewichtszustand zwischen Agglomeration, Deagglomeration und Bruch ein, so dass trotz steigenden spezifischen Energieeintrags kein weiterer Zerkleinerungsfortschritt beobachtet wird. Auf diese Weise können auch Agglomerate entstehen, die größer als die Ausgangspartikelverteilung und fest genug sind, um der Beanspruchung in der Mühle standzuhalten. Um ein besseres Verständnis des Agglomerationsvorgangs während des Zerkleinerns zu erhalten, wurden Experimente mit einem gut charakterisierten Modellsystem monodisperser, nanoskaliger Primärpartikeln durchgeführt. Die Suspension wurde unter verschiedenen Bedingungen destabilisiert und agglomeriert. Der Einfluss der Suspensionsstabilität auf den Agglomerationsvorgang wurde unter perikinetischen und orthokinetischen Bedingungen sowie unter Mühlenbedingungen untersucht. Die Agglomerationskinetik wurde durch dynamische Lichtstreuexperimente (DLS) als Funktion von Partikel- und Elektrolytkonzentration gemessen. Weitere Informationen über den Agglomerationsprozess und die Struktur der Agglomerate wurden durch Neutronenkleinwinkelstreuexperimente (SANS) erhalten. Theoretische Vorhersagen, die auf unabhängig gemessenen Partikel- und Suspensionseigenschaften sowie auf Mühleneigenschaften beruhen, wurden mit experimentellen Ergebnissen verglichen, um zu zeigen, dass die Aggregationskinetik in der Rührwerkskugelmühle durch kolloidale Wechselwirkungen und durch die Mühlenbedingungen gesteuert werden kann.

Die gewonnenen Erkenntnisse wurden wegen des großen industriellen Bedarfs an Nanopartikeln in organischen Lösungsmitteln auf nicht wässrige Systeme übertragen. Es konnte gezeigt werden, dass stabile Suspensionen von Al_2O_3 in Ethanol sowohl mit elektrostatischer als auch mit sterischer Stabilisierung erreicht werden können. Zerkleinerungsversuche mit elektrostatischer Stabilisierung zeigen, dass sich der Abrieb negativ auf die Stabilität der Suspension auswirkt.

Bei der sterischen Stabilisierung hat der Abrieb keinen Einfluss. Allerdings scheint die Polymerhülle um die Partikeln Teile der Zerkleinerungsenergie zu absorbieren und somit Mahlkörperstöße zu dämpfen. Eine weitere wichtige Frage ist, ob eine mechano-chemische Aktivierung, die während der Zerkleinerung in wässriger Phase beobachtet wurde, eine entscheidende Rolle bei der Nanozerkleinerung spielt.

Contents

Inhaltsverzeichnis

This work is dedicated to my father, Dr.-Ing. Ernst Sommer,
who was with enthusiasm engineer and aroused my interest
in technology and in particular in engineering sciences
by his example.

CHAPTER 1

Introduction

Nanoparticles are increasingly used in many areas of the chemical and pharmaceutical industry as well as in the ceramic and microelectronic industry. Applications for sub-micron particles are for example pigments, nanocomposites, drug delivery and ceramic materials. Besides the direct synthesis of these materials by chemical methods, wet grinding in stirred media mills is a suitable method for the production of nanoparticles, since the high energy densities, which are necessary to produce nanoparticles, can be achieved in stirred media mills [**1**]. The manufacturing of fine particles in stirred media mills is influenced next to machine parameters (e.g. design, function and size of the mill) and process parameters (e.g. rotational speed, filling degree etc.) by interparticle interactions. These interactions influence the stability of the milling suspension against coagulation as well as the rheology of the suspension. Particles in the order of 1 μm and below feature a high mobility due to Brownian diffusion. This leads to a high collision frequency between the particles. If non-stabilized particles collide, agglomerates strong enough to withstand the grinding process may be formed. This effect has limited the milling process in the past. A grinding limit was postulated for particle sizes of around 0.5 μm [**3, 4**]. By producing particles smaller than a median particle size of 1 μm a steady state between breakage and agglomeration exists in the milling process. This equilibrium is controlled by interparticle interactions as well as the milling conditions. The more the particles decrease in size the more the interparticle forces between the particles become dominant. Attractive forces lead to agglomerates when the particles collide, thus acting against the comminution process. To prevent this agglomeration process the particles in the mill must be stabilized by increasing the repulsive forces in the suspension. This will move the steady state to smaller particle sizes. To study the grinding limits of particle sizes below 1 μm a detailed understanding of the agglomeration process and its mechanism is needed. This is why this work focuses on the agglomeration process and on the stability of the suspension against agglomeration. In this study primary nanoparticles of a diameter of around 30 nm are considered and the agglomeration process under perikinetic and orthokinetic conditions is observed. On basis of this the agglomeration and dispersing process is studied in a stirred media mill. It could be shown that the agglomeration of the particles is accelerated until the steady state between agglomeration and deagglomeration is reached. Furthermore, it is shown that this steady state can also be reached by real breakage from large particle sizes. This work points out that

nanomilling in stirred media mills is possible in aqueous suspensions with electrostatic stabilization if particle stability and suspension rheology are carefully controlled.

Furthermore, the study was extended to non-aqueous systems, because of the high industrial demand on nanoparticles in organic media. The state and the properties of particle surfaces in the liquid phase are discussed. Based on this, possibilities to influence the interparticle interactions and with it the stabilization of the particles are described. Milling studies with electrostatic and steric stabilization mechanisms in organic solvents were conducted and compared to the milling behavior in water.

Einleitung

Sowohl in der chemisch- pharmazeutischen Industrie als auch in der keramischen und mikroelektronischen Industrie werden immer häufiger Nanopartikel eingesetzt. Anwendungen sind zum Beispiel Pigmente, Nanokomposits, gezielte Pharmakotherapie oder keramische Materialien. Neben der direkten Synthese von diesen Materialien durch chemische Methoden, sind nass betriebene Rührwerkskugelmühlen für die Produktion von Nanopartikeln durch mechanische Zerkleinerung besonders geeignet, da sie die hohen Leistungsdichten zur Verfügung stellen, die für die Zerkleinerung in dem Nanometerbereich erforderlich sind [1]. Die Herstellung von feinen Partikeln in Rührwerkskugelmühlen wird neben Maschinenparametern (z.B. Geometrie, Funktionsweise und Abmessungen der Mühle) und Prozessparametern (z.B. Umfangsgeschwindigkeit, Mahlkörperfüllgrad usw.) von interpartikulären Wechselwirkungen beeinflusst. Diese Wechselwirkungen beeinflussen sowohl die Stabilität der Mahlgutsuspension gegen Koagulation als auch die Rheologie der Suspension. Partikel in der Größenordnung von 1 μm und kleiner besitzen aufgrund der Brownschen Diffusion eine hohe Beweglichkeit. Dies führt zu einer hohen Kollisionsrate zwischen den Partikeln. Wenn nicht stabilisierte Partikel zusammenstoßen, können Agglomerate entstehen, die größer als die Ausgangspartikelverteilung und fest genug sind, um der Beanspruchung in der Mühle standzuhalten. Dies hat in der Vergangenheit den Zerkleinerungsprozess limitiert. So wurde z.B. eine Zerkleinerungsgrenze um 0.5 μm postuliert [3, 4]. Aufgrund dieser Reagglomerationserscheinungen stellt sich nach dem Erreichen einer bestimmten mittleren Partikelgröße ein Gleichgewichtszustand zwischen Agglomeration, Deagglomeration und Bruch ein, so dass trotz steigenden spezifischen Energieeintrags kein weiterer Zerkleinerungsfortschritt beobachtet wird. Dieses Gleichgewicht kann über die interpartikulären Wechselwirkungen und die Mühlenbedingungen eingestellt werden. Mit zunehmender Feinheit der Partikeln werden die interpartikulären Kräfte größer. Die attraktiven Kräfte führen zur Agglomeration, wenn die Partikel kollidieren und wirken somit gegen den Zerkleinerungsprozess. Um diesen Agglomerationsprozess zu verhindern, müssen die Partikeln in der Mühle durch

repulsive Kräfte stabilisiert werden. Dies führt zu kleineren Partikeln. Um ein besseres Verständnis der Vorgänge während des Zerkleinerns unterhalb von 1 μm zu erhalten, muss der Agglomerationsprozeß und dessen Mechanismus genauer untersucht werden. Deswegen wurde in dieser Arbeit ein Schwerpunkt auf den Agglomerationsprozess und die Stabilität gegen Koagulation gesetzt. Es wurden Experimente mit einem gut charakterisierten Modellsystem monodisperser, nanoskaliger Primärpartikeln durchgeführt. Die Suspension wurde unter verschiedenen Bedingungen destabilisiert und agglomeriert. Der Einfluss der Stabilität der Suspension auf den Agglomerationsvorgang wurde unter perikinetischen und orthokinetischen Bedingungen sowie unter Mühlenbedingungen untersucht.

Die gewonnenen Erkenntnisse wurden wegen des großen industriellen Bedarfs an Nanopartikeln in organischen Lösungsmitteln auf nicht wässrige Systeme übertragen. Es konnte gezeigt werden, dass stabile Suspensionen von Al_2O_3 in Ethanol sowohl mit elektrostatischer als auch mit sterischer Stabilisierung erreicht werden können. Zerkleinerungsversuche mit elektrostatischer Stabilisierung zeigen, dass sich der Abrieb negativ auf die Stabilität der Suspension auswirkt. Bei der sterischen Stabilisierung hat der Abrieb keinen Einfluss. Allerdings scheint die Polymerhülle um die Partikeln Teile der Zerkleinerungsenergie zu absorbieren und somit Mahlkörperstöße zu dämpfen. Eine weitere wichtige Frage ist, ob eine mechano-chemische Aktivierung, die während der Zerkleinerung in wässriger Phase beobachtet wurde, eine entscheidende Rolle bei der Nanozerkleinerung spielt.

State of the Art in Wet Media Milling

2.1. Wet Milling in Stirred Media Mills

2.1.1. Influence of Operation Parameters. Stirred media mills belong to the class of comminution machines with loose agitated milling beads. During operation the grinding chamber is filled up to 90% with milling beads. Depending on the milling application the milling beads can consist out of glass, steel, plastics or ceramic. Typically the size of the beads is in the range of 0.1 to 3 mm. In contrast to jar mills, where the motion of grinding beads is generated by rotating the chamber, higher energy inputs can be achieved in stirred media mills, because the energy input in these mills is not restricted by a critical revolution speed. This critical revolution speed in jar mills is reached when the centrifugal force on a milling bead near the wall exceeds the gravitation force. Common rotary speeds in jar mills are in the range of 2/3 to 3/4 of the critical rotary speed. This power limitation results in relative low energy densities. The energy input in stirred media mills is generated in contrast to this by an agitator. Thus higher energy densities can be applied. Stirred media mills are predominantly used for wet milling. They can be operated in continuous or in batch mode. In continuous mode the suspension is pumped axially through the mill. To hold the milling beads back in the mill cutting slits (for milling beads $\geq$ 0.8 mm) or sieving cartridges (for milling beads $\geq$ 0.2 mm) are used. Because smaller milling beads are preferable for the comminution of nanoparticles [1, 2], manufacturers of mills offer nowadays centrifugal separation systems. These avoid the plugging of the sieving cartridge or the clamping of milling beads in the cutting slit. In general three types of stirred media mills can be distinguished: stirred media mills with disc stirrers, pinned disk mills or annular gap mills.

Numerical computations showed that around 90% of the energy is dissipated in 10% of the milling chamber volume [5]. These regions are close to the stirrer disk tip and the milling chamber wall [6]. Hence, grinding media and milling charge have to be transported in these regions. During milling almost 99% of the energy is dissipated into heat [7, 8, 9]. This is why the grinding chambers of stirred media mills are in general equipped with double walls for cooling.

An overview on wet grinding technologies for comminution and dispersing of particles is given e.g. by [9, 10, 11]. Stirred media mills can be operated in different operation modes. Apart from the batch mode one differentiates the pendulum mode with two receiver vessels and the circuit mode with feedback into a stirred tank. The different operation modes affect thereby the residence

time distribution of the suspension in the mill, which has an effect on the width of the particle size distribution. The narrowest particle size distributions are obtained usually with the pendulum mode.

Fundamental investigations of the operational behavior of stirred media mills and the influences of the different operating parameters (e.g. agitating disk peripheral speed, solid concentration, milling chamber size, flow rate, filling degree of milling media) were accomplished for years at the Institute of Mechanical Process Engineering of the TU Braunschweig. Furthermore, the scale up [12], the residence time distribution, the power consumption and the attrition of grinding media was extensively investigated [13, 14, 15, 16].

Research of Stehr [17] and Weit [12] showed that the milling result is dominated by the specific energy (the energy supplied in the milling chamber related to the mass of the product). Further investigations of Bunge [18], Thiel [19], Joost [15], Stadler et al. [20] and Mankosa et al. [21] showed that apart from the specific energy, the milling media size has an impact on the grinding result. Finer product particles can be achieved with smaller milling beads at the same energy consumption as with larger milling beads. However, a minimum bead size is necessary in order to obtain breakage at all. Kwade [22] introduced the characteristic parameters stress energy SE and stress number SN of milling beads. The stress energy is proportional to the maximal kinetic energy of the milling beads:

$$SE \approx \rho_{GM} \cdot v_t^2 \cdot d_{GM}^3. \tag{2.1}$$

This equation can be used for soft and medium hard materials, because in these cases the milling beads are not deformed. By grinding hard materials the deformation of milling beads and the product particles influences the energy transfer during a collision of milling beads. With increasing elastic modulus of the product particles an increasing part of the stress energy is used for the deformation of milling beads. Thus, less energy can be spent for the comminution of product particles. Becker [16] approximated the stress energy of the milling beads with a spring model and the Hertz equations as given by Gross et al. [23] and expanded the model of Kwade with the Young's modulus of the grinding media E_{GM} and with the Young's modulus of the particles E_p:

$$SE \approx \rho_{GM} \cdot v_t^2 \cdot d_{GM}^3 \cdot \left(\frac{E_{GM}}{E_{GM} + E_p} \right). \tag{2.2}$$

The stress number SN can be approximated according to Kwade [22] if the volume concentration of the particles, the filling ratio of milling beads ϕ_{GM}, the porosity of the milling bead bulk freight ϵ_{GM} and the milling time t is known. With the assumption that only one particle is stressed during a collision of milling beads the following equation can be derived:

$$SN \approx \frac{\phi_{GM}\left(1 - \epsilon_{GM}\right)}{\left(1 - \phi_{GM}\left(1 - \epsilon_{GM}\right)\right)c_v} \cdot n_r \cdot t \cdot \left(\frac{x}{d_{GM}}\right)^2 . \tag{2.3}$$

In figure 2.1 the median particle size is plotted over the stress energy. For each curve in the diagram the specific energy is constant. It is obvious that a certain stress intensity is necessary to achieve breakage at all. With increasing stress energy the median particle size decreases until an optimum is reached. At this optimum a minimal particle size is reached at constant specific energy. With further increasing stress energy the particle size increases. The reason for this is that the stress number decreases with increasing stress energy, if the specific energy is constant. For high stress intensities the stress number is too small to break the particles optimally.
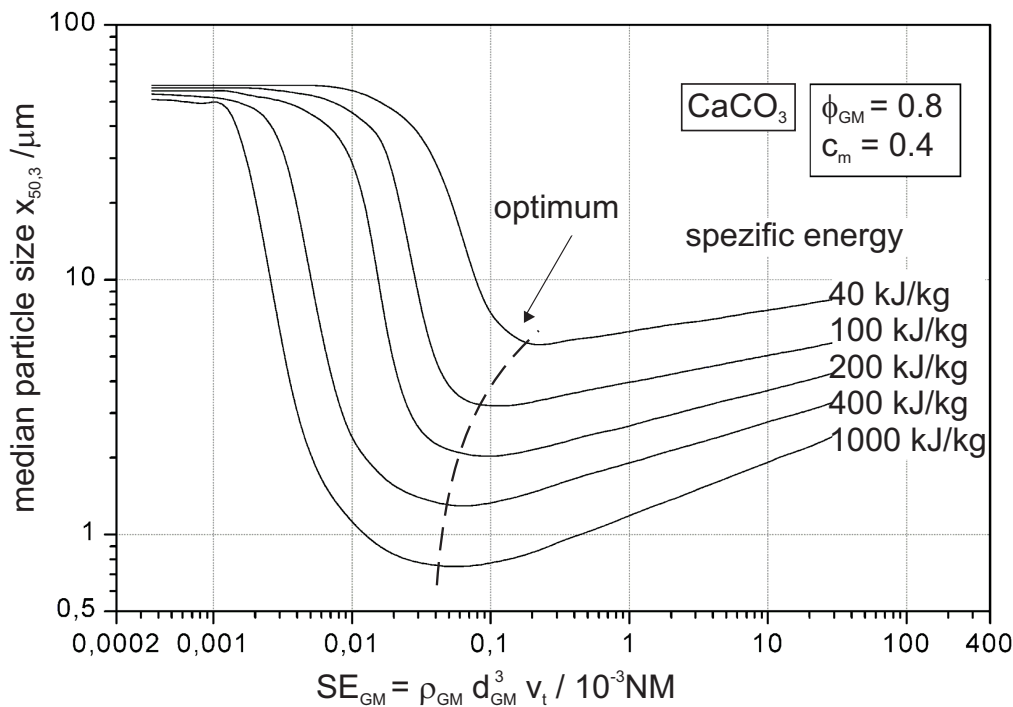
FIGURE 2.1. Optimum of the stress energy of the milling beads for different specific energy inputs for the grinding of limestone [16].

Mende [2] showed that the concept of stress intensity and stress number can be applied for nano-milling as well. Mende investigated nano-milling of alumina suspensions in aqueous phase. In his experiments the suspensions were stabilized against agglomeration electrostatically. Figure 2.2 shows the median particle size $x_{50,3}$ for α-alumina over the specific energy. For the experiments yttrium stabilized ZrO_2 milling beads with diameters between 200 μm and 1300 μm were used. Furthermore, the suspensions were stabilized at pH5 for the whole milling time. It can be seen, that at constant specific energy inputs smaller product particle sizes can be reached with decreasing milling bead

diameter. Furthermore, in these experiments product particles below 10 nm could be produced without reaching a grinding limit.
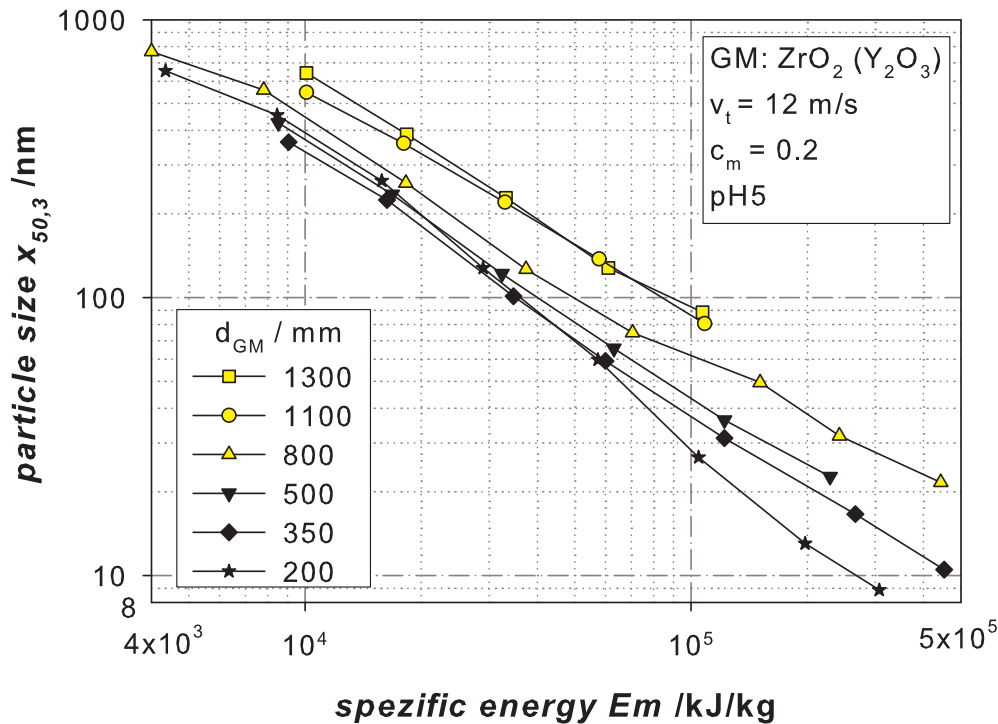
FIGURE 2.2. Influence of the milling bead diameter on the milling of alumina with yttrium stabilized milling beads [14].

Stenger [1] investigated the influence of inter-particle interactions on nano-milling in stirred media mills in aqueous phase and electrostatic stabilization and found that the grinding progress is determined mainly by the superposition of breakage, agglomeration and deagglomeration. The final particle size depends on the stability conditions of the suspension. At good stability conditions final particle sizes measured with an ultrasonic spectrometer of $x_{50,3} \leq 50$ nm for Al_2O_3 and $x_{50,3} \leq 20$ nm for SnO_2 could be achieved. On the other hand the smallest final particle sizes for the material SiO_2 and TiO_2 are only in the size range between 160 and 180 nm. The milling conditions were carefully optimized for alumina and tin oxide, but not yet for titania and silica, so that even finer sizes may be possible for the latter materials.

Stenger further showed that milling of alumina particles in water is strongly influenced by mechano-chemical changes. During milling alumina hydroxide is formed, which dissolves and influences in that way the grinding behavior in the sub micron size range. This fact might explain the possibility to "grind" alumina particles down to median particles sizes below 10 nm. However, by milling SnO_2 no influence of mechano-chemistry was detected at all. Crystallite sizes obtained von Rietveld analysis of the XRD spectrum (line broadening) was almost similar to BET based diameters, i.e. almost single crystals were obtained

for SnO_2. The reasons when a material is influenced by mechano-chemistry are not yet understood.

The most important conditions for producing nanoparticles in stirred media mills are: stress intensity sufficient to break even the very small nanoparticles, high stress frequency to stress enough particles per unit time, and controlled particle-particle interaction so that newly produced fragments are stabilized and the flowability of the suspension remains sufficient.

2.2. Milling in Organic Solvents

Milling experiments with non-aqueous dispersions have not been reported frequently in the scientific literature. However, a variety of papers dealing with planetary ball mills exist. Zheng et al. [24] used for example a planetary ball mill to mill the pigment Vat Blue RS in the presence of organic solvents. They found that in dependency of the used solvent a transformation of the crystal phase can occur. In polar solvents such as water, ethanol, methanol and ethylene glycol the crystal phase was unchanged. However, the amorphous phase increased reducing the color strength and dulling the shade. In weakly polar aromatic solvents (dichlorbenzene, toluene, chlorbenzene and xylene) the pigment completely transformed to the α-form with superior color properties. Lomayeva et al. [25] studied the influence of surfactants on the characteristics of iron powder obtained by mechanical milling in heptane with a planetary ball mill. They found no changes compared to the initial powder after 1 h milling in heptane with Mössbauer spectroscopy. However, for longer milling times Fe_3C was formed. The initial particle size they used was 300 μm. Without surfactant particle sizes of 5 - 20 μm could be reached after 47 h of milling. By using surfactant (oleic acid) particle sizes of 2 - 5 μm were reached. After milling of Fe in heptane the authors found carbon saturated surface layers. Similar results were found by the authors of paper [26].

The authors of reference [27] milled iron powder in different organic environments and studied the influence of the milling environment on the process of the formation of carbides and nitrides. Furthermore, changes of surface and bulk characteristics of the powder hematite and barium ferrite milled in the presence of surfactant have been studied [28, 29]. Papirer et al. [30] milled the mineral muscovite (potassium aluminum silicate hydroxide fluoride) in a series of organic solvents and measured the resulting specific surface area after a grinding time of 12 h in a ball mill. The authors found that the increase in the surface area is dependent on the electron donating properties of the liquids. The specific surface area for the ground muscovite in dimethyl sulphoxid was for example 6 m^2/g, whereas in chloroform the corresponding value was 48 m^2/g under similar grinding conditions.

However, a transfer of the findings in the experiments with ball mills to stirred media mills is questionable, because in both kind of apparatuses different operating conditions are present. In ball mills lower energy inputs and lesser

activation of the particle surfaces can be realized than in stirred media mills. Also the attainable particle size with ball mills (< 100 μm) is clearly larger than in stirred media mills (< 10 μm).

2.3. Influence of Chemical Grinding Additives on Wet Milling

Grinding additives in low concentrations are used in wet mills as well as in dry mills in order to enhance the effectivity of the milling process. Klimpel et al. [31] and Fuerstenau [32] give an overview of frequently used grinding additives.

In the earlier literature the reduction of the mechanical strength of particles by adsorption of grinding additives on the particle surface was discussed, the so called Rehbinder effect [33]. Nowadays it is agreed that the grinding additives act mainly due to their effect on the slurry rheology and their influence on the reagglomeration affinity of freshly produced surfaces rather than on the Rhebinder effect. Now it is known that the breakage energy is is much higher than the surface energy and that an adsorption of surface active substances in the crack tip can be barely influence the breakage [1, 4, 34, 35].

El-Shall and Somasundaran [36] give an overview of the use of grinding additives on base of an extensive literature study. They found that the results of many studies are contradictory and often incomparable, because important parameters as the properties of the particles, the surface characteristics (ζ-potential, pH-value, ionic strength...), temperature, chemical composition of the suspension and last but not least the stressing conditions in the mill are mostly not reported. They summarize that grinding additives influence the milling process due to the following mechanism:

- Influence of the rheology of the suspension during milling.
- Reagglomeartion of the freshly produced surface.
- Interactions of particles, grinding beads and the wall of the milling chamber.
- Interparticle interactions.
- Possibility of foam building during milling.

Wang and Forssberg [37] studied the effect of grinding additives on the suspension rheology of a dolomite suspension. They varied the solid concentration between 65 and 75 wt% as well as the concentration of grinding additive (Dispex N40, from 0.5 to 1.5 wt%) and found that:

- The grinding additive reduces the yield stress in the suspension and reduces the viscosity of the milling suspension.
- An increase of the solid concentration leads with and without grinding additive to an increase of the viscosity.
- By using grinding additives the milling effectiveness and the production of fines is increased with increasing solid concentration.

- With higher concentration of grinding additives smaller particle sizes can be produced, while with a lower concentration the viscosity increases rapidly.
- By milling dolomite organic additives are more effective than inorganic additives. The difference is explained by a different structure of the molecules.
- The authors further found the best milling result at high suspension viscosities if the grinding additive is added periodically to the suspension. A yield stress in the suspension has to be avoided.

The influence of the solid concentration is material and particle size dependent. Contradictory milling studies exist in the literature regarding the effect of the solid concentration [1, 34]. With increasing solid concentration the milling process can be improved but also worsened. However, it is agreed that in higher concentrated suspensions smaller particle sizes can be reached with the help of grinding additives and that higher throughputs can be realized at higher concentrations.

Reinsch [34] found that grinding additives are only effective above a certain solid concentration or accordingly a certain particle size. She further showed that the optimum of the energy consumption can be moved to higher solid concentrations by the help of shear thinning grinding additives. According to Reinsch the median distance between the particles can be used as characteristic to describe the effectiveness of the grinding additive.

Stenger et al. [1, 38, 39, 40, 41] studied nanomilling of oxide materials in stirred media mills and found that the milling result is mainly influenced by the suspension stability. He showed that the suspension stability can be controlled in a wide range by electrostatic stabilization. He further showed that the yield stress can be correlated with the ζ-potential of the suspension. However, no direct influence of the suspension viscosity on the breakage mechanism was found. The suspension viscosity influences rather the ability to pump the suspension and thus influences directly the final particle size.

Zheng et al. [42] studied the effect of additives on stirred media milling of limestone. They found that the energy consumption of the mill can be lowered by adding polymers to the milling suspension, because the additives improve the flowability of the suspension. However, the additive concentration must be optimized. Dosage below or above the optimized value results in both lower product surface area and lower energy efficiency. Also the molecular weight plays an important role. The product fineness and energy efficiency increases with molecular weight until 5000 g/mol and decreases again for higher molecular weights. A higher energy input was observed for larger molecular weights, which could be due to increasing particle flocculation caused by the polymer. Haas et al. [43] studied the properties of commercially available polymeric dispersant regarding their dispersing ability, milling efficiency and stabilization against agglomeration and Ostwald ripening for a broad spectrum of polymers. They

showed that the chemistry of the used polymeric dispersant, the molecular weight and the ratio between hydrophilic and hydrobhobic parts of the polymer are important to the stability of the particles. Although, the authors presented a large screening test of different polymers, further physio-chemical investigations are necessary to get a relationship between the properties of the polymers and their behavior in the formulation.

Although it is known that polymer chains in solution can be disrupted in high shear situations by pure mechanical forces, no systematic studies of the degradation of the polymeric dispersant in stirred media mills are available in the accessible scientific literature. If the chain length of the polymers is reduced due to the stressing conditions in the mill, the polymers might loose their effectiveness for stabilization of the suspension and might change the rheology of the suspension. In chapter 9 of this work the literature of degradation of polymers in shear fields and the theoretical background of chain scission is shortly summarized. Only one study from Karis et al. [44] was found, who studied the mechanical scission of polymers in a stirred media mill.

2.4. Mechano-chemical Changes during Milling

It is commonly known that the mechanical activation of solids by applied stresses can lead to the development of various solid state reactions. The reactivity of such activated solids is strongly influenced by the mechanochemical treatment. Mechano-chemical activation can further lead to phase transformations, improved sinterability, higher solubility of the material or even new material compositions. Thus, a measurement of the particle size alone is not sufficient to describe the milled product completely. The milled product has to be characterized further for mechano-chemical changes. In the following section mechano-chemical changes of alumina and iron oxide particles are summarized.

2.4.1. Mechano-chemical Changes during Milling of Al_2O_3. Many experimental investigations were done studying the influence of different milling devices on texture, structure, phase transformation and thermal behavior of various aluminas and their hydroxides [1, 45, 46, 47, 48]. In general, however, the reported mechano-chemical phenomena are very complex in nature and are often inconsistent with each other due to the different intensities and types of mechanical stresses that are induced by different milling devices. In a wide range of papers mechano-chemical effects during milling of Al_2O_3 in dry grinding processes were described [48, 49, 50, 51, 52]. However, a few authors studied the influence of water on the mechano-chemical reactions induced by wet milling [1, 39, 53, 54, 55, 56]. Fritsch [55] and Oberacker et al. [56] showed that a change of phase composition from α-alumina to an aluminum tri-hydroxide phase can occur during wet milling in aqueous phase. Kikuchi et al. [57] studied the change of mechano-chemical factors such as lattice deformation and lattice strain during wet grinding of α-alumina in a vibration ball

mill over time. They showed that there is a large difference between dry and wet grinding. In contrast to dry milling no lattice deformation occurred during the wet milling process. Stenger et al. [**39**] showed that mechano-chemical changes occur during milling of alumina in water with electrostatic stabilization. In the milling experiments a remarkable amount of bayerite was formed from α-alumina. The emerging bayerite phase could be quantified using dynamic scanning calorimetry (DSC) and thermogravimetric measurements. Stenger [**1**] further showed that these mechano-chemical changes influence the grinding mechanism, because the formed hydroxide phase is dissolved from the particle surface especially at low pH values, leading to particle sizes far below 50 nm.

2.4.2. Mechano-chemical Changes during Milling of Fe$_2$O$_3$. In the literature several studies can be found dealing with mechano-chemical changes of α-Fe$_2$O$_3$ in ball mills. The effects of milling iron oxide particles are complex. Depending on the sample environment and contaminations of the mill material a variety of phases - crystalline, nano-structured as well as amorphous and disordered states can be obtained [**58**]. The partial pressure of oxygen has a critical influence on the transformation from α-Fe$_2$O$_3$ to Fe$_3$O$_4$ (magnetite) when α-Fe$_2$O$_3$ is mechanically milled [**59, 60**]. The transformation is favored when α-Fe$_2$O$_3$ is milled under vacuum or argon atmosphere. The transformation can also take place under ball milling in air if the vial remains closed [**60, 61**]. Hofmann et al. [**58**] milled α-Fe$_2$O$_3$ in vacuum with a small amount of water in a ball mill. They found that a transformation process from α-Fe$_2$O$_3$ to the γ phase occurred as a result of the shearing during low energy ball milling involving movement of the oxygen planes. This behavior was also found by Meillon et al. [**62**]. After longer milling times and continued exposure to impact and shearing forces the oxide surface layers were ruptured leading to an release of oxygen with consequent reduction to Fe$_{3-x}$O$_4$ [**29, 58, 63**]. The main crystalline products were non-stoichiometric magnetite (Fe$_{3-x}$O$_4$) and the untreated α-Fe$_2$O$_3$. Betancur [**64**] showed that magnetite (Fe$_2$O$_3$) is the only phase after ball milling of hematite with water under vacuum in a sealed ball mill. Besides this rupturing process part of the Fe$_3$O$_4$ produced during milling was an effect of wear of the mill which consisted of iron [**58**]. This iron contamination leads to the reaction:

$$4\alpha - \text{Fe}_2\text{O}_3 + \text{Fe} \rightarrow 3\text{Fe}_3\text{O}_4. \tag{2.4}$$
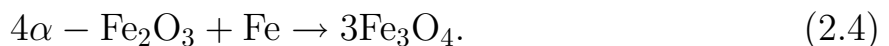
However, Hofmann et al. [**58**] and Linderoth et al. [**61**] concluded that the level of Fe contamination from the mill could not explain the amount of Fe$_3$O$_4$ resulting from ball milling. Zdujic et al. [**60**] and Borzi et al. [**59**] found that hematite remains unchanged by dry milling in an unsealed mill. Due to the availability of oxygen any phase transformations were suppressed and hematite nanoparticles were obtained.

Uehara [65] studied the influence of different solvents on the structural changes of iron oxides. He found that the γ-Fe$_2$O$_3$ phase was stable in water. In polar organic media, neither structural changes nor line broadening of X-ray diffraction patterns was observed. In non-polar solvents γ-Fe$_2$O$_3$ and Fe$_3$O$_4$ were transformed into α-Fe$_2$O$_3$ and α-Fe$_2$O$_3$ remained unchanged. The author further showed that mechano-chemical reactions are most likely a characteristic of milling in steel ball mills. Because, by milling γ-Fe$_2$O$_3$, Fe$_3$O$_4$ and α-Fe$_2$O$_3$ in a ceramic mill no changes in the structure occurred at all. Randrianantoandro et al. milled hematite powder with ethanol in a conventional planetary ball mill and showed that a complete transformation from α-Fe$_2$O$_3$ to maghemite γ-Fe$_2$O$_3$ without the formation of magnetite Fe$_3$O$_4$ is possible [65].

Contradictory to these findings are studies from Sorescu [66] and Dutta [67] who found that magnetite is transformed to hematite by ball milling in air atmosphere. Sorescu further showed that the particle morphology plays a crucial role in determining the phase transformations induced in hematite by high energy ball milling [68]. Furthermore, Sorescu et al. [69] showed that the presence of iron during ball milling of magnetite inhibits the transformation to hematite. By milling of hematite with iron in an inert atmosphere magnetite is formed [70].

In the literature many publications about magnetic properties of hematite particles exists. According to this ideal hematite is weakly antiferromagnetic and shows only a low magnetizability [59, 71]. According to Clauß [71] the magnetizability for synthetic hematite is much lower (0.3 Am^2/kg) than for natural hematite. Below a temperature of $T_M = 263$ K hematite is a perfect antiferromagnet [59, 72, 73]. This temperature is called Morin temperature after F.J. Morin, who discovered this transition point [74]. Between the Morin temperature and the Néel temperature (T$_N$ = 955 K) hematite shows weakly ferromagnetic behavior. The Néel temperature is the critical temperature at which the ferromagnetic behavior changes to paramagnetic behavior. The transition temperatures can spread over a temperature interval in respond to sample preparation, impurities and particle and grain size [59, 71]. The Morin temperature decreases if the particle size decreases or if strain defects appear [71]. Furthermore, the transition temperatures are dependent on the applied field [71]. With higher applied fields the transition temperatures are lower. No magnetic interactions between ball milled hematite particles were noticeable [61, 59]. However, strong magnetic particle interactions could be measured after a magnetic field was applied to the sample [59]. However, these magnetic interactions vanished as the sample was treated with ultrasonic vibrations, because the ordered domains in the particles are able to relax by this treatment. Consequently the sample preparation and milling conditions must be carefully chosen to avoid magnetization of the particles, since ferromagnetic particles can remain magnetized after removal of the field [75]. Initially stable suspension in respect to aggregation in the absence of a magnetic field can be destabilized

by applying a magnetic field. Chin et al. [**76**] studied magnetically induced aggregation and found that magnetic particles respond to an applied magnetic field by forming aggregates corresponding to the field direction [**76**]. However, without applying of a magnetic field they also found no magnetic interactions of their particles.

Theoretical Background

In the following chapter the theoretical background, which is necessary for the understanding of the presented work is shortly summarized. In particular the state and the properties of particle surfaces in the liquid phase are discussed. Based on this, possibilities to influence the interparticle interactions and with it the stabilization of the particles against agglomeration are described. Closely connected to the particle-particle interactions is the flowability of the suspension, which influences the energy consumption of the mill as well as the stressing mechanism of the particles between the milling beads and the amount of attrition.

3.1. Fundamentals of Inter-Particle-Interactions

The properties of colloidal suspensions, like the agglomeration behavior and the suspension rheology, are strongly influenced by interparticle interactions. These are dependent on the surface properties of the particles. The processes at the solid liquid interface leading to interparticle interactions are important for the understanding of the presented work and are therefore introduced in the following. A detailed description of this issue can be found for example in Russel et al. [77], Hunter et al. [78], Israelachvilli [79] and Lagaly et al. [80].

3.1.1. Van der Waals Interactions. Stirred media mills can be used for the comminution of particles down to the nanometer size range [1, 2, 45, 38, 39, 81]. The behavior of particles below 10 μm is increasingly influenced by surface effects. The forces between particles due to van der Waals interactions can be several orders of magnitude larger than the particle weight. The van der Waals interaction affects the physical behavior of the suspension increasingly with decreasing particle size and so influences the operation performance of the mill. Agglomeration of particles can occur in the mill due to the van der Waals attraction leading to an inhibition of the milling progress. At the same time the flowability of the suspension and with it the energy consumption for the comminution are influenced. On the microscopic level the stressing of particles between impacting milling beads is affected, too. The origin of the mostly attractive van der Waals forces is the interaction between induced dipoles, which arise due to orientational effects between molecules with permanent dipoles or induction effects in neutral particles. Dispersion forces are quantum mechanical in origin and depend on the fluctuation of electron clouds. This results in an instantaneous dipole which generates an electric field that polarizes any other nearby atom, inducing a dipole moment in it. The resulting interaction between

the two dipoles gives rise to an instantaneous force between the two atoms. In the classic calculation method according to Hamaker [82] the intermolecular forces are accumulated pairwise while retardation effects are neglected. For two spheres with radius a_1 and a_2 at a surface to surface distance h the interaction Φ_{vdW} becomes:

$$
\begin{aligned}
\Phi_{vdW} = - \frac{A}{6} \cdot \Bigg[&\frac{2a_1 a_2}{h^2 + 2h(a_1 + a_2)} + \frac{2a_1 a_2}{h^2 + 2h(a_1 + a_2) + 4a_1 a_2} + \\
&+ ln \left(\frac{h^2 + 2h(a_1 + a_2)}{h^2 + 2h(a_1 + a_2) + 4a_1 a_2} \right) \Bigg] .
\end{aligned}
\tag{3.1}
$$

In this equation A is the material specific Hamaker constant, which is very difficult to quantify precisely. Hamaker constants can be measured e.g. from adsorption of small molecules interacting only through van der Waals forces [83, 84, 85, 86] or by means of Lifshitz-theory as a function of frequency dependent dielectric constants. The Hamaker constants between different materials may be approximated from known Hamaker constants of the individual materials using combining relations. A frequently used combining law is given by Israelachvilli [79]:

$$
A_{123} \approx \left(\sqrt{A_{11}} - \sqrt{A_{33}} \right) \cdot \left(\sqrt{A_{22}} - \sqrt{A_{33}} \right) .
\tag{3.2}
$$

where A_{123} is the non-retarded Hamaker constant for media 1 and 2 interacting across medium 3. The combining relations are applicable only when dispersion forces dominate the interactions, but they break down when applied to media with high dielectric constants.

Hamaker constants can also be approximated using the Liftshitz theory. Here the problem of additivity is completely avoided since the atomic structure is ignored and the forces between large bodies are treated as continuous media. The Hamaker constant can be calculated using dielectric constants and refractive indices. A calculation requires that the dielectric and optical properties of the materials are known at all wavelengths. Since these full spectra data are difficult to obtain for most materials, a number of approximation equations were developed [87, 88, 89, 90]. Recent Lifshitz calculations for a number of solids (titania, silica, graphite) interacting across water did show that the maximal error induced by equation 3.2 is less than 25% [91]. In this case the full spectra given in literature were used. The following approximation can be used, if the absorption frequencies of all three media are assumed to be the same [79]:

$$
\begin{aligned}
A \approx & \frac{3}{4} kT \left(\frac{\epsilon_1 - \epsilon_3}{\epsilon_1 + \epsilon_3} \right) \left(\frac{\epsilon_2 - \epsilon_3}{\epsilon_2 + \epsilon_3} \right) + \\
& + \frac{3 h \upsilon_e}{8\sqrt{2}} \cdot \frac{\left(n_1^2 - n_3^2 \right) \left(n_2^2 - n_3^2 \right)}{\left(n_1^2 + n_3^2 \right)^{(1/2)} \left(n_2^2 + n_3^2 \right)^{(1/2)} \left[\left(n_1^2 + n_3^2 \right)^{(1/2)} + \left(n_2^2 + n_3^2 \right)^{(1/2)} \right]} .
\end{aligned}
\tag{3.3}
$$

Table 3.1 gives Hamaker constants for oxide minerals interacting in aqueous phase.

TABLE 3.1. Hamaker constants for some typical materials in aqueous phase ($\sharp$: calculated from full spectral data).

Material	Hamaker constant $A/10^{-20}$J
Al_2O_3	4.2-5.3 [79]; 3.11 [91]; 2.75$^\sharp$ [92]
Fe_2O_3	4.52 [77]
SiO_2 (crystalline)	1.7 [77, 79]; 1.6$^\sharp$ [92]
SiO_2 (fused)	0.85 [77]
ZrO_2	13 [79]

3.1.2. Electrostatic Interactions. Interfaces in solvents carry often electrostatic charges. The origin of these charges is discussed in the following sections. There are excellent monographs discussing the subject in much greater detail than it can be presented here [77, 78, 79, 80, 93, 94]. However, most of the work is devoted to an aqueous medium; solvents with low dielectric constant (say < 10) are very sparse. In the next section only the most important topics are summarized.

3.1.2.1. *The Origin of Surface Charges in Aqueous Media.* For the formation of charges in colloidal systems the following mechanisms are known [77, 95]:

- The dissociation of surface groups in liquids with a high dissociation constant explains for many cases the origin of surface charges. Surfaces that carry groups such as sulfates, carboxyl, hydroxyl and oxides will acquire charges, if the free energy of the system favors their dissociation. The formation of counter ions in the liquid maintains the electrical neutrality.
- Solids that have some solubility in their surrounding medium can acquire charge by dissolution of either a cation or an anion from the particle surface. This mechanism acts mainly for inorganic solvents in aqueous media. In case of crystals (e.g. AgJ) the charge arises by dissolution or adsorption of the crystal building ions. In dependency of the composition of the solvent Ag^+ or J^- dissolve from the surface. This leads to a negative (in case of Ag^+- dissolution) or a positive (in case of J^-- dissolution) surface charge. These ions are referred to potential determining ions. Special cases are mineral oxides, like Al_2O_3, TiO_2 or SiO_2. The surface charges of these materials are produced due to adsorption or desorption of protons (H^+) in the surface area. Hence, the surface charge changes with the pH value of the dispersion, as demonstrated in figure 3.1.
- In many systems the adsorption of potential determining ions from solution leads to surface charge.
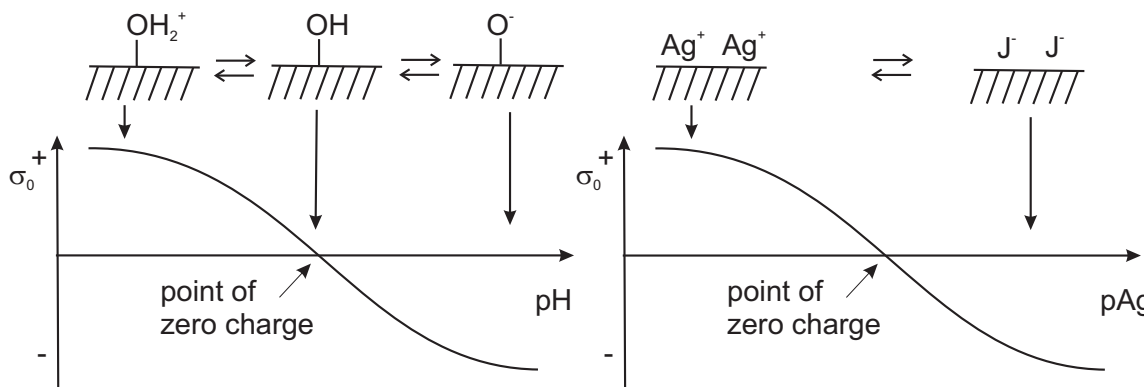
FIGURE 3.1. Influence of potential determining ions.

- The net surface charge is determined by the surface equilibrium constants involved in complex systems including several equilibria.
- Adsorption of polymers with polar end groups leads to surface charges.

The point where the surface charge is zero is defined as the point of zero charge (pzc). The pzc is material dependent and can be determined experimentally by charge titration. It is important to distinguish the isoelectric point (iep), where the measured ζ-potential is zero, from the pzc.

3.1.2.2. *The Origin of Surface Charges in Organic Liquids.* Although the origin of the charge is fairly well known for aqueous dispersions, the mechanisms operating in non-aqueous liquids are not as clearly understood or agreed on. Because of the low dielectric constants of most organic liquids, dissociation of surface groups and ionization of the electrolytes are limited. Often ionic strengths are much lower than 10^{-6} M. Charges on the particle surface in organic media can arise by the following mechanisms:

- Verwey [96] proposed, in 1941, for the surface charge of inorganic oxides suspended in organic liquids an acid-base mechanism involving protons or hydroxyl ions as potential determining ions. Acid-base interactions involving proton transfer are responsible for the creation of surface charge.
- Donor-acceptor interactions with electron transfer between surface and solvent can lead to surface charges. The sign of the surface charge depends on the direction of the electron transfer [97].
- In non-aqueous solvents the adsorption of impurities (even in traces [80]) can lead to charging of the particles.
- Traces of water can change the surface charge, because water can act directly as a base or can transfer a proton to the solvent. In this case OH^--groups of the surface can be bonded.

In case of the acid-base and the donor-acceptor mechanism the surface charge correlates with the donor properties of the solvent, i.e. the Gutmann donicity series [98]. The donor number DN is a qualitative measure of Lewis basicity and is defined as the negative enthalpy value for the reaction of the organic solvent

with the standard Lewis acid $SbCl_5$ in 1,2-dichlorethane [99]. The higher the donor number the easier is the electron transfer between the particle surface and the solvent and the higher is the surface charge. The sign of the surface charge depends on the direction of the electron transfer. Likewise the acceptor number AN was introduced by Gutmann as a scale for the acceptor strength of organic solvents [98]. Extensive tabulation of the donor and acceptor numbers of most organic solvents is given in the literature e.g. [98, 100]. Labib showed [95], that the ζ-potential for α-Al_2O_3 and TiO_2 particles suspended in organic liquids are positive for low donor numbers ($DN < 10$ kcal/mol) and acceptor numbers higher than 20. In this case the acceptor strength of the liquids outweighs their donicity and they behave as acceptors (acids). In solvents with donor numbers around 10 kcal/mol or higher the potential became negative up to -40 mV. With increasing donor numbers the negative charge was declining. In contrast to α-Al_2O_3 and TiO_2 no point of zero charge could be found for SiO_2 particles. The charge for SiO_2 particles was in all solvents negative.

According to Labib [95] the mechanism of charging in protonic organic liquids that have a finite dissociation constant should be similar to that of water. The mechanism is based on the fact that the particle (P) will act for the solvent (S) as a proton donator or acceptor.

$$PH_2^+ + S^- \iff PH + SH \iff P^- + SH_2^+. \tag{3.4}$$
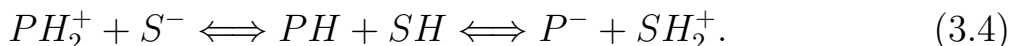
Protonic liquids are liquids which can react by loss or gain of a proton. Examples for dissociation constants are summarized in table 3.2.

TABLE 3.2. Dissociation constants.

H_2O	$K_W = [H^+][OH^-] = 10^{-14}(mol^2l^{-2})$
CH_3OH	$K = [H^+][CH_3O^-] = 10^{-17}(mol^2l^{-2})$
CH_3-CH_2OH	$K = [H^+][CH_3 - CH_2O^-] = 10^{-15.9}(mol^2l^{-2})$
CH_3-$(CH_2)_3$-OH	$K = [H^+][CH_3 - (CH_2)_3 - O^-] = 10^{-17.6}(mol^2l^{-2})$

In aprotic liquids, whose molecules can not accept or donate protons or electrons, e.g. non-polar organic solvents, saturated hydrocarbons or crude oil fractions, charging of particles can only occur by adsorption [80, 95]. In those media only little screening of charges occurs and the Debye-Hückel screening parameter κ is relatively small.

3.1.2.3. *The electrical Double Layer.* Since the system as a whole is electrically neutral the surface charges of the particles are electrically equalized by charges in the dispersion medium of the opposite sign. These charges are carried by counter ions, which move freely under the influence of electrical and thermal forces in the so called diffuse layer. The distribution of the counter ions in dependency of the distance from the particle can be described with the Gouy-Chapman-model with the following simplifying assumptions:

- Ions in solution are point charges.
- The electrolyte is an ideal solution with uniform dielectric properties.
- Surface charges and potentials are evenly spread over the particle surface.

Starting from the Poisson equation, which describes the charge density at a location x in an electrical field with the electrostatic potential φ and the dielectric constant ϵ and a Boltzmann distribution for the ions in the potential field, the Poisson-Boltzmann distribution can be formulated for a symmetrical electrolyte:

$$\frac{d^2\varphi}{dh^2} = \frac{2F \cdot z \cdot c_0}{\epsilon_r \epsilon_0} sinh\left(\frac{z \cdot F \cdot \varphi}{\Re \cdot T}\right). \tag{3.5}$$

where z is the valence of the ions F the Faraday constant and c_0 the concentration of ions in the bulk phase. Linearization of the sinh-function for small potentials, $\varphi \leq 25$ mV, leads to the Debye-Hückel approximation:

$$\frac{d^2\varphi}{dh^2} = \kappa^2 \varphi. \tag{3.6}$$

where κ is the so called Debye-Hückel-parameter:

$$\kappa^2 = \frac{2F^2}{\epsilon_r \epsilon_0 \cdot \Re \cdot T} \cdot \left(z^2 \cdot c_0\right) = \frac{2F^2}{\epsilon_r \epsilon_0 \cdot \Re \cdot T} \cdot I. \tag{3.7}$$

with I being the ionic strength. The Debye-Hückel parameter κ has the dimension of an reciprocal length. κ^{-1} is a measure of the extension of the electric double layer. Solving equation 3.6 leads to:

$$\varphi = \varphi_0 exp\left(-\kappa \cdot h\right). \tag{3.8}$$

where φ_0 denotes the electrostatic potential at the surface ($x = 0$). Hence the potential decays exponentially with the distance from the surface. Stern (1924) and Graham (1947) improved the model from Gouy-Chapman by assuming a finite expansion of the hydrated ions. According to this the concentration of ions at the particle surface is limited and can not exceed a saturation value. Part of the counter ions are adsorbed on the particles surface in a layer of thickness δ_s. The ions in the so called Stern layer are not necessarily connected to the particle surface; especially hydrated ions will be separated from the surface by water molecules. The electrostatic potential in the Stern layer decays in the simplest case linearly from the surface potential φ_0 to a potential φ_s the Stern-potential. Outside of the Stern layer the counter ions are building a diffuse double layer according to the Gouy-Chapman model. If more counter ions are adsorbed as necessary to neutralize the surface charge, a change of the sign of the surface charge will occur. This is especially common for polyvalent ions, which are not bound equivalent but equimolar [80]. Figure 3.2 shows the assembly of the

electrical double layer according to the Stern-Graham model including charge enhancement due to specific adsorption of ions and the resulting potential curve.
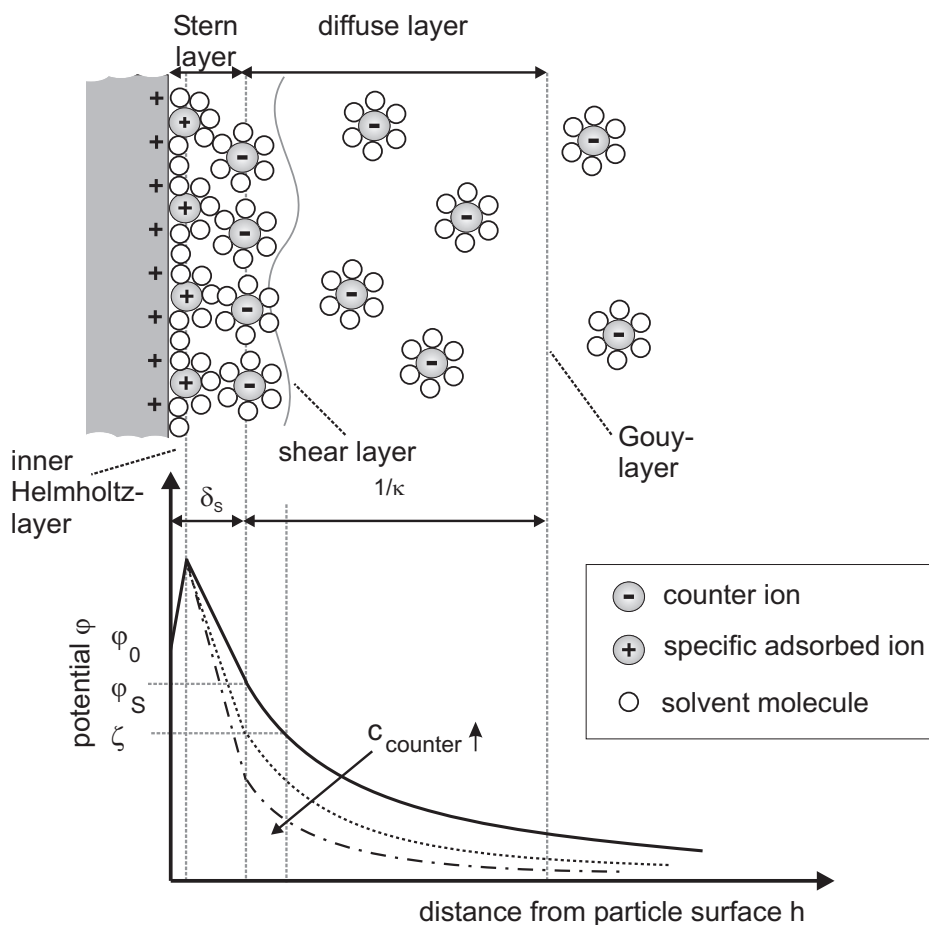
FIGURE 3.2. Assembly of the electrical double layer according to the Stern-Graham model including charge enhancement due to specific absorption of ions [1].

Furthermore, figure 3.2 shows the influence of electrolyte concentration on the potential development. With increasing ion concentration the screening of the surface charge is enhanced and the decay of the electrostatic potential is steeper. The valence of ions in solution has a similar effect. Polyvalent ions are able to screen charges of the surface more effectively. This leads to a compression of the double layer.

Experimental examinations of charged particle surfaces exploit mostly titrations or electrokinetic phenomena. A charged particle will move with a certain velocity in an electric field. This phenomenon is called electrophoresis. The particle's mobility is related to the dielectric constant and viscosity of the suspending liquid and to the electrical potential at the boundary between the moving particle and the liquid. This boundary is called the shear plane and is usually defined as the point where the Stern layer and the diffuse layer meet. The Stern layer is considered to be rigidly attached to the colloid, while the diffuse layer is not. As a result, the electrical potential at this junction is related to the mobility of the particle and is called the ζ-potential. Experimentally the

ζ-potential can be determined with the methods of electrophoresis, streaming potential, electroosmosis or electroacoustics [**94**].

A new promising technique to measure surface electrostatic potentials and surface charge densities directly is the method of second harmonic spectroscopy (SHG) [**101, 102**]. This method has some advantages over traditional techniques, since no assumptions have to be made to determine the surface charge. In order to obtain the surface potential using traditional techniques from the ζ-potential assumptions about the distance between the shear layer and the interface have to be made, since it is not precisely known where the shear surface is located.

3.1.2.4. *Electrostatic Double Layer Interaction.* If two charged particles in an electrolyte solution are approaching each other so closely that their double layers overlap an electrostatic repulsive force is generated. This force is due to the repulsion of identically charged surfaces and due to an osmotic pressure, which is based on dilution effects of the salt concentration in the gap between the two approaching spheres. The repulsive force can be obtained from the numerical solution of the Poisson-Boltzmann equation. However, a variety of approximations exist. The Derjaguin approximation [**103**], for example, is applicable for small separations compared to the radius of the spheres. It is assumed that each sphere is divided into infinitesimal elements, which are considered to be parallel planar elements at the same separation. The total interaction is the sum over the interactions of the infinitesimally small elements. An analytical solution of the differential equation requires further assumptions, which are mostly the two borderline cases: constant surface potential or constant surface charge. Both conditions are barely applicable to real systems. The error for constant potential boundary remains small for small separations and is larger for longer distances. Conversely, the constant charge boundary condition is invalid at separations smaller than the Debye thickness. A good discussion of the differences between electrostatic interactions at constant charge and constant potential is given by Russel et al. [**77**].

A further method to approximate the repulsive energy is the linear superposition of single sphere potentials. This method is a good compromise between the two borderline cases and is therefore often used in practice. For a detailed discussion of the technique see [**104**]. Table 3.3 lists approximate forms of the electrostatic energy for two spheres with radius a over surface to surface distance h in a symmetric electrolyte.

3.1.3. Born Interactions. If two particles approach each other to very small distances the electron clouds of the atoms overlap and a resulting strong repulsive force - the Born repulsion arises. This repulsive force is characterized by having short range efficacy and increases very sharply if two molecules come closely together. Strictly, the distance dependency of the Born interaction should be described by quantum mechanical theory. Instead, simplifying

TABLE 3.3. Approximate forms of the electrostatic energy.

Constraint	Electrostatic energy
Constant potential	$\Phi_{el} = 2\pi\epsilon_r\epsilon_0 \left(\dfrac{kT}{ze}\right)^2 a \cdot \left(\dfrac{\varphi_s ez}{kT}\right)^2 ln\left(1 + e^{-\kappa \cdot h}\right)$ (3.9)
Constant charge	$\Phi_{el} = -2\pi\epsilon_r\epsilon_0 \left(\dfrac{kT}{ze}\right)^2 aq^2 \cdot ln\left(1 - e^{-\kappa \cdot h}\right)$ (3.10)
Superposition	$\Phi_{el} = 32\pi\epsilon_r\epsilon_0 \left(\dfrac{kT}{ze}\right)^2 a \cdot tanh^2\left(\dfrac{\varphi_s ez}{4kT}\right) exp\left(-\kappa h\right)$ (3.11)

approximations are established. The three most common of such potentials are the hard sphere potential, the inverse power-law potential (exponent -12) and the exponential potential [79].

3.1.4. Solvation, Structural and Hydration Interactions. At small separations between two particle surfaces closer than a few nanometers the continuum theories for attractive van der Waals and repulsive double layer interactions often fail to describe the interactions. This is either because the continuum assumption of one or both types of interactions is not valid or because additional non-DLVO forces come into play [105]. These forces can be attractive, repulsive or oscillatory and they can be much stronger than the DLVO forces at small separations [79]. These repulsive forces appear due to a structural effect of the suspending fluid near particle surfaces, because at small separations the solvent molecules have to be squeezed out of the gap between the two approaching surfaces leading to an oscillating force with exponential increasing amplitude. These oscillatory forces are dependent on the type of solvent molecules. While linear chain molecules (e.g. n-decan) show significant high oscillations, molecules with an irregular structure, which cannot be ordered into regular layers, do not. An ordered layer around the particle can also be disrupted by surface roughness, even if the roughness is in the order of only a few Angstrom.

In aqueous suspensions an additional repulsive interaction was observed for the material SiO_2 [106]. Due to hydrogen bonding between silanol-groups and surrounding water molecules a structured layer of water molecules on the silica surface is formed, leading to the additional hydration force. The density of silanol-groups increases as the pH-value decreases. This is leading to a surprisingly large hydration force at low pH values and to very stable suspensions near the isoelectric point [107].

3.2. Stabilization of Particles against Aggregation

3.2.1. Introduction. Under stabilization different topics can be understood. A distinction can be drawn between:

- stabilization against chemical reactions (e.g. oxidation)
- stability against phase changes
- stability against sedimentation
- stability against coagulation
- stability against ripening of primary particles into a hard agglomerate

In the following only the stabilization against coagulation is considered. The relative motion of particles (especially of nanoparticles) as well as attractive interactions can lead to coagulation. Thus agglomerates are built, which can affect the handling and the properties of the final product considerably. Typical undesirable phenomena include:

- sedimentation
- building of solid bridges (Ostwald ripening)
- difficulties by redispersing of particles
- defect formation during manufacturing of compact molds, e.g. ceramics.

Thus finely dispersed systems, especially with particle size below 1 μm, have to be stabilized often against coagulation. Applications where defined agglomerate structures are desired are not discussed here. Fundamentally, fine particles can be stabilized electrostatically due to unipolar charging of particles, by the adsorption of molecules (sterically) or by a combination of both (electrosterically).

a) electrostatic   b) electrosteric stabilization   c) steric stabilization due to
stabilization   adsorption of polymers
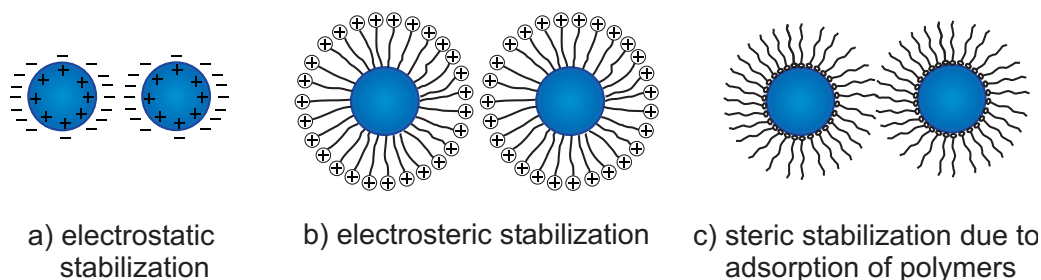
FIGURE 3.3. Possibilities for stabilization.

3.2.2. Electrostatic Stabilization.

3.2.2.1. *The DLVO-Theory.* The superposition of the van der Waals attraction and electrostatic repulsion can be traced back to the independent research of Derjaguin and Landau [108] as well as Verwey and Overbeek [109] and is referred to as DLVO theory. Mostly the repulsive Born interaction is added so that the net interaction energy consists out of:

$$\Phi_{tot} = \Phi_{vdW} + \Phi_{el} + \Phi_B. \tag{3.12}$$

A typical plot of the total interaction energy is shown in figure 3.4. Negative values denote an attraction and positive values a repulsion of two approaching particles. At very small separations the Born repulsion is dominating. The primary minimum $\Phi_{tot,min1}$ is dominated by the van der Waals interaction and Born repulsion. Particles in the deep primary minimum are thermodynamically stable and are often bound irreversibly since in addition to the van der Waals forces chemical bonds can be formed, e.g. by hydrolysis of hydroxyl-groups on the surface of oxides. The energy maximum $\Phi_{tot,max}$ depends on the superposition of van der Waals attraction and electrostatic repulsion. This maximum represents an energy barrier for dispersed particles, which has to be overcome to agglomerate approaching particles. Stability criteria are usually based on either the potential barrier or the maximum force (see equation 3.13). The height of the potential barrier indicates how stable the system is against Brownian agglomeration. In order to avoid agglomeration the energy barrier should be at least 15 kT [**80**]. Next to the height of the energy barrier the slope of the total interaction energy from the energy maximum is important. The steeper the slope the higher the repulsive force F:

$$F = -\frac{d\Phi}{dh}. \tag{3.13}$$

In sheared systems this force F must be larger than the hydrodynamic force to ensure stability. At larger distances from the surface a secondary minimum $\Phi_{tot,min2}$ might be reached. This secondary minimum suggests loose reversible aggregation. To disperse particles agglomerated in the secondary minimum a low energy input is sufficient. Furthermore, the inset of figure 3.4 shows the influence of surface potential and electrolyte concentration on the total interaction energy. With decreasing surface potential as well as increasing electrolyte concentration the influence of the repulsive electrostatic interaction and with it the height of the energy barrier is reduced. Increasing electrolyte concentration causes a compression of the electric double layer and thus a reduction of the range of the electrostatic repulsion. Therefore a high surface potential and low ion concentrations are preferable to effectively stabilize the suspension electrostatically against agglomeration.

3.2.3. Steric Stabilization. For many applications elecrostatic stabilization is insufficient. For example, particles can not be dispersed in the presence of high salt concentrations in polar or non polar solvents. Also dispersions with high percentage of solid phase and a low dielectric constant cannot be dispersed efficiently with electrostatic stabilization. In these cases one has to consider different stabilization mechanisms, e.g. the steric or electrosteric stabilization mechanism. The steric stabilization mechanism is based mainly on the adsorption or chemisorption of polymer chains on the surface of particles [**110**].
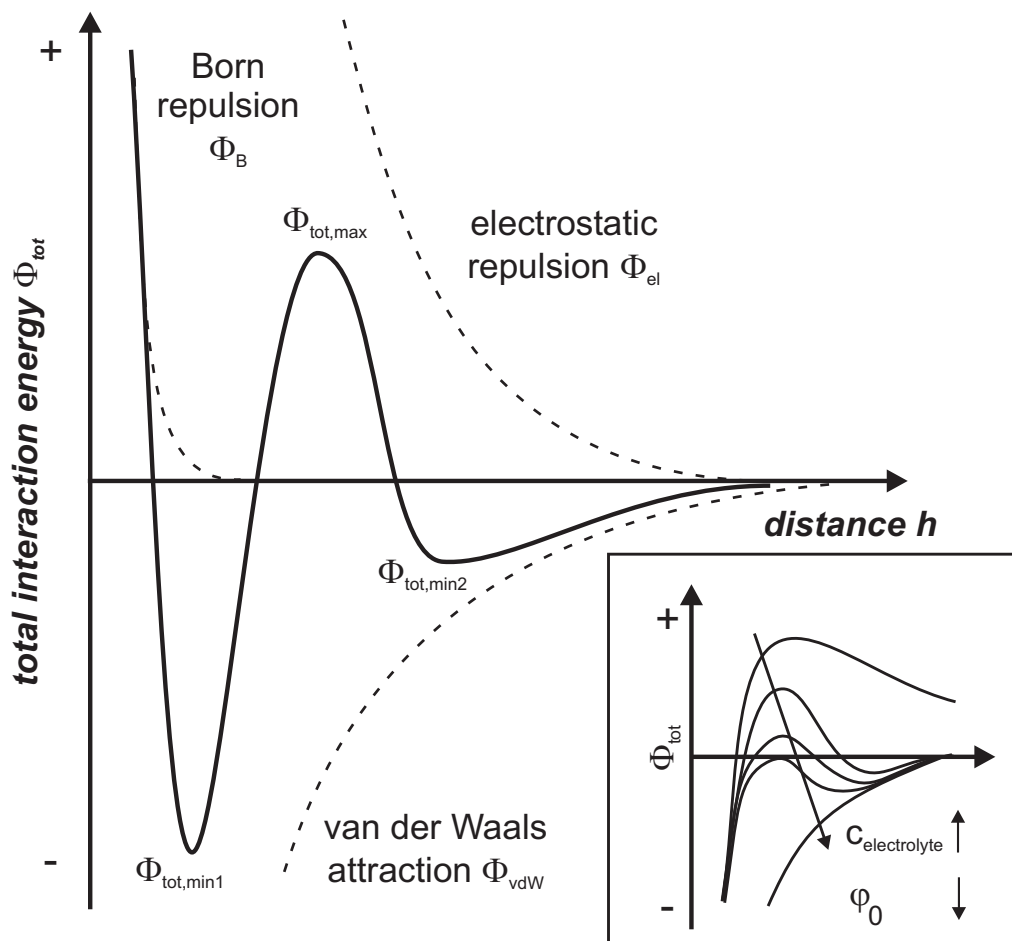
FIGURE 3.4. Typical energy versus distance profiles of DLVO theory.

The polymers act as spacers between the particles. Coagulation is prevented by a reduction of the strongly distance dependent van der Waals force. The concentration of the polymer must be high enough to reach a sufficient coverage of the particle surface by adsorbed polymer chains. If the polymer concentration is low, e.g. if less than half of the particle surface is covered with polymer, bridging flocculation may occur [80]. In bridging flocculation one polymer chain adsorbs on the surface of two particles at the same time. The influence of the polymer on the stability depends strongly on the interactions between polymer and solvent. The quality of a solvent can be expressed in reference to the Theta point. This point is defined as the temperature (Theta-temperature) or solvent composition (Theta-solvent) where interactions between solvent molecules and segments of the polymer chain are energetically equal to the interactions between polymer segments [111]. The Flory-Huggins parameter χ records the interactions of the macromolecules with the solvent. χ is equal to 0.5 at the Theta point. In a good solvent where polymer solvent contacts are favored over polymer contacts among each other, then $\chi < 0.5$ holds. In a poor solvent χ is larger than 0.5. The thickness of the adsorbed polymer layer is influenced by the quality of the solvent. The better the solvent the longer the polymer chains reach into solution and the stronger the steric repulsion force.

If two particles coated with a protective shielding of polymer are approaching each other, one can distinguish three distance regimes [112]. At large distances between the particles the polymer layers don't overlap. In this case no repulsive forces are acting. At closer distances, the polymer chains start to overlap, a densification of the polymer chains is detected and solvent molecules are depleted out of the overlap area into the solvent. In a good solvent the entanglement of polymer chains is thermodynamically disadvantageous, because the entanglement means a separation of polymer segments and solvent molecules. A good solvent prevents the entanglement and increases the stability of the dispersion; a poor solvent increases the entanglement and decreases the stability of the dispersion. The chemical potential of the solvent molecules is in the overlap area higher than in the bulk solvent. Due to this potential difference an osmotic pressure arises, which in fact is the reason for the repulsion. If particles approach each other even closer the polymer layer is compressed. In this case one has to consider, in addition to osmotic forces, forces due to the compression of the polymer layers. The steric interactions are a function of the segment density distributions, which substantially depend on the conformation of the macromolecules on the particle surface. This is determined by the chemical constitution of the polymer, the chemical nature and the geometric shape of the interface, the composition of the solvent, the conformation of the polymer on the surface (loops, tails or trains) and the density of the macromolecules on the surface [80]. The number of loops is higher in case of adsorption from a poor solvent than in case of adsorption from a good solvent. However, the amount of brushes is widely independent of the quality of the solvent [80]. This is why the quadratically averaged thickness and the hydrodynamic thickness of the adsorbed layer are independent from the solvent quality, because the tails reach longer into the solution than the loops. With increasing polymer concentration the number of tails increases and the number of trains decreases while the number of loops is constant [80]. At volume fractions $c_v > 10^{-2}$ the ratio of tails increases conspicuously. The tails consume almost two thirds of a polymer chain at the transition to the melt ($c_v \to 1$) [80].

While the Flory-Huggins parameter χ describes the interactions between the polymer segments and the solvent, the adsorption energy parameter χ_s accounts for the difference between the free transfer energy of a segment from the solvent to the surface and a solvent molecule from the pure solvent to the surface. The segment is preferably adsorbed onto the particle surface $\chi_s > 0$. Otherwise a solvent molecule is preferably adsorbed on the surface. The difference between the adsorption of small molecules and the adsorption of polymers is that χ_s has to exceed a critical value before it adsorbs. The reason for this is that the loss of conformation entropy by the adsorption of a flexible macromolecule has to be compensated by the gain of adsorption energy.

Evans and Napper [113] calculated the total interaction potential $\Phi_{tot} = \Phi_{steric} + \Phi_{vdW}$ with the following equation:

$$\Phi_{tot} = \frac{(2\pi)^{5/2}}{27} \left\langle r^2 \right\rangle^{3/2} \cdot \nu_p^2 \cdot \left(\alpha^2 - 1\right) \cdot a \cdot S \cdot k \cdot T - \frac{A_{eff} \cdot a}{12 \left\langle r^2 \right\rangle^{1/2} \delta_0}. \qquad (3.14)$$

Here the root mean square end to end distance of the polymer chains $\left\langle r^2 \right\rangle^{1/2}$ and the expansion factor α refer to the structure of the polymer in solution. ν_p is the number of polymer chains sticking to the surface per unit surface. The exact value of ν_p must be detected from adsorption measurements. According to Evans and Napper this can be estimated with $\nu_p \approx \left\langle r^2 \right\rangle$. a is the particle radius, A_{eff} the effective Hamaker-constant and $\delta_0 = h / \left(\left\langle r^2 \right\rangle^{1/2} \right)$ the normalized distance between two particles. S is a geometric constant, which depends on the polymer conformation and on δ_0. Values of S are tabulated from Evans and Napper [113]. The osmotic term Φ_{steric}^{osm} dominates for distances $\delta < h < 2\delta$. For this term Vincent used simplified equations [114]. The osmotic term is dependent on the segment density distribution in the polymer cover. The segment density distribution is dependent on the conformation of the polymer on the particle surface. The conformation is determined by:

- The chemical composition of the polymer.
- The chemical nature and the shape of the interface.
- The nature of the solvent.
- The number of trains, loops and tails on the surface.

In practice the necessary values to characterize the polymer layer around the particles are mostly unknown. Hence, calculations are carried out mostly with default segment density distributions. In figure 3.5 four commonly used segment density distributions are illustrated. The less probable density distribution functions are the constant and linear decreasing segment density functions.
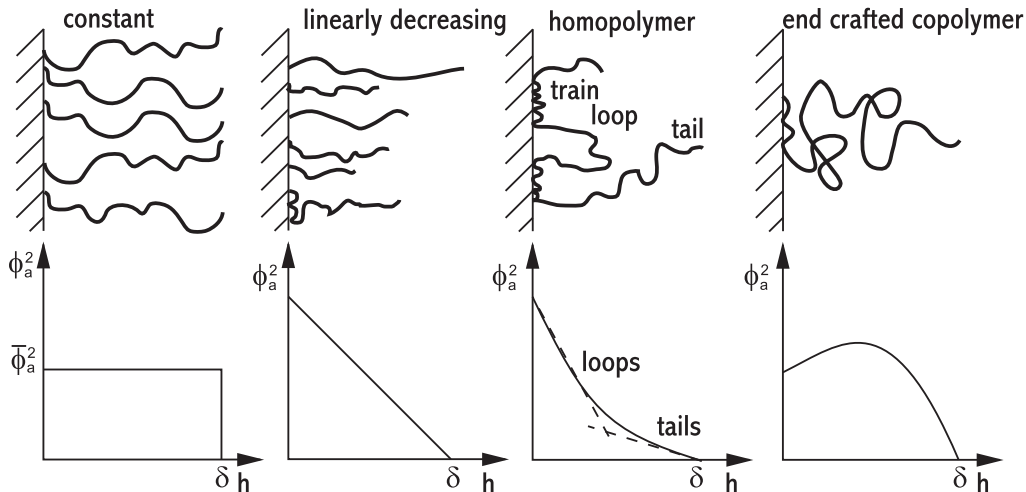
FIGURE 3.5. Segment density distribution.

For the different segment density distributions the following equations apply in the area $\delta < h < 2\delta$ and $h << a$:

Constant segment density:

$$\Phi_{steric}^{osm} = \frac{4\pi a k T}{\nu_1} \left(\bar{\phi}_2^a\right)^2 \cdot (0.5 - \chi) \cdot \left(\delta - \frac{h}{2}\right)^2. \qquad (3.15)$$

Linearly decreasing segment density:

$$\Phi_{steric}^{osm} = \frac{16\pi a k T}{3\nu_1\delta^2} \left(\bar{\phi}_2^a\right)^2 \cdot (0.5 - \chi) \cdot \left(\delta - \frac{h}{2}\right)^4. \qquad (3.16)$$

Homopolymer:

$$\Phi_{steric}^{osm} = \frac{32\pi a k T}{5\nu_1\delta^4} \left(\bar{\phi}_2^a\right)^2 \cdot (0.5 - \chi) \cdot \left(\delta - \frac{h}{2}\right)^6. \qquad (3.17)$$

End crafted with tails:

$$\Phi_{steric}^{osm} = \frac{32\pi a k T}{5\nu_1\delta^4} \left(\bar{\phi}_2^a\right)^2 \cdot (0.5 - \chi) \cdot$$
$$\cdot \left[10\delta^2 \left(\delta - \frac{h}{2}\right)^4 - 12\delta \left(\delta - \frac{h}{2}\right)^5 + 3\left(\delta - \frac{h}{2}\right)^6\right]. \qquad (3.18)$$

here ν_1 is the molar volume of the solvent, $\bar{\phi}_2^a$ the median volume fraction of the segments on the adsorbed layer, δ the thickness of the polymer layer, h the distance between the particle surfaces and χ the Flory Huggins parameter. For distances $h < \delta$ the polymer chains are not only overlapping they are being additionally compressed. This leads to a high repulsive force which can be calculated according to [77]:

$$\Phi_{comp}^{osm} = \nu_p k T \left[\frac{\pi^2 \cdot n_s \cdot l^2}{3h^2}\right] + ln\left(\frac{3h^2}{8\pi \cdot l^2 \cdot n_s}\right). \qquad (3.19)$$

The dispersions starts to flocculate at a certain polymer concentration due to depletion effects, if more polymers are in solution than can be adsorbed to the particle surfaces. However, a dispersion destabilized by depletion floccu-lation can be stabilized again at higher polymer concentrations. However, the stabilization of dispersions at higher polymer concentrations plays a minor role in comparison to the steric stabilization, where polymers are adsorbed to the surface.

The kinetics of the stabilization depend on the material transport (convec-tion and diffusion) from the free solvent to the particle surface as well as the allocation kinetics at the surface. The material transport to the surface can be correlated with diffusion coefficient and the Reynolds number. The diffu-sion coefficient depends on the molecular weight. The following equation for

spherical particles with the hydrodynamic radius r_H applies according to Stokes Einstein:

$$D_{DLS} = \frac{kT}{6\pi \cdot \eta \cdot r_H}. \tag{3.20}$$

Herein η denotes the dynamic viscosity T the temperature and k the Boltzmann constant. Typical diffusion coefficients in a diluted solvent are in the order of 10^{-10} to 10^{-11} m^2/s. With the viscosity law of Einstein (see equation 3.35) the hydrodynamic radius r_H can be estimated for the borderline case of infinite dilution ($c \to 0$):

$$[\eta] = \lim_{c \to 0} \frac{\eta_r - 1}{c} = \frac{2.5 \cdot \pi \cdot N_A \cdot 8}{6M_n} r_H^3. \tag{3.21}$$

Little is known on the adsorption kinetics of polymers. Investigations of the adsorption of polyethylene oxide (PEO) in water on SiO$_2$ surfaces showed that in this case the adsorption kinetics is, up to 75% surface coverage, independent of the allocation kinetics [115]. At higher coverages an inhibition of the adsorption kinetics in dependence of the molecular weight was detected. As far as this result can be generalized the stabilization kinetics in a stirred media mill will depend on the material transport assuming that a coverage of 75% is sufficient.

A selection of polymers is carried out mostly empirically. Amphipathic block and graft copolymers are optimal synthetic particle stabilizers. Usually the anchor part of the polymer is insoluble in the solvent while the tails, which reach in the suspension, are soluble. In this case the anchor adsorbs on the particle surface and the tails reach in solution and cause steric stabilization. The anchor of the surface active substrate is bound to the particle surface either by physical adsorption, by van-der-Waals forces, dipole interactions, hydrogen bridges or by chemisorption. The chemisorption produces relatively strong covalent bonds. A reasonable preselection can be made due to the following guideline based on the specific interactions of the particular groups with the surface and the solvent [116]:

- For cationic and anionic surfaces, respectively, a polymer with an oppositely charged ionic group is necessary.
- For polar and non polar surfaces a polymer with corresponding polar or non polar groups has to be chosen. The same applies for lipophilic or lipophobic surfaces.

The following hints are especially for hydrophobic chains:

- The longer the hydrophobic chain length of the polymer, the worse the solubility in water and the better in organic solvents.
- Entanglements in the hydrophobic chain enhance the solubility of the polymer in water as well as in organic solvents.
- Aromatic rings within the hydrophobic chain enhance the adsorption behavior of the polymer on polar surfaces.

3.2.4. Electro-Steric Stabilization. Polyelectrolytes carry ionic groups along the polymer chains. The charge of these groups depends on its nature and on the pH value. In principle polyelectrolytes can be classified according to the kind of the charge in cationic, anionic or zwitterionic polyelectrolytes. Some important polyelectrolytes are shown in figure 3.6 [31].
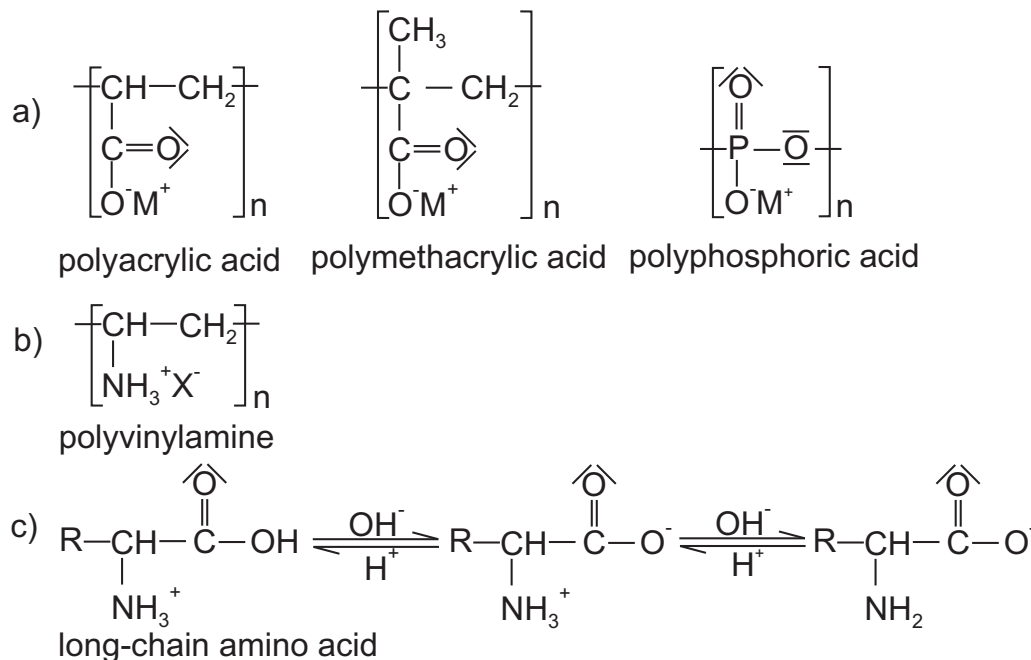
FIGURE 3.6. Chemical structure of some polyelectrolytes.

The effectiveness of the polyelectrolytes depends strongly on the dissociation degree of the polyelectrolyte. The dissociation degree is influenced by the pH value and can be determined for example by potentiometric titration. Neutral particles can be stabilized by polyelectrolytes electro-statically. The non polar ends of the polymers adsorb favorably on hydrophobic particles in polar surroundings, while the polar ends reach into the polar solvent. This leads to the development of a double layer. This means the principle of the DLVO theory can be applied. Consequently, the ionic strength should not be too high to avoid the compression of the double layer. The stabilization is strengthened by the polymer layer due to the steric effect. If polyelectrolytes are used at high ionic strengths they only act as steric stabilisers.

3.2.5. Summary. A comparison of the steric and electrostatic mechanisms is shown in table 3.4. Both mechanisms feature advantages as well as disadvantages. Therefore a selection of the stabilization mechanism must be adjusted carefully to the particular process and the product properties.
The advantages of steric stabilization are [80]:
  (1) The stabilization can be carried out as well in aqueous as in non-aqueous dispersions.
  (2) Steric stabilization is possible in non polar solvents and in aqueous solutions with high salt concentrations.

TABLE 3.4. Comparison between electrostatic and steric stabilization.

property	electrostatic	steric
kinetic	fast, diffusion of ions	slow, diffusion of macromolecules
contamination	ions, pH-value	due to polymers and their fragments
measuring technique	online detection (electroacoustic, pH, conductivity)	difficult to measure
application range	• low ionic strengths and polar solvents • high particle concentration can lead to gel formation	• works in aqueous and in non-aqueous dispersions • effective at low and high solid concentration
handling properties	yield stress can be controlled	viscosity is considerably lower at high solid concentrations in comparison to electrostatically stabilized suspensions
subsequent treatment	irreversible solid bridges can be formed during drying	good redispersing behavior, because solid bridges are prevented due to polymer coverage

(3) The steric stabilization is effective at low and high solid concentrations.
(4) While electrostatically stabilized dispersions at high solid concentrations often builds gels the viscosity for sterically stabilized dispersions is considerably lower.

Despite these advantages also significant disadvantages exist for the application in stirred media milling. High molecular polymers can be degraded due to the high energy input during the grinding process. Moreover, on the particle surface adsorbed polymers can be desorbed by the high shear forces and by resiliencies in the mill. Furthermore, the stabilizing polymers can contaminate the product. This may be prohibitive for example for pharmaceutical applications. However, the largest disadvantage lies in the slower and mostly unknown adsorption kinetics for high molecular weight molecules.

3.3. Fundamentals on the Aggregation Process and its Mechanism

Besides the breakage kinetics two further kinetic processes are important in nano-milling: the agglomeration kinetics and the stabilization kinetics. It has to be assured that the stabilization process of newly formed particles is

fast enough to certainly stabilize the suspension. Therefore it should always be checked if the fast electrostatic stabilization is feasible.

Three fundamental issues govern the type of clusters formed during aggregation: the mode of motion that brings particles into contact, the probability of the particles sticking upon contact and the mobility of the subsequent aggregate.

The aggregation event can be modeled by a second order kinetic process of the particle concentration N. The proportionality constant β_0 is dependent on the transport mechanism. β_0 is a measure of the probability of a collision of two particles due to the acting transport mechanism within a time unit in the absence of interparticle forces. As transport mechanisms Brownian motion for particles < 1 μm (perikinetic agglomeration) and laminar or turbulent shear (orthokinetic agglomeration) are considered. In the literature a number of equations exist to describe the aggregation kernel. In table 3.5 the most common collision kernels based on a physical base are presented.

TABLE 3.5. Collision kernels for different transport mechanisms.

Mechanism	Collision kernel $\beta_0 =$	
Brownian diffusion [117]	$\dfrac{2kT}{3\eta}\left(x_1 + x_2\right)\left(\dfrac{1}{x_1} + \dfrac{1}{x_2}\right)$	(3.22)
Sedimentation [117]	$\pi g \left[\left(\dfrac{x_1}{2}\right)^2 + \left(\dfrac{x_2}{2}\right)^2\right]^2 \left(1 - \left(\dfrac{\rho_f}{\rho_p}\right)\right)\left|\left(\dfrac{x_1}{2}\right)^2 - \left(\dfrac{x_2}{2}\right)^2\right|\left(\dfrac{2\rho_p}{9\eta}\right)$	(3.23)
Laminar shear [117]	$\dfrac{3}{4}\dot{\gamma}\left[\left(\dfrac{x_1}{2}\right) + \left(\dfrac{x_2}{2}\right)\right]^3$	(3.24)
Turbulent shear [118]	$\sqrt{\dfrac{8\pi\rho_F \bar{E}}{15\eta}}\left[\left(\dfrac{x_1}{2}\right) + \left(\dfrac{x_2}{2}\right)\right]^3$	(3.25)

All described equations disregard interparticular and hydrodynamic interactions. Furthermore, in equation 3.25 it is assumed that the particles are small compared to the Kolmogorov-vortex size, which is admittedly the case for stirred media mills. Stenger [1] estimated the influence of the different agglomeration mechanisms in a stirred media mill. According to his calculations, the turbulent agglomeration kernel dominates for particles larger than approx. 80 nm, while smaller particles are mainly influenced by Brownian agglomeration.

The collision probability and adhesion of particles are described in the agglomeration literature mostly by a sticking probability. The particle sticking

probability leads to two universal limiting aggregate regimes: diffusion and reaction limited aggregation. In diffusion limited colloidal aggregation (DLCA) the absence of a strong repulsive barrier leads to a high sticking probability and the particles stick on contact [119], whereas a strong repulsive barrier leads to the reaction limited regime (RLCA) [120]. Several light scattering studies [119, 120, 121, 122, 123, 124, 125, 126] of the agglomeration kinetics have shown that the average agglomerate size grow in a characteristic way for each regime. In the DLCA regime the agglomerate size growth follows a power law behavior, while in the RLCA process the agglomerate size grows exponentially. Whether coagulation is slow or rapid and whether it occurs by a perikinetic (diffusion) or an orthokinetic (shear-influenced aggregation) mechanism [127, 128], the structure of the resulting aggregates will be different [77]. Fast coagulating suspensions will form loose and open aggregate structures. Slowly coagulating systems on the other hand form dense very compact aggregates. The degree of openness of a colloidal aggregate is best represented by its mass fractal dimension d_F with $1 \leq d_F \leq 3$ (where $d_F = 3$ is the limit of a compact spherical aggregate). The fractal dimension d_F reflects the internal structure of the flocs and depends on the mode of aggregation. For rapid, irreversible Brownian flocculation without subsequent rearrangement a value of 2.5 is found for d_F in computer simulations [77], if the flocs grow by adding one particle at a time. For diffusion limited aggregation, in which cluster-cluster interactions are dominating, the fractal dimension is around 1.7 to 1.8. The fractal dimension for reaction-limited aggregation will be between 2.0 and 2.2 [77].

If electrostatic and hydrodynamic interactions are accounted for, not every theoretical collision leads to sticking of particles. The collision frequency β is reduced by a collision efficiency α or a stability factor $W = 1/\alpha$. The stability factor is defined as the ratio of the number of collisions between hard spheres and the number of collisions between particles with interparticle interactions that result in coagulation [129, 130]:

$$W = \frac{\beta_0}{\beta} = 2a \int_{2a}^{\infty} exp\left(\frac{\Phi_{tot,max}}{kT}\right) \frac{dr}{r^2 G(r)}. \qquad (3.26)$$

where r is the particle center to center distance and $G(r)$ a correction accounting for the effect of hydrodynamic interaction according to Honig [131].

In the strict sense computation of W requires the numerical integration of the overall interaction potential. However, a value of the stability factor W can be estimated according to equation 3.27 as long as $\Phi_{tot,max} >> kT$ [132].

$$W = \frac{exp\left(\frac{\Phi_{tot,max}}{kT}\right)}{2a \cdot \kappa}. \qquad (3.27)$$

For large energy barriers ($\Phi_{tot,max}/kT \geq 3$) the stability ratio W can also be approximated according to Prieve and Ruckenstein [77, 133] using an empirical relation, which relates the stability ratio and the energy barrier:

$$W \approx W_\infty + 0.25 \cdot \left[exp \left(\frac{\Phi_{max}}{kT} \right) - 1 \right]. \tag{3.28}$$

where W_∞ is the rapid coagulation value of the stability ratio, which is in most cases slightly larger than one [122].

In practice, however, the estimate of the stability ratio W requires a good characterization of the particle surface since the total interaction energy is very sensitive to surface charge, hydration, hydrophobicity, chain adsorption, etc. Small uncertainties in these surface properties can lead to large errors in the computed value of W [77, 121]. The stability ratio W can be measured experimentally by determining the rate of doublet formation [121, 134, 135]. Several techniques can detect doublet formation for limited ranges of particle sizes: In this work the coagulation rate for perikinetic agglomeration β was directly estimated from dynamic light scattering data for the very initial state of the aggregation using a method from Lattuada et al. [121]. The aggregation rate constant β_0 for rapid coagulation can be calculated for initially monodisperse suspension using the Brownian kernel [117]:

$$\beta_0 = \frac{8kT}{3\eta}. \tag{3.29}$$

Whether the aggregation process is dominated by a perikinetic or orthokinetic mechanism is dependent on the Peclet number Pe:

$$Pe = \frac{3\pi\eta a^3}{kT}\dot{\gamma}. \tag{3.30}$$

For $Pe << 1$ the aggregation process is controlled by Brownian motion while for $Pe >> 1$ the process is dominated by convection [77, 136]. Agglomeration in a stirred media mill is rather complex and will depend on the spatial turbulence and thus shear stress distribution in the mill. The mill can be divided in different areas in which either the perikinetic or the orthokinetic agglomeration mechanism is dominating.

The number of particles in an aggregate N is related to the aggregate radius of gyration R_g and single particle radius a, through:

$$N = \left(\frac{R_g}{a} \right)^{d_F}. \tag{3.31}$$

3.4. Influence of Particle Interactions on Suspension Rheology in Stirred Media Mills

Particle-particle interactions play a dominant role in the nano size range strongly influencing the suspension rheology which in turn is often the limiting factor of the production process due to various rheological, non-Newtonian phenomena including shear thinning, shear thickening, yielding and thixotropy. Thus, the control of the flow behavior of these suspensions is critically important to the unit operation itself and the following process steps. Thus it is necessary to control the rheological properties of the milling suspension throughout the whole milling process especially at high solid loading. This can only be achieved by understanding the different influencing parameters on the rheology of concentrated suspensions and further by influencing them in a way that the suspension displays a well-defined and desired flow-behavior. In the following sections a short review of different rheological models describing suspension rheology under various flow and suspension conditions is presented.

3.4.1. Suspension Rheology. The suspension rheology is influenced next to the solid loading by the particle size distribution and particle shape, which determines the interparticle interactions as well as the hydrodynamics of the system. To determine the rheological behavior of suspensions the shear stress function $\tau\left(\dot{\gamma}\right)$ or alternatively the viscosity function $\eta\left(\dot{\gamma}\right)$ has to be measured in stationary shear experiments. Both functions are connected by the shear stress law:

$$\tau\left(\dot{\gamma}\right) = \eta\left(\dot{\gamma}\right) \cdot \dot{\gamma}. \tag{3.32}$$

here $\dot{\gamma}$ is the shear rate, which is applied by the rheometer, and $\eta\left(\dot{\gamma}\right)$ a characteristic material function which describes the flow behavior of the fluid for given fluid mechanical conditions. In figure 3.7 some typical flow characteristics are shown.
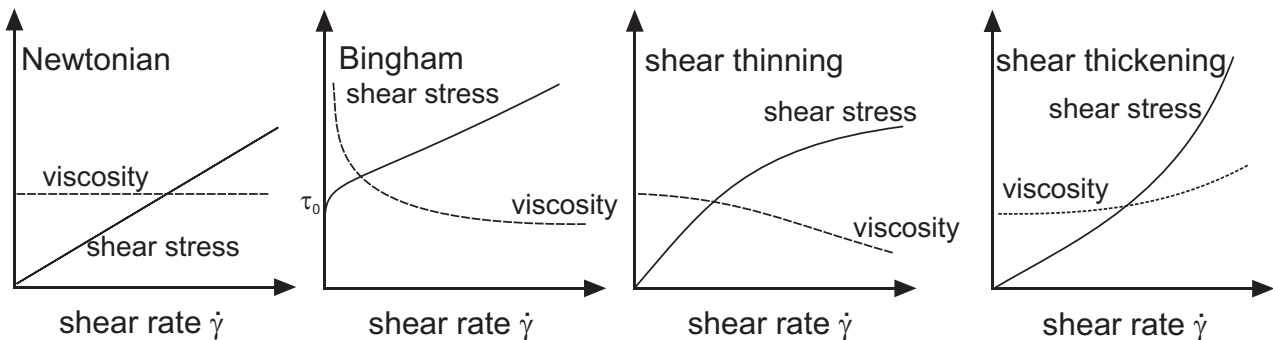
FIGURE 3.7. Common flow behavior.

Dilute suspensions with particles interacting through Brownian and hydrodynamic forces alone (Brownian hard spheres), show Newtonian behavior and can be described by the well-known equation of Einstein [137]. Concentrated

suspensions show in general a non-Newtonian flow behavior. One typical flow behavior of concentrated suspensions is shear thickening, which is defined as a strong increase of viscosity with increasing shear rate whereas a decrease in viscosity with higher shear rates is called shear thinning. During shear thinning structures formed by the solvents and particles are destroyed or degraded with increasing shear rates. This leads to lower viscosities. Both rheological behaviors can be observed in suspensions in dependency of the particle concentration and the particle size. Shear thickening mostly occurs at high solid loadings and high shear rates. Hereby an abrupt rise of the viscosity and respectively the shear stress in order of several tens of magnitude occurs at a certain shear rate [138]. This is caused by the transition of the suspension from an ordered to a disordered state [139, 140] or through a reversible hydrodynamic cluster formation [141]. In general shear thickening is undesired, because the extremely high stress may lead to a failure of the apparatus.

The flow curves of suspensions can be described by an empirical constitutive equation according to Ostwald de Waele [78]:

$$\tau\left(\dot{\gamma}\right) = \eta_0 \dot{\gamma}^n. \tag{3.33}$$

Herein, η_0 is the viscosity for $\dot{\gamma} \to 0$ and n is the so-called flow index. Both parameters have to be determined experimentally. For shear thinning the values of n are in the range of 0 and 1 whereas shear thickening can be described with $n > 1$.

A suspension is called a Bingham fluid, if a certain shear stress has to be applied before the suspension starts to flow with a following Newtonian behavior. This behavior can be described, according to Herschel and Bulkley [78]:

$$\tau\left(\dot{\gamma}\right) = \tau_0 + K \dot{\gamma}^n. \tag{3.34}$$

$n = 1$ describes a Bingham fluid. Suspensions with high particle concentrations tending to agglomeration are best described by this approach [142, 143]. Furthermore, there are many other empirical correlations in the literature, which specify the rheological behavior of suspensions. Detailed information is given for example in the work of Macosco [144].

The flow behavior of suspensions can qualitatively be classified into two regimes: at low shear rates particle-particle interactions dominate (if they are larger than the hydrodynamic interactions). In this case the suspension exhibits a yield stress (Bingham-fluid). When attractive forces are present a three dimensional particulate network structure exists whose strength is determined by the sum of the overall interactions. The yield stress increases with increasing particle concentration and decreasing particle size. The maximal yield stress can be found at the isoelectric point ($\zeta = 0$) since here the repulsive forces vanish and only attractive forces occur.

Often the rheology of concentrated suspensions is described by a relative viscosity η_r. This relates the viscosity of the suspension η to the viscosity of

the matrix fluid η_0. Some examples for empirical equations for this are listed in table 3.6.

TABLE 3.6. Equations for the relative viscosity for hard sphere suspensions.

author	relative viscosity η_r	
Einstein [137]	$\eta_r = 1 + 2.5 \cdot c_v, \qquad c_v \leq 5 vol\%$	(3.35)
Batchelor [145]	$\eta_r = 1 + 2.5 \cdot c_v + 6.2 \cdot c_v^2$	(3.36)
Krieger, Dougherty [146]	$\eta_r = \dfrac{1}{\left(1 - \frac{1}{c_v}\right)^{p_{max}[\eta]}}$ $p_{max} = $ maximal packing density $[\eta] = $ intrinsic viscosity $= lim_{c_v \to 0} \left(\frac{1}{c_v}\right) (\eta_r - 1)$	(3.37)

At higher shear rates hydrodynamic forces dominate over the interparticle interactions. In this case the flow behavior of the suspension can be described with the stress equivalent inner shear rate model according to Gleißle and Baloch [147]. The ratio of the forces between the particles and the hydrodynamic forces determine the border of the two regimes.

The stress equivalent inner shear rate model is valid in the hydrodynamic determined shear rate range or for hard spheres, respectively. In this model it is assumed that particles dispersed in the matrix fluid reduce the space of the matrix fluid in the shear gap. This leads to an increase of the inner shear rate of the fluid between the particles. By introducing a shift factor B a master curve in the hydrodynamic regime can be build. This shift factor relates the shear rates of the suspension $\dot{\gamma}_{susp}(\tau)$ to the shear rate of the matrix fluid $\dot{\gamma}_m(\tau)$ at an equal shear stress and is only dependent on the solid concentration for non flocculated suspensions. The advantage of this model is that the flow behavior of the suspension can be described by a single mastercurve and the shift factor B.

$$B = \frac{\dot{\gamma}_m(\tau)}{\dot{\gamma}_{susp}(\tau)} = \frac{1}{1 - c_v} = \frac{1}{1 - c_m \cdot \frac{\rho_p + \rho_f}{\rho_p}}. \qquad (3.38)$$

<div align="center">

CHAPTER 4

Experimental Setup

</div>

The milling experiments were carried out in three different mills, which are described in the following sections.

4.1. Stirred Media Mill for Aqueous Suspensions

The milling experiments for aqueous suspensions were carried out in a six disc stirred media mill with a content of 0.95 liter. The used grinding chamber is shown in figure 4.1. The axially arranged stirrer shaft is sealed against the grinding chamber by a double acting slide ring sealing (Hecker, type Aegira HN439D-4155B). The drive unit, the grinding chamber and the top cover are connected by quick opening devices, which can be detached and assembled easily for cleaning purpose. The suspension flows axial through the mill. A sieving cartridge with die gaps of 100 μm holds back the grinding media in the mill. The grinding chamber is lined for wear protection reasons with ceramic walls (SiSiC) and the stirrer is equipped with discs from Polyurethane (PU). Furthermore, the sieving cartridge consists out of zirconium oxide. Because the energy input in the mill is mostly dissipated into heat [7, 8] the grinding chamber is equipped with a double wall for cooling. The mill was connected to a cooling water system with a water temperature of 12 °C. The mill was filled with wear resistant yttrium stabilized zirconium dioxide milling beads with a filling degree of 80% dumping volume. The drive unit consists of a low voltage motor (Siemens, 1LA7113-2AA10-Z), which can be controlled continuously by a frequency converter (Siemens, Micromaster Vector MMV 750). The maximal drive capacity of the mill is 5 kW and the rotational speed can be adjusted continuously between 0 and 3000 rpm. Mill and drive unit are assembled on a rocking frame. During operation the mill is placed in the horizontal position. The mill can be pivoted upward and downward during filling and cleaning, respectively.

The experimental set-up provides a circuit mode comminution of the product. The suspension is pumped with a hose pump (Ponndorf, type PD 15-GM/FU) from the grinding chamber into a stirred vessel and from there back into the grinding chamber. The flow rate of the suspension can be adjusted continuously between 20 and 100 l/h by a frequency converter. Before the product suspension is pumped back into the mill, the suspension flows through an instrument (Dispersion Technology, DT1200), which measures the ζ-potential and the particle size (see section 5.1.6).
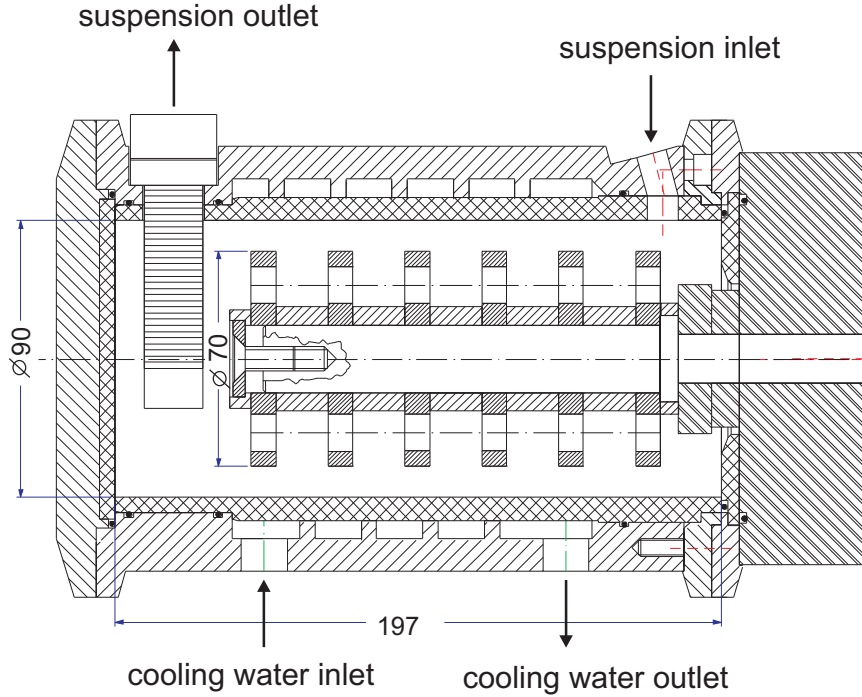
FIGURE 4.1. Grinding chamber of the stirred media mill [1].

4.1.1. Data Acquisition. The torque and the rotatory speed of the stirrer shaft were monitored in all experiments. Furthermore, the temperature, the pH-value and the conductivity of the suspension were measured in the stirred tank and recorded to a computer. The recording of the data was accomplished with an analog-to-digital converter (National Instruments, type NI 6020E) and a program written in LabView 6i. The data were saved in a 10 Hz frequency, because of the long measuring time.

4.1.1.1. *Measurement of Power Consumption.* Torque and number of revolutions were measured by a torque sensor shaft (Staiger Mohilo, type 01610 DM10L) which is installed between the drive shaft of the low voltage motor and the shaft of the stirred media mill. The sensor has a measuring range up to 10 Nm for the torque and until 20 000 min^{-1} for the rotary speed. The measured torque can not be used directly for a calculation of the power input P into the grinding chamber, because part of the torque is used to transcend friction in the bearings and the slide ring sealing. This part is stored in the idle torque $M_{d,0}$. The idle torque of the machine depends on the operating temperature and the rotary speed n_r. With increasing rotary speed and decreasing temperature the torque is increasing. Hence, the mill was warmed up for 15 min at operation speed without filling before the idle torque was measured. The power input in the mill can be calculated with the rotary speed n_r:

$$P = (M_d - M_{d,0}) \cdot 2\pi n_r. \tag{4.1}$$

Usually values between 0.8 and 1.1 Nm were measured for the idle torque $M_{d,0}$.

The specific energy input E_m can be calculated by integrating the power input P over the time and dividing by the total milling charge mass m_{MG}.

$$E_m(t) = \frac{\int_0^t P(\tau)d\tau}{m_{MG}}. \tag{4.2}$$

4.1.1.2. Acquisition and Control of the pH-value. The pH-value, the temperature and the conductivity are measured in the stirred tank. The pH-measurements were accomplished with a glass electrode (Metrohm, 6.0258.000) having a fixed ground-joint diaphragm and an integrated temperature sensor. In combination with a microprocessor controlled (Metrohm, Titroprocessor 686) metering unit (Metrohm, Dosimat 665) the pH-value can be controlled to an constant value using an end point titration.

Next to the pH-value the concentration of ions plays an important role on the stability of suspensions. The ion concentration and ionic strength can be estimated from measurements of defined conductivity values using Ostwald's dilution law. The conductivity was measured with a precision conductivity meter (WTW, LF530) and a conductivity sensor (WTW, TetraCon 96). The calibration before each measurement was done with a KCL-standard (Qualilab, Merck) of a defined conductivity (1.413 mS/cm at 25 °C).

The temperature was measured with a temperature sensor (WTW, TFK 530).

4.1.2. Testing Method. The milling experiments were executed in the following routine:

- Warming up the machine for 15 min and measuring of the idle torque.
- Turning the grinding chamber in vertical position and filling the chamber with grinding media.
- Closing the grinding chamber with the top cover and pivoting the mill in operation position.
- Filling the stirred tank with solvent and starting of the hose pump.
- Removing air out of the grinding chamber and the hoses by setting the mill in a gently inclined position and by kneading the hoses.
- Starting the stirrer in the stirred tank and adding the appropriate amount of solids.
- Starting the data acquisition software and the mill.
- Taking samples out of the stirred tank at defined milling times.
- Stopping the machine and emptying the grinding chamber.
- Cleaning the milling beads with water. Drying the beads in an oven. Weighing and sieving the beads.
- Cleaning the milling chamber and sieving cartridge.

For an estimation of the grinding media wear the mass of the grinding media m_{GM} is weighted before and after every experiment. The mass difference is called the grinding media wear Δm_{GM}.

4.2. Batch Mill PE075

A laboratory stirred media mill PE 075 from Netzsch (Germany) has been used for formulation experiments. This media mill has a chamber volume of 0.6 liter. The grinding chamber is equipped with a double wall for cooling and was connected to a thermostat (Physica, Viscotherm VT10). The stirrer is equipped with three perforated discs. During milling the stirrer is assembled vertically. In order to reduce the amount of wear from the materials of the mill, the grinding chamber is made of ceramic (Al_2O_3) and the stirrer is equipped with discs from ZrO_2. The experimental set-up provides a batch mode comminution of the product.

The number of revolutions of the stirrer per unit time n_r can be adjusted continuously by the rotary speed controller from 233 to 2100 rpm. The maximal drive capacity of the mill is 0.25 kW. The mill is constructed explosion save according to directive 94/9EG.

4.2.1. Testing Method. The milling experiments were executed in the following routine:

- Placing the ceramic grinding chamber in the support.
- Opening the cooling water valves.
- Fixing the stirrer in the boring socket and lifting the milling chamber to milling position.
- Filling milling beads in the mill until they cover all discs of the stirrer.
- Adding the suspension (approx. 200 ml).
- Starting the machine at lowest speed.
- Raising the speed until operation speed. Thereby a building of a water-spout should be avoided. If necessary milling beads or suspension have to be added in order to suppress the waterspout.
- Closing the lid and operating the mill for the specified milling time.
- Controlling the mill to lowest speed before switch-off.
- Removing the grinding chamber and emptying it over a sieve.
- Cleaning of grinding chamber and stirrer.

4.3. Explosion-proof Mill LabStar

The milling experiments with organic liquids were carried out in a commercial laboratory mill (LabStar, Netzsch, Germany). The mill has an explosion-proof design according to the European Community Directive 94/9/EG (CE Ex II G c IIB T3). To meet these requirements the mill was operated in an exhaustion hood and a compressed air stirrer was used in the stirred tank (PLR11, Gebr. Buddeberg GmbH, Germany). The suspension was circulated with a hose pump (501RLA, Watson-Marlow Ltd., UK). The rotational speed of the agitator is continuously adjustable with a frequency converter between 1000 and 4500 rpm. The maximal drive capacity of the mill is 3 kW. The mill is
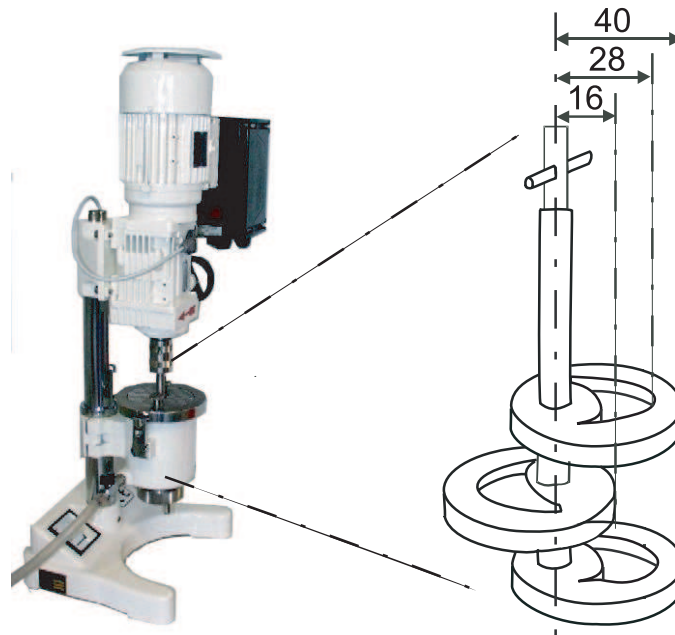
FIGURE 4.2. Design and stirrer geometry of the laboratory batch mill PE75.

equipped with a centrifugal separating systems for the milling beads (see appendix A.5). This allows the use of small grinding media down to 0.1 mm. For wear protection reasons the grinding discs and the sieving cartridge consists out of ZrO_2. Furthermore, the grinding chamber is lined with ZrO_2. The mill as well as the stirred tank are equipped with a double wall cooling system and were operated with cooling water of 12°C. The data acquisition was carried out with a program written in LabView 6i. Because it was not possible to equip the mill with a torque shaft sensor, the specific energy input was determined with the power consumption of the mill. By doing so the idle torque power consumption was subtracted to get the effective power input.

The experimental routine is the same already described in section 4.1.

CHAPTER 5

Analytic Methods

To analyze complex colloidal systems like milling suspensions a variety of physical and chemical characterization methods are required. The most important physical properties of particles are their geometric features (e.g. chord length, surface area, projection area and volume), mass, density, settling velocity and interaction with external fields. Besides the physical particle properties chemical properties (e.g. phase composition, solubility, reactivity and thermal behavior) are important and can influence the measurements of the physical particle properties. For the characterization of these properties a variety of methods exists. In this chapter the methods used in this study and their basic principles are shortly described.

5.1. Physical Characterization of Milling Material

5.1.1. Laser Diffraction. The method of laser diffraction uses the different scattering behavior of particles of different size and shape. If laser light of a certain wavelength λ hits a particle, the light is scattered, refracted, diffracted and absorbed. The result is an interference pattern, which has characteristic maxima and minima for each particle size. To avoid multiple scattering a measurement is only possible for diluted samples. In dependence of the particle size different theories are used to analyze the samples. If the particle size is larger than the wavelength of the incident light ($x >> \lambda$) the Fraunhofer theory is used. In this case the analysis of the scattering pattern is carried out mainly in forward direction on a ring detector. For particles, smaller than the wavelength of the incident light ($x < \lambda$) the Mie-theory is used. Smaller particles scatter the light at larger angles than larger particles. This light is detected on detectors arranged at different angles to the incident beam. To use the Mie theory, it is necessary to know the complex refractive index of both the sample and the medium [148, 149]. The real part of this complex refractive index is the standard refractive index and the imaginary part represents the absorption. Excellent descriptions of Mie scattering were given by van de Hulst [150] and by Bohren and Huffman [151]. In this work the particle size analysis via the method of laser diffraction was accomplished with a Malvern Mastersizer 2000 from Malvern Instruments. The dispersion of the samples can be processed in this equipment directly by ultrasonification and stirring. The Mastersizer 2000 is equipped with a HeNe laser ($\lambda = 632.8$ nm) and an additional source of light with a shorter wavelength (blue laser diode). In this instrument small particle sizes can be measured because the light detectors are ordered in such a

way that forward and backward scattering can be detected. The manufacturer specifies that a particle size range of 20 nm to 2 mm can be measured with this equipment [152]. More realistic are values between 100 nm and 1 mm.

5.1.2. Dynamic Light Scattering (DLS). The dynamic light scattering instruments Microtrac Ultrafine Particle Analyzer (UPA) from Honeywell and the Zetasizer Nano ZS ZEN 3600 from Malvern Instruments were used to determine particle size distributions. The UPA instrument is equipped with a 3 mW semiconductor laser with a wavelength of 780 nm and the Zetasizer with a red helium neon laser with a wavelength of 633 nm.

In the method of Dynamic Light Scattering (DLS), which is also known as Photon Correlation Spectroscopy or Quasi-Elastic Light Scattering, the laser light is scattered at the particles in the suspension. A temporally fast fluctuating scattering pattern can be measured with a detector which is attached at a fixed angle to the incoming beam. This pattern arises due to interference of the light waves which are scattered at the particles. The signal fluctuates fast because the location of the particles is changing due to Brownian motion. The autocorrelation function of the intensity fluctuation is an exponential function. The decay constant of this function is related to the particle diffusivity. From this diffusivity the intensity averaged hydrodynamic particle radius can be calculated for spherical particles with the Stokes-Einstein equation 3.20. The constraints for DLS measurements are that the particles are diluted in suspension to avoid multiple scattering.

5.1.3. Static Light Scattering (SLS). Light scattering experiments under shear flow were performed with a Rheo- Optical Analyzer (ROA) from Rheometric Scientific. The instrument consists out of a plane polarized helium-neon laser (632.8 nm), a flow cell, a screen and a digital imaging camera. The flow cell device consists out of parallel glass plates in which the shear flow results from the rotation of the upper glass plate of the cell. The temperature in the cell is kept constant at 289 K by a thermostat. To minimize multiple scattering the gap size was adjusted to 280 ± 20 μm. The scattered light is intercepted on a screen that consists of a semitransparent paper with a beam stop. The resulting image is recorded on a CCD camera, which is mounted under the screen.

5.1.4. Small Angle Neutron Scattering (SANS). The neutron scattering was performed on the NG-3 SANS beam line at the National Institute for Standard and Technology (NIST) Center for Neutron Research (NCNR). A description of the instrument can be found by Glinka, et al. [153]. The measurement range of the instrument extends from 0.015 to nearly 6 nm^{-1} in scattering wave vector q. It is suitable for examining structural features in materials ranging from roughly 1 to 500 nm. The parameters chosen for the experiments are shown in table 5.1.

TABLE 5.1. SANS experimental parameters

wavelength	$6\overset{\circ}{A}$
wavelength resolution	15% $\Delta\lambda/\lambda$
source-sample distance	14.12 m
sample-detector distance	12 m
beam diameter	7.23 cm
beam stop diameter	7.62 cm
beam intensity	1 008 201 counts/sec
minimum q value	0.0036 $\overset{\circ}{A}$
maximum horizontal q value	0.0267 $\overset{\circ}{A}$
maximum vertical q value	0.0267 $\overset{\circ}{A}$
maximum q value	0.0377 $\overset{\circ}{A}$
number of guides	1
detector center offset	0.00 cm
sample size	5-25 mm diameter
size regime	16.6 to $\sim$ 174.5 nm
used equipment	NIST-Boulder Shear Cell

The NIST-Boulder Couette-type shear cell was used for the orthokinetic agglomeration experiments. The cell consists of an inner quartz cylindrical stator (outer diameter = 59 mm for 1 mm gap) and an outer quartz cylindrical rotor (inner diameter = 61 mm). Sample volumes required are approximately 20 ml to fill the 1 mm gap cell. The shear cell is capable of producing steady shear rates from $1 \cdot 10^{-5}$ revolutions per second (rps) to 10 rps, with conversion factors being 191 Hz/rps for the 1 mm gap cell.

Standard data reduction protocols recommended by NIST were followed to reduce the measurements to an absolute, corrected scattering spectra.

During SANS and light scattering experiments multiple scattering can occur at higher solid concentrations with large particles, that means that already scattered light is scattered again. The effect of multiple scattering increases with increasing concentration, particle size and refractive index. Furthermore, the thickness of the measuring volume plays an important role. Due to multiple scattering structural details of the scattering curve are smeared and the scattering curve becomes flatter and flatter until it is independent of the scattering angle. In this case the effect of multiple scattering dominates the effect of the structure factor (interparticle interactions and interparticular scattering). Multiple scattering always has to be expected in turbid suspensions. The strategy to avoid multiple scattering during the light and neutron scattering

experiments was to dilute the suspensions and to keep the measuring volume as small as possible.

5.1.5. Specific Surface Area (BET). A further method to characterize the particles physically is the BET-surface analysis. The measurements were performed on a fully automatic sorption analyzer (Nova 2000) from Quantachrom Corporation. The measuring method of the instrument is based on nitrogen gas adsorption on the particle surfaces. To prepare the samples for the BET measurement, the suspensions were dried over night in a laboratory oven at 85 °C. Before executing gas sorption experiments, the solid surfaces were freed from contaminations. The surface cleaning (degassing) was carried out by placing the sample in the glass cell of the instrument and heating it at 300 °C under vacuum for 15 h. Once clean, the sample is brought to a constant temperature of 77.4 K by means of an external liquid nitrogen bath and the measurement is started. The determination of the BET-surface area was done with a standard four point method at relative pressures p/p_0 of 0.1, 0.2, 0.2 and 0.4. The determined surface areas S_m were converted into a median diameter $x_{1,2}$ to compare the different methods used for particle size analysis.

$$x_{1,2} = \frac{6}{\rho_P \cdot S_m} = \frac{1}{M_{-1,3}} = \frac{1}{\int_{min}^{max} x^{-1} \cdot q_3(x)\, dx}. \tag{5.1}$$

The complete adsorption-isotherms were recorded at 32 relative pressures for the adsorption and 22 points for the desorption in order to determine pores in the material. The analysis of micro pores was accomplished with the V-t-method described in appendix A.2.

5.1.6. ζ-Potential Measurements.

5.1.6.1. *Acoustic and Electroacoustic Spectroscopy.* These measurements were made using an ElectroAcoustic Spectrometer DT1200 (Dispersion Technology). The device is equipped with different sensors to measure simultaneously the temperature, the pH-value, the conductivity, the particle size distribution as well as the ζ-potential.

To measure the ζ-potential a 1 MHz acoustic signal is applied to the suspension by a piezoelectric actor. Because of the density difference between the particles and the solvent, there will be a relative motion between the two in the acoustic wave. Ions, which are adsorbed in the Stern layer, move with the particles while ions further away from the particle move with the solvent. Thus, ions in the outer layers around the particle are sheared away and oscillating dipoles are created. The sum of all created dipoles can be measured at an electrode on the face of the acoustic actor as alternating current, the so called colloid vibration current (CVI). The ζ-potential can be calculated from the CVI if the particle size is known. The particle size distribution can also be determined with electroacoustic spectroscopy. Therefore the disperse system is excited to oscillation by an ultrasound transmitter with acoustic waves in

the frequency range between 3 and 100 MHz. While the ultrasound wave is spreading through the suspension it interacts with the disperse particles and to a lesser extend with the solvent. As a result the sound wave changes due to viscous, thermal, scattering, intrinsic, electrokinetic and structural losses. The attenuation of the signal is measured with an opposite mounted receiver. The measured attenuated signal is dependent on the physical and thermal material properties of the disperse and fluid phase. The main influence parameters on the attenuation signal are the density difference between disperse and fluid phase and the solid mass concentration.

This measuring method is applicable in a wide range of solid concentrations due to a variable adjustable gap (0.1 - 20 mm) between ultrasound transmitter and receiver. The manufacturer specifies a concentration range from 1-50 vol% and a median particle size between 5 nm and 10 μm.

5.1.6.2. *Laser Doppler Electrophoresis.* The ζ-potential is measured with the Zetasizer Nano ZS ZEN 3600 from Malvern Instruments using a combination of the measurement techniques: Electrophoresis and Laser Doppler Velocimetry, sometimes called Laser Doppler Electrophoresis. This method measures how fast a particle moves in a liquid when an electrical field is applied i.e. its velocity.

5.1.7. SEM/TEM pictures. Scanning electron microscopy (SEM) measurements of the samples were carried out in the "Bayreuther Institut für Makromolekül Forschung (BIMF)" at the University of Bayreuth. In the BIMF, a state-of-the-art high resolution field emission scanning electron microscope LEO 1530 with an EDX system from OXFORD is available. For the sample preparation, the concentrated feed and milled suspensions were dispersed by sonification (Bandelin SONEREX TK 52, 200 W) for 3 minutes and diluted with the respective solvents to 10^{-5} vol %. In order to remove dust particles from the surface of a Si-wafer which is used as an object carrier, the Si-Wafer was washed with the organic solvents propanol, ethanol and acetone, before it was heated to red-heat for one minute. One drop of the diluted suspension was placed on the Si-Wafer and subsequently dried under dust free conditions.

5.1.8. Rheology. Rheological measurements of the suspensions were carried out on the rheometers CVO 120 HR from Bohlin instruments and UDS 200 from Paar Physica. All experiments were performed with a double gap measuring geometry. In case of the Bohlin instrument the measuring system with the identification marking DG24/27 was used. For this measuring system a sample volume of 10 ml is necessary. The UDS 200 uses the Z1 geometry according to DIN 54453 for the double gap measuring system. In this case a sample volume of 22.5 ml is necessary. Both equipments were connected to a thermostat to ensure a constant temperature of 25°C during the experiment. To avoid errors due to shear history of the samples a preconditioning at a constant shear rate of 1000 s^{-1} for 60 s was accomplished before rheological flow curves were recorded

stepwise between 0.1 and 1000 s^{-1}. Each measurement consists out of a delay time and an integration time. The necessary delay time to reach equilibrium conditions was investigated in preliminary tests. It was shown that a delay time of 60 s is sufficient. In the following 60 s data were gathered and recorded as average values. All experiments were conducted from high shear rates to low shear rates.

5.2. Chemical Characterization of Milling Material

5.2.1. X-ray Structure Analysis (XRD).
X-ray diffraction is a powerful non-destructive technique for investigation of structural properties of crystalline materials. A diffraction pattern is produced when a crystalline material is irradiated with a collimated beam of X-ray. The diffraction pattern and the intensity of each diffracted X-ray as a function of the diffraction angle can provide information such as crystal structures, phase purity and grain size etc. X-ray diffraction measurements were carried out in the Department of Chemical Reaction Technology, at the University of Erlangen. A PANalyticals X'Pert Pro MPD multi purpose X-ray diffraction system was used, which uses radiations from a CuK-α at a wavelength of $\lambda = 0.15418$ nm, and records the diffraction angle from $2\theta = 10°$ to $50°$. Each angle was measured with a time difference of 10 seconds. The instrument measures data in the reflection mode.

5.2.2. Dynamic Differential Calorimetry (DSC).
A differential scanning calorimeter (DSC) determines the temperature and heat flow associated with material transitions as a function of time and temperature. The method provides quantitative and qualitative data on endothermic and exothermic processes of materials during phase changes, oxidations, melting and other heat-related changes.

The measurements in this work were carried out on a DSC 2920 measuring device supplied by TA Instruments at a heating rate of 2 °C/min up to 400 °C. Nitrogen was used as a purge gas with a flow rate of 40 ml/min in order to avoid reactions of the sample with air. The sample powder was spread evenly across the bottom of the pan to minimize thermal gradients.

The measuring device of the instrument consists out of an oven, in which an aluminum pan with approximately 10 mg of sample and an empty reference aluminum pan are heated at a controlled rate. The temperatures of both pans, which are placed on thermoconducting plates, are measured continuously.

If a sample and an inert reference are heated at a known rate in a controlled environment, the increase of sample and reference temperature will be about the same, unless a heat-related change takes place in the sample. If this change takes place, the sample temperature either evolves or absorbs heat.

5.2.3. Thermal Gravimetric Analysis (TGA).
Thermogravimetric Analysis (TGA) measures weight changes in a material as a function of temperature

(or time) under a controlled atmosphere. Its principal uses include measurement of a material's thermal stability and composition. A TGA Q50 from TA Instruments was used in this work.

5.2.4. FT-IR. Fourier transformed infrared spectra were recorded for the samples pilled with KBr powder by a Varian Excalibur FTS 3100 spectrometer wit a resolution of 43 cm^{-1} using the EasiDiff reflectance accessory. The obtained spectra were converted into absorbance-like spectra by performing a Kubelka-Munk transform on the recorded data.

5.2.5. Gel Permeation Chromatography (GPC). GPC measurements were performed at the Institute of Polymer Materials of the University Erlangen-Nürnberg with a room-temperature instrument which is equipped with the columns Waters HWM7, Waters Styragel 10^5, Waters Styragel 10^4 and Waters 10^3. The measurements were performed at 25°C in tetrahydrofuran. The injection volume was 0.1 ml and the concentration 1 g/l at a flow rate of 1 ml/min.

Materials and Sample Preparation

6.1. Milling Material

6.1.1. SiO$_2$.

6.1.1.1. *Ludox TM-50.* The colloidal silica Ludox TM-50 from Sigma-Aldrich was used as a colloidal model system for agglomeration and dispersing experiments. Ludox TM-50 is an aqueous colloidal dispersion of silica particles of primary particle size of around 30 nm diameter. Figure 6.1 shows a TEM picture of the Ludox particles at a volume concentration of $c_v = 10^{-4}$. The original suspension has a pH value of 8.84 and has a solid concentration of 50 wt%. The experiments have been carried out at a 5 wt% Ludox suspension except were noted. Therefore, the Ludox was diluted down in aqueous KOH solution with a pH of 8.84. The properties of the particles are given in table 6.1.

The aggregation of the Ludox particles was monitored until gelation using light and neutron scattering. To start the aggregation process, the desired amount of 3 M KNO$_3$ solution was rapidly added to the Ludox suspension under vigorous stirring. A hydration layer, which causes a steric barrier to agglomeration, was suppressed by performing the experiments at the original pH value of the Ludox as supplied. The experiments were carried out at ambient temperature of 25°C. For small angle neutron scattering the particles were diluted in D$_2$O instead of H$_2$O to the same molar concentrations of particles. The 3 M stock solution of KNO$_3$ was also prepared in D$_2$O, to minimize incoherent scattering.

TABLE 6.1. Particle properties

x_{SANS}/nm	30
$x_{SANS}(Guinier)/nm$	30.77 ± 1.9
x_{DLS}/nm	37
$A_{eff}/10^{-20}J$	0.85
ζ/mV @ pH8.84	-35
ϵ_r	78.50

6.1.1.2. *Mikrosil LS500.* The silica Mikrosil LS500 used in this work was supplied by Westdeutsche Quarzwerke Dr. Müller GmbH. The material has a density of 2.65 g/cm^3, a specific surface area of 8.7 cm^2/g and a median particle size of 1 μm. The manufacturer declares that the chemical purity of SiO$_2$ is
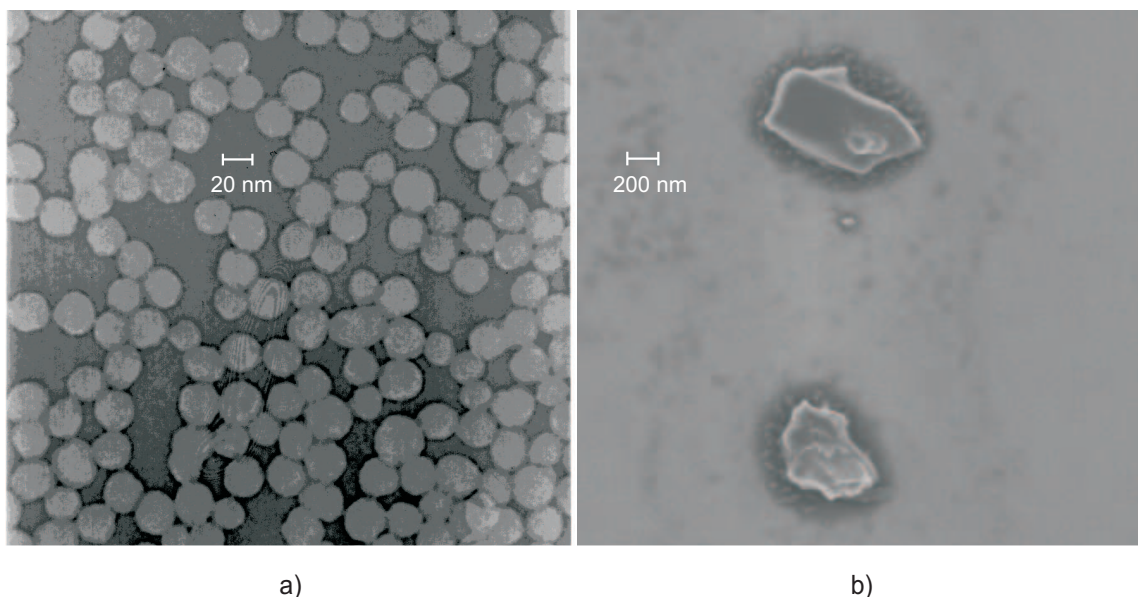
FIGURE 6.1. a) TEM picture of Ludox TM50 ($c_v = 10^{-4}$) b) TEM picture of SiO_2 Mikrosil LS500 particles.

99.5 wt%. A SEM picture of the material is shown in figure 6.1b. The picture displays that the SiO_2 particles are not sintered and not agglomerated.

6.1.2. Al_2O_3. The fused alumina with the trade name F320 was used in the milling experiments. The manufacturer (Lonza Werke, Germany) specifies the chemical composition as 99.61% Al_2O_3, 0.26% Na_2O as well as traces of other oxides. The density of the material is according to the manufacturer 3930 kg/m^3. This could be proved by a pycnometerial measurement. The median particle size measured with laser diffraction is $x_{50,3} = 33.8$ μm. A BET measurement resulted in a specific surface area of 0.27 m^2/g. In figure 7.43a a SEM picture of the feed material is presented. The picture shows that the used fused alumina is a feed material, which is not sintered and not agglomerated.

For the preliminary experiments described in chapter 7.3.1 and 7.3.2 the α-alumina AKP30 (Sumitomo Chemical Co. Ltd. Japan) was used. The manufacturer specifies the chemical composition as 99.99% Al_2O_3 and other traces of sodium and magnesium metals. An average particle size $x_{50,3} = 300$ nm was measured with dynamic light scattering and a surface area of 10.1 m^2/g with BET.

According to the literature [154] no dissolution of the aluminum from the particle surface could be measured in ethanol with inductive plasma spectroscopy. Furthermore, the alumina particles are almost insoluble in water. The solubility of aluminum in water at 20°C is 0.1 mg/l [1, 155].

6.1.3. Hematite (Fe_2O_3). The hematite used in the milling experiments described in chapter 7.4 has an iodometrically determined Fe^{3+}-content of 97.3% and 1% water soluble salts [156]. The pH-value of a slurry is pH5 at 20°C. The solids have a density of 5.2 g/cm^3 and are almost insoluble in water at 20°C

[157]. According to Cromieres [158] the solubility of hematite in water of natural pH value is 10^{-13} M. The Hamaker constant A for a aqueous dispersion of Fe_2O_3 results according to equation 6.1 in $4.52 \cdot 10^{-20}$ J [80]:

$$A = \left(\sqrt{A_{\alpha-Fe_2O_3}} - \sqrt{A_{H_2O}} \right)^2 . \tag{6.1}$$

The Hamaker constant of pure hematite has a value of $16.4 \cdot 10^{-20}$ J [159] and the Hamaker constant of water is $3.7 \cdot 10^{-20}$ J [79]. The particle size distribution of Fe_2O_3 in 0.01 molar $NaNO_3$ solution at pH10.2 and T = 25°C measured with dynamic light scattering is shown in figure 6.2a. As it can be seen, the median particle size $x_{50,3}$ is 250 nm. A scanning electron microscopy (SEM) picture of the material is shown in figure 6.2b. The particle sizes cannot be determined exactly from this picture, because different image planes overlap in it. However, the picture shows besides agglomerates with a primary particle size of 150 to 200 nm single particles with particle sizes of around 1.7 μm. Furthermore, it can be seen that the used iron(III)oxid is a feed material with primary particles which are not sintered. Furthermore, a specific surface area of 11.5 m^2/g was measured.
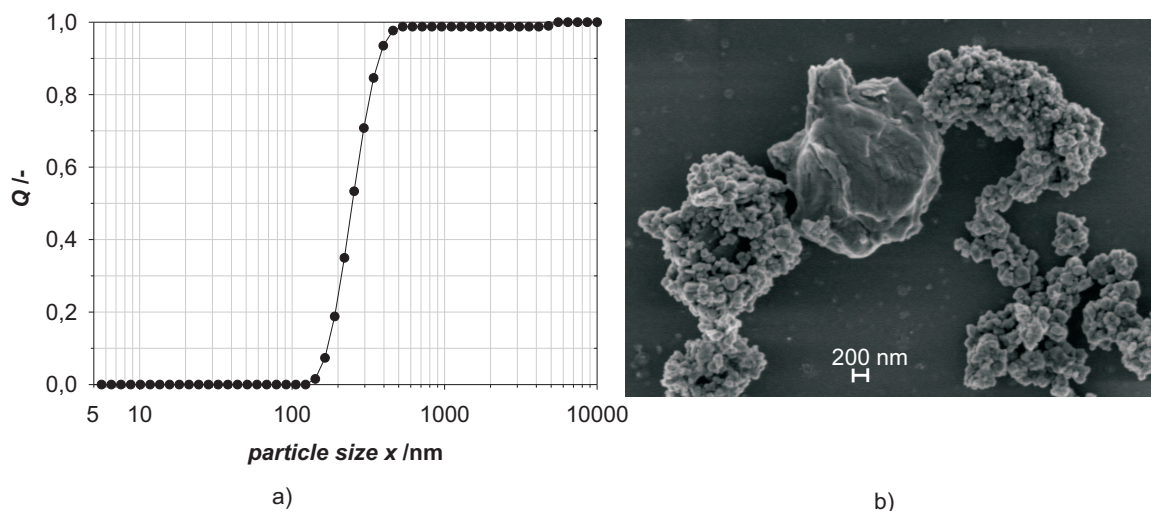
FIGURE 6.2. Measured particle size distribution (a) and SEM picture (b) of the used Fe_2O_3 in 0.01 M $NaNO_3$-solution at pH10.2 and T = 25°C.

6.1.4. Solvents. The solvents 2-butanol, ethanol and toluene were supplied by Merck KGaA, Germany. The degree of purity is for all solvents for synthesis. In the experiments with aqueous suspensions distilled water from the house water pipe was used.

6.1.5. Dispersing Agents.

6.1.5.1. *DAPRAL.* As dispersing agent the polymer DAPRAL GE 202 (Akzo Nobel Chemicals, Italy) an alternate maleic anhydride α-olefin copolymer with lipophobic poly(ethylene glycol) and lipophilic polyolefin side chains was used. Due to its unique structure that incorporates both lipophilic and lipophobic side chains this polymer may be adsorbed on oxide surfaces from various solvents of different polarity in various conformations. The structural formula of the used polymer is shown in figure 6.3.
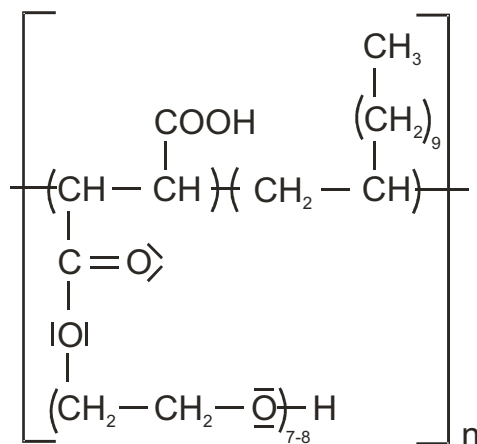
FIGURE 6.3. Structure of the polymer DAPRAL.

Figure 6.4 shows GPC measurements of three different grades of DAPRAL. The grades of DAPRAL differ in the chain length. The kinematic viscosities for the different grades were measured at 40 °C in a capillary viscometer. The GPC measurements were performed at the Institute of Polymer Materials of the University Erlangen-Nürnberg with a room-temperature instrument which is equipped with the columns Waters HWM7, Waters Styragel 10^5, Waters Styragel 10^4 and Waters 10^3. The measurements were performed at 25°C in tetrahydrofuran. The injection volume was 0.1 ml and the concentration 1 g/l at a flow rate of 1 ml/min.

In this study DAPRAL of a viscosity of 56.05 cm^2/s measured at 40 °C in a capillary viscometer was used except were noted. The synthesis of this type of polymer is described elsewhere [160].

NaAOT (Dioctyl Sulfosuccinate, Sodium Salt) an anionic surfactant with a sulfonate group on its polar head and two branched hydrocarbon tails was used as a background salt in ethanol and was supplied by Sigma-Aldrich Chemie GmbH, Germany. Other chemicals NaNO$_3$, LiCl, Y(NO$_3$)$_3$, LiNO$_3$ were obtained from Merck KGaA (Germany).

6.2. Grinding Media

Wear resistant commercially available yttrium stabilized zirconia (ZrO$_2$) milling beads in the size range of 0.5 to 0.63 mm were used in the milling
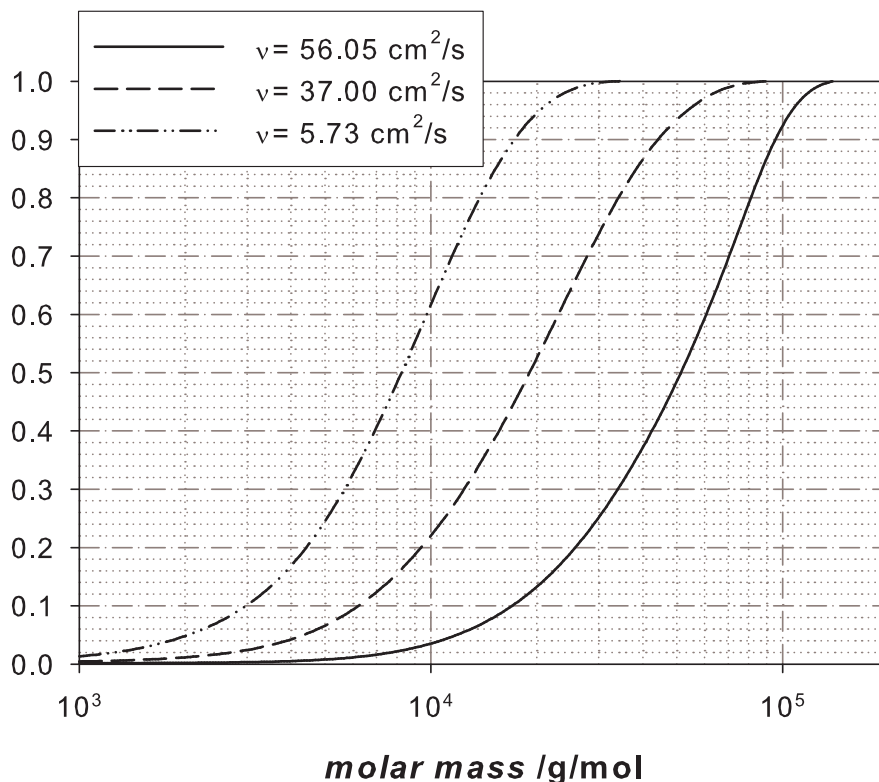
FIGURE 6.4. Gel permeation chromatography measurements of the used DAPRAL polymers (the kinematic viscosities for the different grades of DAPRAL were measured at 40 °C in a capillary viscometer).

experiments. According to the manufacturer they have a specific density of 6065 kg/m^3 and a chemical composition of 94.5% ZrO_2 and 5.0% Y_2O_3 as well as trace elements. These kind of milling beads display a good stability of the pH-value and a low impact on the suspension conductivity [1], which is necessary to effectively stabilize the suspensions.

Al_2O_3 milling beads in the size range of 0.63 to 0.8 mm were used for autogenous grinding of alumina particles. The manufacturer Draiswerke Inc. specifies the density of the beads as 2100 kg/m^3.

CHAPTER 7

Results and Discussion

7.1. Perikinetic and Orthokinetic Aggregation Kinetics of a Nanoparticle Dispersion

By producing particles smaller than a median particle size of 1 μm a steady state between breakage, deagglomeration and agglomeration exists in the milling process. This equilibrium is controlled by interparticle interactions as well as the milling conditions. As particles decrease in size the interparticle forces between the particles become dominant. Attractive forces lead to agglomerates when the particles collide, thus acting against the comminution process. To prevent this agglomeration process the particles in the mill must be stabilized by increasing the repulsive forces in the suspension. This will move the steady state to smaller particle sizes. To produce particle sizes below 1 μm in stirred media mills a detailed understanding of the agglomeration process and its mechanism is needed. In the following chapter the importance of controlling agglomeration is demonstrated. Experiments are performed on a well characterized model system of monodisperse primary SiO_2 nanoparticles that are salt destabilized and aggregated under various conditions. Perikinetic and orthokinetic aggregation are measured, with the latter in a laminar shear flow as well as in a stirred media mill, to examine the effects of colloidal stability and flow on the aggregation process. The agglomeration kinetics are measured using dynamic light scattering (DLS) as a function of electrolyte concentrations. Further information on the agglomeration process and the structure of the agglomerates are also obtained from small angle neutron scattering (SANS) experiments both at rest and under flow.

7.1.1. DLS Results. Figure 7.1 shows the measured effective aggregate diameter as a function of time with the salt concentration as parameter for perikinetic aggregation. Aggregation rates increase with added salt as expected. In all experiments the particle diameter starts at around 37 nm at $t = 0$ min. This corresponds to the average primary particle size with diluted Ludox in the absence of added salt. The primary particle size is larger than the primary particle size obtained with small angle neutron scattering, which is a known consequence of the particle polydispersity and the different weighting methods of the techniques. The maximum particle size measurable with the DLS-instrument is 3 μm. The linear curves in this semilog-plot indicate that the agglomeration mechanism is *reaction limited* colloid aggregation, in which a repulsive barrier limits the efficacy of collisions, allowing some clusters to

enter the interior of the growing aggregate [122]. Reaction limited aggregation generally produces a denser fractal and a larger fractal dimension d_F than diffusion limited aggregation [122]. The influence of the particle concentration on the aggregation kinetic is shown in A.1. The aggregation rate increases with increasing solid concentration as expected.
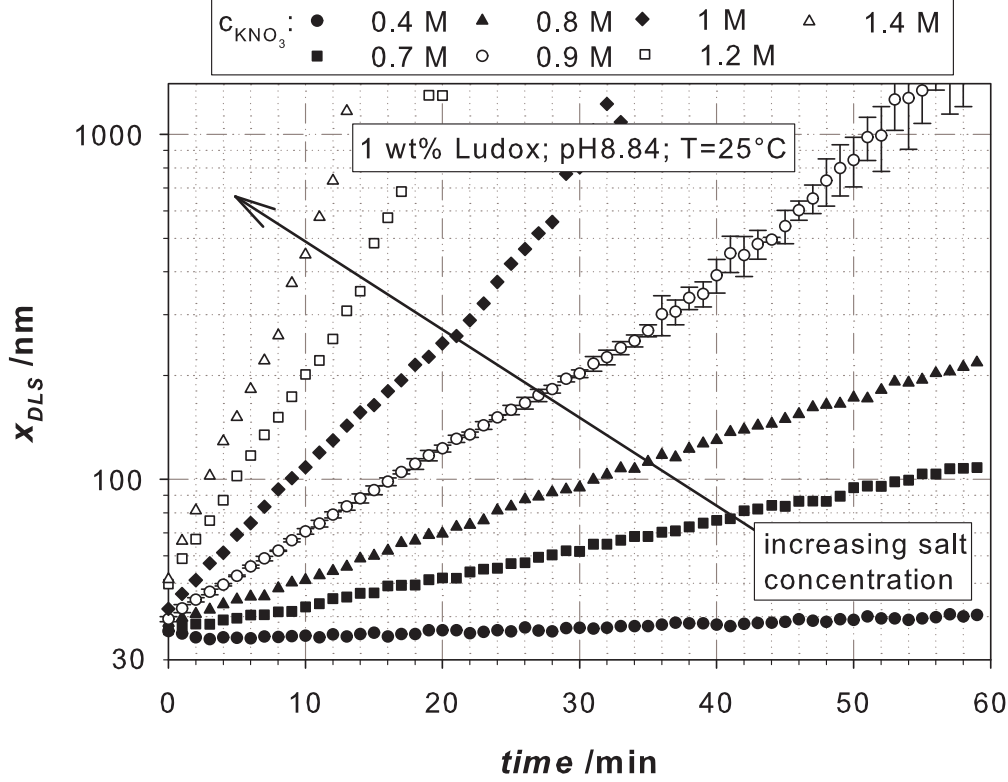
FIGURE 7.1. Effective DLS diameter as a function of time for 1 wt% Ludox TM50 with the salt concentration as parameter.

Figure 7.2 shows that all aggregation curves can be reduced to a single master curve if the dimensionless radius R_{DLS}/a is plotted over the dimensionless time. The DLS measured radius is made dimensionless with the radius of the primary particles a. The dimensionless time τ is proportional to the stability factor and defined as [121]:

$$\tau = \frac{N_0 \cdot k_{hardsphere}}{W} \cdot t. \tag{7.1}$$

Figure 7.3 shows the experimentally determined and calculated stability ratio W as function of KNO_3 concentration. The stability ratio is the ratio of the measured aggregation rate to the rate of perikinetic aggregation in the absence of interparticle and hydrodynamic interactions, $W = k_{hardsphere}/k_{agg}$. The aggregation rate constant $k_{hardsphere}$ was calculated using following equation derived by von Smoluchowski:

$$k_{hardsphere} = \frac{8kT}{3\eta}. \tag{7.2}$$
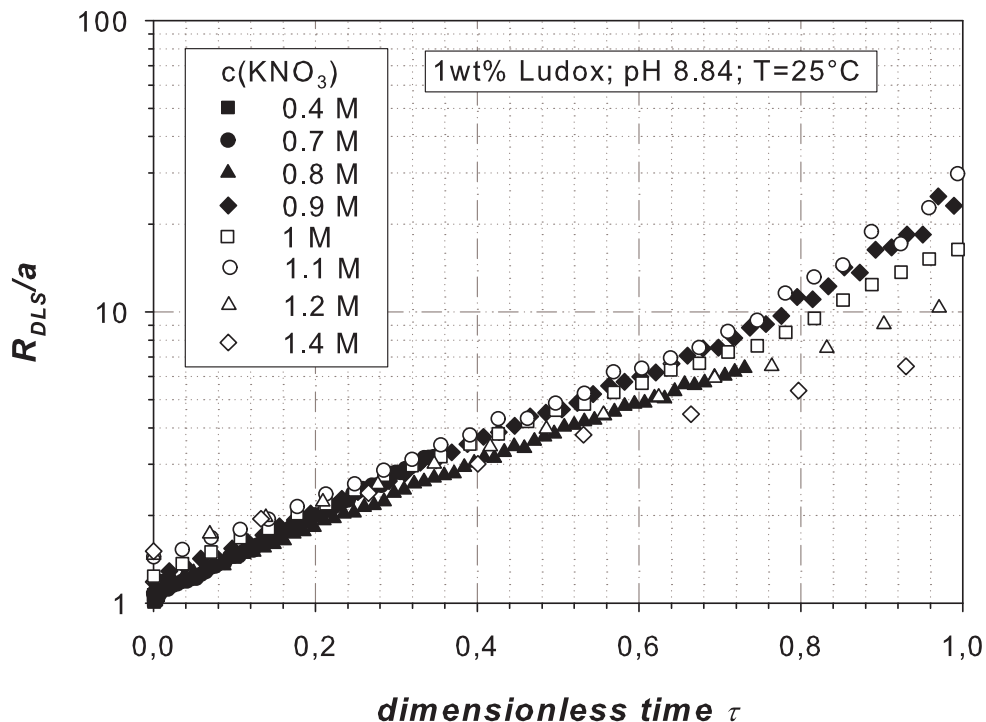
FIGURE 7.2. Mastercurve of the aggregation data presented in figure 7.1.

The rates k_{agg} were estimated for the very initial state of the aggregation directly from the DLS data using a method from Lattuada et al.[121].

The stability ratio W is also calculated using the following approximation from Prieve and Ruckenstein [12]:

$$W \approx W_\infty + 0.25 \cdot \left[exp \left(\frac{\Phi_{max}}{kT} \right) - 1 \right]. \qquad (7.3)$$

where $W_\infty = 1.7$ is the rapid coagulation value of the stability ratio. Typical values for W_∞ are slightly larger than one. Russel, Saville and Schowalter [77] reported for example for polystyrene latices in water values of W_∞ spreading between 1.6 and two. Values of W_∞ are hard to measure, because of the fast agglomeration at high salt concentration. However, the value of W_∞ is insensitive for the calculation of the stability ratio in the salt concentration range considered here. The height of the energy barrier Φ_{max} was calculated using the DLVO theory. There are some uncertainties in the calculation of the kinetic constant k_{agg} and thus the stability factor W because the initial slope of the size versus time curve was used, which surely amounts to much more than dimers. Therefore the particle diameter was adjusted slightly in the calculation of Φ_{max}, using a slightly larger particle size than the primary particles, namely 40 nm. By doing so good agreement between the DLS based and DLVO predicted stability ratio is observed using a Stern layer thickness of 0.1 nm, which is the estimate of the radius of a bare K^+ ion [79].
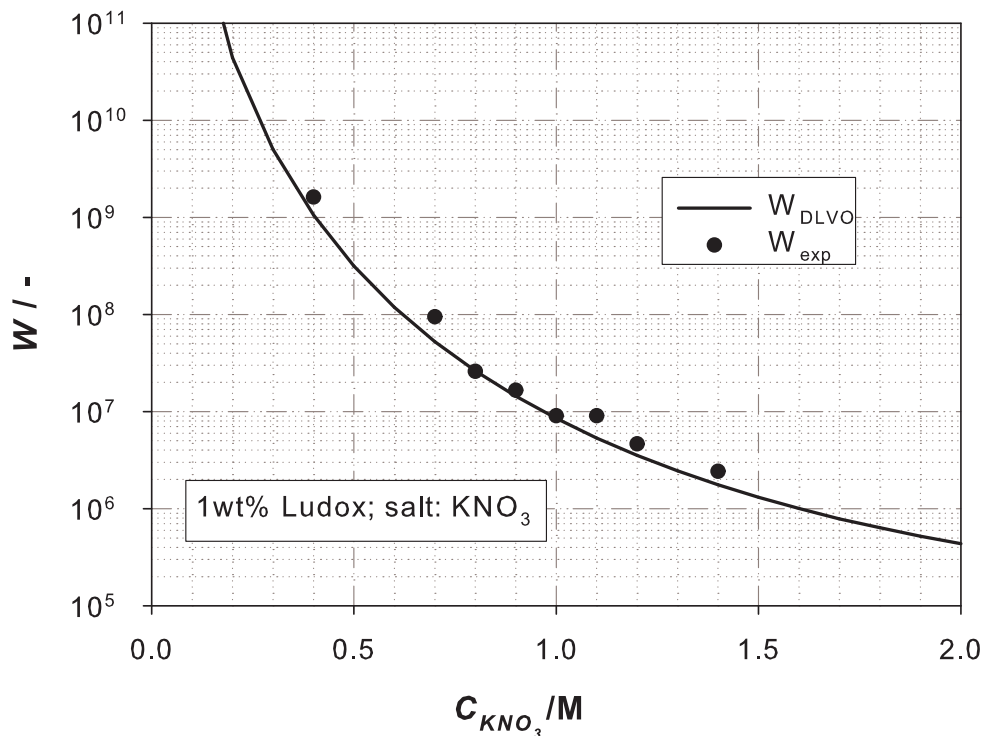
FIGURE 7.3. Calculated and measured stability ratio W as a function of KNO_3 concentration (parameters: $\Delta = 0.1$ nm, $T = 25°C$, $|\zeta| = 35$ mV, $\epsilon_r = 78.5$, $\eta = 9.76 \cdot 10^{-4}$ Pas, $a = 40$ nm, $W_\infty = 1.7$, $A_{eff}(0)/kT = 2.065$).

Figure 7.4 shows the DLVO interaction energies calculated with equation 3.12 [122] for a range of KNO_3 concentrations. By accounting for the Stern layer thickness the theoretical critical coagulation concentration (CCC) is around 1.7 M KNO_3, which is never reached in the experiments. This explains the observed behavior consistent with reaction limited aggregation, as DLCA is not observed until the CCC and above.
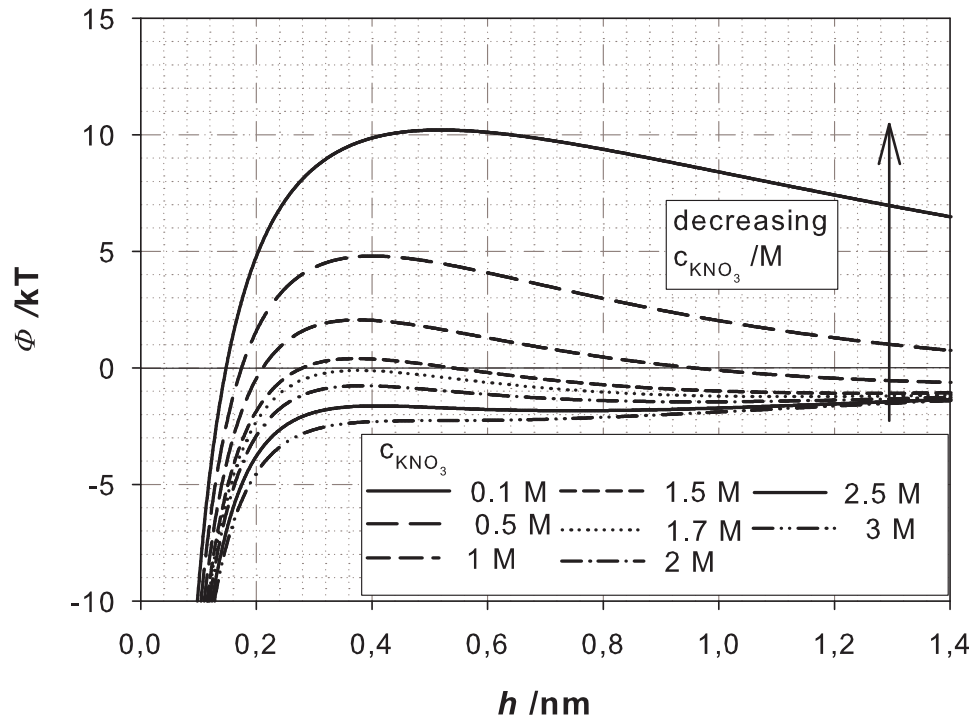
FIGURE 7.4. Plots of DLVO interaction energies as function of increasing KNO_3 concentration using a constant surface potential (parameters: $\Delta = 0.1$ nm, $T = 25°C$, $|\zeta| = 35$ mV, $\epsilon_r = 78.5$, $\eta = 9.76 \cdot 10^{-4}$ Pas, $a = 40$ nm, $W_\infty = 1.7$, $A_{eff}(0)/kT = 2.065$).

7.1.2. SANS Results. The small angle neutron scattering experiments were performed with the goal to obtain further information on the agglomeration process and to determine agglomerate structures under Brownian motion as well as under shear flow, similar to the motion in stirred media mills. For small angle neutron scattering measurements the deionized water was replaced by D_2O, to minimize incoherent scattering. Figure 7.5 shows agglomeration studies for 5 wt% Ludox suspensions. The curve with the unfilled symbols was measured for Brownian agglomeration alone in dialyzed water. To see the differences in the agglomeration behavior in different solvents, perikinetic agglomeration were also measured with DLS under the same conditions but with D_2O as solvent. The results are the curve with the filled symbols. Good agreement is observed for the aggregation kinetics in D_2O as compared to H_2O when the viscosity and molecular weight difference of the solvents are properly accounted for.
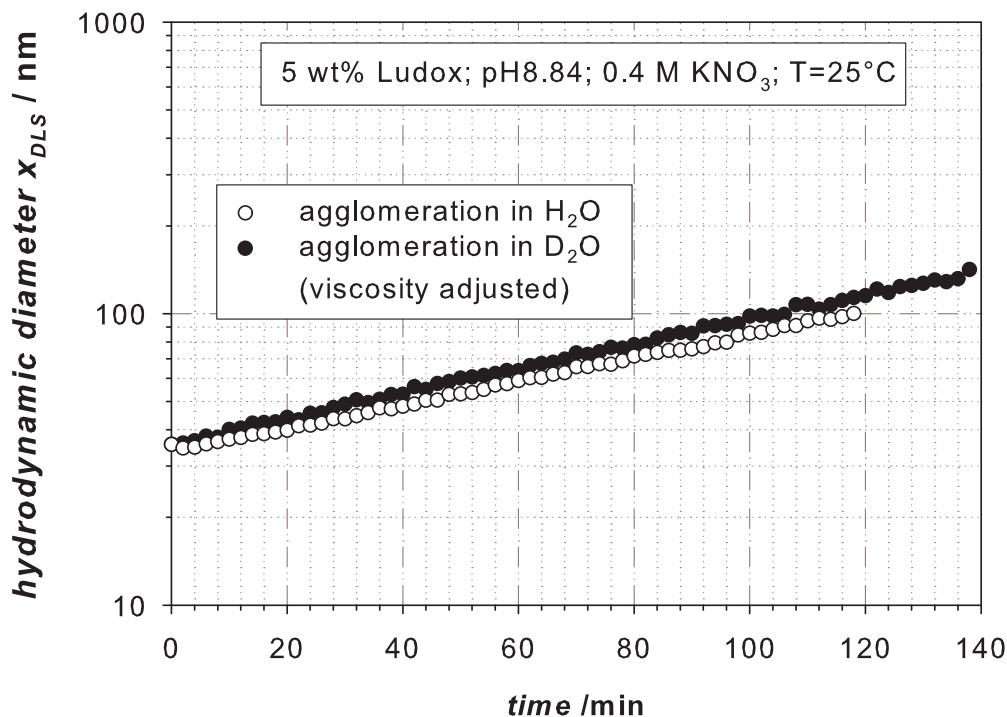
FIGURE 7.5. Effective diameter as a function of time for 5 wt% Ludox TM50 quiescent in H_2O and D_2O.

Figure 7.6 shows SANS results for 1 wt% Ludox under stable conditions with no added salt. In this case, no fractal agglomerates are observed and we obtain the scattering curve of the primary particles. The particles show the same behavior as monodisperse spheres with a diameter of 31.6 nm. A sphere of a radius a gives the following scattering intensity [161]:

$$I(q) = \left(3\frac{sin(q \cdot a) - (q \cdot a) \cdot cos(q \cdot a)}{(q \cdot a)^3}\right)^2 . \tag{7.4}$$

In neutron scattering the wavelength profile $W(\lambda')$ has to be taken into account [161]. The appropriate smearing integral is [161]:

$$|I(q)| = \int_0^\infty W(\lambda') \cdot I\left(\frac{q}{\lambda'}\right) d\lambda'. \tag{7.5}$$

whereas $\lambda' = \lambda/\lambda_0$ and λ_0 is the median reference wavelength. For the wavelength profile $W(\lambda')$ a Gausian distribution was assumed.

The theoretical curve for these spheres was added to the plot with and without accounting for instrument broadening.
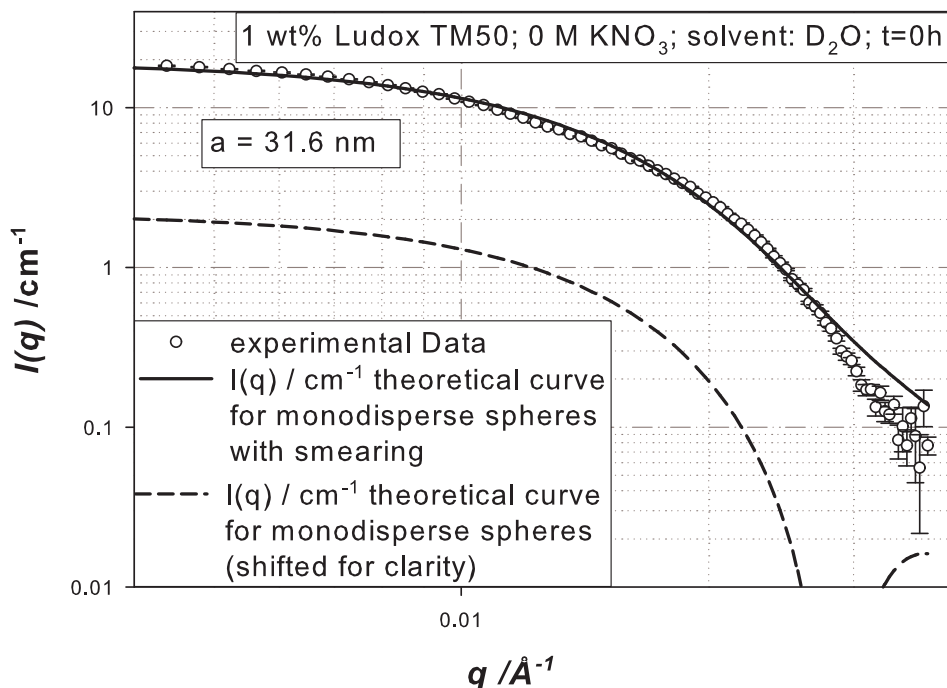
FIGURE 7.6. SANS experiments for 1 wt% Ludox under stable conditions with no added salt.

The radius of gyration is extracted using the method of Guinier [162]. In this method, the logarithmic scattering intensity is plotted over the square of the scattering vector. The slope of the curve in the median range of scattering vector is proportional to the primary particle radius. The radius of gyration is defined according to Guinier [162] as:

$$R_g^2 = \frac{\int \rho(r) \cdot r^2 \cdot dV}{\int \rho(r) \cdot dV}. \tag{7.6}$$

where ρ is the scattering length density, V the volume and r is the distance from the particle center. The scattering intensity is related to the radius of gyration by:

$$I(q) = I(0) \cdot e^{-\frac{q^2 R_g^2}{3}}. \tag{7.7}$$

An example of a Guinier plot is shown in figure 7.7. The average of the primary particle diameter is 30.77 ± 1.9 nm, which is smaller than the particle diameter of 37 nm obtained from the dynamic light scattering experiments, but consist with the value obtained from fitting the entire spectra.
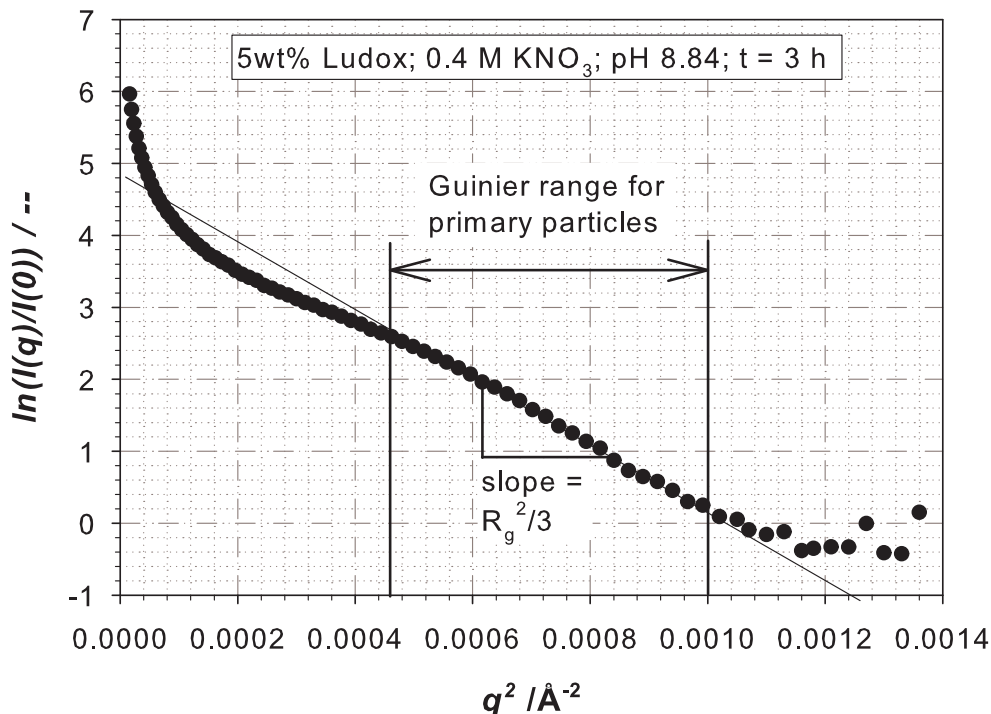
FIGURE 7.7. Guinier plot.

Figure 7.8 shows combined results from SANS and static light scattering (SLS) experiments. The logarithmic intensity is plotted over the logarithmic scattering vector for a 5 wt% Ludox suspension with 0.4 M KNO_3 aggregated under perikinetic conditions. The light scattering data is not absolute and was shifted to align with the SANS results. However the shifting was done with the same shift factor for all spectra. Note the excellent agreement despite given that two independent measurements performed on separate samples and equipment.

The theoretical line for the scattering intensity of homogeneous spheres is calculated over the entire q range obtained for light and neutron scattering (see equation 7.4 and 7.5). To describe the scattering intensity of fractal structures the intensity $I(q)$ calculated for homogeneous spheres was multiplied by a structure factor, which was calculated according to Teixeira [163]:

$$S(q) = \left(1 + \frac{1}{(q \cdot a)^{d_F}} \frac{d_F \cdot \Gamma(d_F - 1)}{\left(1 + \frac{1}{q^2 \cdot \xi^2} \right)^{(d_F - 1)/2}} \cdot \sin \left[(d_F - 1) \cdot \tan^{-1}(q \cdot \xi) \right] \right). \quad (7.8)$$

Where a is the radius of the primary particles and ξ is the aggregate radius. The fitting parameters $I(0)$, d_F, ξ and a were chosen to minimize the mean

deviation between model and experiment. From the slope of the scattering curve, the fractal dimension can be estimated.

Figure 7.9 compares the fractal dimensions extracted from the orthokinetic SANS data as compared to the perikinetic data. At the beginning of the agglomeration process, the agglomerate consists only of a few particles and therefore, cannot be accurately described as fractal (for reference: a long, linear chain of particles has a fractal dimension approaching $d_F = 1$ and a sphere has a fractal dimension $d_F = 3$). Hence, the slope extracted for long times are probably not an accurate reflection of the aggregate structure and size distribution. However, after sufficient growth, a clear fractal signature is evident in the scattering. For the Brownian regime a fractal dimension of 2.0 is obtained for long times. According to the literature [**93**] this fractal dimension suggests a reaction limited cluster-cluster aggregation mechanism (RLCCA), which is consistent with DLS and SLS measurements. Due to experimental limitations, aggregate size could not be extracted from SANS.

After the final aggregate structure was reached the structure obtained from Brownian agglomeration was destroyed by application of laminar shear in the NIST shear cell. The SANS and SLS data were collected after the sample was aggregated for 3.5 hours under perikinetic conditions. First a shear rate of $100~s^{-1}$ was applied for five minutes. Immediately after that the shear rate was set to $1000~s^{-1}$ for five minutes. In the following five minutes measurements under rest were taken. The fractal dimension rises from 2.0 to 2.19 after the shear rate of $100~s^{-1}$ was applied. By further increasing the shear rate to $1000~s^{-1}$ the fractal dimension rises to 2.28. The resulting structures are shown quantitatively in the insert of figure 7.9. After flow cessation no restructuring of the sample was observed.

To make global predictions for the restructuring of clusters after shear induced microstructural rearrangement of flocs is according to [**164**] difficult, because the restructuring is system dependent. The main influence parameters are the size of the flocs, the size of the primary particles, the strength of the particle bonds, the macroscopic shear rate, the concentration and the magnitude of the hydrodynamic interactions between the flocs. For example, Collins et al. [**164**] could measure considerable micro structural reorientation upon the application of stress to a suspension of strongly aggregated carbon black particles in dodecane. In contrast, Torres et al. found no change in the fractal dimension of polystyrene particles after the suspension had been sheared in a Couette-Taylor apparatus [**165, 166**].

The increase of fractal dimension with increasing shear rate can be interpreted as a densification of the agglomerates due to the shear forces. This densification of agglomerates after the application of significant shear forces was often observed in the literature (e.g.[**165, 167, 168, 169**]) as well. Careful examinations of the SANS patterns indicated no anisotropy in the scattering, showing that the fractals remain, on average, spherical. This is consistent

with observations in the literature (e.g. [168]). However, many authors observed the developing of an anisotropic microstructure and the break down of the self-similarity of the structure during shear at higher volume fractions [167, 168, 170, 171, 172, 173, 174].

SANS measurements were also performed under constant shearing conditions at the same composition to ascertain the effects of high shear flow on the agglomerates growth rate and fractal structure. It is observed that a denser, more compact aggregate is more rapidly formed than under equivalent, but perikinetic aggregation times. The aggregate growth under a constant shear force with a shear rate of $1000 \ s^{-1}$ is leading to a fractal dimension of 2.75 as it can be seen in figure 7.9. Note that a solid, coalesced silica sphere would have a theoretical maximum fractal dimension of three, such that the application of shear flow during aggregation leads to significant densification of the agglomerates.

The Peclet number (see equation 3.30) at this shear rate for the primary particles is $Pe = 0.03$ indicating that the rate of doublet formation is controlled by Brownian motion in the initial aggregation process. The process is dominated by convection when the agglomerates grow to approximately three times the diameter of the primary particles, and orthokinetic conditions are expected to dominate thereafter.
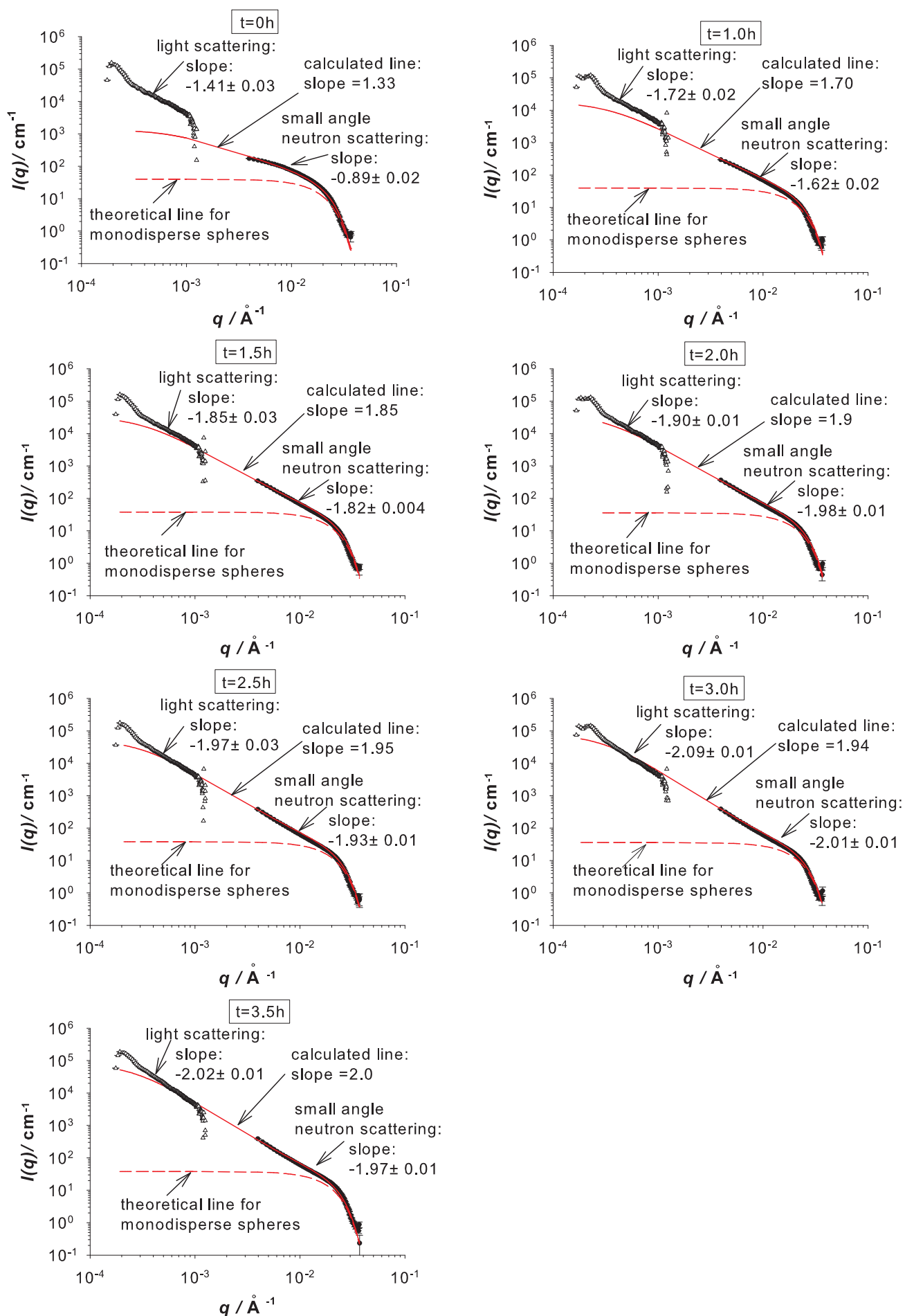
FIGURE 7.8. Comparison between SANS and SLS experiments for perikinetic aggregation (5 wt% Ludox TM-50, 0.4 M KNO$_3$ solvent: D$_2$O).
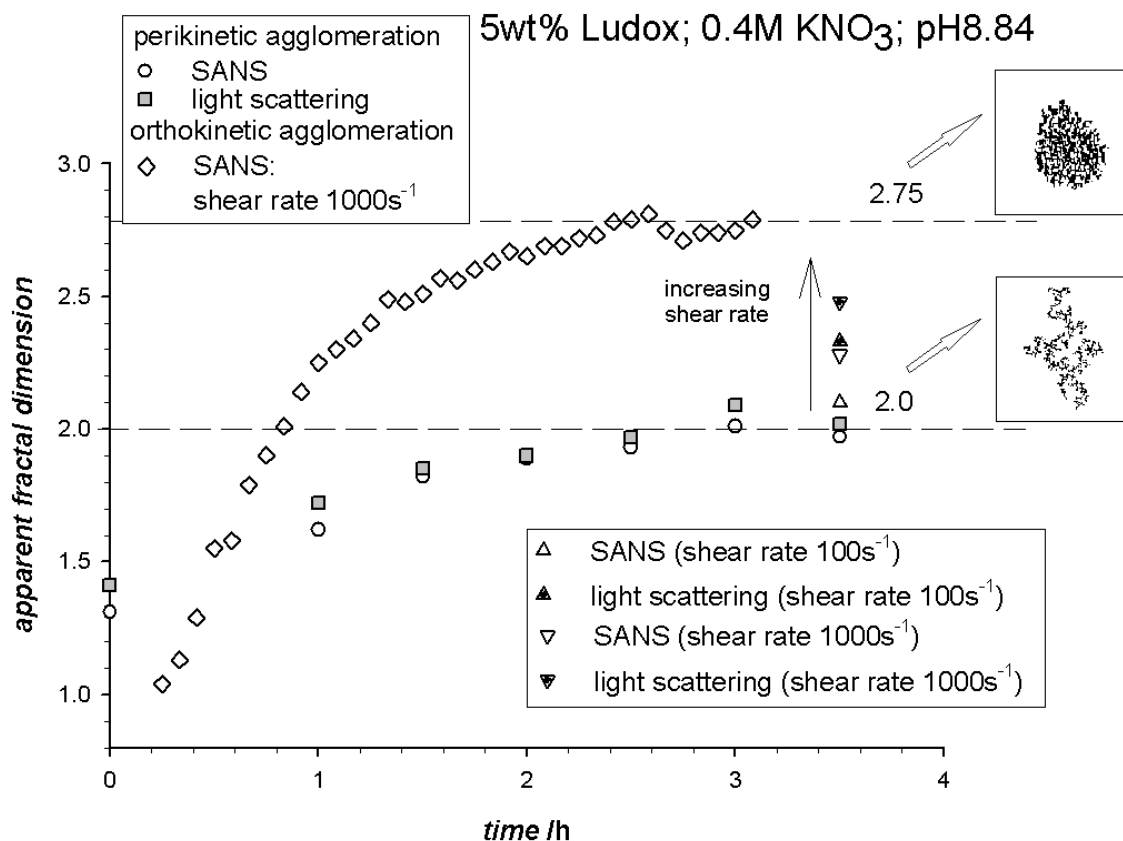
FIGURE 7.9. Fractal dimension for perikinetic and orthokinetic aggregation for 5 wt% Ludox and 0.4 M KNO_3.

7.2. Agglomeration and Dispersing in a Stirred Media Mill

7.2.1. Preliminary Investigations. Experiments similar to stirred media milling were performed in lab scale using a mini bead beater from BIOSPEC Products (see appendix A.6). A vial of 2 ml volume with a media milling loading of about 30% was shaken with high intensity. The milling beats consist out of glass spheres with a diameter of 0.5 mm. Figure 7.10 shows a comparison of the perikinetic and orthokinetic aggregation behavior of the Ludox dispersion. The experiments under shear stress show that the agglomeration process is much faster as under Brownian agglomeration alone. The coagulation rates are greatly increased by the shear stress provided by the bead beater. The shear increases the aggregation rates over normal diffusion. This interesting result points toward an enhancement in the aggregation rate in the presence of convection (as generated in the bead mill). The Peclet number Pe in the bead beater was estimated to have values between 1 and 100 indicating that the process runs in the intermediate range between diffusion and convection driven regimes [77].
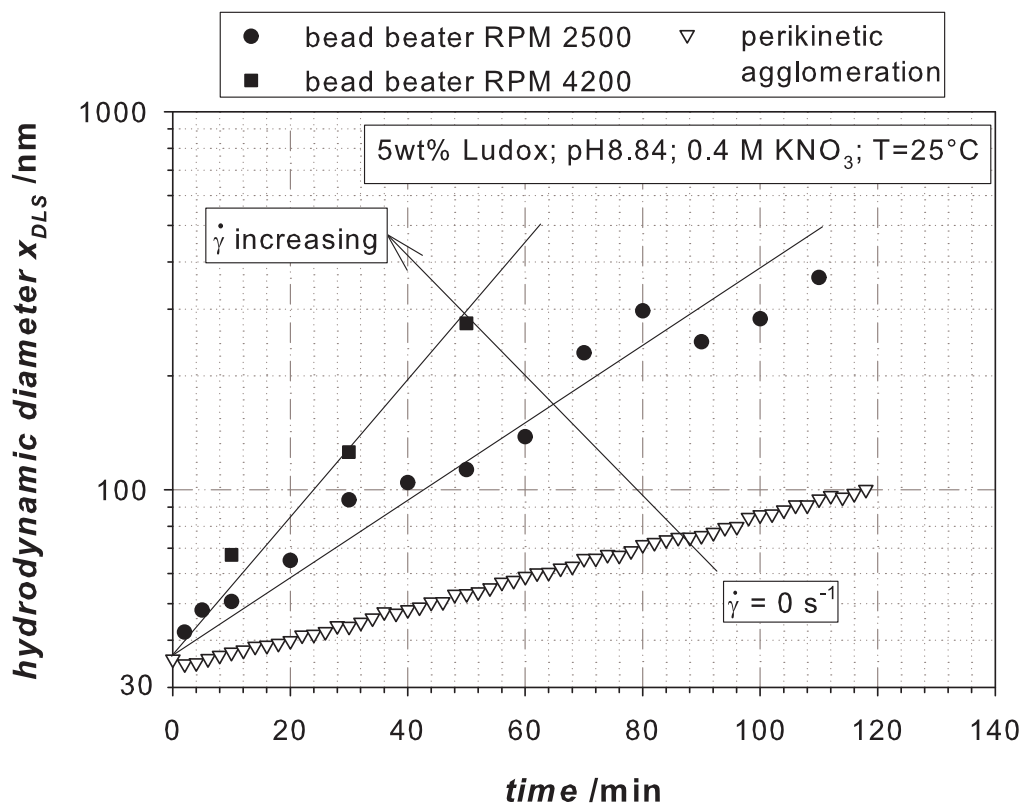
FIGURE 7.10. Effective diameter as a function of time for 5 wt% Ludox TM50 under perikinetic and orthokinetic conditions (see text).

7.2.2. Milling Results. The milling experiments presented in this chapter are performed on the mill for aqueous suspensions described in chapter 4.1. The samples were taken directly from the suspension outlet of the mill and were immediately diluted in order to avoid further agglomeration and multiple scattering. Figure 7.11 shows the evolution of the hydrodynamic diameter over time for a 5 wt% Ludox suspension with 0.6 M KNO_3 under perikinetic and under milling conditions. To slow down the agglomeration kinetics the temperature was set to 12° C. The curve with the filled circles shows the perikinetic agglomeration of the Ludox suspension. Under milling conditions the agglomeration of the particles is accelerated until the steady state between agglomeration and deagglomeration is reached. This steady state is strongly dependent on the energy input. As can be seen in figure 7.11 the steady state particle size decreases with increasing stirrer tip speed. Similar results were found from other authors as well [**127, 128, 166, 175, 176, 177, 178, 179**]. However, these authors studied particles in the size range of several microns. None of them used a stirred media mill for their studies; instead they worked in Couette flow systems. The data in figure 7.11 show that these findings can also be transferred to stirred media milling and that agglomeration plays a significant role by producing particles in the nanosize range. As can be seen in this figure the agglomeration kinetics is increasing for an increasing stirrer tip speed. However, the steady state size between agglomeration and dispersing is smaller for higher tip speeds.
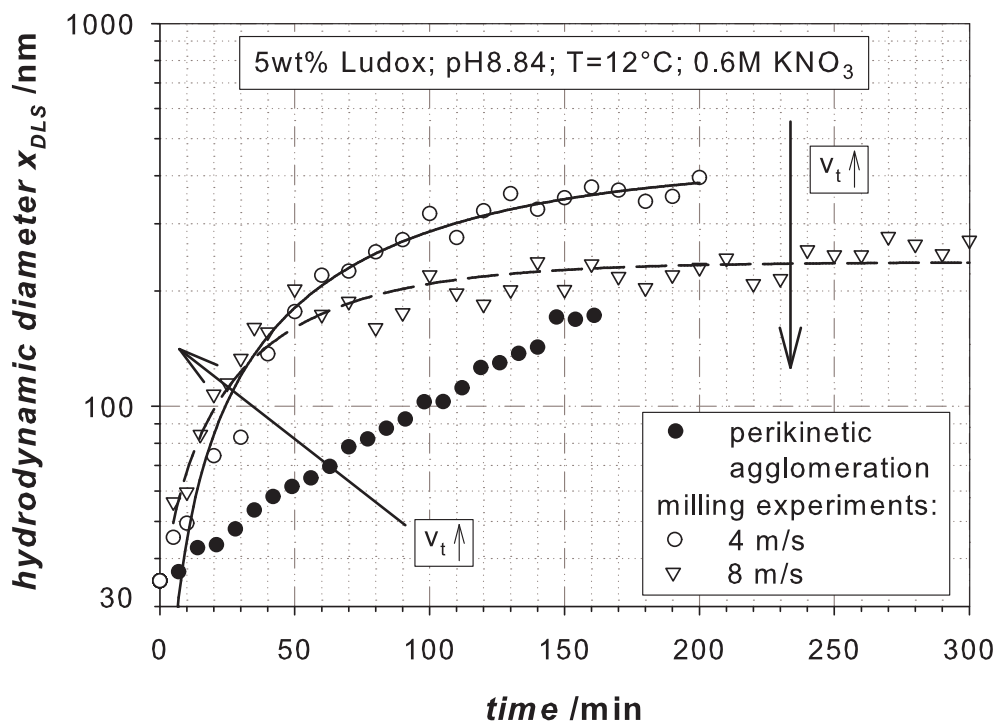
FIGURE 7.11. Influence of the tip speed on the agglomeration under milling conditions (mill discribed in chapter 4.1).

Figure 7.12 shows the evolution of the hydrodynamic diameter over time for a 5 wt% Ludox suspension with the salt concentration as parameter. The experiments were carried out at a constant tip speed of 4 m/s. Under milling conditions the agglomeration of the particles is accelerated until the steady state between agglomeration and deagglomeration is reached. This steady state is dependent on the salt concentration. With increasing salt concentration the median particle size is larger and the agglomeration kinetics is faster.

Figure 7.13 shows that the steady state between breakage and agglomeration can also be reached by real breakage of solid particles. In this diagram the hydrodynamic diameter is plotted over the milling time. The lower abscissa is for the agglomeration and dispersing data of Ludox particles. Because the time scale of real breakage of SiO_2 is different from the agglomeration and dispersing data (filled symbols) a second abscissa for the grinding experiments with SiO_2 Mikrosil LS500 (open symbols) was introduced. The data with the filled symbols are for milling experiments with 5 wt% Ludox in 0.6 M KNO_3. For this system the agglomeration dominates the process and the steady state is reached starting from small particles. To show that the steady state can also be reached from larger particle sizes, SiO_2 Mikrosil (Westdeutsche Quarzwerke) with a median particle size of 6 μm was used as feed material. The experiments were performed at pH8.84, there the maximal ζ-potential of -35 mV was measured. The data with the half filled circles were measured for a 20 wt% SiO_2 suspension at a tip speed of 8 m/s. In this experiment no salt was added to show were the minimal median particle size $x_{50,3}$ under stable conditions lays for these milling parameters. A median particle size of 100 nm was reached.
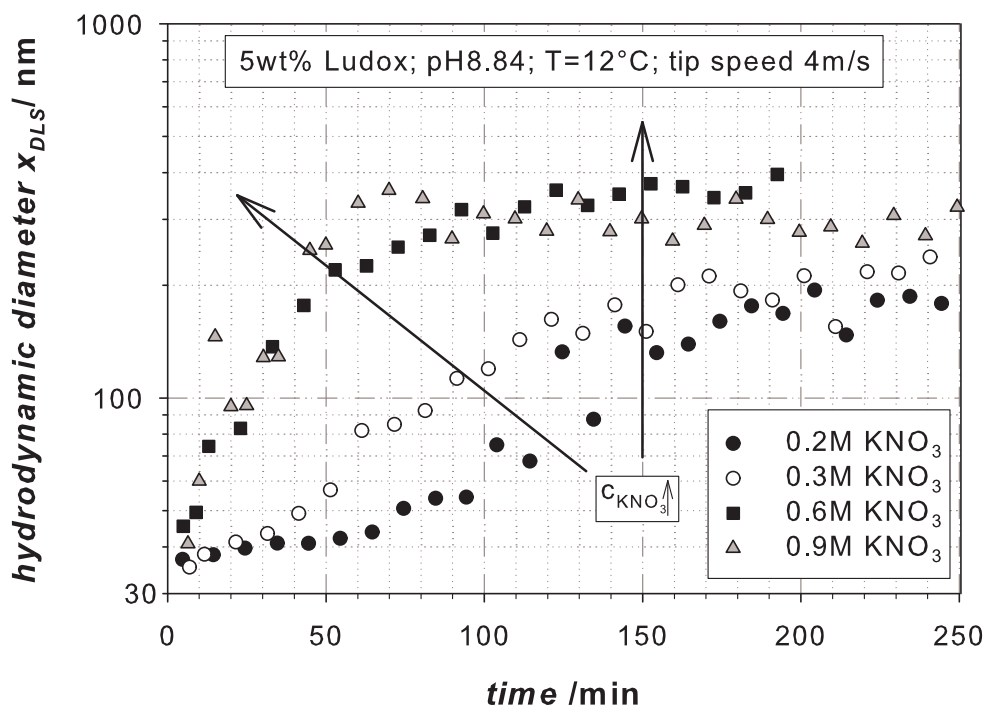
FIGURE 7.12. Influence of different salt concentrations on the agglomeration under milling conditions.

In a further experiment 0.6 M KNO_3 was added to the feed suspension at the starting time of the experiment. The addition of salt increases the agglomeration rate and the steady state moves in favor of agglomeration. The median particle size of the steady state for a 20 wt% SiO_2 suspension is 500 nm. To compare these experiments with the agglomeration and dispersing experiments for Ludox an experiment under 5 wt% SiO_2 was performed. The steady state at these conditions is with 390 nm lower than for the experiments with 20 wt%. However, the steady state for the milling experiments with Ludox lies below this result at the same conditions. The reason for the difference may be due to the different manufacturing techniques of the solids and associating to this different impurities, which influence the stability of the particles.
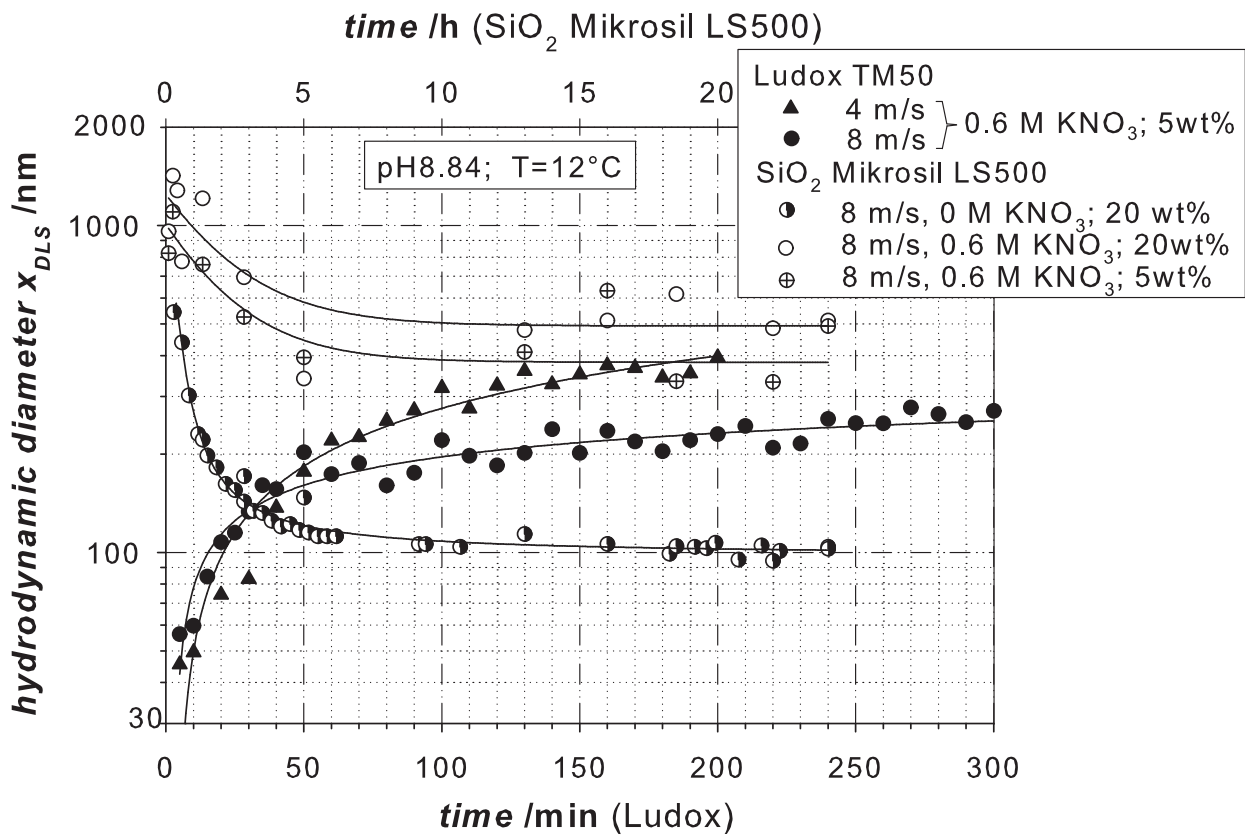
FIGURE 7.13. Evolution of the hydrodynamic diameter over time for milling experiments with Ludox and SiO_2.

7.3. Comparison of Aqueous and Non-aqueous Solvents in Stirred Media Mills

So far the possibility to produce nano fine particles by wet milling in the aqueous phase was demonstrated [1]. Because the high industrial demand on nanoparticles in organic solvents the study was extended to non-aqueous systems. The experimental results presented in this section are organized in three subsections. In the first two subsections preliminary experiments regarding the stability of alumina particles in organic solvents are presented. Steric as well as electrostatic stabilization of the particles are considered. Finally, in subsection 7.3.3 a milling study with steric and electrosteric stabilization in different solvents is shown.

7.3.1. Steric Stabilization.

An estimation of the total interaction energy of sterically stabilized α-alumina in water is shown in figure 7.14 and 7.15. In this approximation the energies are calculated with equation 3.15 and 3.19 with the assumption that water is a good solvent. This means that the segment density in the polymer layer is constant, that the polymer chains are fully stretched and that the polymer density at the particle surface can be calculated with $\nu = l^{-2}$ [77]. As figure 7.15 shows, a molecular weight of $M_n = 5000$ g/mol is not sufficient to effectively stabilize the suspension. In this case a weak coagulation is expected even though a "better than Theta solvent" is assumed in the calculation. At molecular weights $M_n = 10\ 000$ and $15\ 000$ g/mol the repulsive force is mainly influenced by the compression of the polymer chains, since the force of the osmotic term is relatively low. The molecular weight of the polymer chains must be high enough to effectively stabilize the particles. The estimation shows that a polymer weight of $20\ 000$ g/mol is necessary to stabilize the dispersion if an ideal solvent is assumed. For this case a layer thickness of the polymer of 15 nm is estimated. This thick adsorbed layer on the particles surface may lead on the one hand to a strong quenching of van der Waals forces. On the other hand thick polymer layers may adsorb the mechanical energy needed for grinding.

In this work the polymer DAPRAL was used as dispersing agent for the experiments with steric stabilization. This polymer can be used in wet milling with organic solvents of different polarities. The adsorption of the polymer on oxide surfaces in organic media depends according to Somasundaran [180] mainly on the interactions between hydroxyl groups of the oxide surface and the polar regions of the surface active macromolecules. The hydrophilic side chains of the polymer are responsible for the adsorption of DAPRAL on the Al_2O_3 surface and the steric stabilization mechanism is archived by the polymer chains reaching in the solution.

Figure 7.16 shows adsorption isotherms for DAPRAL on α-alumina dispersed in different solvents. For the measurements alumina (AKP-30) with a median particle size of $x_{50,3} = 300$ nm was used. 6.25 wt% of alumina particles were
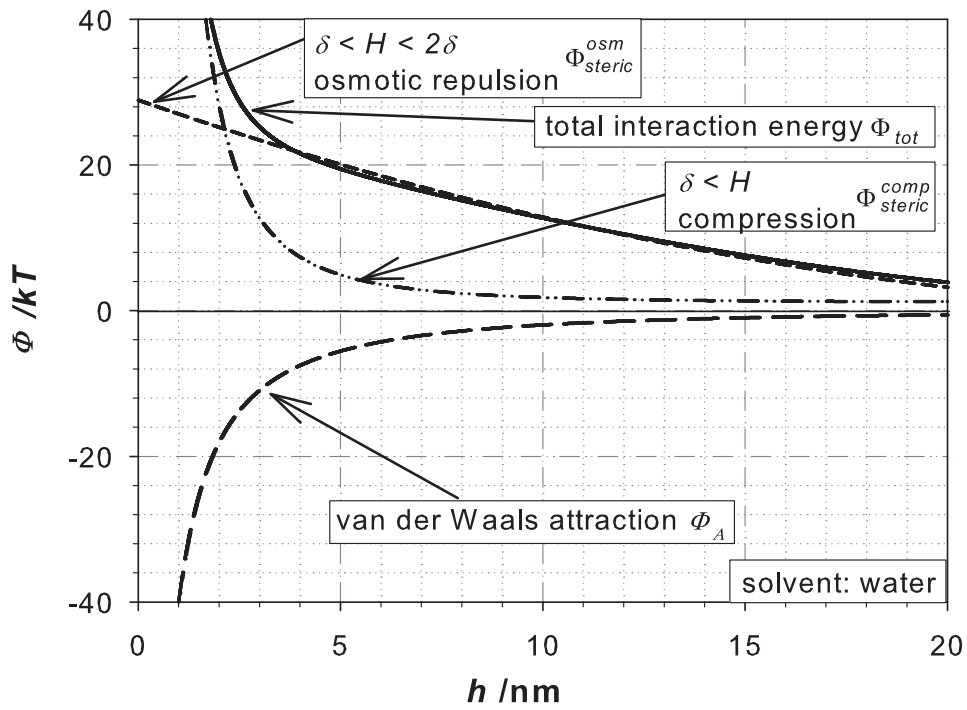
FIGURE 7.14. Interaction potential for sterically stabilized α-Al$_2$O$_3$.
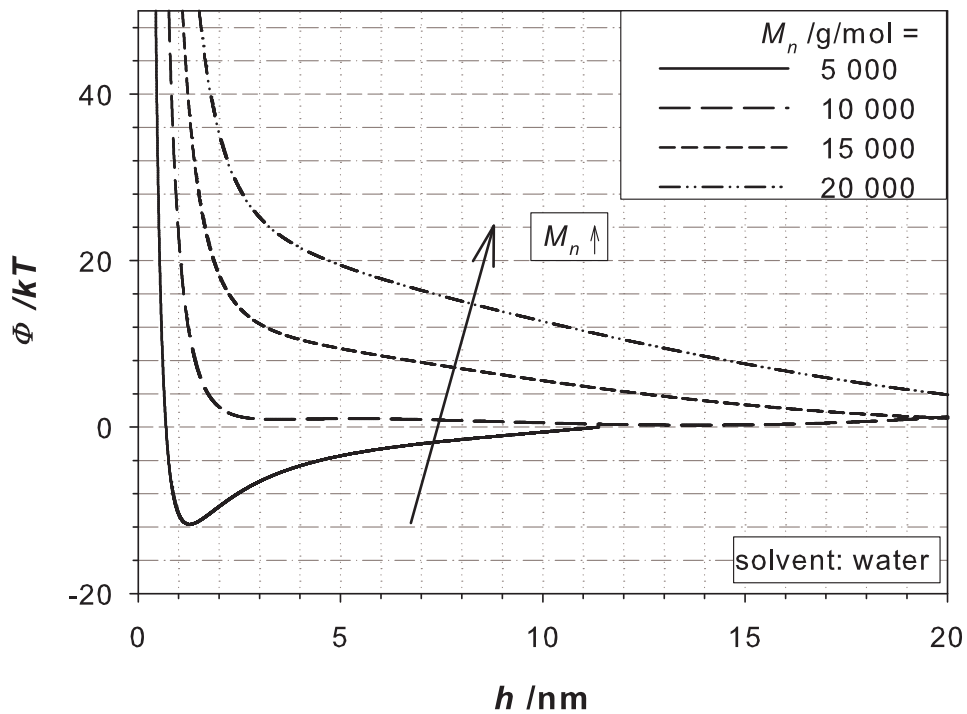
FIGURE 7.15. Interaction potential for sterically stabilized α-Al$_2$O$_3$ with the chain length as parameter.

added to the respective solvents which contained different polymer concentrations, ranging from 0.6 to 2.5 mg/ml. The suspensions were allowed to stand over night under gentle stirring in order to reach the adsorption equilibria. To separate particles from free and not adsorbed polymer chains, the suspensions were centrifuged at 3500 rpm for 30 min in a Heraus Labofuge 400 and washed with pure solvent for five times. The centrifuged particles were dried and the adsorbed polymer amount was thermogravimetrically determined with a heating rate of 10 K/min under nitrogen atmosphere. Based on the specific surface area of the alumina particles (10.1 m^2/g) the amount of adsorbed polymer per unit area can be calculated. In figure 7.16 the adsorbed amount of polymer is plotted against the dimensionless concentration $c_{DAPRAL}/c_{alumina}$. At a dimensionless concentration $c_{DAPRAL}/c_{alumina}$ hiher than 0.025 a plateau region is reached independent of the kind of the solvent. That means from this ratio onwards a complete coverage of the particle surface with polymer chains is attained. However, the amount of adsorbed polymer depends on the quality of the solvent. The lowest amount of adsorbed polymer of 1.2 mg/m^2 was measured for alumina particles in water and the highest amount was detected in 2-butanol. The adsorbed amount in toluene (1.5 mg/m^2) and ethanol (1.7 mg/m^2) lays between these values. A hydroxide layer around the α-alumina particles has no influence on the amount of adsorbed polymers in aqueous phase.
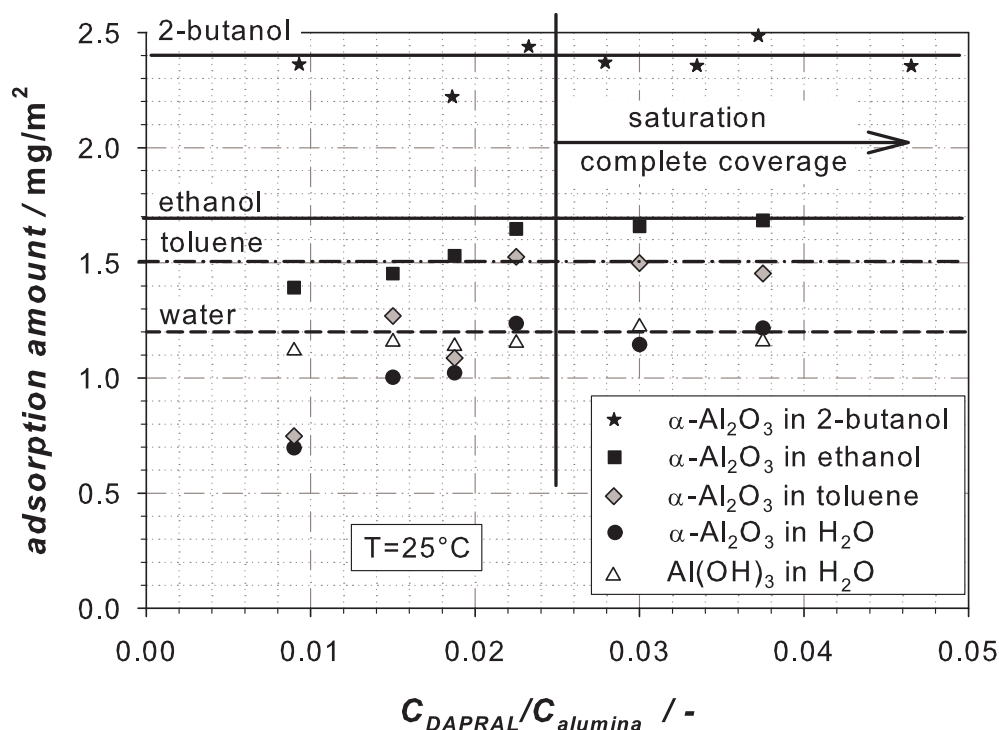
FIGURE 7.16. Adsorption isotherm of DAPRAL on alumina particles in different solvents.

Figure 7.17 shows the influence of molecular weight of the polymer on the adsorption isotherm on alumina particles in 2-butanol. For DAPRAL with a viscosity of 56.05 cm^2/s measured at 40°C in a capillary viscosimeter an

adsorbed amount of 2.5 mg/m² was determined, while for DAPRAL with a viscosity of 5.73 cm²/s an adsorbed amount of 1.6 mg/m² was measured.
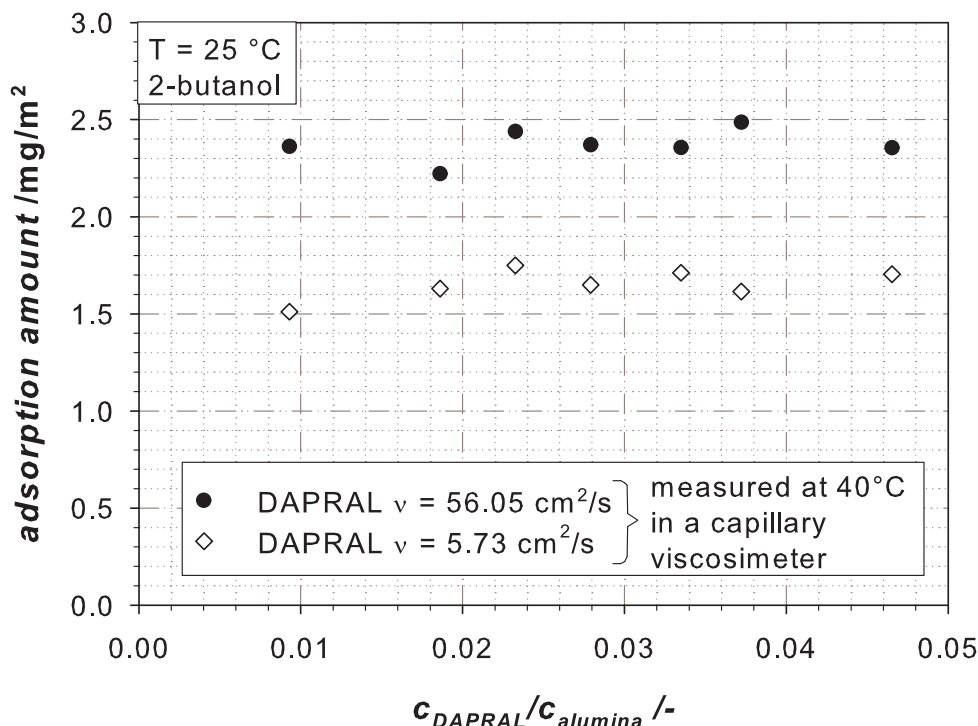
FIGURE 7.17. Adsorption isotherm for DAPRAL with different chain lengths on alumina particles in 2-butanol.

Figure 7.18 shows dispersing experiments for α-Al$_2$O$_3$ in water and ethanol. In this diagram the median particle size $x_{50,3}$ is plotted against the dimensionless concentration $c_{DAPRAL}/c_{Al_2O_3}$. The samples were shaken for 24 h at room temperature in order to reach the adsorption equilibrium. Subsequently the samples were stressed with ultra sound for three minutes to destroy weak agglomerate structures. Afterwards the particle size measurements were performed with dynamic light scattering (ZetaSizer Nano see chapter 5.1.2). As it can be seen in figure 7.18, the agglomerates can be dispersed to their primary particle size if the concentration of DAPRAL is in the plateau region of the adsorption isotherm. In this region the surface is covered completely with polymer.

In figure 7.19 the ζ-potential and the pH-value are plotted against the dimensionless DAPRAL concentration in aqueous phase. With increasing DAPRAL concentration the pH value decreases from pH6 to pH5.3, because the polymer reacts acidly due to the carboxylic acid group. Simultaneously, the ζ-potential decreases from -4.5 mV to -14 mV.

7.3.1.1. *Rheology of Sterically Stabilized Suspensions.* In this section the case is discussed where polymer chains are adsorbed on single particles. The phenomenon where a single polymer chain is adsorbed onto different particles, which is desirable for flocculation, is not covered here.
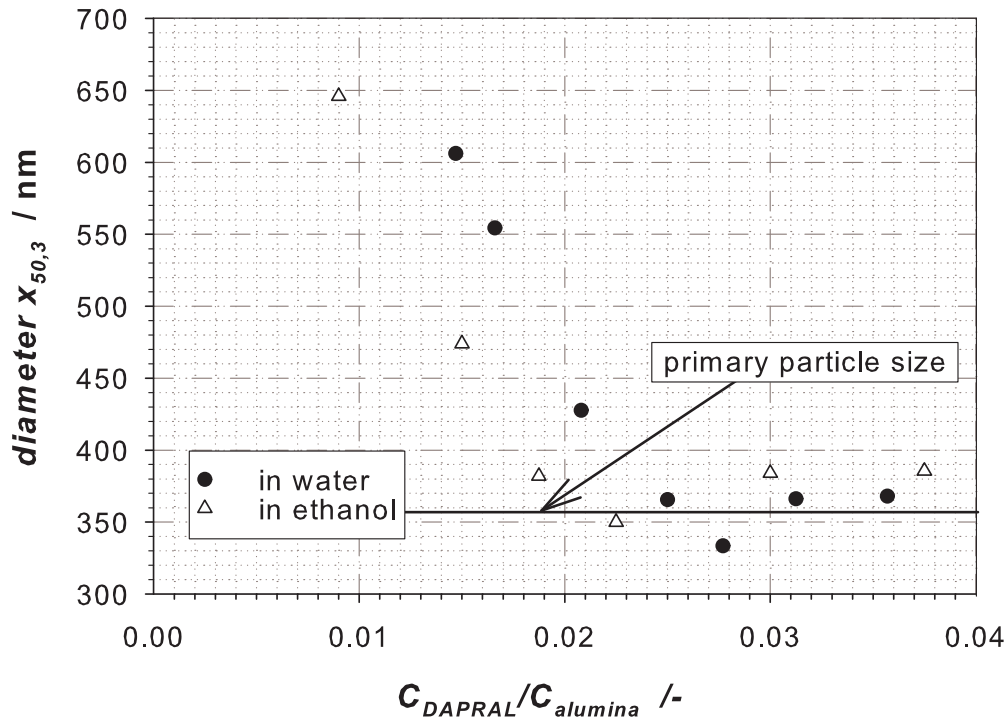
FIGURE 7.18. Dispersing experiments for α-Al$_2$O$_3$ stabilized with DAPRAL in water and ethanol.
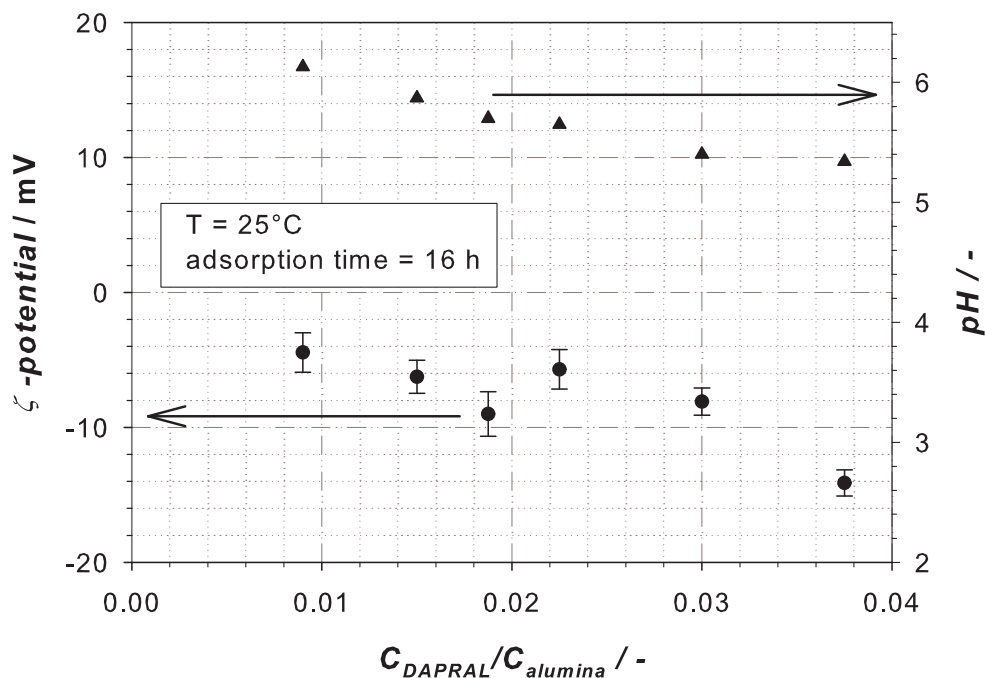
FIGURE 7.19. Influence of DAPRAL concentration on pH-value and ζ-potential.

If the polymer concentration is sufficiently low and the adsorption equilibrium is preferable, then the polymer chains are adsorbed on the particle surface. An example for this case is shown 7.20 and 7.21. Here the rheological behavior

of sterically stabilized α-Al_2O_3 suspended in water and ethanol, respectively, is shown in dependency of the mass concentration of alumina. The experiments are carried out on a Physica rheometer at 25°C using a double gap geometry. In order to effectively stabilize the particles sterically the polymer concentration was selected from the plateau region of the adsorption isotherm (see Figure 7.16). Thus the DAPRAL to alumina concentration was chosen to be $c_{DAPRAL}/c_{Al_2O_3} = 0.03$.
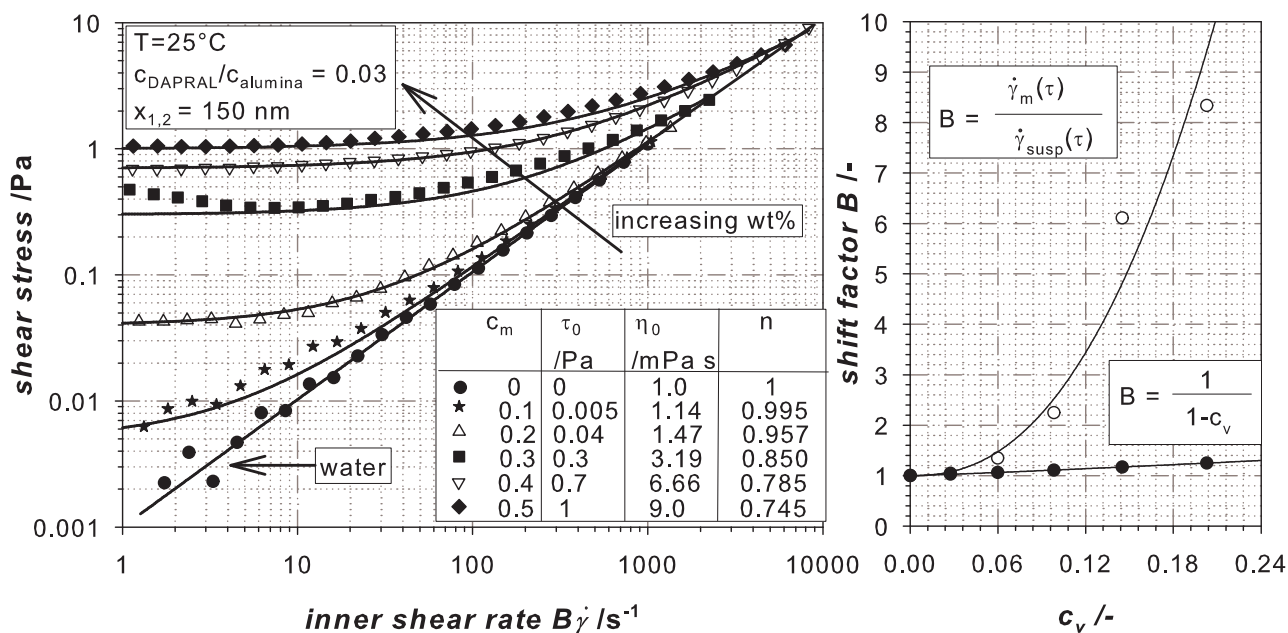
FIGURE 7.20. Flow curves of sterically stabilized α-Al_2O_3 in water in dependency of the particle concentration.

The parameters used to model the data according to the model of Herschel and Bulkley (see equation 3.34) are shown in the legend of the plot. All suspensions show nonlinear flow curves and exhibit a yield stress. With increasing wt% of alumina particles the yield stress increases. The flow curves of Al_2O_3 particles in ethanol are similar to the flow curves in water. However, the zero shear viscosity and the yield stress are conspicuously smaller for Al_2O_3 particles in ethanol than in water, especially at high mass concentrations. The flow curves are shifted to a mastercurve at high shear rates according to the concept of shear equivalent inner shear rate from Gleißle and Baloch [147], where the system is determined by hydrodynamic interactions and not by interparticle interactions. The shift factor is calculated by equation (3.38) with the measured shear rate at a constant shear stress. The resulting shift factors are much larger than the theoretical shift factors determined by the volume fraction of particles. The reason for this could be adsorbed polymer chains on the particles, which increase the volume fraction of the particles c_v to an effective volume fraction
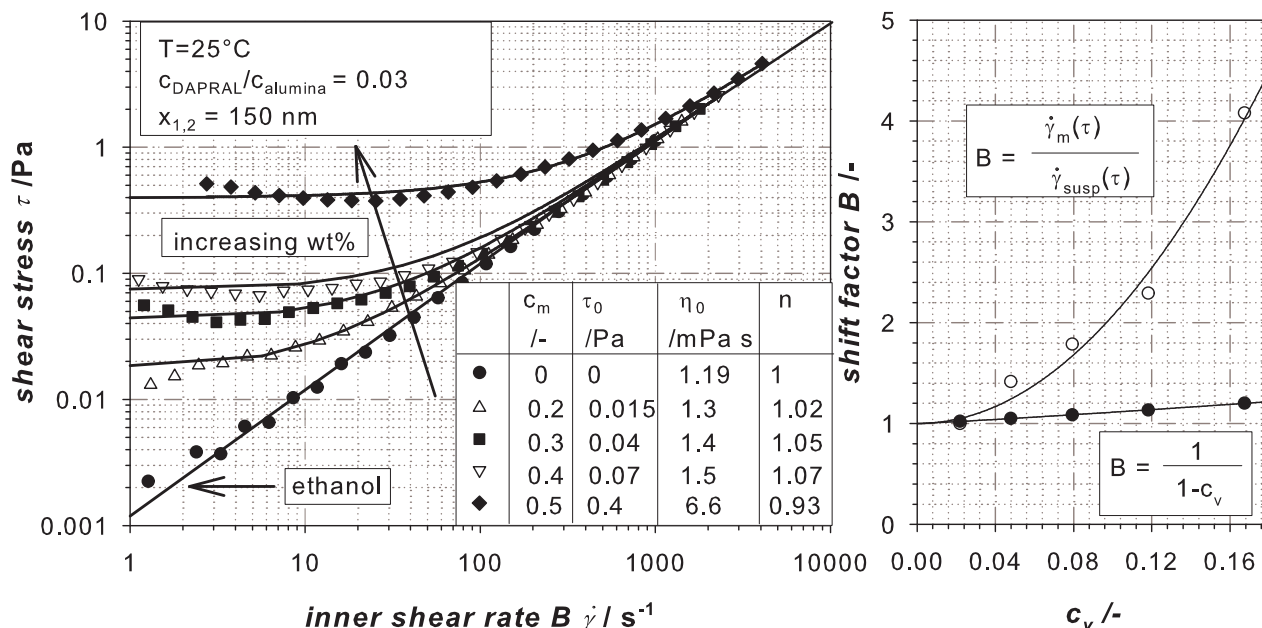
FIGURE 7.21. Flow curves of sterically stabilized α-Al$_2$O$_3$ in ethanol in dependency of the particle concentration.

$c_{v,eff}$. In this case the polymer cover around the particles is added to the particle volume. The layer thickness of adsorbed polymer can be estimated with the dependency of the measured shift factor on the particle volume concentration:

$$c_{v,eff} = \frac{B-1}{B}. \tag{7.9}$$

$$x_{p+2\delta} = \sqrt[3]{\frac{6 \cdot c_{v,eff} \cdot V_{tot}}{\pi \cdot N}}. \tag{7.10}$$

$$\delta = \frac{x_{p+2\delta} - x_p}{2}. \tag{7.11}$$

According to equation 7.9-7.11 a layer thickness of about 50 to 55 nm is estimated in ethanol and 40 to 45 nm in water.

A different method to estimate the layer thickness rheologically is shown in figure 7.22 and 7.23. Here the elastic and viscous moduli are plotted over the weight fraction of alumina particles stabilized with polymer. The experiments were performed at a constant frequency of 1 Hz and a strain of 0.01 at 25°C. The cross over point at which the elastic modulus G' is equal to the viscous modulus G'' can be taken as an indication of the volume fraction at which the adsorbed layers just overlapped [181, 182], because this point characterizes the transition between liquid like and solid like behavior. The crossover point occurs at a weight fraction of 0.38 in water and 0.35 in ethanol. An approximation of the median distance between the particles at this volume fraction provides a chain length of 42 nm in water and 53 nm in ethanol. In this approximation it is assumed that the particles are ordered in a cubic densest packing of spheres.

These estimated chain lengths correspond to the used DAPRAL with the molecular weight of 40 000 - 50 000 g/mol. These results could be verified with gel permeation chromatography (GPC). The measured median chain length of the used polymer in tetrahydrofuran (THF) is 50 000 g/mol (see chapter 6.1.5.1).

Hence, the milling experiments should be carried out below a weight fraction of 0.35, because an overlap of the polymer chains would restrict the free motion of not yet adsorbed polymers in the suspension. The position of the crossing-point in dependence of the weight-fraction of particles may also serve as a first estimate of the maximal achievable mass concentration and determines thus the economy of the process.
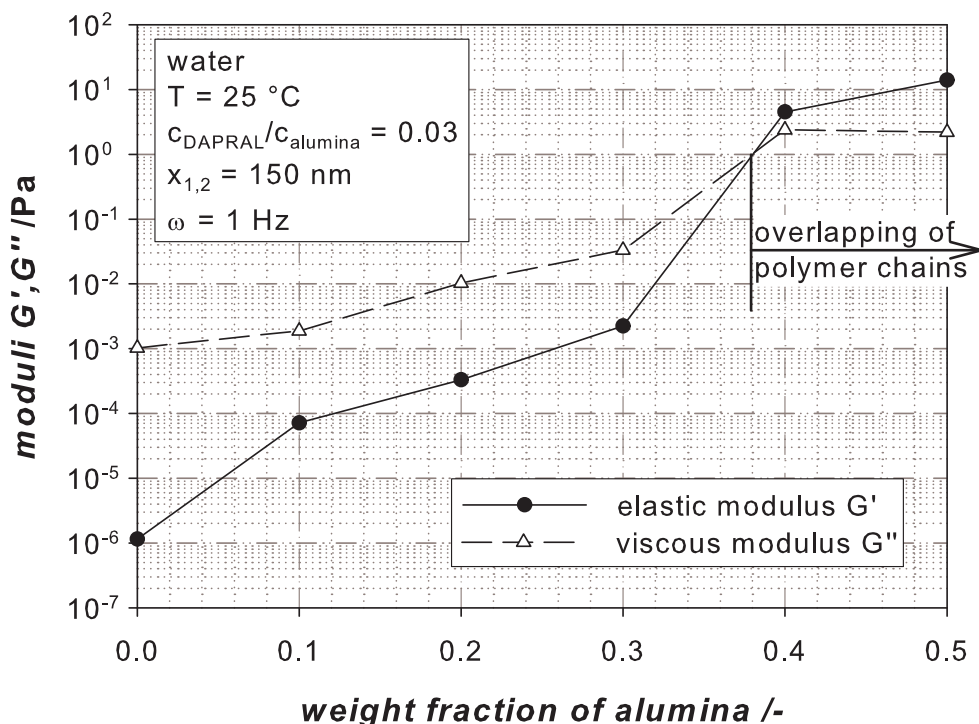
FIGURE 7.22. Plot of moduli as a function of weight fraction at a constant frequency of 1 Hz for sterically stabilized alumina in water.
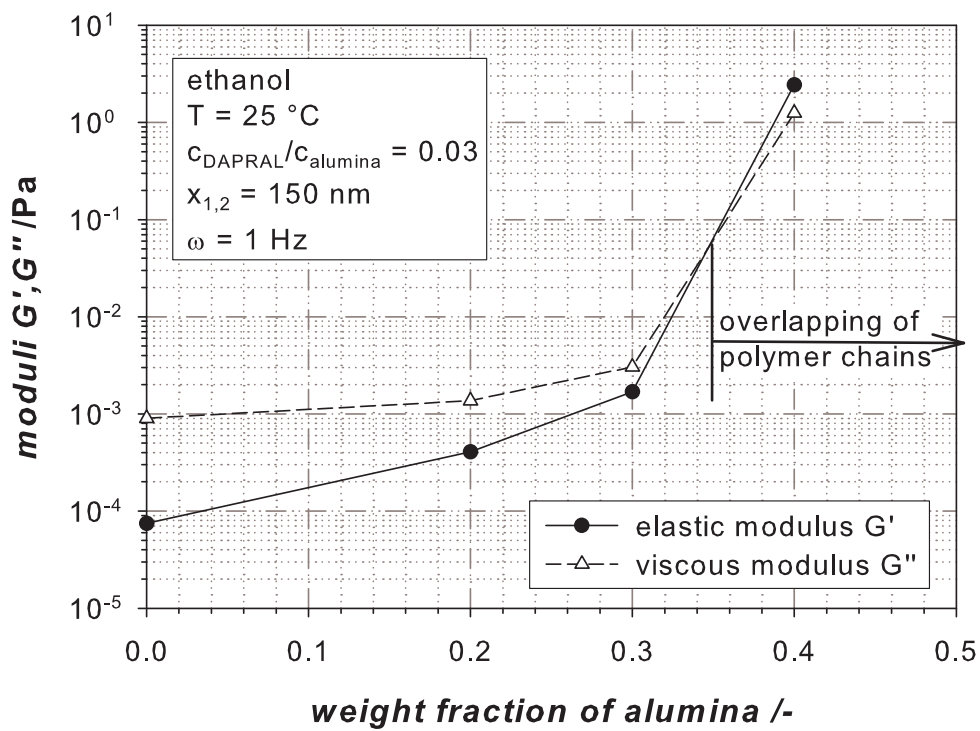
FIGURE 7.23. Plot of moduli as a function of weight fraction at a constant frequency of 1 Hz for sterically stabilized alumina in ethanol.

7.3.2. Electrostatic Stabilization. Figure 7.24 shows ζ-potentials for Al_2O_3 particles in an ethanol/water mixture measured by electroacoustics (DT1200). A ζ-potential of 44 mV was measured for alumina particles in pure water. With increasing volume concentration of ethanol a decrease in the ζ-potential was observed. In pure ethanol a ζ-potential of 18 mV was measured.
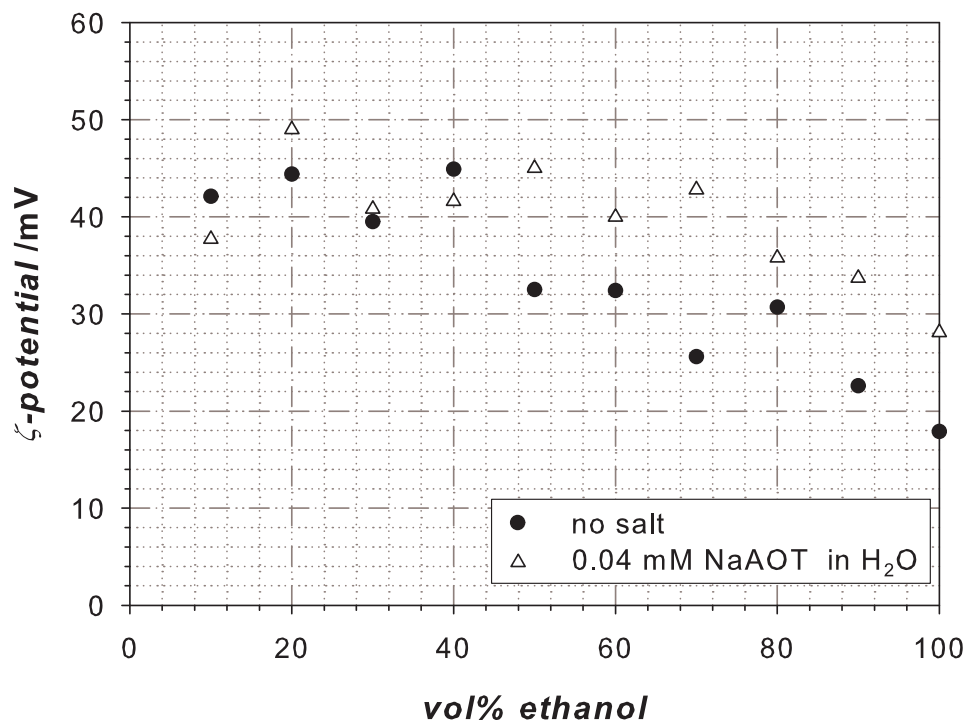
FIGURE 7.24. ζ-potential for α-Al_2O_3 in an ethanol/water mixture.

The ζ-potentials plotted here are corrected for double layer thickness effects. The ζ-potentials reported by the instrument are calculated based on a thin boundary layer assumption ($\kappa a \gg 1$) and significantly underestimates the actual ζ-potentials in the range of double layer thicknesses considered here ($\kappa a \approx 1 - 40$). Generally the measured electrophoretic mobility μ is calculated into a ζ-potential by:

$$\mu = \frac{2}{3} \cdot \frac{\epsilon_0 \epsilon_r \zeta}{\eta} \cdot f\left(\kappa a, a/d\right). \tag{7.12}$$

where the function f goes to 1 for thick double layers compared with the size of the particles ($\kappa a \ll 1$) and to 1.5 for thin double layers $\kappa a \gg 1$. This leads to the well known relations between μ and ζ:

$\kappa a \ll 1$, Hückel-Onsager-equation:

$$\mu = \frac{2\epsilon_0 \epsilon_r}{3\eta} \cdot \zeta. \tag{7.13}$$

$\kappa a >> 1$, Helmholtz-Smoluchowski-equation:

$$\mu = \frac{\epsilon_0 \epsilon_r}{\eta} \cdot \zeta. \tag{7.14}$$

The measurement range considered here lies in between these two borderline cases.

In the intermediate regime ($0.1 < \kappa a < 100$) the electrophoretic retardation must be accounted for. This retardation exists because the counter ions move opposite to the direction of the particles. By this the movement of the particles is restrained. According to Henry the function $f(\kappa a)$ rises from 1 at $\kappa a = 0$ to 1.45 at $\kappa a = 100$ and reaches the saturation value of 1.5 at $\kappa a = 1000$.

Sawatzky and Babchin [183] have developed a theory for arbitrary double layer thicknesses. They developed an equation for $f(\kappa a, a/d)$, which gives the ratio of the actual dynamic electrophoretic mobility to the mobility calculated assuming a thin double layer. The parameter

$$d = \left(\frac{2\eta}{\rho_f \varpi} \right)^{\frac{1}{2}} \tag{7.15}$$

is a characteristic distance over which disturbances are generated by the oscillating particle decay. As the parameter $a/d \to 0$ the function f goes to the function $f(\kappa a)$ of Henry [154, 183, 184]. The electroacoustic measurements used here were performed at a frequency of 1 MHz, which in ethanol gives a value for d of 1.65 μm. Van Tassel and Randall showed that the error in using the adjustment factor of Henry over the more complex formulation of Sawatzky and Babchin is for particles smaller than 0.15 μm always less than 10% under these conditions [154]. Therefore the adjustment of ζ-potential values was done using the Henry formula. In table 7.1 the properties of α-alumina suspensions in ethanol are shown exemplary for yttrium background ions.

TABLE 7.1. Properties of α-alumina suspensions with yttrium background ions.

bulk molarity /mM	conduc-tivity /μS/cm	Debye length /nm	κa	mobility /μm·cm/V·s	potential /mV	corrected potential /mV
0.004	186.3	4.72	24.7	3.59	39.1	41.5
0.01	187.8	4.79	25.1	3.74	41.1	44.7
0.04	186.3	4.71	24.8	4.35	46.9	51.2
0.1	188.4	4.73	26.6	5.08	56.1	61.2
0.4	189.2	4.65	30.0	3.29	36.1	39.4
1	193.4	4.65	37.6	1.74	19.8	22.9
4	203.2	4.57	41.2	0.54	-1.9	-2
10	216.4	4.4	60.5	0.02	-0.1	-0.1

Figure 7.25 shows the influence of different ions and ion concentrations on the ζ-potential for electrostatically stabilized Al_2O_3 in ethanol. The alumina

powder in ethanol develops a significant positive surface charge. According to van Tassel [154] the alumina surface acts as a catalyst for the autoprotolysis reaction of ethanol:

$$CH_3CH_2OH \Leftrightarrow CH_3CH_2O^- + H^+. \tag{7.16}$$
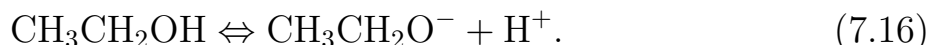
He proposed that an ethanol molecule adsorbs to the surface by its polar hydroxide group, dissociates and desorbs as an ethoxide ion, leaving a proton on the surface. This explains the positive surface charge of the alumina particles in ethanol. The alumina surface acts as a Lewis base, an electron donor. The effect of the autoprotolysis reaction is that the particle surrounds itself with its own ionic atmosphere. Significant concentrations of ethoxide ions can be measured around the alumina particles [154].

When salt is added to the suspension the concentration of the ethoxide ions in the bulk solvent is reduced due to reaction with the added ions, leading to a rise in surface charge and in the ζ-potential. Simultaneously there is an adsorption of negative salt ions on the surface by substitution of the salt ions for the ethoxide ions at the surface. According to van Tassel [154] the surface charge becomes now a function of the equilibrium dissolution of the salt ions from the surface.

The influence of the counter ions is at first sight contradictory to the lyotropic series, which goes back to Hofmeister (1888) [185]. In this series ions of the same charge are compared regarding their influence on the stability. The flocculation tendency increases according to this from left to right:

Ion:	Li^+		Na^+		K^+		NH_4^+		Rb^+		Cs^+
Ion radius /nm:	0.068	<	0.095	<	0.133	<		<	0.147	<	0.170

stable $\longleftarrow \qquad\qquad\qquad\qquad \longrightarrow$ *unstable*

Ion:	I^-		NO_3^-		Br^-		Cl^-		F^-
Ion radius /nm:	0.216	<	0.264	<	0.195	<	0.181	<	0.247

The specific influence of the ions in the Hofmeister series is an effect of their size, which has on the one hand side a direct influence and on the other hand an impact due to the solvent structure. The size of the ions influences according to van de Ven [186, 187] the hydrodynamic resistance of two approaching particles. The critical coagulation concentration increases if the ion radius decreases. However, the Hofmeister series is not a strict rule, which always applies. Sometimes the order of the ions change or the whole series can be inverted [188]. This seems to be a consequence of specific ion adsorption. Consequently the Hofmeister series can not attributed to a pure electrostatic effect, due to the electrostatic double layer. The adsorption behavior is mainly determined by the ratio of charge/ion radius. The smaller the charge density, the higher is the polarizability. Furthermore, the structure of the solvent around the ion has to be accounted for.

According to Pearson (in [189]) acids and bases can be classified as hard (difficult to polarize) or soft (easy to polarize). He postulated that hard acids are preferred to join hard bases and soft acids soft bases (HSAB-principle). A classification of Lewis acids and bases is shown in table 7.2. The hardness of a Lewis acid increases with decreasing ion radius and with increasing charge, oxidation state and electro negativity.

TABLE 7.2. Classification of Lewis acids and bases according to the HSAB-principle (in [99]).

Lewis acids

hard	transition regime	soft
H^+, Li^+, Na^+, K^+, Be^{2+}, Mg^{2+}, Ca^{2+}, Al^{3+}, Fe^{3+}, Cr^{3+}, Ti^{4+}	Fe^{2+}, Co^{2+}, Ni^{2+}, Cu^{2+}, Pb^{2+}, Zn^{2+}, Sn^{2+}	Pd^{2+}, Pt^{2+}, Cu^+, Ag^+, Au^+, Hg^+, Hg^{2+}, Tl^+, Cd^{2+}

Lewis bases

hard	transition regime	soft
F^-, OH^-, O^{2-}, ClO_4^{2-}, SO_4^{2-}, NO_3^-, PO_4^{3-}, CO_3^{2-}	Br^-, NO_2^-, SO_3^-, N_3^-	H^-, I^-, CN^-, SCN^-, S^{2-}, $S_2O_3^-$

The ζ-potential values in figure 7.25 are smaller for harder ions. This is reasonable if the influence of the solvent around the alumina particle is considered. If a hard Lewis acid is introduced, it has a high affinity to the hard ethoxide ion, leading to a solvent cover around the ions. This influences the size of the ions in solution and with it their mobility. The hydrodynamic resistance is larger for harder ions, since these ions have a larger solvent cover. The larger the solvent cover around the ions the harder they can approach the surface and the harder they can be enriched in the Stern layer. This leads to an lowered ζ-potential for hard ions. With increasing salt concentration an increasing ζ-potential is observed. Because the ethoxide ions are bound by the hard ions the ethoxide ion concentration in the double layer is reduced. This is leading to the increasing ζ-potential with increasing salt concentration. If the ethoxide is exhausted and replaced by the counter ions the ζ-potential decreases again for higher salt concentrations, because of a compression of the double layer. The harder the Lewis acids are the earlier the ethoxide ions are exhausted and the earlier the peak in the ζ-potential is reached. For Li^+ which is a very hard Lewis acid the peak is reached at 0.01 mM while the peak for Na^+ and Y^{3+} appears later at a concentration of 0.1 mM.
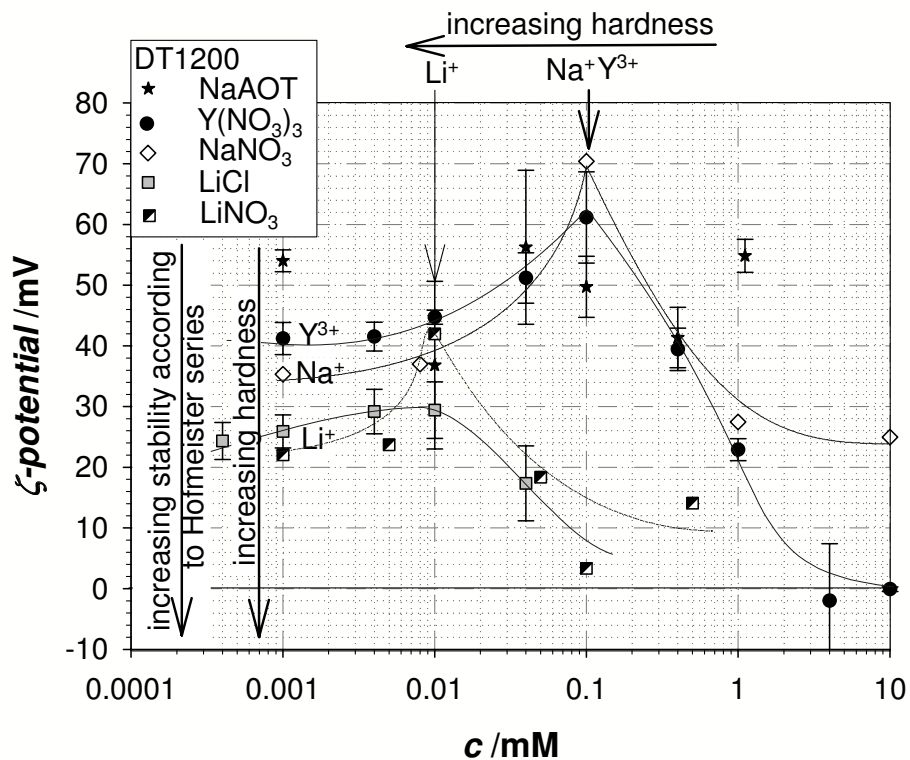
FIGURE 7.25. Influence of different ions on the ζ-potential for electrostatically stabilized Al_2O_3 in ethanol.

7.3.3. Milling Results. Figure 7.26 shows the influence of the stabilization mechanism on the milling results for α-Al_2O_3 particles in ethanol. The Sauter mean diameter $x_{1,2}$ measured with dynamic light scattering and BET is plotted in this diagram over the measured specific energy input. The experiments were carried out with a Netzsch mill (Labstar) at a rotary speed of 2000 $\min^{-1}$ ($v_t = 8.5$ m/s). Yttrium stabilized ZrO_2 milling beads ($d_{GM} = 0.5$ - 0.6 mm), at a filling ratio of 0.8, were used and the solid mass concentration of the alumina particles was set to $c_m = 0.2$. With increasing specific energy input the particle size decreases independent of the stabilization mechanism until approximate 100 nm. With further increasing specific energy input the particle size decreases for the sterically stabilized alumina particles. A final particle size of $x_{1,2} = 60$ nm measured by DLS was reached after 24 h milling time (120 000 kJ/kg). In contrast to this the particle size increases up to 400 nm for the electrostatically stabilized suspensions at higher energy inputs. However, the particle size determined by BET analysis decreases for electrostatically stabilized suspensions continuously down to 25 nm. The continuous decrease of the particle size measured by BET indicates an increasing fines of primary particles. The slope of the curve for electrostatically stabilized suspensions measured with BET is steeper than the BET curve for sterically stabilized suspensions. The reason for this could be that the polymer layer around the particles adsorbs part of the grinding energy during the impact of two grinding beads and cushions the comminution. The final particle size for the sterically stabilized suspension is 40 nm measured with BET. The slopes of the curves determined with BET and dynamic light scattering are equal for the sterically stabilized suspension. The narrow difference between the particle size measured with BET and dynamic light scattering shows that the particles are dispersed and sufficiently stabilized.

These experiments were designed to show the differences between the stabilization mechanisms and not to show the smallest reachable particle size. Hence, the milling experiments were not performed at the optimal milling conditions (see figure 2.1). Therefore, even smaller particle sizes are expected if the rotary speed is reduced and smaller milling beads are used.

The diagram further shows milling results performed under the same conditions as the experiment with 0.04 mM $NaNO_3$, but with alumina instead of zirconia milling beads. For this autogenous milling experiment the primary particle size measured with BET is 25 nm. This is the same final particle size measured as in the experiment with zirconia beads. Also the particle size determined with dynamic light scattering increases to 320 nm in the same way as in the experiment with zirconia milling beads. Although the kind of the milling beads seem to have no effect on the development of the particle size and the state of agglomeration, clear differences in the ζ-potential, the conductivity, rheology and in the floc strength have been observed. These differences are discussed in the course of this chapter.
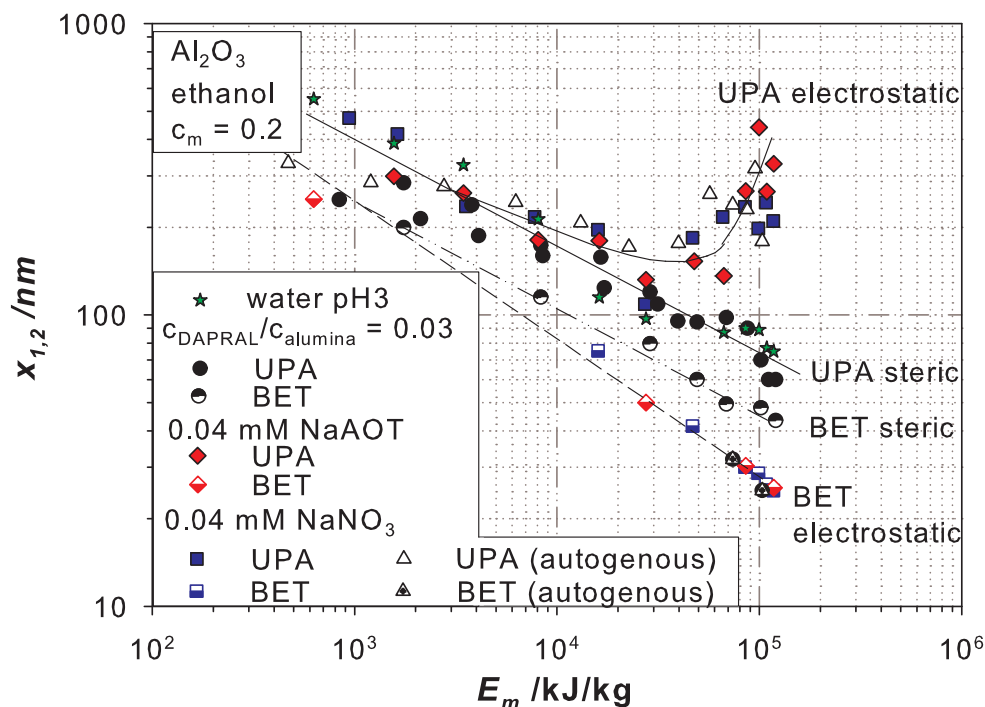
FIGURE 7.26. Influence of the stabilization mechanism on the evolution of the median particle size $x_{1,2}$ with the specific energy input E_m for α-Al$_2$O$_3$ in ethanol (Labstar, $v_t = 8.5$ m/s, $d_{GM} = 0.5 - 0.6$ mm , $c_m = 0.2$).

To examine if alumina hydroxide was formed during milling, calorimetric measurements of the samples were accomplished in a DSC cell. In figure 7.27 the measured heat flow is plotted over the temperature. The diagram shows measurements for α-alumina samples milled in water, toluene and ethanol. Furthermore a reference measurement of a pure bayerite sample is shown [1]. The results of the DSC analysis show endothermic heat flow peaks for the samples milled in water. The temperature at which the heat flow peaks appear corresponds to the conversion temperature from Al(OH)$_3$ to Al$_2$O$_3$. The areas under the curves correlate to the conversion enthalpies. The amount of the generated hydroxide can be calculated by comparing the conversion enthalpies of the milled sample to the enthalpy of pure bayerite. For the electrostatically as well as for the sterically milled sample in water 14% of alumina hydroxide was formed. In contrast to this no mechanochemical changes could be determined for the samples milled in ethanol and toluene.

Stenger [45] showed that the hydroxide layer around the alumina particles has an influence on the measured specific surface area. Micropores are formed in the particles due to the phase transformation of the surface layer from bayerite to α-Al$_2$O$_3$ during outgasing of the sample leading to an increase of the specific surface area. However, no influence of the outgasing temperature could be measured for particles milled in organic solvents, because no hydroxide layer develops on the surface of the particles. Furthermore, no micro pores could be

detected using the V-t method according to de Boer [**190**] (see appendix A.2). Because no hydroxide develops during milling in organic phase, the particle sizes determined with BET measurements (see figure 7.26) are more reliably than in aqueous phase.

FIGURE 7.27. DSC measurements of α-Al$_2$O$_3$ milled in different solvents using different stabilization mechanisms.

Another method to detect mechanochemical changes of particles during milling is X-ray diffraction. The peak positions, widths and shapes of the measured diffraction intensities provide important information about the structure of the material. As can be seen in figure 7.28 and 7.29, the peak intensities for pure α-alumina particles are bright and sharp indicating the crystallinity of the sample. For alumina particles milled in ethanol, the reduction in intensity and widening of the peaks indicates that a phase transformation from crystalline to amorphous has taken place and that the particle size is reduced. However, no further new peaks could be observed indicating that no phase transformation of alumina to alumina hydroxide phase has taken place during milling in organic solvents.

From the XRD data the development of crystallite sizes t_{cryst} with specific energy was evaluated by the Rietveld method. In figure 7.30 the results of this analysis are compared to particle size measurements for electrostatic stabilized alumina particles milled in ethanol which were already presented in figure 7.26. From figure 7.30 it can be seen that the primary particle size approaches more and more to the crystallite size during the milling experiment. From an energy input of 10^4 kJ/kg to the end of the experiment the primary particle size and the crystallite size fall on the same line. This is very surprising since in the calculation of the particle size from the measured surface area S_m it is assumed
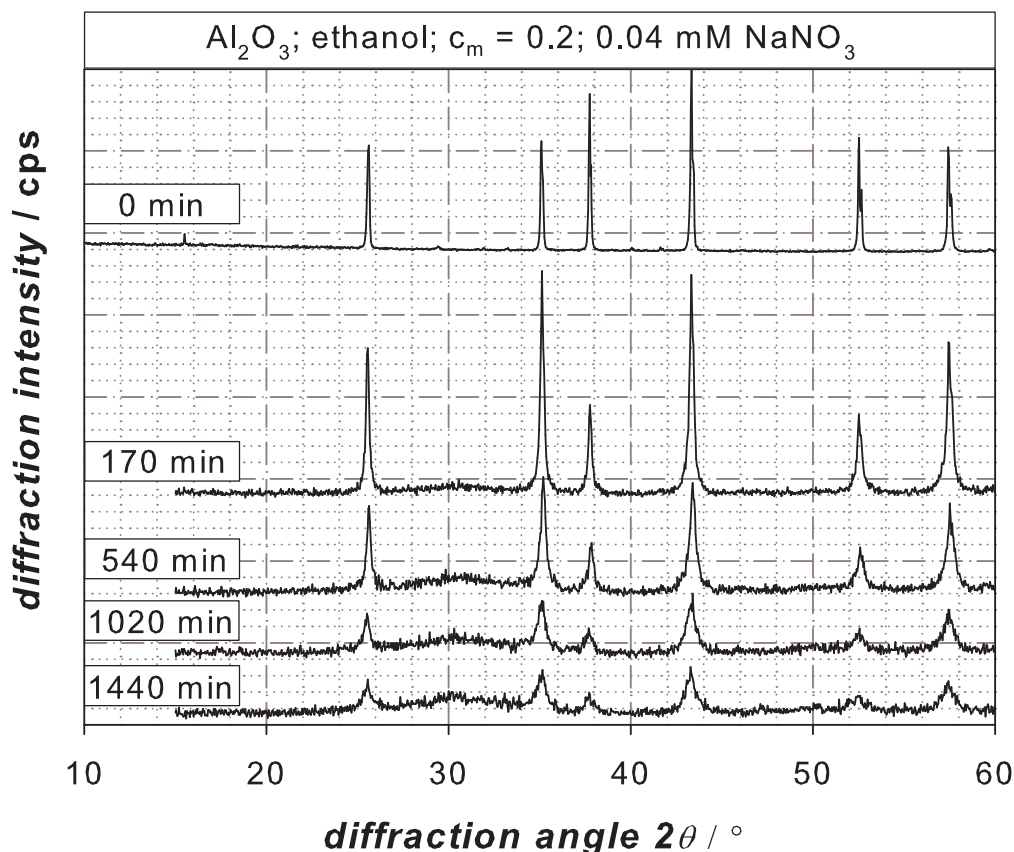
FIGURE 7.28. XRD-diagram for alumina particles milled in ethanol with 0.04 mM NaNO$_3$.

that the particles are spheres with the equivalent surface area. Strictly, the crystallite size should be smaller than the primary particle size.

The same trends can be see for sterically stabilized alumina particles milled in ethanol (see figure 7.31). The primary particle size measured with BET is after an energy input of approximate 10^4 kJ/kg in the order of the crystallite size determined with the Rietfeld analysis. The crystallite size for the sterically stabilized alumina particles is higher than the crystallite size determined for the milled particles which were electrostatically stabilized. This an other indication for the damping of the impact of two grinding beads during milling. The polymer layer around the particles adsorbs part of the grinding energy and cushions the comminution.

Furthermore, thermogravimetric measurements were performed as described in chapter 5.2.3. The results are presented in figure 7.32 as relative mass loss $\Delta m/m$ as a function of the temperature. No mass loss could be measured for the untreated feed particles as well as for the feed particles, which were stirred for 24 h in ethanol with 0.04 mM NaNO$_3$. The relative mass loss up to 240°C for the milled samples can be explained with desorption of physical bound solvent at the particle surface. The steep rise in the relative mass loss at 260°C, which arises for the sample milled in water and the bayerite corresponds to the conversion temperature from Al(OH)$_3$ to Al$_2$O$_3$. This temperature agrees very well
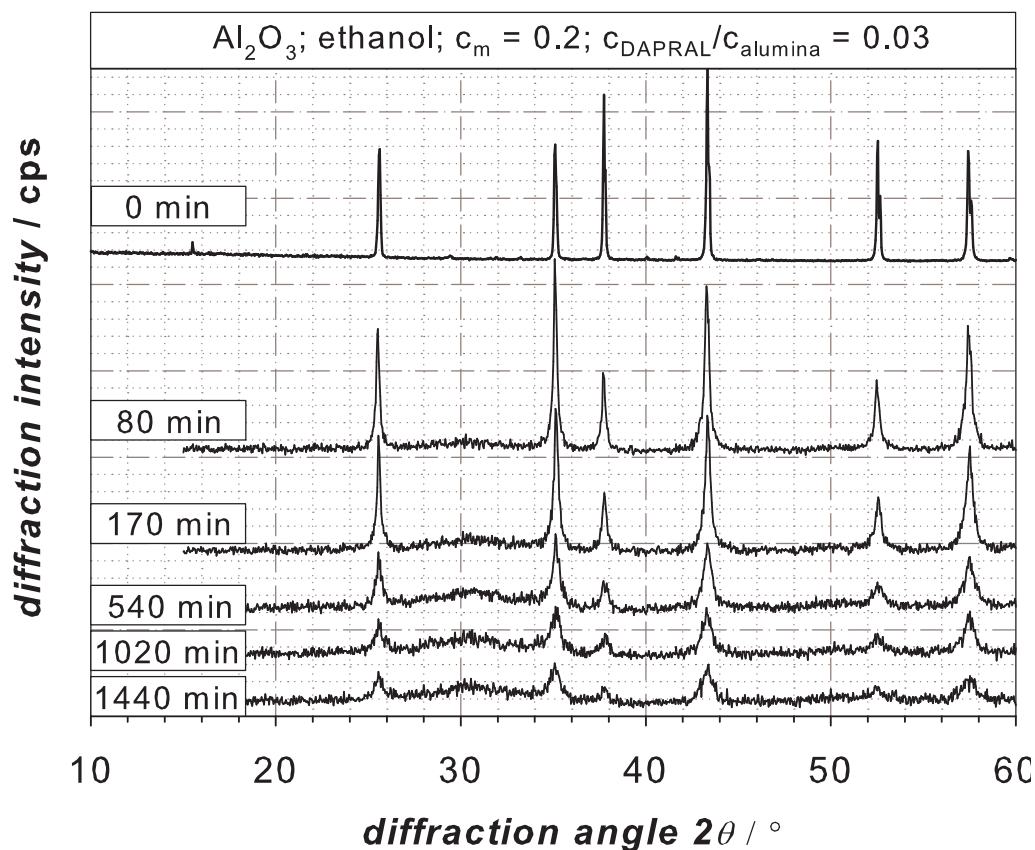
FIGURE 7.29. XRD-diagram for sterically stabilized alumina particles milled in ethanol.
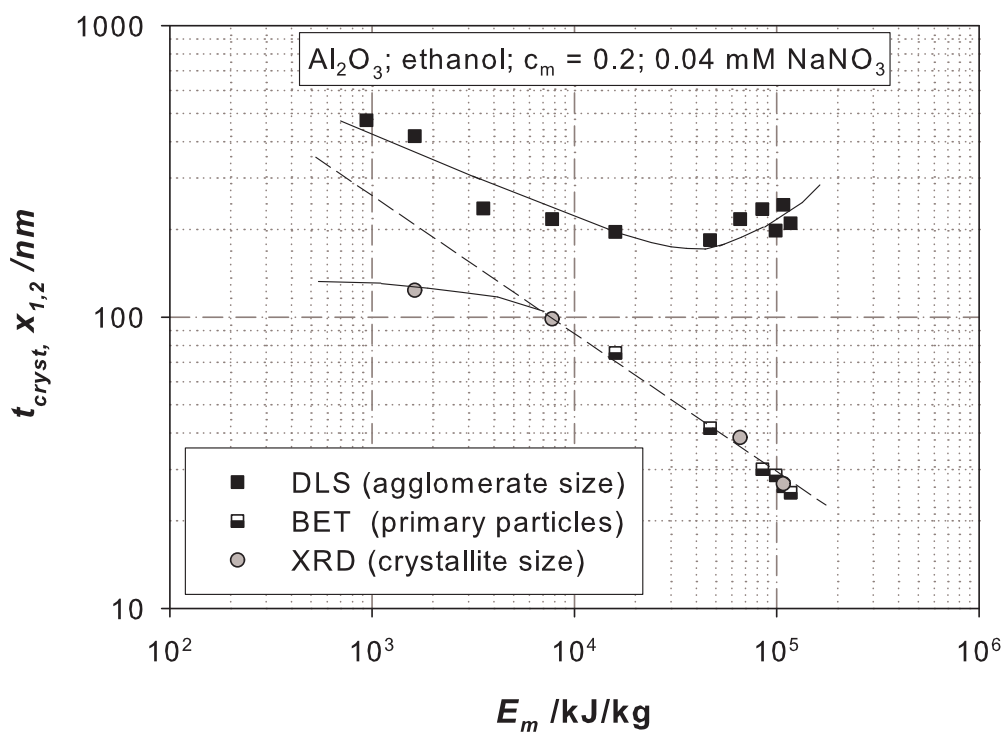
FIGURE 7.30. Comparison of particle and crystallite size for electrostatically stabilized alumina particles milled in ethanol.
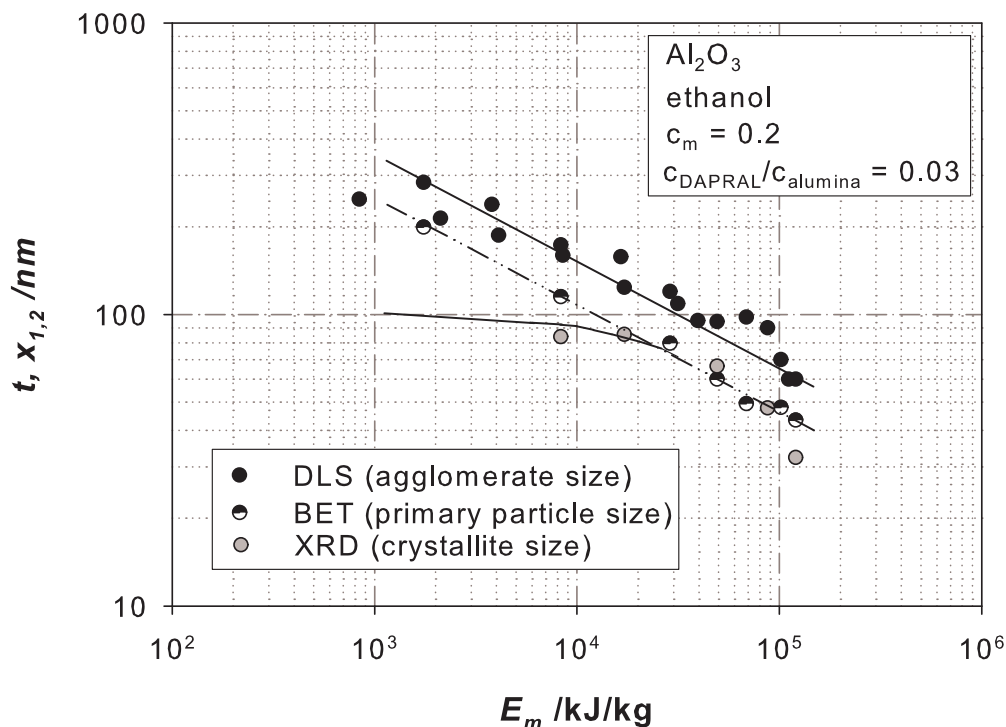
FIGURE 7.31. Comparison of particle and crystallite size for sterically stabilized alumina particles milled in ethanol.

with the conversion temperature in the DSC measurement (see figure 7.27). By comparing the relative mass loss of the milled sample and the bayerite reference sample, the amount of hydroxide formed during milling can be determined. For the sample milled in water an amount of hydroxide of 17.3% was determined. This is consistent with the amount of 14.3% measured with DSC. The TGA measurements show that during milling in ethanol no transformation from alumina to alumina hydroxide occurs. However, during milling with electrostatic stabilization in ethanol physical adsorbed solvent could be detected.

The formation of surface species during milling was additionally studied with FT-IR. Figure 7.33 shows the infrared spectra of alumina particles milled in aqueous HNO_3 of pH3. The curve labeled with one is the infrared spectra for the feed material. The spectrum of the feed material shows a wide band between 3600 and 3000 cm^{-1}, which can be associated with physically adsorbed solvent at the surface. After milling α-Al_2O_3 in aqueous HNO_3 of pH3 for 24 h (120 000 kJ/kg, LabStar mill, $v_t = 8.5$ m/s, $d_{GM} = 0.5 - 0.6$ mm, $c_m = 0.2$) additional bands are generated (see spectrum labeled with two). In the literature [45, 191] the infrared bands at 3620-3624, 3527 and 3460 cm^{-1} along with a doublet at 3396 and 3382 cm^{-1} were associated with the OH stretching mode of gibbsite-type hydroxide ($\gamma-Al_2O_3$). Bands of bayerite ($\alpha-Al_2O_3$) should be located at 3655, 3546 - 3550 and 3465 - 3477 along with a doublet at 3440 and 3427. After heating the sample up to 900 °C with a heating rate of 10 K/min in nitrogen atmosphere (see spectra 3), the characteristic bands
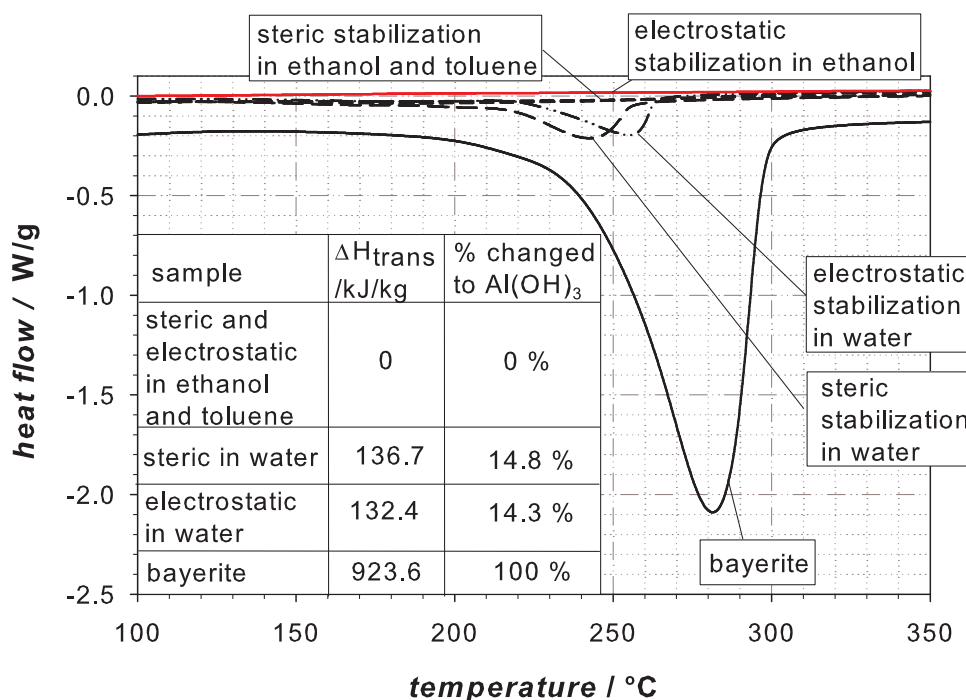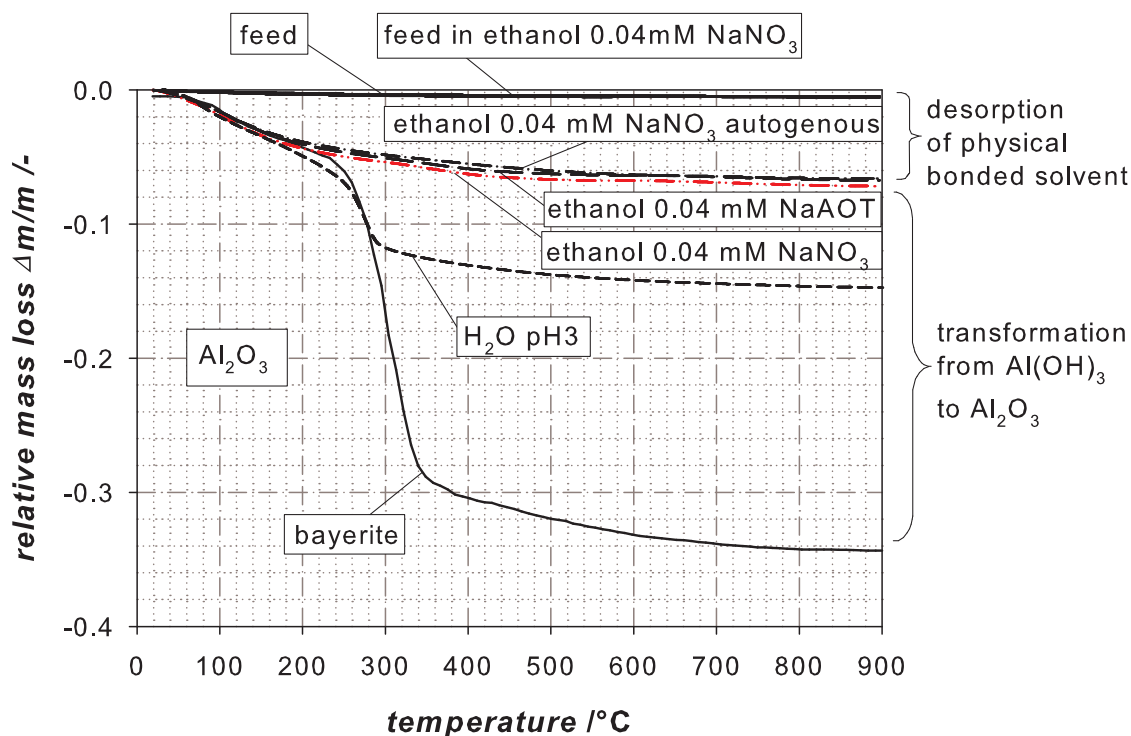
FIGURE 7.32. TGA measurements of α-Al$_2$O$_3$ milled in different solvents using different stabilization mechanisms.

for alumina hydroxide disappear. Instead a wide band between 3600 and 3000 cm^{-1} can be seen. The intensity of the infrared band of the heated sample is higher than the intensity of the infrared band of the feed material, which can be explained with a higher surface area of the milled particles in comparison to the feed particles.

Figure 7.34 shows infrared spectra for alumina milled in ethanol with 0.04 mM NaNO$_3$ as background salt. The spectrum labeled with two was measured on a sample milled with the LabStar mill for 24 h with yttrium stabilized zirconia milling beads (120 000 kJ/kg, $v_t = 8.5$ m/s, $d_{GM} = 0.5$ - 0.6 mm, $c_m = 0.2$). The spectrum labeled with three was measured on a sample milled under the same conditions as sample two, but with alumina milling beads ($d_{GM} = 0.65$ - 0.8 mm). In contrast to the milling experiment in water no additional bands are generated during milling in ethanol. This means no hydroxide phases are being formed during milling in ethanol. However, a wide band between 3600 and 3000 cm^{-1} could be detected, which can be associated with physically combined solvent at the surface. After heating the samples up to 900 °C with a heating rate of 10 K/min in nitrogen atmosphere (see spectra 4 and 5), these bands are still present. However, the intensity of the bands is reduced. The intensity of the infrared bands of the heated samples is still higher than the intensity of the infrared band of the feed material, which can be explained with a higher surface area of the milled particles in comparison to the feed particles. The same trends can be found for alumina particles milled in ethanol with 0.04 mM NaAOT as background salt (see appendix A.3).

1) feed   2) H$_2$O pH3 milled 24h (LabStar)

3) H$_2$O pH3 milled 24h (LabStar) heated 900°C
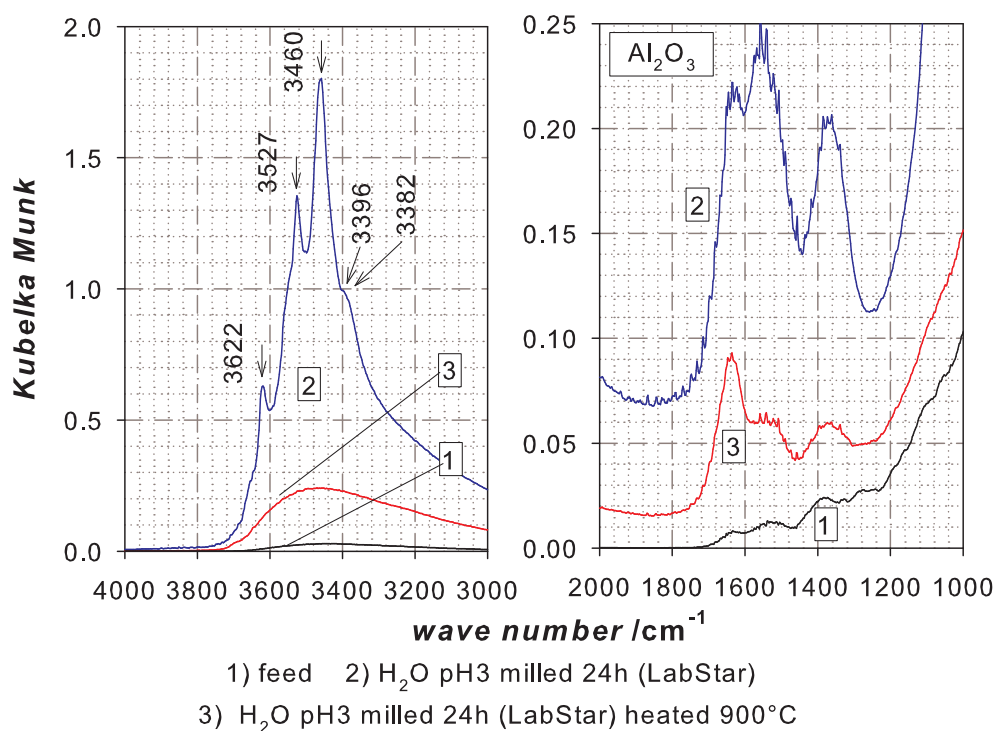
FIGURE 7.33. Infrared spectra of α-Al$_2$O$_3$ milled in aqueous HNO$_3$ at pH3.

1) feed   2) milled 24 h   3) milled 24h, autogenous
4) milled 24h, heated 900°C 5) milled 24h, autogenous, heated 900°C
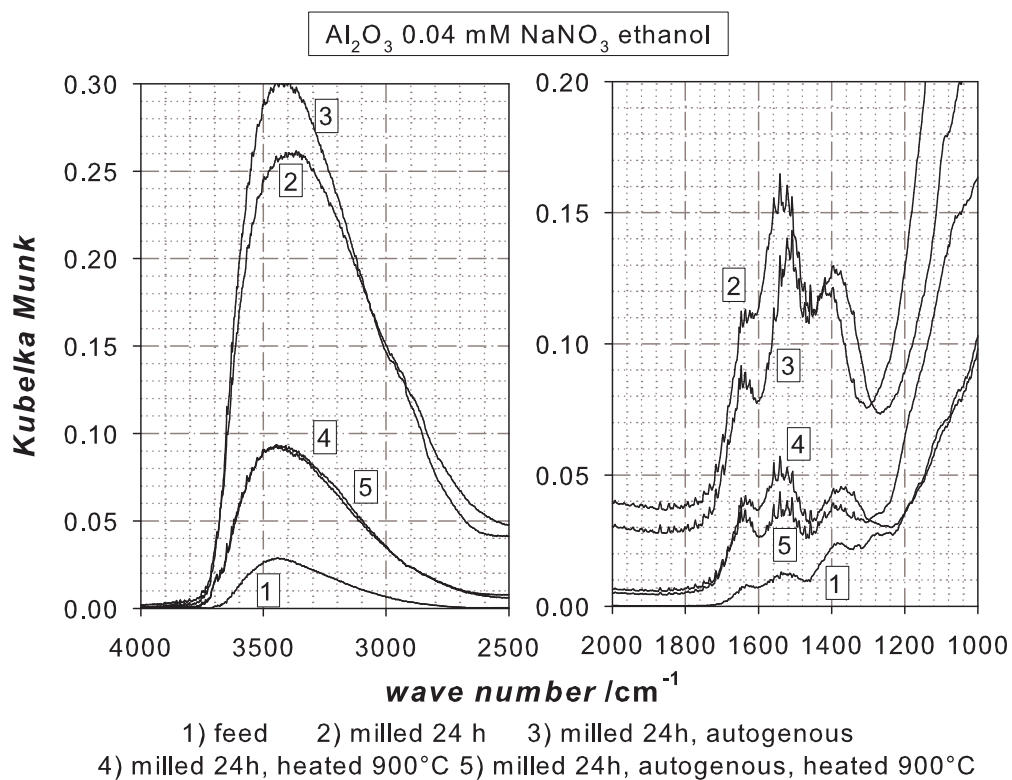
FIGURE 7.34. FT-IR measurements of α-Al$_2$O$_3$ milled in ethanol and 0.04 mM
NaNO$_3$ (LabStar).

Figure 7.35 shows the evolution of the ζ-potential for the milling experiments presented in figure 7.26. The ζ-potentials of the suspensions are decreasing rapidly from positive values to negative potentials. The reason could be that solvent molecules are bond to the freshly created alumina surface. The newly generated surface sites seem to be of different nature than older surface sites. The newly created surface acts in contrast to the older one as Lewis acid, an electron acceptor. Ethanol or water molecules, which are always present in ethanol, because ethanol is very hydrophilic, can be bond to this surface sites, leaving a negative charge on the surface. This assumption is supported by the FT-IR measurements shown in figure 7.34. After a milling time of 5 h (27 506 kJ/kg) the ζ-potential increases with further energy input to -28 mV in case of the experiments with NaAOT and NaNO$_3$ background salts. This increasing surface charge can be an effect of the media wear. As table 7.3 shows a large amount of media wear contaminates the suspension during milling, especially in the experiments with zirconia milling beads. Here around 11% of the beads were attrited. In the autogenous milling experiment only 3.84% of attrition occurred. However, it was noticed that the stirrer and the milling chamber were exposed to higher wear than using zirconia milling beads.
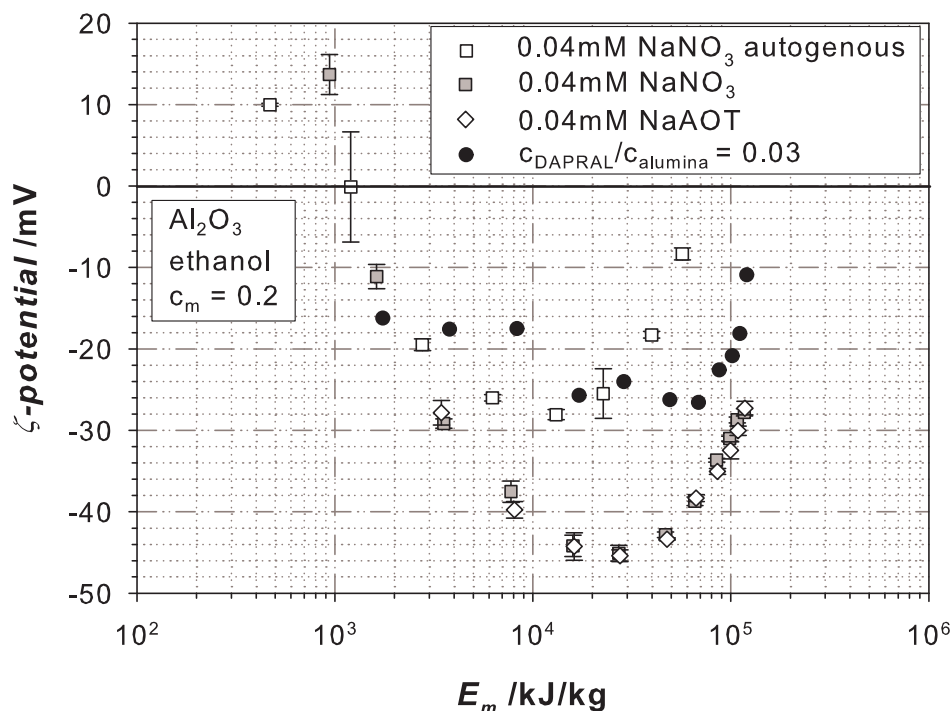
FIGURE 7.35. Influence of different salts on the evolution of the ζ-potential during milling of α-Al$_2$O$_3$ in ethanol ($v_t = 8.5$ m/s, $d_{GM} = 0.5 - 0.6$ mm, $c_m = 0.2$).

To simulate the influence of media wear ZrO$_2$/Y$_2$O$_3$ particles (Saint-Gobain, France) of $x_{50,3} = 500$ nm were added to a suspension with 20 wt% α-alumina milled for 5 h (27 506 kJ/kg) in ethanol with 0.04 mM NaAOT as background salt. Figure 7.36 shows the results of the ζ-potential measurements in the

TABLE 7.3. Amount of attrition during the milling experiments.

milling experiment	milling beads	attrition
0.04 mM NaNO$_3$	Al$_2$O$_3$	3.84%
0.04 mM NaNO$_3$	ZrO$_2$	10.86%
0.04 mM NaAOT	ZrO$_2$	11.23%
sterically stabilized	ZrO$_2$	11.6%

mixed component system. With increasing amount of ZrO$_2$/Y$_2$O$_3$ particles the ζ-potential of the suspension decreases rapidly to almost 0 mV. This might be an effect of a violation of the assumption in the electroacoustic theory that all particles have the same ζ-potential. However, for pure ZrO$_2$/Y$_2$O$_3$ particles in ethanol a ζ-potential of 2.3 mV was measured. This leads to increasing attractive interactions in the mixed component suspension because negatively and positively charged particles agglomerate. This can be seen in the increasing particle size in figure 7.26 and in the rheological data (see figure 7.39 to 7.41).
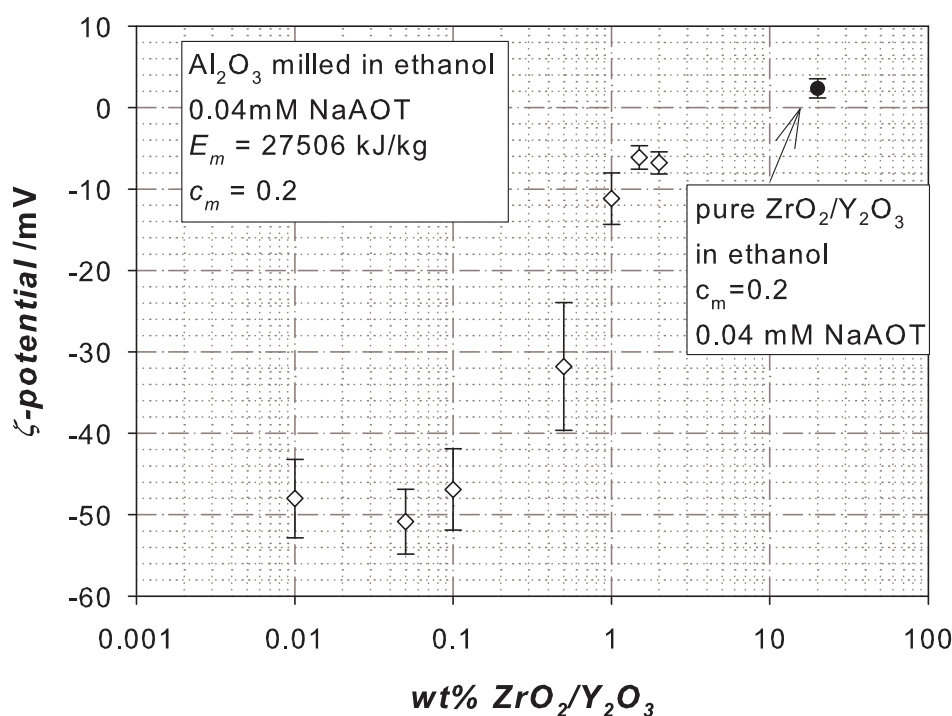
FIGURE 7.36. Influence of attrition on the ζ-potential of a α-Al$_2$O$_3$ suspension milled in ethanol ($v_t = 8.5$ m/s, $d_{GM} = 0.5 - 0.6$ mm, $c_m = 0.2$).

The development of the surface charge density during the milling experiment can be calculated from the measured ζ-potentials with an empirical equation according to Loeb et al. [192]:

$$q = \frac{\epsilon_0 \epsilon_r kT}{e} \kappa \left(2 sinh \left(\frac{\tilde{\zeta}}{2} \right) + \frac{4}{\kappa a} tanh \left(\frac{\tilde{\zeta}}{4} \right) \right). \qquad (7.17)$$

This equation is valid for spherical colloid particles and a 1-1 electrolyte system. Loeb et al. showed that the error in the calculation of the surface charge q is less than 1% compared to an exact numerical solution for the range and double layer thicknesses considered here. In the calculation a reduced potential $\tilde{\zeta}$ is used, which is made nondimensional with:

$$\tilde{\zeta} = \frac{ez\zeta}{kT}. \tag{7.18}$$
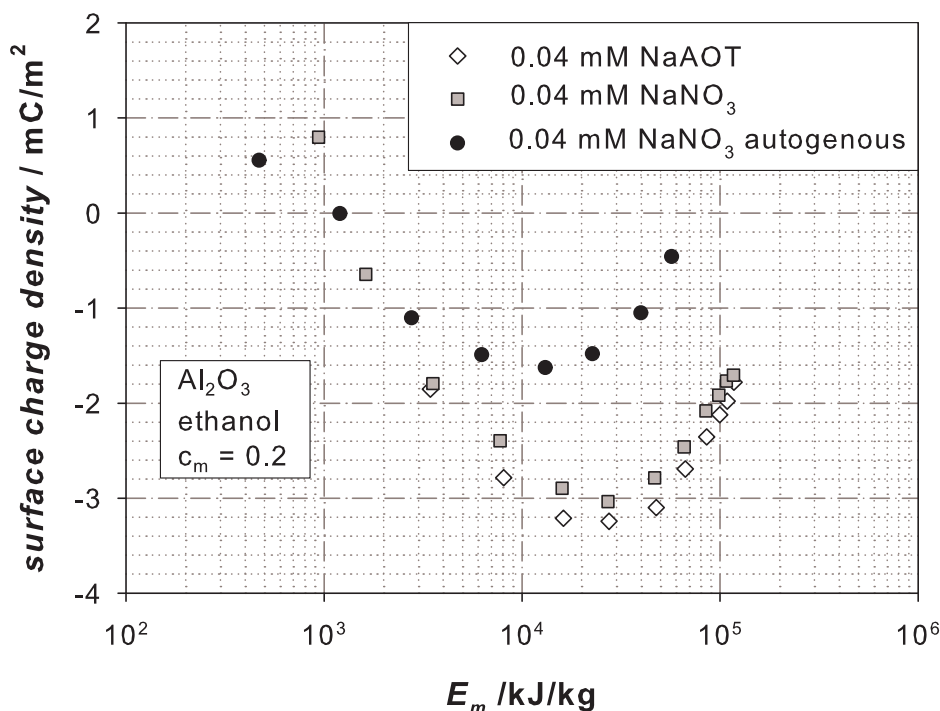
FIGURE 7.37. Influence of different salts on the evolution of the surface charge during milling of α-Al$_2$O$_3$ in ethanol ($v_t = 8.5$ m/s, $d_{GM} = 0.5 - 0.6$ mm, $c_m = 0.2$).

The originally positive surface charge changes the sign in the early state of the milling experiment to negative values as it can be seen in figure 7.37. The charge decreases during the experiment to a maximal value of -3 mC/m^2 at a milling time of 5 h (27 506 kJ/kg) and increases with further energy input to -1.7 mC/m^2. In the autogenous milling experiment the measured surface charge density is much lower than in the milling experiment with ZrO$_2$ milling beads. The attrition of the ZrO$_2$ milling beads seems to increase the magnitude of the surface charge density by the adsorption of ions on the surface of the particles. However the mechanism is not understood jet and should be further investigated.

Figure 7.38 shows the evolution of the conductivity for the milling experiments shown in figure 7.26. In all experiments a slowly decreasing conductivity

is measured. This decreasing conductivity is a further evidence for the agglomeration of negatively charged product particles and positively charged media wear particles.
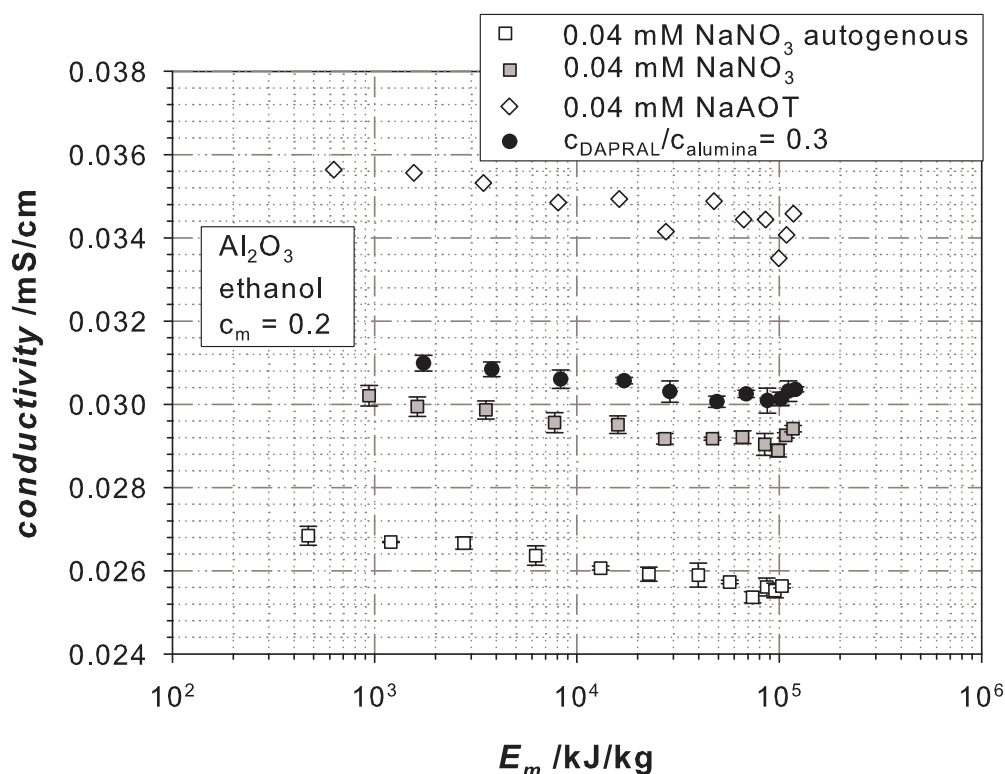
FIGURE 7.38. Influence of the different stabilization conditions on the evolution of the conductivity during milling of α-Al$_2$O$_3$ in ethanol ($v_t = 8.5$ m/s, $d_{GM} = 0.5$ - 0.6 mm, $c_m = 0.2$).

Figure 7.39 shows the rheological flow behavior of the suspension milled in 0.04 mM NaNO$_3$ (see figure 7.26) in dependency of the milling time. The graph corresponds to the ζ-potential measurements shown in figure 7.35. At the beginning of the experiment a yield stress of 0.03 Pa is measured. With increasing milling time the absolute values of the ζ-potential are increasing resulting in a decreasing yield stress. After a milling time of 5 h the absolute value of the ζ-potential of 45.1 mV is reached. At this time the rheological behavior of the milling suspension is Newtonian and the flow behavior is determined by the hydrodynamic interactions. The interactions between the particles can be almost neglected. With further energy input the ζ-potential and with it the interparticle interactions are increasing, resulting in an increasing yield stress. In the final suspension a yield stress of 1 Pa was measured. In figure 7.40 the yield stress of the suspensions of all milling experiments shown in figure 7.26 are plotted over the specific energy input. All suspensions show a similar behavior in the development of the yield stress. A yield stress of 0.001 Pa was measured for all suspensions, except for the autogenous milling experiment, at an energy input of approx. 10^4 kJ/kg. This is the stress of pure ethanol at a shear rate of 1 s^{-1}. The yield stress measured in the autogenous milling experiment is

higher than for the suspensions milled with zirconia milling beads. The reason could be that different impurities are added to the suspension by attrition of the beads.
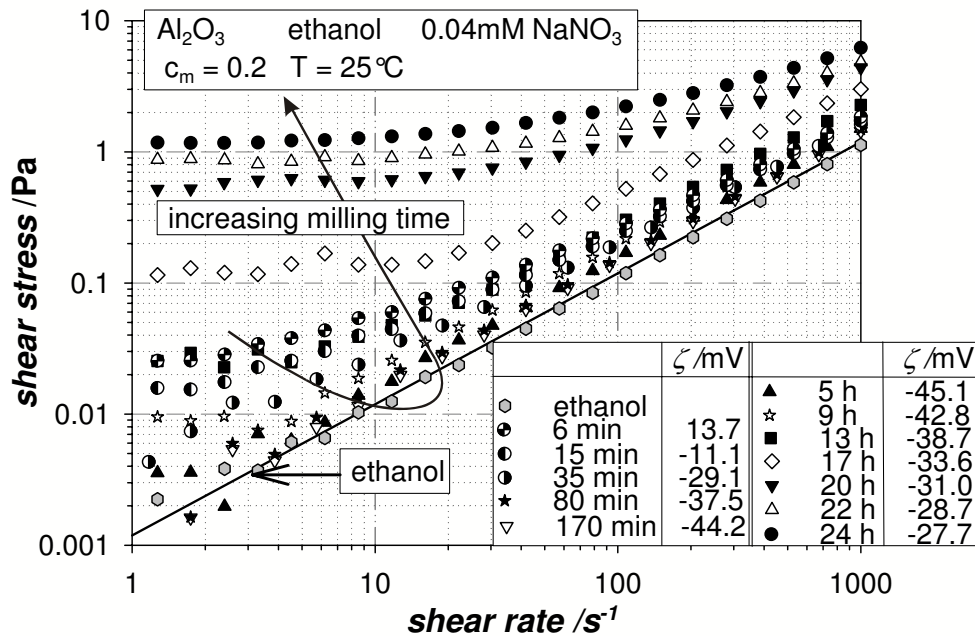
FIGURE 7.39. Flow curves of α-Al$_2$O$_3$ in ethanol with 0.04 mM NaNO$_3$ in dependency of the specific energy input E_m ($v_t = 8.5$ m/s, $d_{GM} = 0.5$ - 0.6 mm, $c_m = 0.2$).
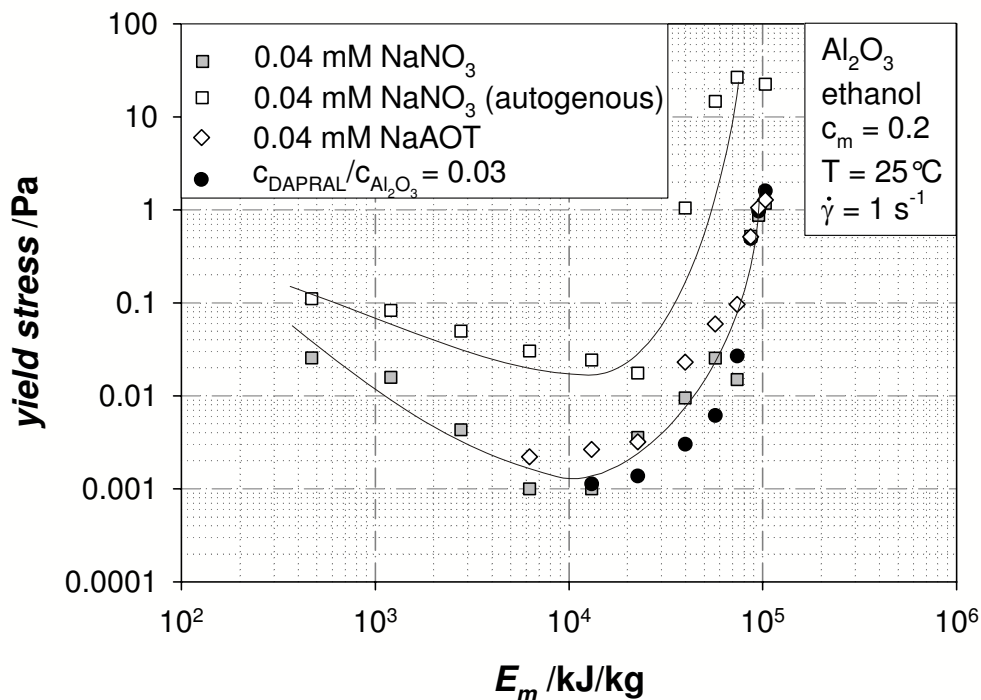
FIGURE 7.40. Yield stress of α-Al$_2$O$_3$ suspensions milled in ethanol.

Figure 7.41 shows the corresponding shift factors for the rheological flow curves in dependency of the milling time. Stenger [1] showed that the shift factor for Newtonian suspensions without a yield stress is only dependent on the volume fraction and not on the median particle size. Figure 7.42 shows that the mass concentration of the suspension increases during milling. The reason for the increasing concentration is that ethanol evaporates during milling and that the media wear increases during the experiment. The change of mass concentration during the experiment is similar for all experiments. However, the shift factor increases with increasing specific energy input for all milling suspensions more than expected. The reason for the increasing shift factor is next to media wear and evaporation of solvent that the particles are not totally dispersed even at high shear rates. The volume fraction of the particles c_v increases to an effective volume fraction $c_{v,eff}$ due to immobilized solvent in the cavities of the agglomerates. The agglomerate size increases with increasing bond strength of the agglomerates, which increases with decreasing particle size. The shift factors for the milling experiments with $NaNO_3$ and NaAOT as background salt fall on the same curve and the increase of the shift factor is moderate. In contrast to this the increase of the shift factor for the sterically stabilized suspension is stronger. This is reasonable because polymers are bonded on the particle surface, which increases the effective volume fraction and leads to a higher shift factor. A very strong increase in the shift factor was observed for the suspension milled with alumina milling beads. This is consistent to the lower ζ-potential and the higher yield stress measured in the autogenous milling experiment as compared to the suspensions milled with zirconia milling beads. This shows that the suspension milled with alumina milling beads was highly flocculated. The attrition of ZrO_2 milling beads seems to increase the stability of the suspension. However, this effect is not clearly understood and should be further investigated, for example by adding a defined amount of ZrO_2 during an autogenous milling experiment.
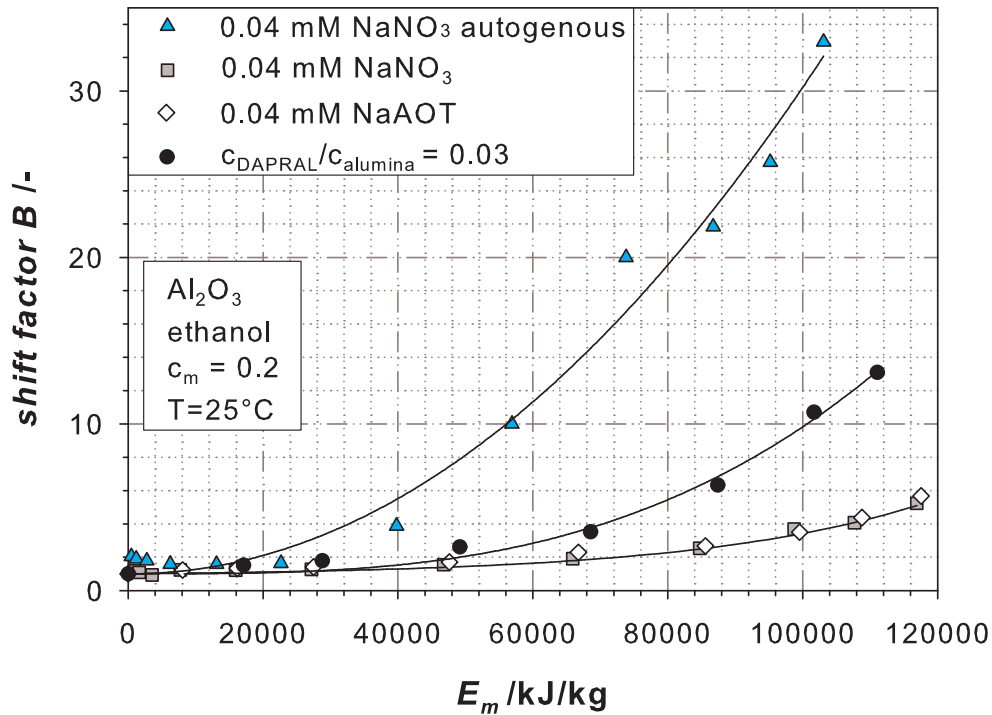
FIGURE 7.41. Shift factor B in dependency of the specific energy input E_m (v_t = 8.5 m/s, d_{GM} = 0.5 - 0.6 mm , c_m = 0.2).
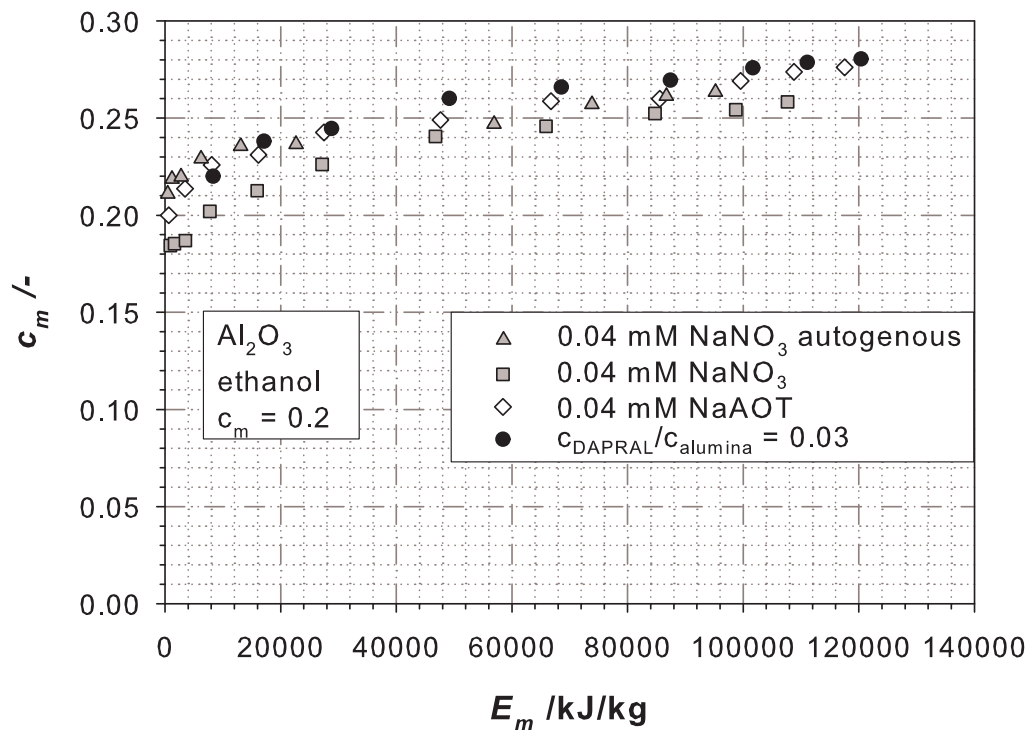
FIGURE 7.42. Mass concentration of the suspension in dependency of the specific energy input E_m (v_t = 8.5 m/s, d_{GM} = 0.5 - 0.6 mm , c_m = 0.2).

To further illustrate the milling results a study of SEM pictures of the feed and the final particles milled in different solvents is shown. In figure 7.43a) a SEM picture of the feed material is presented. The median particle size of the feed particles is around 35 μm. Furthermore, the picture shows that the used fused alumina is a feed material, which is not sintered and not agglomerated. In the same figure SEM pictures of the final milled material in water and ethanol are presented (see figure 7.26). The milling experiments were accomplished in the LabStar mill, described in chapter 4.3, under the same milling conditions.

Figure 7.43b) shows a SEM picture of alumina particles, which were milled in water electrostatically stabilized at pH3. The median particle size of the sample milled in water is 50 to 150 nm. This result is consistent with dynamic light scattering experiments, which showed a median particle size $x_{1,2}$ of 70 nm. The particle size calculated from BET experiments on the other hand is with 15 nm conspicuously lower. However, by milling α-alumina particles in water at pH3 mechano-chemical changes do occur. The generated hydroxide phases falsify the measurements, because the decomposition of the aluminum hydroxide is inducing micro pores in the particles leading to an increase of the specific surface area.

In figure 7.43c) a SEM picture of the particles milled in ethanol under the same conditions is presented. The particles were stabilized sterically in this experiment. A median particle size of around 40 nm is observed. The particle size calculated from the measured BET surface area is 43 nm. In addition, the median particle size determined from dynamic light scattering experiments is 60 nm. The fact, that the differences of the values measured with different methods are so small, shows that the particles are dispersed and stabilized to the primary particles. In comparison to the particles milled in water the particle size is perspicuously smaller. The spherical appearance is misleading and an effect of the insufficient resolution of the instrument. To confirm that no different breakage mechanism acts a TEM picture of the same sample is shown in figure 7.44a. The TEM picture shows fractured surfaces and edges, which are generated by real breakage.

Furthermore, figure 7.43d) shows a SEM picture of α-Al$_2$O$_3$, which was milled in ethanol under electrostatic conditions (0.04 mM NaAOT). The picture shows particles in the size range of 50 to 150 nm. This result is confirmed in a TEM picture of the final product (see figure 7.44b)), which shows a particle of 50 nm diameter. However, with dynamic light scattering a particle size of 330 nm was measured. The huge difference, especially to the BET-measurements, allow the conclusion that the particles remain as agglomerates in the suspension.
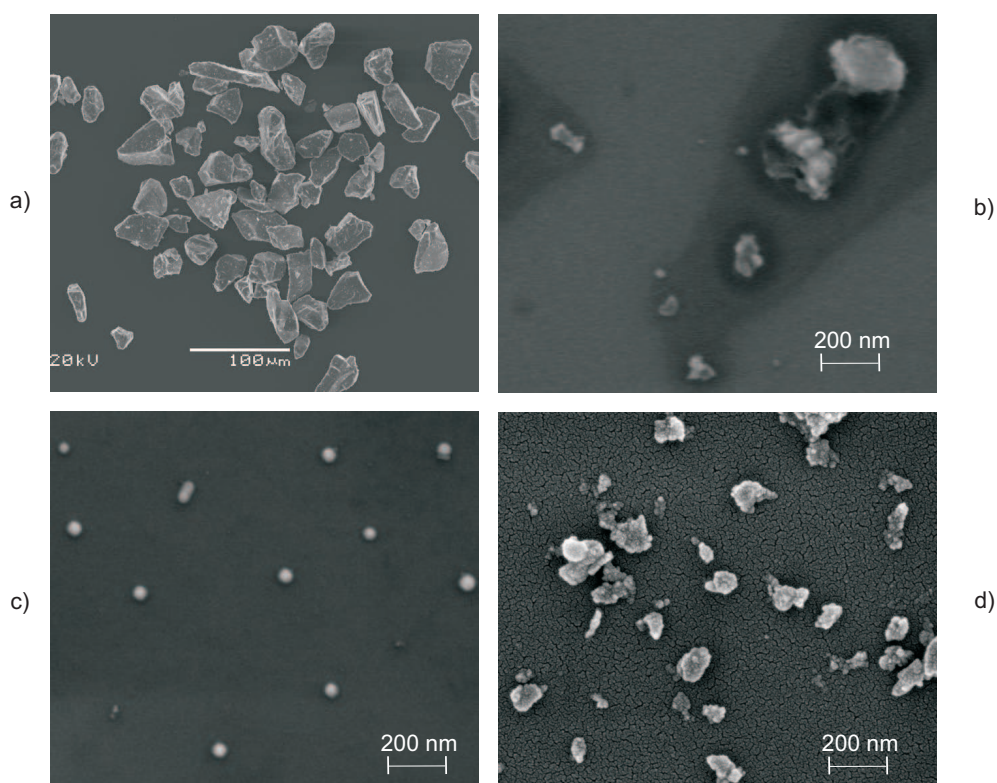
FIGURE 7.43. SEM-pictures for $\alpha - Al_2O_3$: a) feed material b) milled in water, electrostatically stabilized at pH3 c) milled in ethanol, sterically stabilized d) milled in ethanol, electrostatically stabilized (0.04 mM NaAOT).
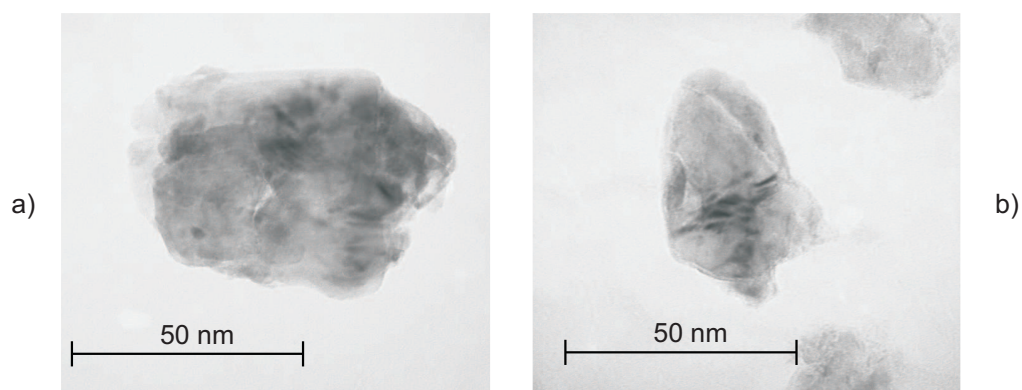
FIGURE 7.44. TEM-pictures for $\alpha - Al_2O_3$: a) milled in ethanol, sterically stabilized b) milled in ethanol, electrostatically stabilized (0.04 mM NaAOT).

7.4. Transfer to Iron Oxide

The milling experiments of Fe_2O_3 presented here are divide into three sections. In the first section preliminary experiments characterizing the material are shown. The second section encloses milling experiments at different stability conditions in water and in ethanol. In the last section mechano-chemical changes during milling of hematite at the different environments are discussed.

7.4.1. Preliminary Experiments.

For electro-chemical characterization of the system the ζ-potential of the feed material was determined. Figure 7.45 shows the influence of different ions on the ζ-potential for electrostatically stabilized Fe_2O_3 particles in water. The data were measured by electroacoustics (DT1200). The solid concentration of Fe_2O_3 is 5% by weight. The adjustment of the pH value in the acid regime was done with 0.1 and 1 M HNO_3 respectively. The alkaline pH values were adjusted by adding 0.1 and 1 molar caustic soda. The maximum of the ζ-potential is reached for the background ions $NaNO_3$ and $LiNO_3$ in the alkaline range at a pH value of 11 with around -51 mV. The isoelectrical point (iep) lays at pH 3.2. In the literature different values for the isoelectrical point of hematite are reported. According to Kosmulski [188] the iep values of hematite are in the range of pH 3 to pH 7. Kosmulski traces this large range back to the purity of the material as most important factor. For natural hematite from Elba, Italy, an isoelectric point in 0.01 molar $NaNO_3$-solution of 4.6 is reported, while natural hematite from Clinton, New York, has an iep-value of pH 8.2 in 0.01 molar $NaNO_3$ solution [193]. For synthetic Fe_2O_3 an isoelecric point of pH < 3 is reported in 0.001 molar $NaNO_3$ solution [194]. An explanation for the smaller iep-values of synthetic hematite lies in the production process of Fe_2O_3 from $FeCl_3$. In this case the particle surface is affected by including of chloride ions into the hematite matrix [158]. According to manufacturer data [157] the used hematite powder is produced synthetically. The powder does not exhibit an analytical purity, the iodometrically determined Fe^{3+}-content is 97.3%. An energy dispersive X-ray fluorescent analysis was accomplished at the chair for Inorganic and Analytic Chemistry of the University of Erlangen in order to investigate if the used hematite substance contains impurities. The result of the analysis showed that traces of chromium contaminate the hematite powder. The instrument is not sensible enough for detection of chloride ions, contained in the hematite matrix.

The ζ-potential curves for different ionic strengths shown in figure 7.45 collapse in a single iep. This is an indication for no specific adsorption of Na^+, Li^+ or NO^{3-} ions on the hematite surface. If $Fe(NO_3)_3$ is used as background salt a shift in the iep is observed. At a salt concentration of 10^{-5} M the iep has a value of pH6.3. At a salt concentration of 10^{-4} M the iep further shifts to pH8.2. The reason for the shift is that Fe^{3+} adsorbs to the iron oxide surface. The specific adsorption of the three valence iron ion leads to a positive charge of the particles.
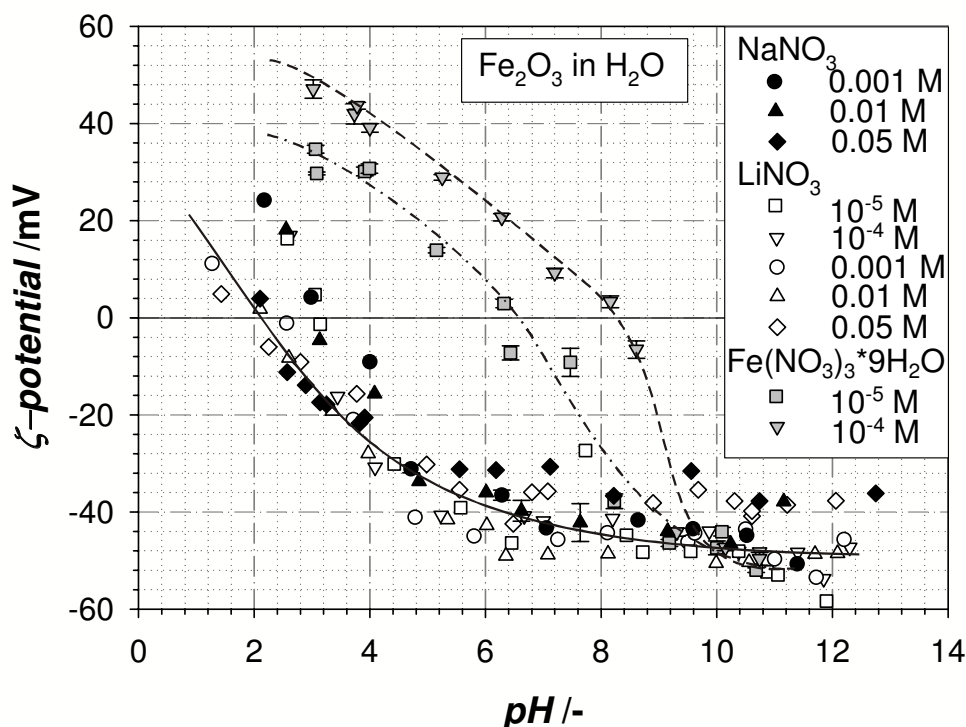
FIGURE 7.45. Influence of different ions on the ζ-potential for electrosatic stabilized Fe_2O_3 in water.

To characterize the material further the possibility of iron hydroxide formation was considered. All possible complexes of Fe^{3+}, which can be formed, were computed by chemical equilibrium calculations with the program "Medusa" and the integrated material database "Hydra". The mentioned program was downloaded from the homepage of the Royal Institute of Technology in Stockholm, Sweden [195]. It was validated, with calculations of the equilibrium rates of the different complexes of $Al(OH)_3$ at different pH values. The results agreed very well with those calculated from Stenger [1] by means of the program $MINEQL^+$.

The computation for the material system Fe_2O_3 requires the knowledge of the concentration of Fe^{3+}-ions, which can be calculated from the balance reaction and the solubility product of iron hydroxide to $2.07 \cdot 10^{10}$ mol/l.

$$Fe^{3+} + 3OH^- \leftrightarrow Fe(OH)_3. \tag{7.19}$$
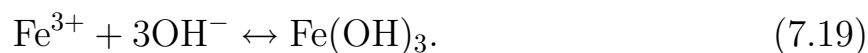
$$L = c_{Fe^{3+}} \cdot c_{OH^-}^3. \tag{7.20}$$

$$c_{Fe^{3+}} = \frac{1}{3} \cdot c_{OH^-}. \tag{7.21}$$

As solubility product $L = 5 \cdot 10^{-10}$ mol^4/l^4 was used [196]. The following balance reactions of Fe^{3+} are specified in equation 7.22 to 7.27:

$$Fe^{3+} + H_2O \leftrightarrow H^+ + Fe(OH)^{2+}, \qquad logK = -2.19. \tag{7.22}$$

$$2Fe^{3+} + 2H_2O \leftrightarrow 2H^+ + Fe_2(OH)_2^{4+}, \qquad logK = -2.95. \qquad (7.23)$$

$$Fe^{3+} + 2H_2O \leftrightarrow 2H^+ + Fe(OH)_2^+, \qquad logK = -5.67. \qquad (7.24)$$

$$3Fe^{3+} + 4H_2O \leftrightarrow 4H^+ + Fe_3(OH)_4^{5+}, \qquad logK = -6.30. \qquad (7.25)$$

$$Fe^{3+} + 4H_2O \leftrightarrow 3H^+ + Fe(OH)_3, \qquad logK = -12.56. \qquad (7.26)$$

$$Fe^{3+} + 4H_2O \leftrightarrow 4H^+ + Fe(OH)_4^-, \qquad logK = -21.60. \qquad (7.27)$$
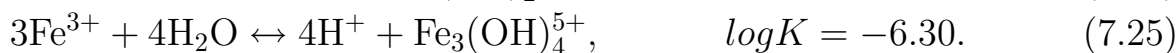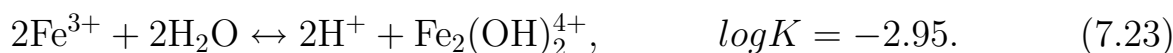
Figure 7.46 shows the equilibrium amounts of the different hydroxide complexes of the Fe^{3+}-ions at different pH values. The amounts of $Fe_3(OH)_4^{5+}$, $Fe_2(OH)_2^{4+}$ and $Fe(OH)_3$ are so small that they do not appear in the figure. The optimal range for milling experiments lies between pH6 and pH10, because only Fe_2O_3 and no hydroxide complexes are present there. Therefore no mechanochemical changes are expected within this range.
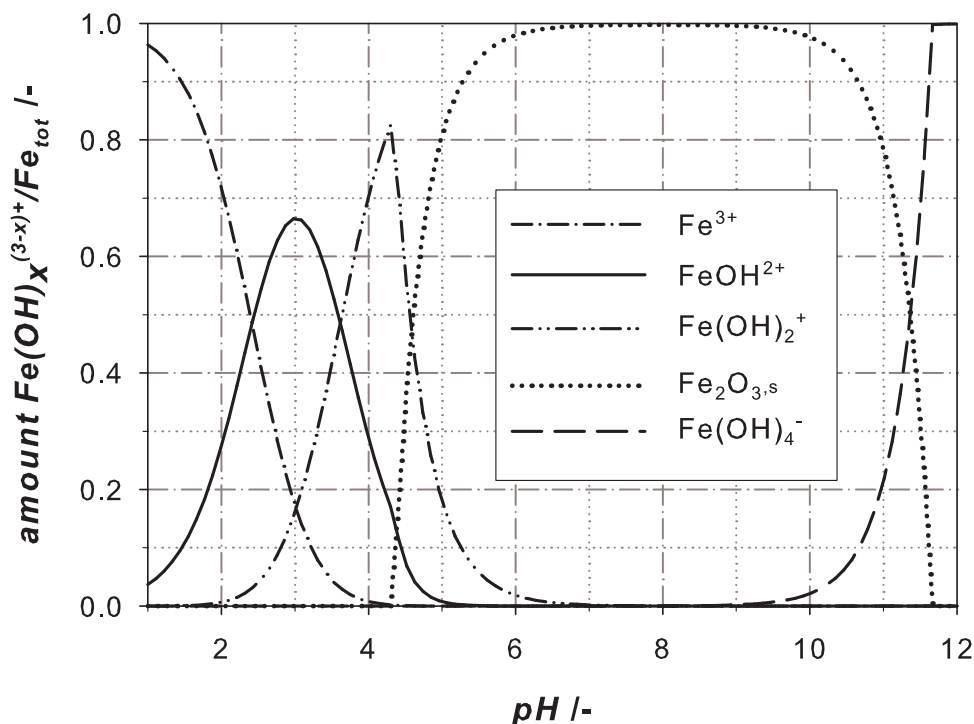
FIGURE 7.46. Calculated equilibrium amounts of the different complexes of $Fe(OH)_3$ and Fe_2O_3 at different pH-values.

7.4.2. Milling Experiments of Hematite in Water and Ethanol.

7.4.2.1. *Milling Experiments in Aqueous Phase at pH7.* A pH value of seven was selected for the milling experiments, because for this pH value no hydroxide complexes are expected and a ζ-potential of -40 mV is present, which should be sufficient for the stabilization of the suspension. The Fe_2O_3 powder was dispersed in distilled water at a concentration of 20% by weight. The temperature during the milling experiment was set to 16°C and the peripheral velocity of the agitating disk was adjusted to 10 m/s, as in all milling experiments for Fe_2O_3. Hence, the milling experiments were not performed at the optimum

stress energy. The aim of the experiments is to compare the results of milling in different environments; water at different pH values and ethanol. Therefore even smaller particle sizes are possible if the optimum stress energy for milling is selected.

The particle sizes were measured with the ZetaSizer (as described in chapter 5.1.2) by means of dynamic light scattering and with the MasterSizer 2000 (see chapter 5.1.1) by means of laser diffraction. The particle sizes measured with the different analysis methods were converted with equation 5.1 into a Sauter mean diameter $x_{1,2}$ in order to compare their results.

In figure 7.47 the calculated particle sizes $x_{1,2}$ are plotted over the specific energy input for the milling experiment at pH7. The particle size for dynamic light scattering lies in the range of 136 nm to 239 nm. The particle size range measured with laser diffraction reaches from 281 nm to 351 nm. With both methods a reduction of the particle diameter with rising specific energy is observed. The mean particle sizes measured with dynamic light scattering are smaller than the particle sizes measured with laser diffraction. The measured mean particle diameters are in the range of the Mie theory, which extends for the used laser wavelength $\lambda = 633$ nm according to equation 7.28 over the range from 20 nm to 2 μm:

$$\alpha = \frac{\pi \cdot x}{\lambda}. \tag{7.28}$$

The length parameter α ranges from 0.1 to 10 for the Mie-theory. The particle size influences in laser diffraction the measured scattering light intensity, according to Mie, with the power of four. Thus larger particles supply a strong measuring signal and can cover with it the signals of smaller particles. This phenomenon is even more emphasized for small particles measured in the Rayleigh regime. Here the particle size influences the light intensity with the power of six. Thus, during dynamic light scattering a few large particles can affect the measuring signal. The error results from wrong weighing of the few large particles by inverting the frequency spectrum into an intensity distribution.

At the beginning of the milling experiment a particle diameter of 227 nm was measured by means of dynamic light scattering and at the end a particle size of 136 nm. Mean particle sizes of 351 nm were measured with laser diffraction at the beginning of the milling experiment and at the end of 338 nm. The experiment was conducted over a period of 21 hours (85 276 kJ/kg). In figure 7.48 the ζ-potential, measured with the ZetaSizer, the conductivity and the pH value are plotted over the specific energy input. A negative ζ-potential results in the suspension between -26 mV and -7.7 mV. A decreasing ζ-potential is observed with increasing specific energy. A compression of the double layer can be excluded in this experiment since no potential-determining ions were added during the experiment. However, the decreasing ζ-potential may be explained by specific adsorption of Y^{3+} ions from the media wear. Y^{3+} ions in the suspension result in a lower ζ-potential as figure 7.45 shows. Stenger

[1] showed by means of inductively coupled plasma analysis that Y^{3+} ions can be dissolved out of yttrium stabilized zirconia milling beads during milling . He observed an increasing ζ-potential for the material SnO_2 milled in water at different pH-values. Also Greenwood et al. [197] observed dissolution of yttrium ions from yttrium stabilized zirconia powder under acid conditions. They showed that the ζ-potential for a zirconia suspension increased because of the yttrium dissolution with time.
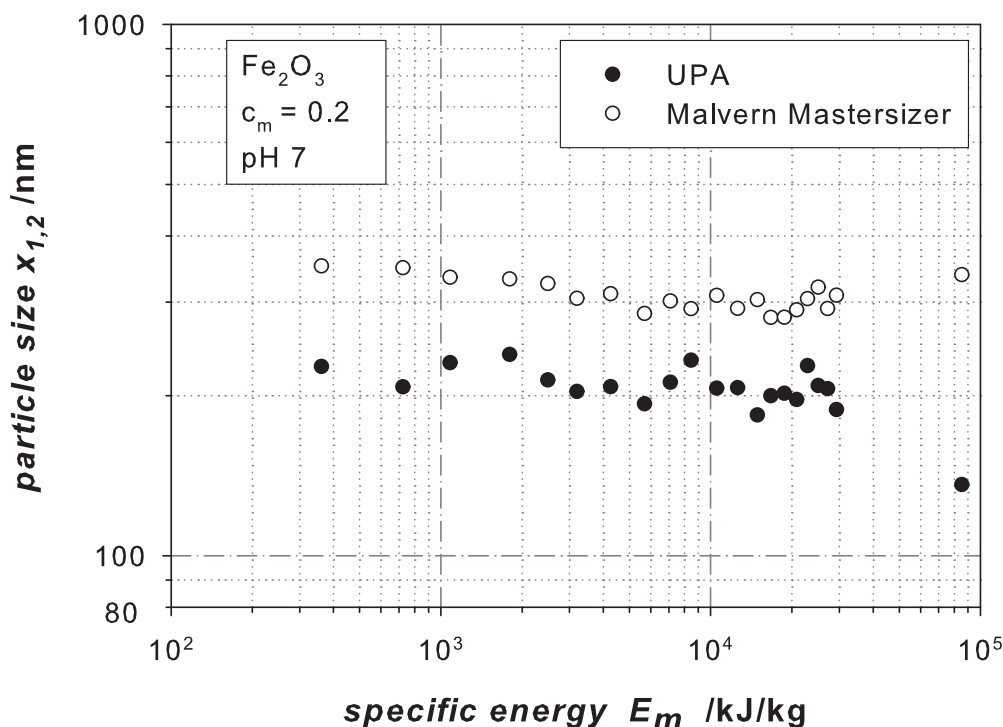
FIGURE 7.47. Measured particle size for Fe_2O_3 in dependence on the specific energy.

In figure 7.48 the measured pH value is plotted in dependence of the specific energy. During the duration of the test the suspension adjusts itself to a pH value from 6.4 to 7.3. In the course of the milling experiment a slow rise of the pH value is recognized, which drops toward the end of the experiment again. At the beginning of the experiment a pH value of 7.0 was obtained after the addition of the Fe_2O_3 powder to the distilled water. At the end of the milling experiment a pH value of 6.6 was measured. The conductivity of the suspension increases during the experiment from 0.073 to 0.121 mS/cm.

7.4.2.2. *Milling Experiments in Aqueous Phase at pH10.* The results of the milling experiments at pH 7 without addition of background salt could not satisfy with a final median particle size of 136 nm measured by dynamic light scattering. Therefore in the following experiments the suspension was stabilized by the addition of a background salt solution and a change in the pH value, in order to decrease the reagglomeration phenomena arising in the milling experiment with pH 7.
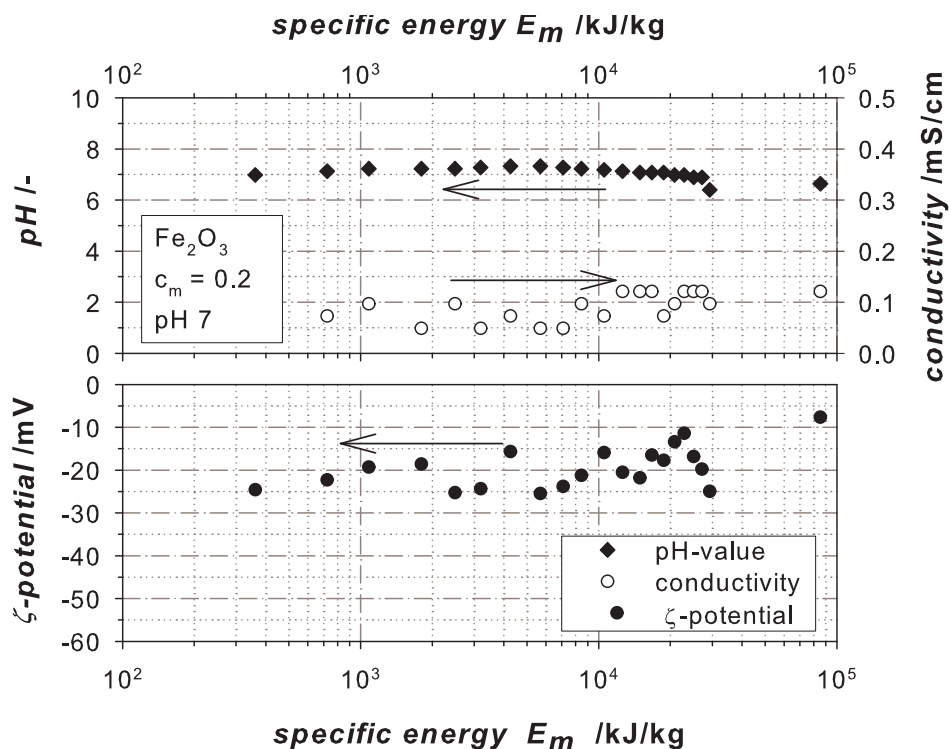
FIGURE 7.48. Measured ζ-potential, conductivity and pH value for Fe_2O_3 in dependence on the specific energy.

In figure 7.49 a comparison between the particle sizes measured with dynamic light scattering and the particle sizes computed with BET surface area analysis is presented. The measured samples originate from a milling experiment, which was accomplished with a solid concentration of 20% by weight in 0.01 molar $NaNO_3$-solution at pH10 and a temperature of 16 °C. The pH value was kept constant by titration of 0.1 molar NaOH solution in the stirred tank. The peripheral speed of the agitating disk was set to 10 m/s. The particle sizes were measured with dynamic light scattering with the Microtrac Ultrafine Particle Analyzer UPA 150 (Honeywell) and the ZetaSizer nano ZS ZEN 3600 (Malvern) (see chapter 5.1.2). The specific surface area was determined by means of BET-analysis from dried samples of the experiment. With the specific surface area the Sauter mean diameter was computed according to equation 5.1. In figure 7.49 the particle size $x_{1,2}$ is plotted over the specific energy. The particle size measured with dynamic light scattering decreases with increasing specific energy input almost linearly on a double logarithmic plot. A particle diameter of 226 nm was measured at the beginning of the experiment with the ZetaSizer and at the end of the experiment a value of 99 nm was reached. Thus a smaller median particle diameter was obtained by the selected stability conditions than without the addition background salt in the milling experiment at pH7. The initial value for the particle size measurement with the UPA is 370 nm. Towards the end of the experiment a median particle size of 98 nm is reached. Thus the two instruments supply approximately the same results for the milling process. The experiment duration was 24 hours (94 672 kJ/kg). The particle

sizes computed from the BET-analysis decreased also with increasing specific energy input. However, the measured values decrease faster. The reason for this is, that in BET-analysis a different particle characteristic is measured with the specific surface area, as in dynamic light scattering with the scattered light intensity. With the data from the BET- measurements a pore size analysis was accomplished for each sample according the V-t-method described in appendix A.2. The analysis of these data shows that the samples do not exhibit pores. Thus it can be excluded that the computed mean diameters $x_{1,2}$ appear substantially smaller because of a larger internal surface area. At the beginning of the experiment the computed particle size is 94 nm. At the end of the milling experiment a particle size of 17 nm was measured.
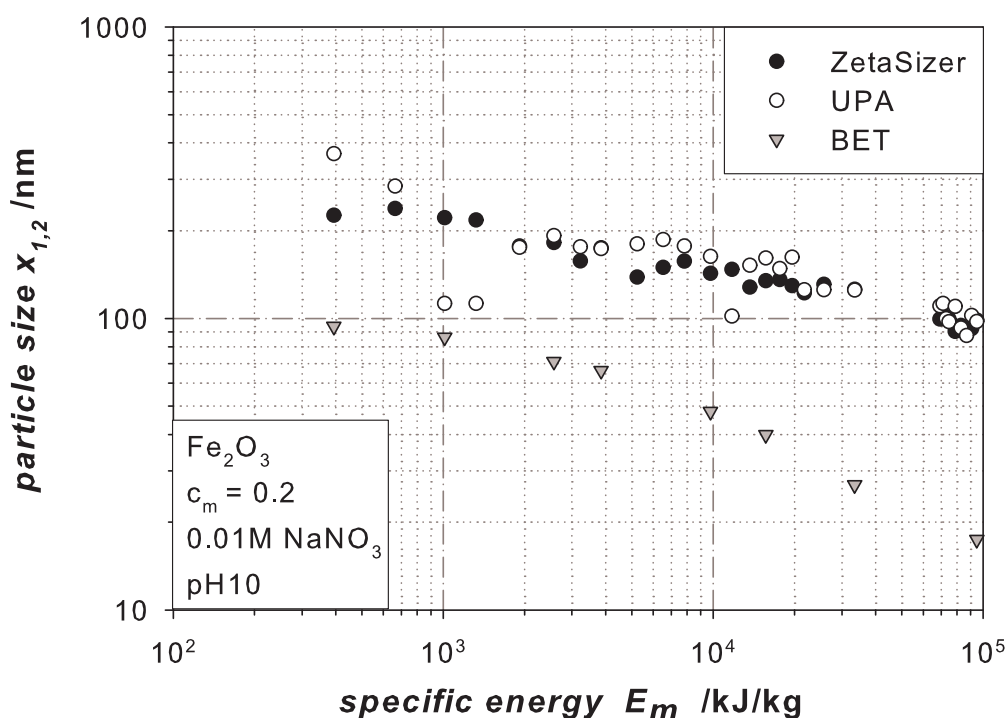
FIGURE 7.49. Measured particle size in dependence on the specific energy input for a milling experiment at ph10.

In figure 7.53 the measured ζ-potential and the conductivity is plotted in dependency of the specific energy input. The ζ-potential measurement was performed online in the concentrated suspension with the ultrasonic spectrometer DT 1200 (see chapter 5.1.2). These data are compared to measurements of the ζ-potential which were performed on diluted suspensions with the ZetaSizer. The ζ-potentials measured with the ZetaSizer are slightly larger according to amount than the potentials measured with the DT1200. The measurement range reaches from -30 mV to -50 mV. The decrease of the magnitude of the ζ-potential can be explained by the compression of the double layer, because during the experiment HNO_3 was titrated to the suspension in order to keep the pH value constant. The addition of HNO_3 further leads to an increase

in the conductivity as it can be seen in figure 7.53. However, the ζ-potential measured during the experiment is large enough to ensure the stability of the dispersion over the entire duration of the test, which can also bee seen in the linear decrease of the mean particle diameter (see figure 7.49).

In comparison to this the experiment at pH7 without the addition salt has at the end of the experiment a ζ-potential of -7.7 mV. The ζ-potential in this experiment is decreasing and the suspension is destabilizing with progressing milling time. The steady state between breakage, agglomeration and dispersing shifts therefore with rising specific energy input toward agglomeration. The consequence of the reagglomeration phenomena is a slower milling progress, which shows up in a slower decrease of median particle size with increasing specific energy input (see figure 7.47).
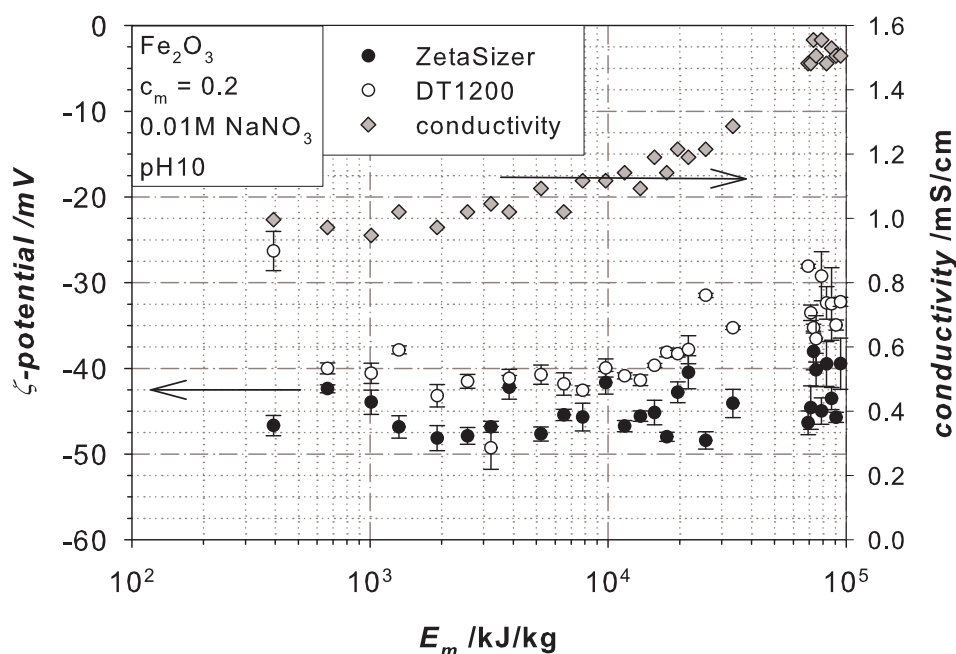
FIGURE 7.50. ζ-potential for a Fe_2O_3-suspension milled at pH10.

A scanning electron microscope picture of the used raw material can be seen in figure 7.51a. The picture shows besides agglomerates with a primary particle size of 150 to 200 nm single particles with particle sizes of around 1.7 μm. Furthermore, figure 7.51b shows hematite particles milled at pH10 for 24 hours (94 672 kJ/kg). On the picture single particles with a primary particle size of approximate 15 to 140 nm can be recognized. However, also agglomerates of these particles can be seen. The sample preparation can be responsible for this phenomenon, since the suspensions have to be dried in order to make a SEM picture. Thus, the mean particle size, which was computed from the BET-analysis data, for the hematite particles milled at pH10 is 17 nm.

7.4.2.3. *Milling Experiments in Aqueous Phase at pH3.* A clear shift of the iep can bee seen in figure 7.45 if $Fe(NO_3)_3$ is used as background salt. This

a)   b)
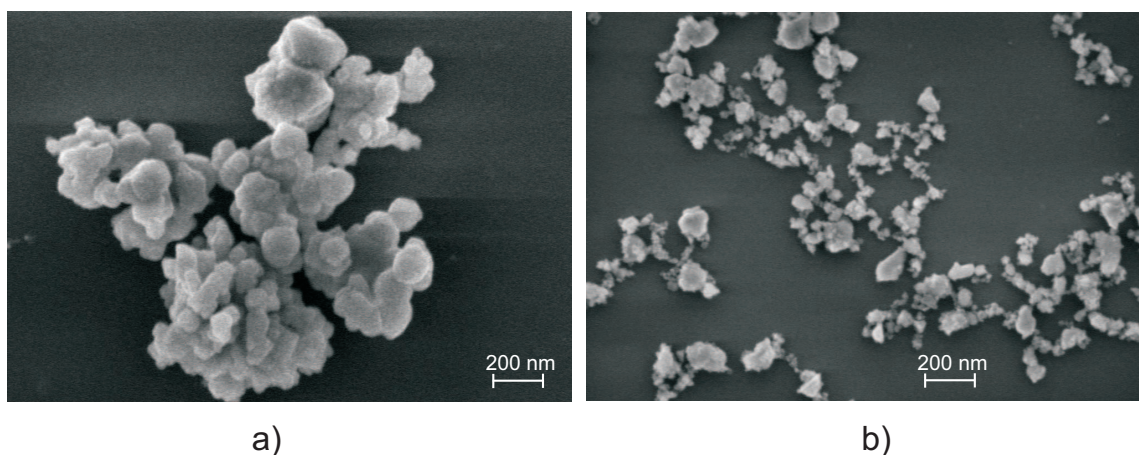
FIGURE 7.51. Scanning electron microscope picture of a) the used raw material and b) hematite particles milled at pH10.

shift suggests a specific adsorption of Fe^{3+}-ions at the particle surface of Fe_2O_3. Because of this, a high ζ-potential value of approx. 50 mV could be measured at pH3. This value is sufficiently high, in order to stabilize the suspension. Thus, milling experiments could be performed at pH3. These milling experiments were accomplished with the same milling conditions as described in the previous chapter. The suspension was adjusted with 10 M HNO_3 to the respective pH value. The median particle sizes $x_{1,2}$ measured with dynamic light scattering are shown in figure 7.52. The median particle size decreases during the experiment to approx. 60 nm. Thus the particle size reached at pH3 is smaller than the mean particle size reached in the experiments, which were accomplished with pH7 (136 nm) and with pH10 (85 nm). The figure further shows median particle sizes $x_{1,2}$ calculated from BET measurements. The final particle size measured with BET is 12 nm.

In figure 7.53 the measured ζ-potential and the conductivity are plotted in dependence of the specific energy for the milling experiment performed at pH3. The ζ-potential measurement were performed off-line directly after the sampling in concentrated form with the ultrasonic spectrometer DT1200.

The ζ-potential is almost constant during the whole experiment. The value of the ζ-potential lies between 40 and 50 mV. Thus the suspension is stabilized during the whole experiment. During the experiment the pH value was kept constant at pH3 by titration of 10 M HNO_3 solution in the stirred tank. By the addition of acid to the suspension the conductivity increases from initially 0.75 mS/cm to 7 mS/cm.
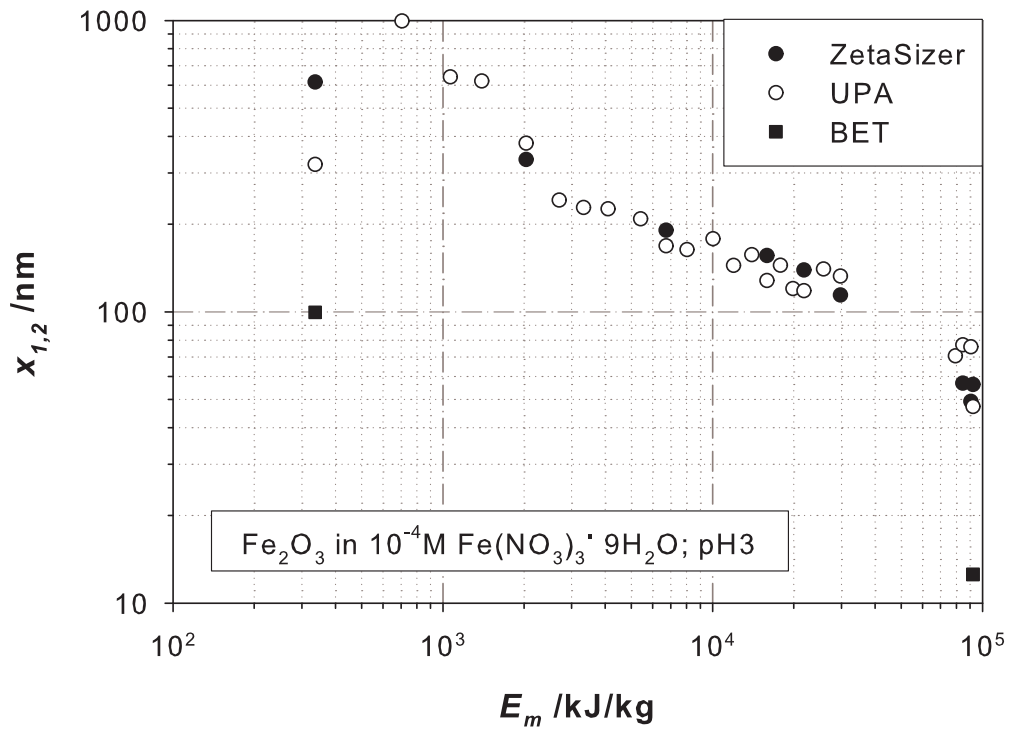
FIGURE 7.52. Measured particle size for Fe_2O_3 milled at pH3.
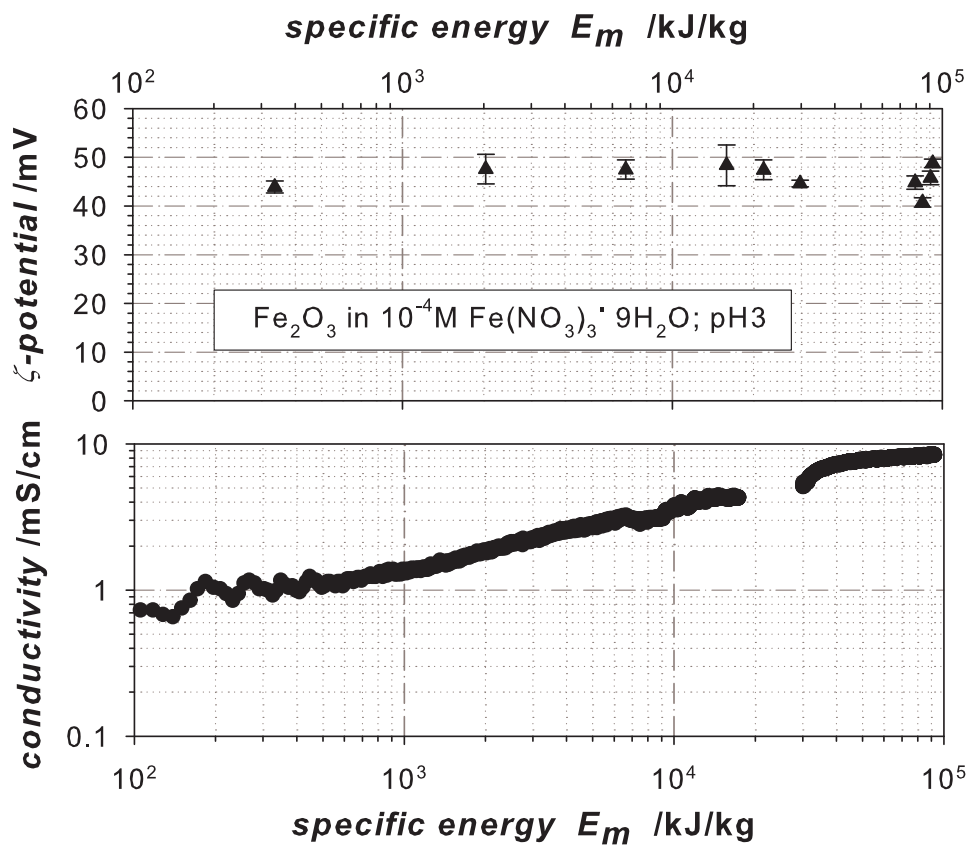
FIGURE 7.53. ζ-potential and conductivity in dependence on the energy input for a Fe_2O_3 suspension milled at pH3.

7.4.2.4. *Milling Experiments in Ethanol.* Figure 7.54 shows the adsorption isotherm of DAPRAL on hematite particles in ethanol. For the measurements the feed particles with a median particle size of $x_{50,3} = 250$ nm were suspended in ethanol with the corresponding amount of polymer. The suspensions were gently stirred over night to ensure that the adsorption equilibrium is reached. To separate the particles from free and not adsorbed polymer chains, the suspensions were centrifuged at 3500 rpm for 30 min in a Heraus Labofuge 400 and washed with pure solvents for five times. The centrifuged particles were dried and the adsorbed amount of polymer was thermogravimetrically determined with a heating rate of 10 K/min under nitrogen atmosphere. The adsorbed amount of polymer per unit area was then calculated based on the measured BET surface area of 11.5 m^2/g. In figure 7.54 it can be seen that an adsorbed amount of polymer of 1.7 mg/m^2 was measured in the plateau region. The same amount of adsorbed polymer was mesured for α-Al$_2$O$_3$ in ethanol (see figure 7.16).
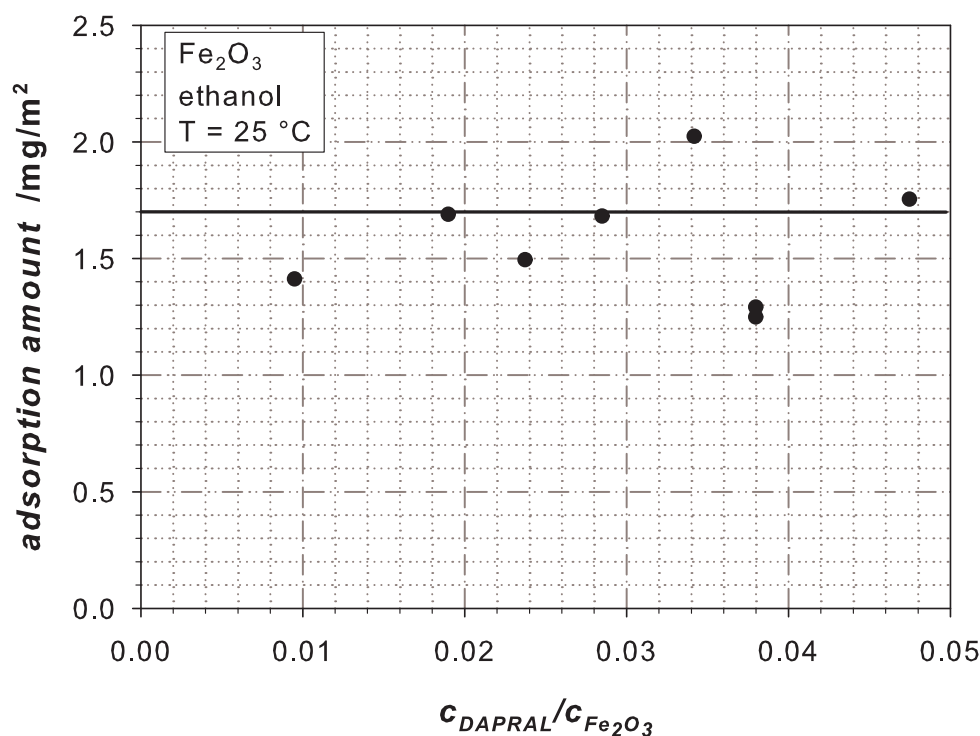
FIGURE 7.54. Adsorption isotherm of DAPRAL on α-Fe$_2$O$_3$ in ethanol.

In figure 7.55 the particle size measured with dynamic light scattering is plotted over the milling time. The milling experiment was performed in the batch mill at a constant temperature of 15°C as described in chapter 4.2 with a rotary speed of 1500 rpm. The Sauter mean diameter $x_{1,2}$ of the hematite particles decreases down to 50 nm at the end of the experiment, which is in the size range of the particles milled in aqueous phase at pH3.

In figure 7.56 the ζ-potential is plotted over the milling time. The ζ-potential was measured with the ZetaSizer (see chapter 5.1.6). It can be seen, that the magnitude of the ζ-potential decreases from initially 17 mV to almost 0 mV at
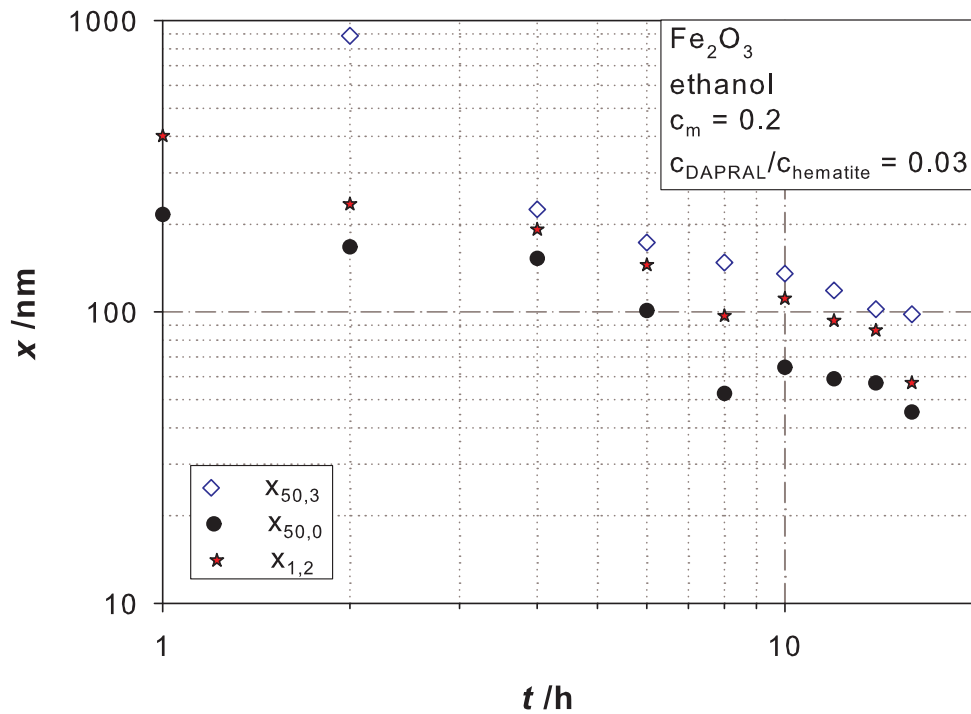
FIGURE 7.55. Measured particle size for steric stabilized Fe_2O_3 milled in ethanol.

8 h milling time. This decreasing ζ-potential can be an effect of the media wear. The positively charged media wear particles attach preferable on the negative charged iron oxide particles leading to a reduced ζ-potential.
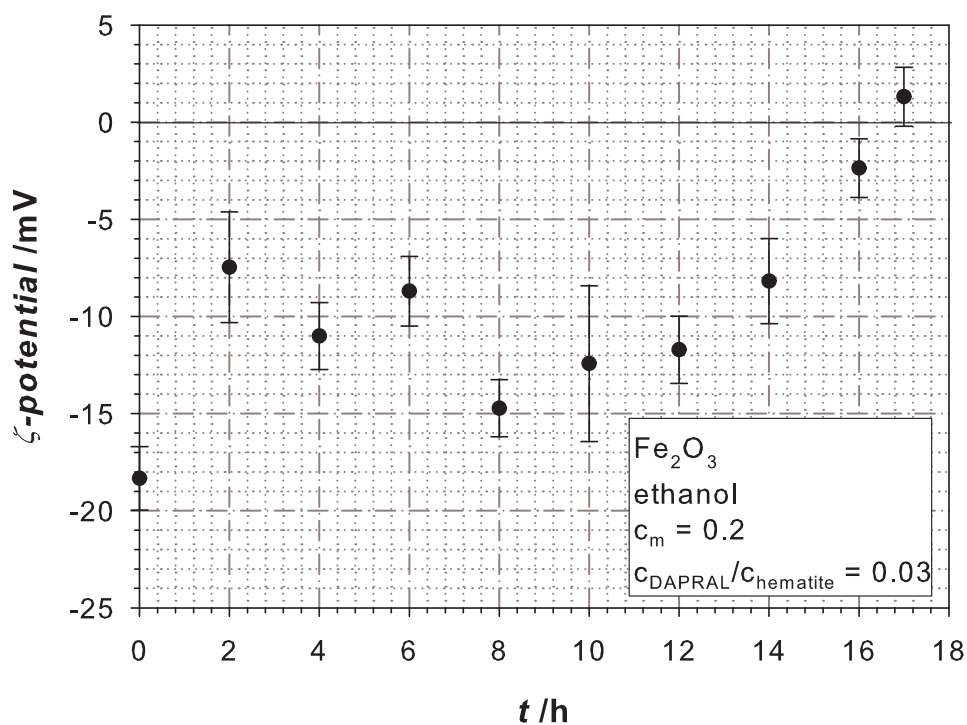
FIGURE 7.56. ζ-potential in dependency of the milling time for a steric stabilized Fe_2O_3 suspension milled in ethanol.

As for alumina particles an electrostatic stabilization of hematite particles in ethanol is possible as well. In figure 7.57 the ζ-potential of hematite particles in ethanol is plotted over the salt concentration for a variety of salts. Fe_2O_3 suspended in ethanol has originally a negative surface charge and a ζ-potential of around -80 mV. With increasing salt concentration the ζ-potential decreases according to amount because of the compression of the double layer. No influence of different salts on the ζ-potential was noticed, except for $Fe(NO_3)_3$. The Fe^{3+} ions cause in a faster reduction of the amount of the ζ-potential due to its ionic valence of three.
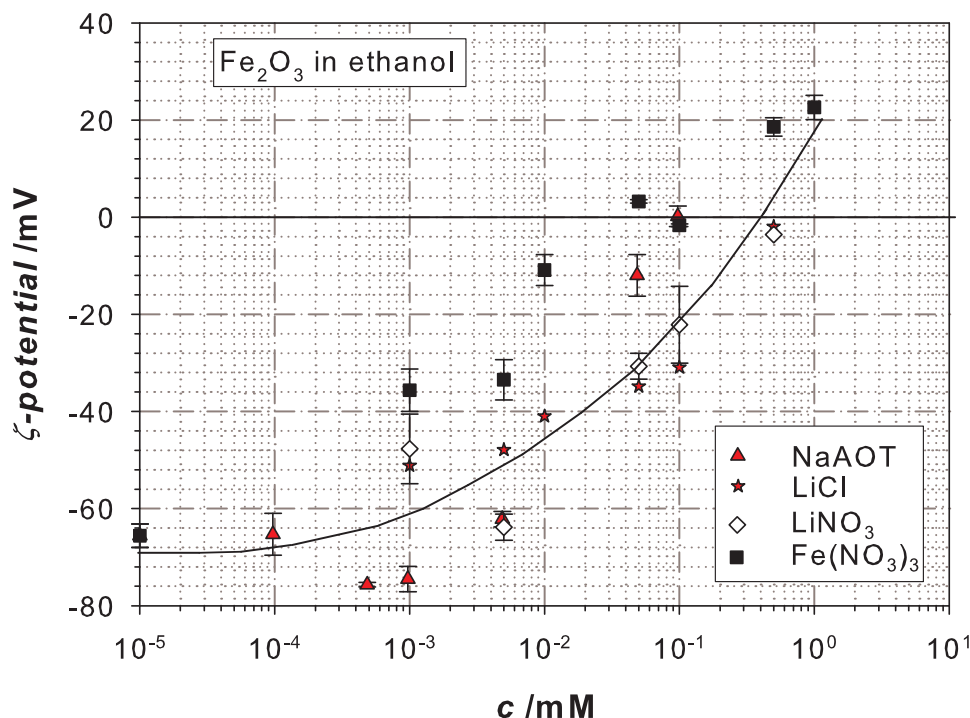
FIGURE 7.57. Influence of different ions on the ζ-potential for electrostatic stabilized Fe_2O_3 in ethanol.

In figure 7.58 the particle size measured with dynamic light scattering is plotted over the milling time. In this experiment the iron oxide suspension was electrostatic stabilized and 10^{-4} mM NaAOT was added as background salt. The final particle size for electrostatic stabilized hematite particle is clearly larger than the particle sizes achieved in the milling experiments with steric stabilization.
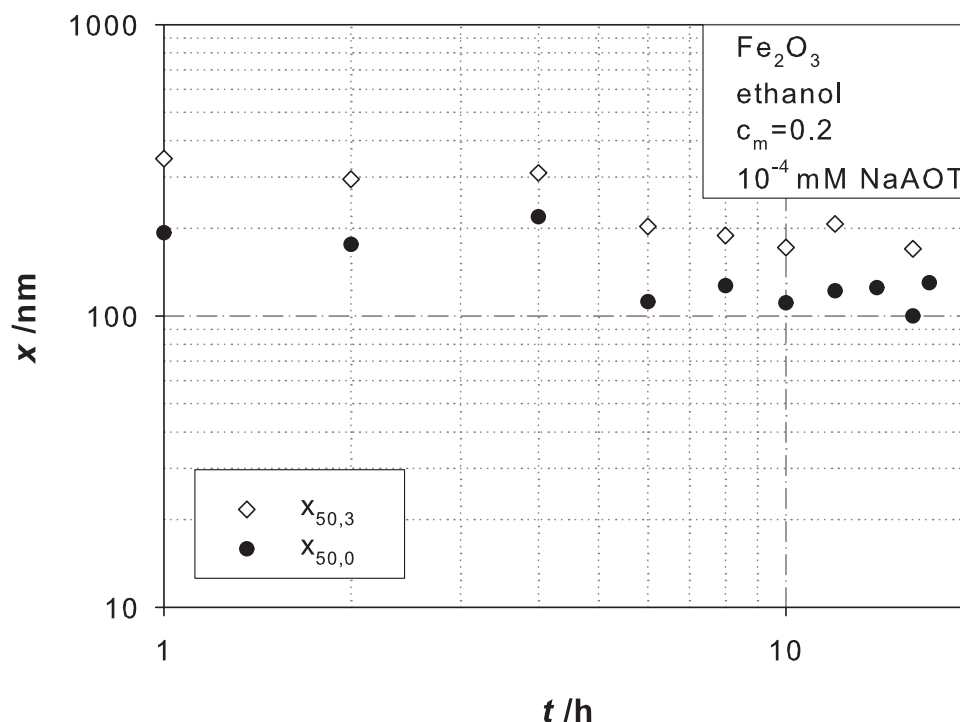
FIGURE 7.58. Measured particle size for electrostatic stabilized Fe_2O_3 milled in ethanol.

7.4.3. Mechano-chemical Changes During Milling of Fe_2O_3. The mechanical stressing of the hematite particles in the stirred media mill can lead, in addition to the size reduction, to structural changes and reactions of the solid with the surrounding medium. In order to investigate these possible mechano-chemical changes a X-ray structure analysis was performed on the the original suspension and on the milled samples. The sampling took place during the experiment directly at the mill exit before introduction into the stirred tank. As it can be seen in figure 7.59, the peak intensities for the original particles are bright and sharp indicating the crystallinity of the sample. Furthermore, the diffraction pattern of the feed particles shows that the original substance already exhibits a high amorphous phase apart from the crystalline structure. This amorphous phase has increased during milling. The comparison of the feed material with the samples milled in aqueous phase at pH3, pH10 and in ethanol (1260 min) shows a reduction of the diffraction intensities, as well as a widening of the reflexes. This indicates that a phase transformation from crystalline to amorphous has taken place and that particles are reduced in size. However, no further new peaks could be observed indicating that no phase transformation of hematite has taken place during milling. The structure of the hematite remains unchanged during milling and no foreign phase shows up. The evaluation of the measuring data with the program X'Pert Highscore and the data base Powder Diffraction (file release 1998 of the International Center for Diffraction Data (ICDD)) showed good agreement with synthetic hematite for the feed as well as for the milled samples.
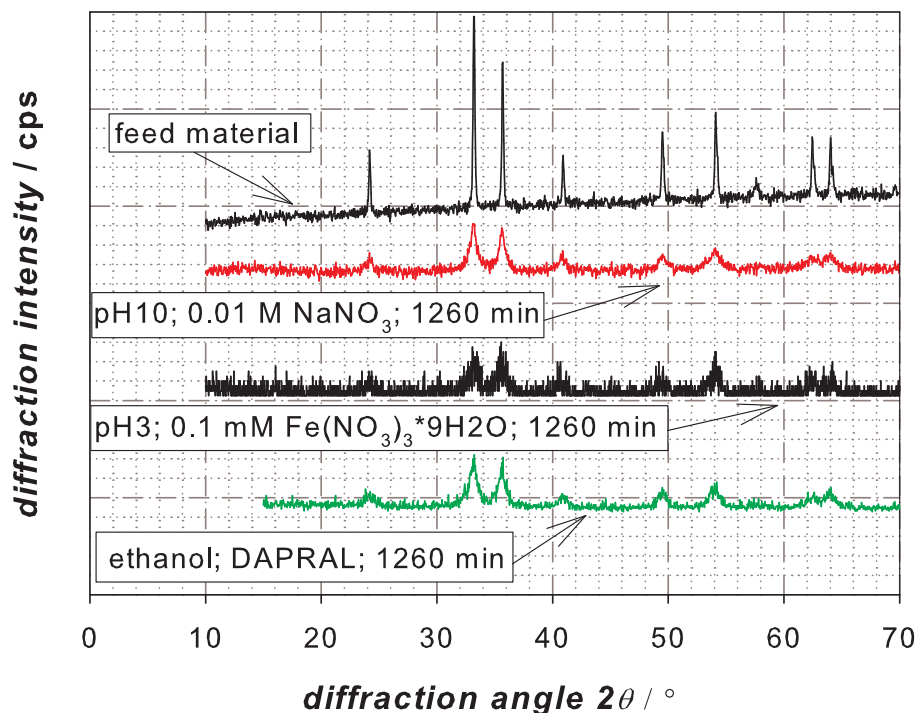
FIGURE 7.59. XRD diffraction patterns for the feed particles and milled samples in water at pH10 and pH3 and in ethanol.

A further method to detect mechano-chemical changes during milling is the method of dynamic scanning calorimetry (DSC). The results of the DSC analysis for the milled samples and the reference sample are shown in figure 7.60. The measured heat flow is plotted in this diagram over the temperature. For all samples no heat flow peaks were observed, which would refer to a thermal change. Thus, no phase transformations arise during the milling experiment.

However, a color change of the suspensions during milling was observed in all experiments. This color change appeared in particular during milling of sterically stabilized hematite particles in ethanol and in the aqueous phase at pH3. The original color of the hematite suspension was bright red. During milling of sterically stabilized particles in ethanol and in the aqueous phase at pH3 the suspensions changed their color to deep black. In the aqueous experiment at pH10 this phenomenon was not as clear as in the other experiments. However, the suspensions milled in water at pH10 was getting slightly darker with time as well. To document this phenomenon the absorbance of of the suspensions were measured with UV-Vis-absorption spectroscopy. For the measurements the milled samples were diluted 1:100 with clear solvent. The results of the UV-Vis measurements for hematite milled in ethanol are plotted in figure 7.61. In this figure the absorbance of the sample is plotted over the wavelength. It can be see that the absorbance increases for smaller wavelengths with increasing milling time or smaller particle sizes, respectively. To explain this increase of absorbance at small wavelengths the absorption of homogeneous dielectric
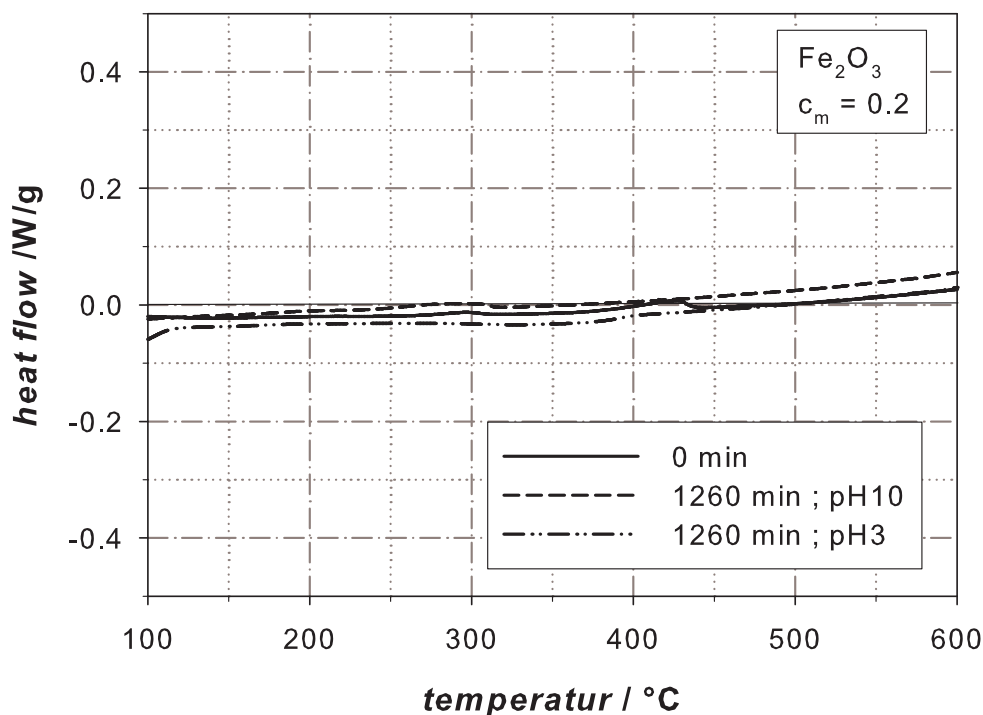
FIGURE 7.60. DSC measurements of Fe_2O_3.

spheres without change in the magnetic permeability between inside and outside of the particles was calculated with the Mie theory. For the calculations Matlab functions for Mie scattering and absorption from Mätzler [198] were used. His program goes back to the formalism of Bohren and Huffman [151]. Required input parameters are the complex refractive index of the spheres relative to the ambient medium and the size parameter ka, where a is the sphere radius and k the wavenumber in the ambient medium. The complex refractive index for hematite is according to [199] 2.94+1i at a wavelength $\lambda = 0.5$ μm. At other wavelengths considered here values between 2.74+1i and 3.0+1i were reported in the literature. However, this can also be an effect of different origins of the hematite samples. The results of the absorbance calculations are plotted in figure 7.61. With decreasing particle size the absorbance at small wavelengths increases as in the measured sample. This indicates that the color change of the suspension during milling is an effect of the particle size. The experimentally determined absorbance does not match the calculated absorbance exactly, because in the milled sample the particles are not monodisperse and the particles have irregular shapes. Furthermore, fluctuations in the concentration due to sampling and dilution influences the measurements. However, due to the similar characteristics of the calculated and the measured data a strong evidence is given that the color change is due to the decreasing particle size in the milling experiment.
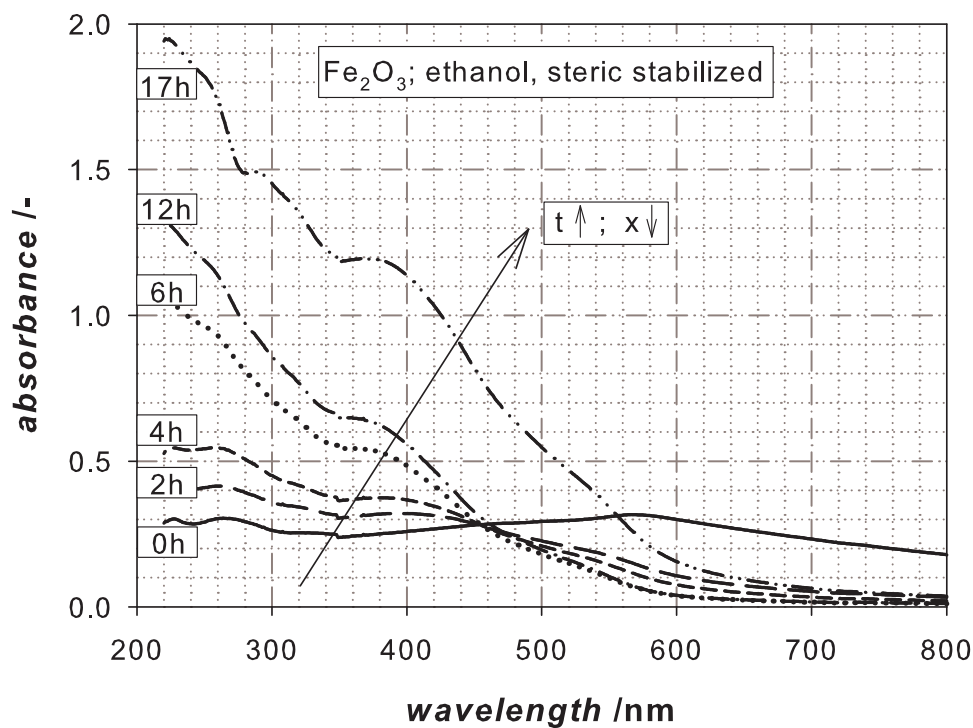
FIGURE 7.61. UV-Vis spectra for steric stabilized Fe_2O_3 particles milled in ethanol.
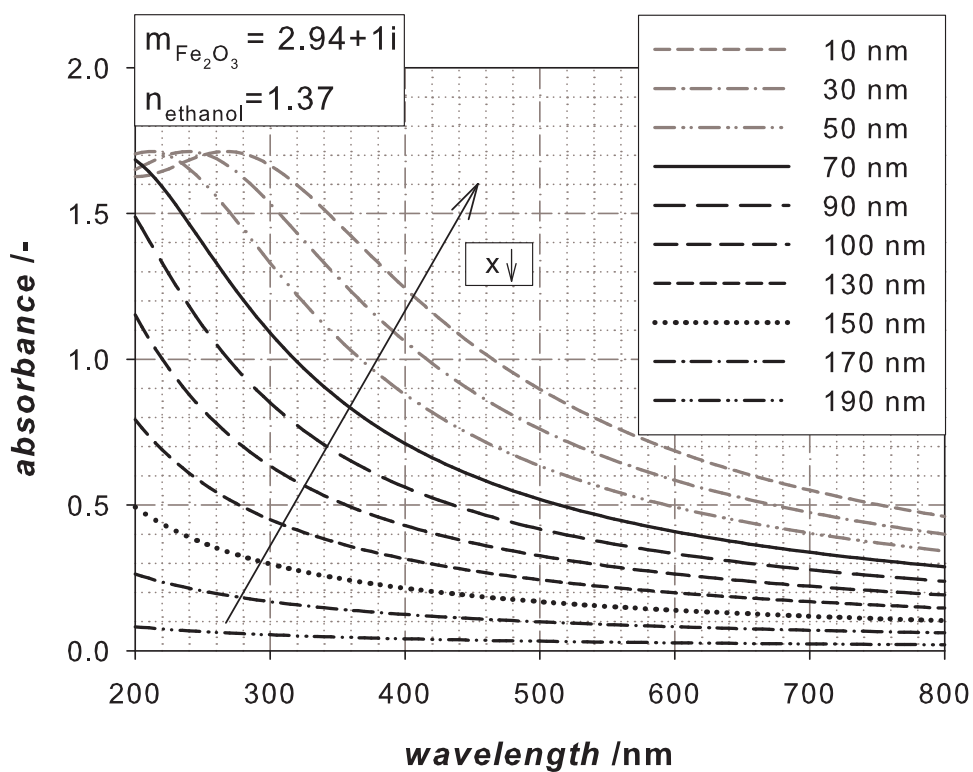
FIGURE 7.62. Calculated absorbance for spherical Fe_2O_3 particles in ethanol using the Mie-theory.

CHAPTER 8

Simulation

By population balance modeling not only the dynamic development of spatial distribution of particles in a process can be balanced, but also the particle number with regard to a certain property. Properties of particles may be for instance size, color, form, imperfection density, charge, porosity or surface energy. In order to implement this, the term of particle phase space is introduced. It encompasses the distribution of particle properties with regard to a set of independent variables. The variables are divided into external and internal variables. The external variables describe the spatial distribution of the particles in the three directions in space. The internal variables describe the distribution with regard to the respective particle property that is additionally observed.

The total number of variables results from the three spatial and m internal variables, there m is the number of properties observed. Accordingly the particle phase space is $(m+3)$-dimensional.

The basic population balance equation can be derived from the general equation of continuum mechanics for a field quantity F. However, the additional internal variables have to be considered. In this work the number concentration distribution function $n(V,t)$, representing the number of particles per system volume with size V at time t, is balanced.

The general population balance for a differential volume element in number concentration is:

$$\frac{\partial n}{\partial t} + \nabla\left(\vec{\nu}_e \cdot n\right) + \nabla\left(\vec{\nu}_i \cdot n\right) = B - D + \nabla\left(\vec{j}\right). \qquad (8.1)$$

The temporal change of the number concentration n as well as the change due to displacement in the dimensions of the internal and external coordinates $(\vec{\nu}_i, \vec{\nu}_e)$ must be equal to source (birth, B) and sink (death, D) terms in the interior of the accounted volume and additionally changes due to diffuse exchanges over the surface $(\vec{j})$.

This general equation can be simplified with the following assumptions:

- The system is completely back mixed, i.e. there are no concentration gradients in the whole volume V. Furthermore, a batch mill is considered in the first instance. That means there are no inlet and outlet flows. From this follows that $\nabla\left(\vec{\nu}_e \cdot n\right) = 0$.

- There is no particle exchange over the wall of the grinding chamber, resulting in $\nabla\left(\vec{j}\right) = 0$.

- The internal variables are not changed, e.g. there is no growth of particles. This leads to $\nabla\left(\vec{\nu}_i \cdot n\right) = 0$.

8.1. Breakage

The breakage processes is described in the population balance by means of a breakage rate kernel $\tilde{\Gamma}(V)$, describing the probability that a particle with a certain volume V breaks within a time step, and a breakage function $b(\phi, V)$, which describes the distribution of fractions with volume ϕ when a particle with volume V breaks.

In this work a breakage rate kernel according to Kapur [200] was used which has a power-law dependence on parent particle volume.

$$\tilde{\Gamma}(V) = \hat{\Gamma} \cdot V^{\mu}. \tag{8.2}$$

where the value of μ is usually around $1/3$ to be consistent with the theoretical expectation that breakage rate is proportional to the particle diameter [201]. The breakage rate coefficient for shear induced fragmentation $\hat{\Gamma}$ is according to Spicer and Pratsinis [178] related to the shear rate by:

$$\hat{\Gamma} = A' \cdot \dot{\gamma}^{y}. \tag{8.3}$$

where y is a constant inversely proportional to the floc strength and A' is a proportionality constant which can be determined experimentally.

For the breakage function a generalized form of Hill and Ng's power law breakage distribution [202] was used:

$$b(\phi, V) = \frac{p \cdot \phi^{c} \cdot (V - \phi)^{c + (c+1) \cdot (p-2)} \cdot [c + (c+1) \cdot (p-1)]!}{V^{p \cdot c + p - 1} \cdot c! \cdot [c + (c+1) \cdot (p-2)]!}. \tag{8.4}$$

Equation (8.4) can be simplified using the Gamma function and substituting $z = \frac{\phi}{V}$:

$$b(\phi, V) = \frac{p \cdot z^{c} \cdot (1 - z)^{c + (c+1) \cdot (p-2)} \cdot \Gamma[c + (c+1) \cdot (p-1) + 1]}{V \cdot \Gamma(c+1) \cdot \Gamma[c + (c+1) \cdot (p-2) + 1]}. \tag{8.5}$$

This is in the self-similar form in that the dependence of the breakage function on daughter size is only in terms of the daughter to parent ratio.

$$b(\phi, V) = \frac{\Phi(z)}{V}. \tag{8.6}$$

$$\Phi(z) = \frac{p \cdot z^{c} \cdot (1 - z)^{c + (c+1) \cdot (p-2)} \cdot \Gamma[c + (c+1) \cdot (p-1) + 1]}{\Gamma(c+1) \cdot \Gamma[c + (c+1) \cdot (p-2) + 1]}. \tag{8.7}$$

Figure 8.1 shows that the parameter c governs the shape of the distribution and the parameter p the location. According to Hill and Ng the parameter p denotes the number of fragments and can be obtained from the 0th moment b_0 of the daughter distribution function which is a number balance:

$$b_0 = \int_0^1 \Phi(z) \cdot dz = p. \tag{8.8}$$
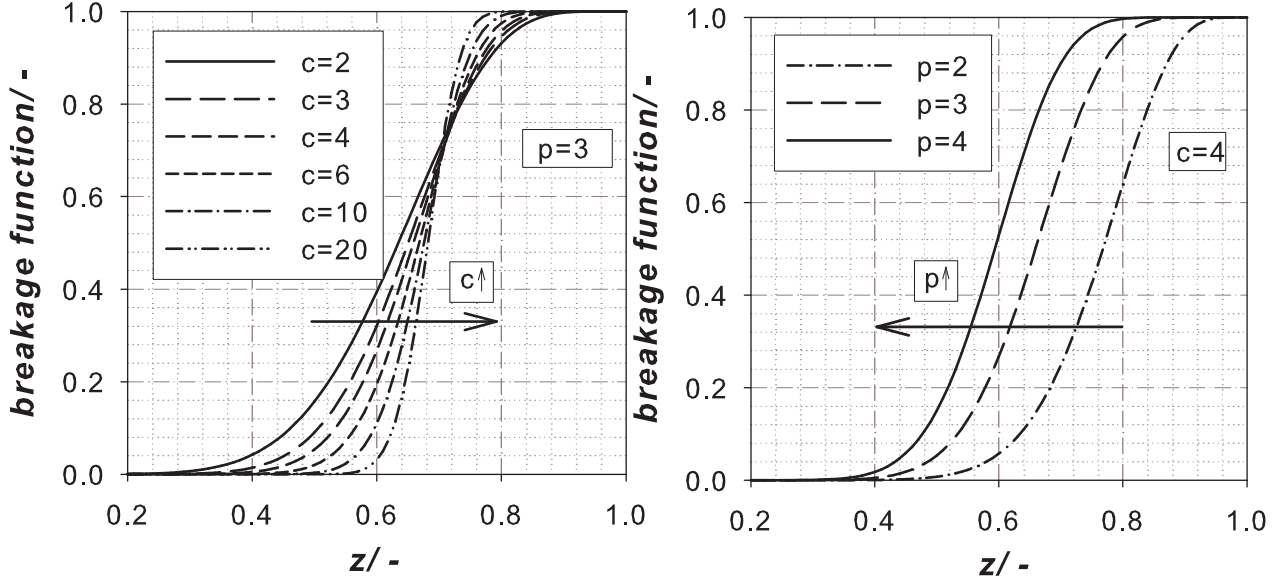
FIGURE 8.1. Hill and Ng's powerlaw breakage for p=2 (binary breakage)

The 1st moment b_1 of the daughter distribution function $\Phi(z)$ must fulfill the mass balance requirements:

$$b_1 = z \cdot \int_0^1 \Phi(z) \cdot dz = 1. \tag{8.9}$$

The moment b_k can be simplified using the Gamma Function [203]:

$$b_k = \int_0^1 z^k \cdot \phi(z) \cdot dz. \tag{8.10}$$

$$b_k = \frac{p \cdot \Gamma[c + (c + 1) \cdot (p - 1) + 1]}{\Gamma(c + 1) \cdot \Gamma[(c + 1) \cdot (p - 2) + c + 1]} \int_0^1 z^{(c+k)} \cdot (1 - z)^{c+(c+1)\cdot(p-2)} \, dz. \tag{8.11}$$

$$b_k = \frac{p \cdot \Gamma[c + (c + 1) \cdot (p - 1) + 1] \cdot \Gamma(c + k + 1) \cdot \Gamma[c + (c + 1) \cdot (p - 2) + 1]}{\Gamma(c + 1) \cdot \Gamma[(c + 1) \cdot (p - 2) + c + 1] \cdot \Gamma[2c + k + 2 + (c + 1) \cdot (p - 2)]}. \tag{8.12}$$

8.2. Agglomeration

The balance for agglomeration can be described similar to the population balance for breakage, with birth and death terms. The population balance for agglomeration in continuous form is:

$$\frac{dn\left(\phi\right)}{dt} = \frac{1}{2} \cdot \int_0^\phi \beta(V, \phi - V) \cdot n(V) \cdot n(\phi - V) \cdot dV -$$
$$- n(\phi) \cdot \int_0^\infty \beta(V, \phi) \cdot n(V) \cdot dV. \tag{8.13}$$

The terms on the right hand side of equation (8.13) are describing the birth and death terms for the agglomeration process. The proportionally factor β is known as the agglomeration kernel. The factor $1/2$ prevents the double counting of collisions. Physically based models for the aggregation kernel that depend on the transport mechanisms can be found in section 3.3.

The system of integro- differential equations shown in equation (8.14) describes the simultaneous event of agglomeration and breakage that can only be solved numerically (see chapter 8.3). Only a few investigations are known from literature about the simultaneous solving of these equations [**1, 178, 204, 205, 203, 206, 207, 208**]. However, only a few of them dealing with the continuous form including particle-particle interactions which is done in this work.

The population balance equation for agglomeration and breakage written in a continuous form is:

$$\frac{dn\left(\phi\right)}{dt} = \underbrace{\int_\phi^\infty \tilde{\Gamma}\left(V\right) \cdot b\left(\phi, V\right) \cdot n\left(V\right) \cdot dV}_{1} - \underbrace{\tilde{\Gamma}\left(\phi\right) \cdot n\left(\phi\right)}_{2}$$
$$+ \underbrace{\frac{1}{2} \cdot \int_0^\phi \beta(V, \phi - V) \cdot n(V) \cdot n(\phi - V) \cdot dV}_{3} - \underbrace{n(\phi) \cdot \int_0^\infty \beta(V, \phi) \cdot n(V) \cdot dV}_{4}.$$
$$\tag{8.14}$$

where $n(V, t)$ is the number concentration distribution function, representing the number of particles per system volume with size V at time t. $\Gamma(V)$ is the breakage rate kernel and $b(\phi, V)$ is the probability of making a daughter of size ϕ from a parent of size V.

The terms of the right hand side of equation (8.14) have the following meaning:

(1) rate of birth of particles of volume ϕ due to fragmentation of bigger particles,
(2) rate of death of particles of volume ϕ due to fragmentation.
(3) rate of birth of particles of volume ϕ due to aggregation of smaller particles
(4) rate of death of particles of volume ϕ due to aggregation with other particles

8.3. Solving the Population Balance Equation

For solving the complex system of partial differential equations there are generally five methods known from literature that are described by Ramkrishna [**209**]. Besides the method of successive approximations and the method of Laplace transformation that can both only be applied to problems with certain kernels (e.g. constant or sum kernel) the Monte Carlo simulation method is restricted to systems with only small numbers of particles due to the computational effort. The most successful approach so far is done by discretization of the particle space domain that divides the continuous size range into discrete size classes. Hounslow et al. [**210**] and Litster et al. [**211**] developed a discretization procedure for the aggregation problem that was extended to the breakage problem by Vanni [**207**]. Kumar and Ramkrishna [**212**] developed a new method of discretization (pivot technique) that involves a selective refinement of a relatively coarse grid while the number of sections is kept to a minimum. This method was successfully applied to agglomeration/breakage problems. Numerical problems with the conservation of mass and/or the correct total number of particles can be overcome by correction factors that have to be derived for each agglomeration and breakage kernel separately. In this work two other methods that can include particle-particle interactions were tested and evaluated in terms of accuracy of the particle size distribution and computational effort. Both of which are described in the following in more detail.

8.3.1. PARSIVAL. The commercially available software package PARSIVAL (Particle Size Evaluation) uses the fully adaptive Galerkin h-p method which was developed for the simulation of molecular weight distributions in polymerization reactions [**213**]. It is based on a generalized finite-element scheme with self-adaptive grid- and order construction and is connected to a time discretization of Rothes type. It uses an automatic error control for the time discretization as well as for the discretization of the property coordinate [**214**]. In addition no assumptions concerning the shape of the particle size distribution and the structure of the used kernels have to be made. The method is implemented in a dynamic flow sheet simulator that allows the combination of all different kinds of processes (e.g. agglomeration, breakage, nucleation, growth, erosion,...) and runs on a standard personal computer.

8.3.2. Moment Method. Equation 8.13 can be reduced from an integro-differential equation to a series of ODES by forming moments of the distribution. The advantage is computational expedience but at the cost of loss of information. Here, the the recent methodology proposed by Diemer and Olsen [**204, 205, 203, 208**] is followed. The moment methodology is a technique developed with a view toward coupling population balances and computational

fluid dynamic simulations or with process flow sheet simulations involving particle processing unit operations. This method allows the calculation of agglomeration and breakage problems by solving a differential equation of moments that is derived from the original particle size distribution (the derivation of this equation can be found in [208]):

$$\frac{d}{dt}\left(ln(m_k)\right) = \hat{\Gamma} \cdot (b_k - 1) \cdot \frac{m_{k+\mu}}{m_k} \cdot \left(\frac{M_1}{\hat{M}_0^\infty}\right)^\mu +$$

$$+ \frac{1}{2} \cdot \hat{\beta} \cdot \sum_{s=0}^{k} \sum_{r=0}^{3} \binom{k}{s} \binom{3}{r} \frac{m_{k-s+\frac{3-r}{3}} \cdot m_{s+\frac{r}{3}}}{m_k} \cdot (M_1) - \qquad (8.15)$$

$$- \hat{\beta} \cdot \sum_{s=0}^{3} \binom{3}{s} \frac{m_{\frac{3-s}{3}} \cdot m_{k+\frac{s}{3}}}{m_k} \cdot (M_1).$$

for $k = 0$

$$\frac{d}{dt}\left(ln(m_0)\right) = \hat{\Gamma} \cdot (b_0 - 1) \cdot \frac{m_\mu}{m_0} \cdot \left(\frac{M_1}{\hat{M}_0^\infty}\right)^\mu - \hat{\beta} \cdot (M_1) \frac{3 \cdot m_{\frac{1}{3}} \cdot m_{\frac{2}{3}} + m_0}{m_0}. \quad (8.16)$$

for $k = 1$

$$\frac{d}{dt}\left(ln(m_1)\right) = 0. \qquad (8.17)$$

for $k \geq 2$

$$\frac{d}{dt}\left(ln(m_k)\right) = \hat{\Gamma} \cdot (b_k - 1) \cdot \frac{m_{k+\mu}}{m_k} \cdot \left(\frac{M_1}{\hat{M}_0^\infty}\right)^\mu +$$

$$+ \hat{\beta} \cdot M_1 \cdot \sum_{s=1}^{k-1} \binom{k}{s} \frac{m_{k-s+1} \cdot m_s + 3 \cdot m_{k-s+\frac{2}{3}} \cdot m_{s+\frac{1}{3}}}{m_k}. \qquad (8.18)$$

The differential equation system is solved using a Runge-Kutta differential equation solver (ode23tb in MATLAB). The missing fractal moments are approximated using a 9th order polynomial closure rule. This technique was first suggested by Frenklach and Harris [215]. The value of any missing moment m_j can be found with:

$$ln(m_j) = ln(\gamma_j) - (j - 1) \cdot ln(m_0). \qquad (8.19)$$

where γ_j is defined as:

$$\gamma_j = m_j \cdot m_0^{j-1}. \qquad (8.20)$$

The missing moments are interpolated with:

$$ln(\gamma_j) = \sum_{k=2}^{9} c_k \cdot \left(j^k - j\right). \qquad (8.21)$$

The coefficients c_k of a kth order polynomial are found by solving:

$$\underline{\underline{A}}^{-1} \cdot ln\left(\underline{\gamma}\right) = \underline{c}. \tag{8.22}$$

where $ln\left(\underline{\gamma}\right)$ is a $k+1$ vector of integer ordered normalized moments, $\underline{c}$ is the $k + 1$ dimensional vector of polynomial coefficients $c_0, c_1..c_k$ and $\underline{\underline{A}}$ is a matrix with $a_{m,k} = m^k$.

Usually the moments alone are not the target of the model. In order to get the full distribution function from the momenta a reconstruction of the distribution from its moments is necessary. This is known as an inversion problem, which is difficult to solve because it is mostly ill posed. Diemer suggests a reconstruction technique of the distribution from the moments by utilizing a nonlinear regression technique [205]. However, this method involves a large amount of parameters leading to ambiguous reconstructed distributions. A different method to solve the inversion problem would be a generalized regularization method for nonlinear ill-posed problems enhanced for nonlinear regularization terms [216].

8.4. Results and Discussion

8.4.1. Model Validation. The model and both methods to solve the population balance are validated to experimental data of Oles [175] and model predictions of Spicer and Pratsinis [178], who employed the same kernels but a sectional method. Good agreement between the calculation and the literature data is observed as shown in appendix A.7.1.

8.4.2. Comparison of the Moment Method with PARSIVAL for Model Suspensions. A parameter study and a comparison between the two simulation methods was done for designated model distributions for a batch grinding process. The results of this comparison are published in *Chemical Engineering Science* [208]. Hence, here only the main findings are summarized.

The initial model distributions were calculated with:

$$q_3\left(x\right) = \frac{1}{x\sigma\sqrt{2\pi}}exp\left(-0.5\left(\frac{ln\left(x\right) - ln\left(x_{50}\right)}{\sigma}\right)^2\right) \tag{8.23}$$

Two initial distributions were investigated, one with $\sigma = 0.4$ and one with $\sigma = 0.8$. The value for $x_{50,3}$ was in both cases equal to $3 \cdot 10^{-5}$ m. The two initial distributions are shown in figure 8.2. Table 8.1 shows the parameters used in the simulation.

The results of the parameter study calculated with the moment method are shown in figure 8.3 - 8.5. The study shows that the parameter c, which influences the shape of the daughter distribution, has little influence. The calculated mean values and the standard deviation of the distribution are the same for a wide and a narrow daughter distribution. Skewness, kurtosis and geometric standard

TABLE 8.1. Parameters used for simulation of figures 8.3 -8.7.

parameter	value	unit
μ	0.41	–
ρ_p	3940	kg/m^3
ρ_f	997	kg/m^3
η	$1.01 \cdot 10^{-3}$	Pa ·s
ϵ	400	W/kg
c_m	0.2	–
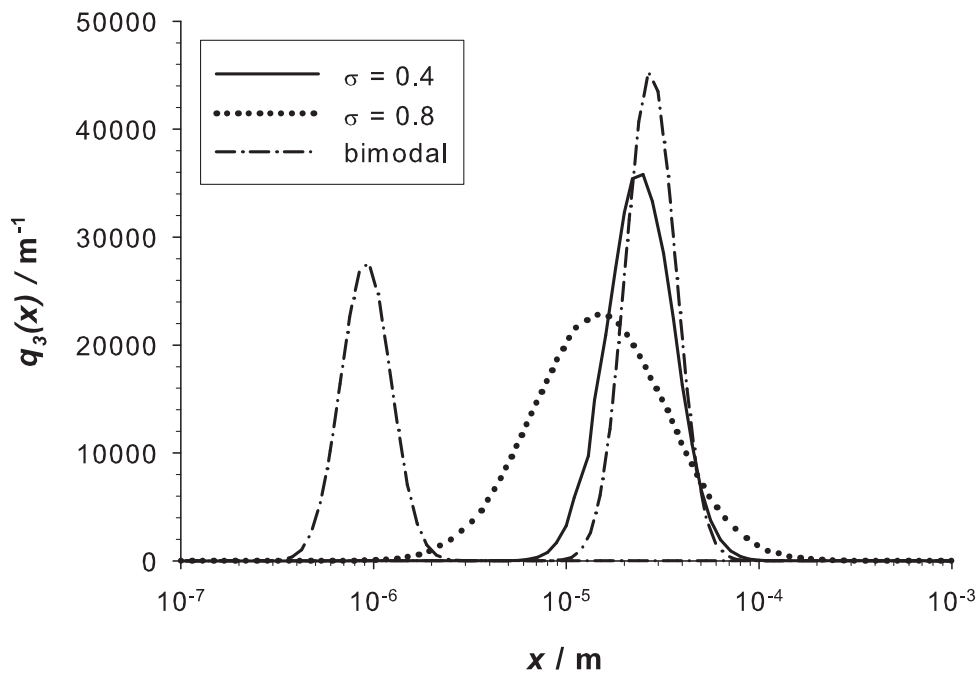
FIGURE 8.2. Initial distributions for the comparison of the two models.

distribution are slightly lower for higher c values. Higher c values correspond to narrower daughter distributions as can be seen in figure 8.1.

The parameter p, which stands for the number of fragments per breakage event, has big influence on the mean values as well as on the shape of the distribution. A higher p value leads to smaller mean values and to a smaller standard deviation while geometric standard deviation, skewness and kurtosis are rising.

The higher the stability factor W the lower the steady state values of the arithmetic number mean and the volume mean. This is reasonable because a higher stability factor inhibits agglomeration and breakage gets more emphasized. The stability factor has no influence on the shape of the final distribution. However, the final distribution is reached later if the stability factor W is larger.

Furthermore, the influence of different initial distributions on the simulation results was investigated. Figure 8.4.2-8.6 show the influence of different initial distributions on the simulation result. The steady state distributions are the same regardless the initial distribution. In addition to the wide and narrow monomodal distributions a bimodal distribution was investigated (see figure 8.2). Also with a bimodal distribution as initial conditions the same steady state values were reached.

A comparison of the two methods in terms of the arithmetic number mean $V_{1,n}$ and the volume mean $V_{1,v}$ particle size in volume units is shown in figure 8.7. Here only results for the wider distribution with $\sigma = 0.8$ are shown. The simulation results for the narrower distribution are showing the same trends. The lines indicate the results calculated with the moment method and the points indicate the results achieved with PARSIVAL. The PARSIVAL method calculates the full distribution $q_3(x)$ at each time step. To compare these results with the results of the moment method the volume density function $q_3(x)$ had to be converted in a volume concentration function $n_3(V)$ and the internal coordinate had to be changed from diameter x to volume V. For the same set of parameters the mean values calculated with the moment method are generally higher. On the other hand the shape of the distributions show better agreement. Especially the results for the geometric standard distribution are in good agreement, while the deviation between the results calculated with the moment method and PARSVAL is large. This is the case because the kurtosis is calculated from higher moments. That are more error afflicted than the lower moments.
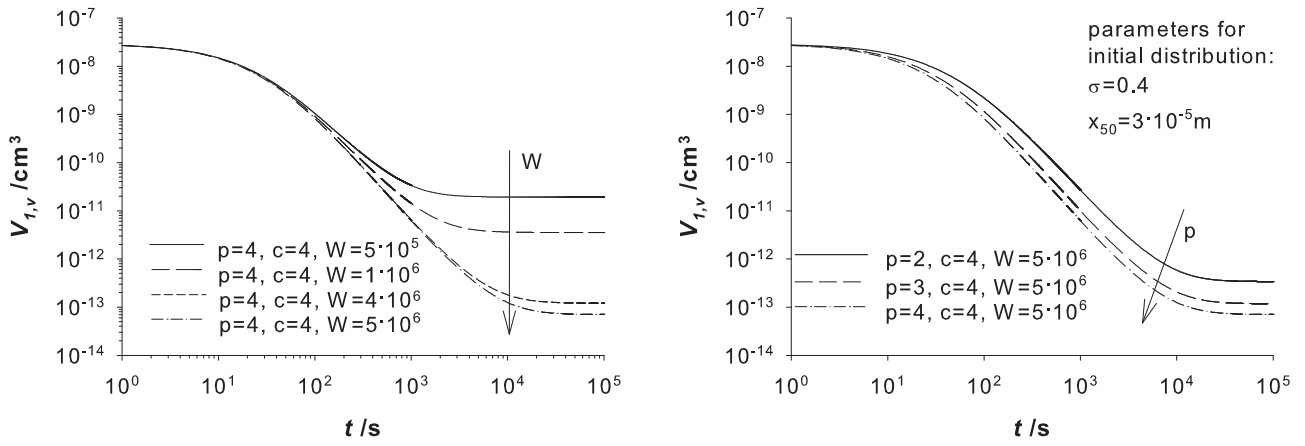
FIGURE 8.3. Volume mean particle size.
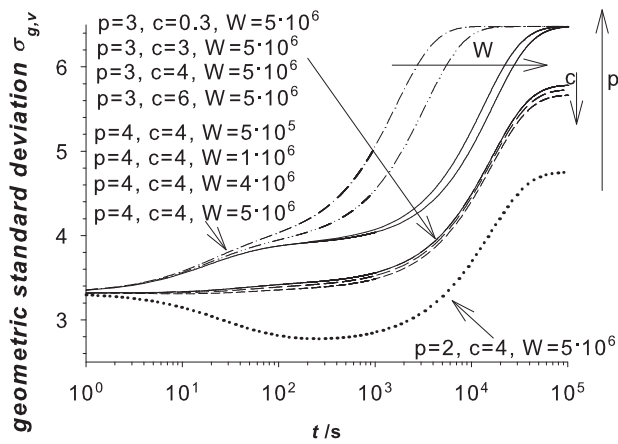
FIGURE 8.4. Geometric standard deviation.
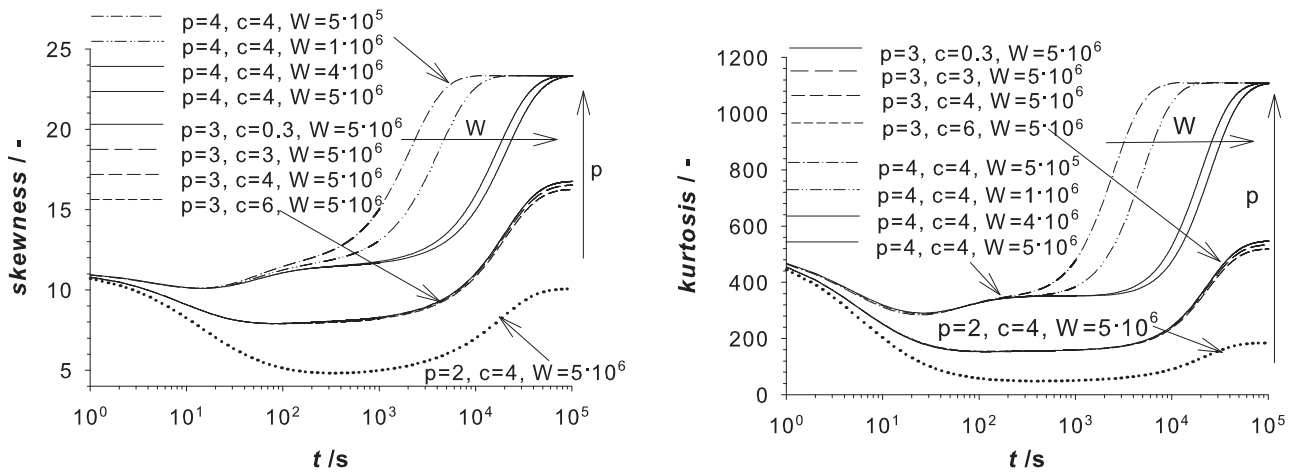
FIGURE 8.5. Skewness and Kurtosis.
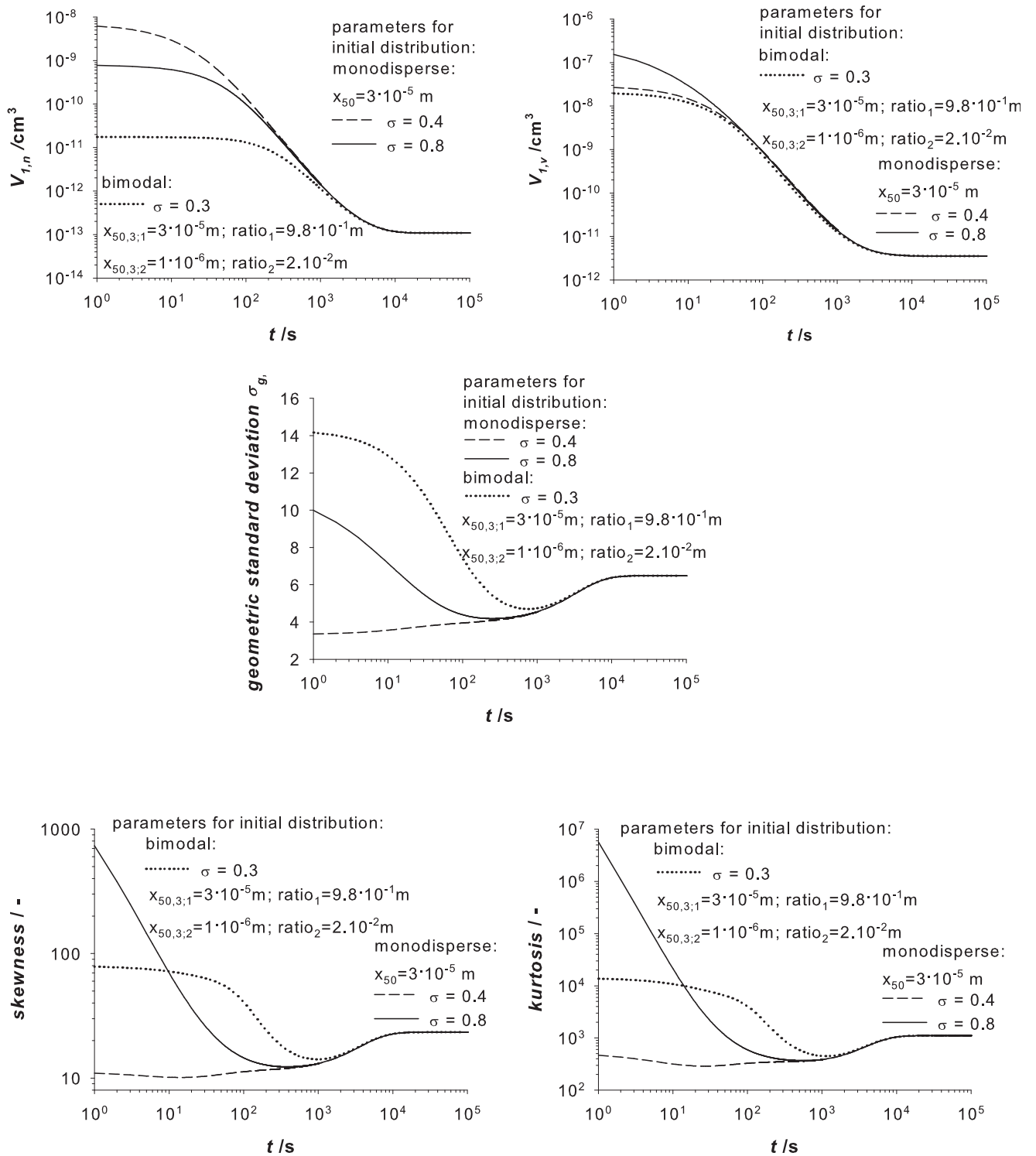
FIGURE 8.6. Influence of different initial distributions (Model parameters: $W = 1 \cdot 10^6$, $p = 4$, $c = 4$).
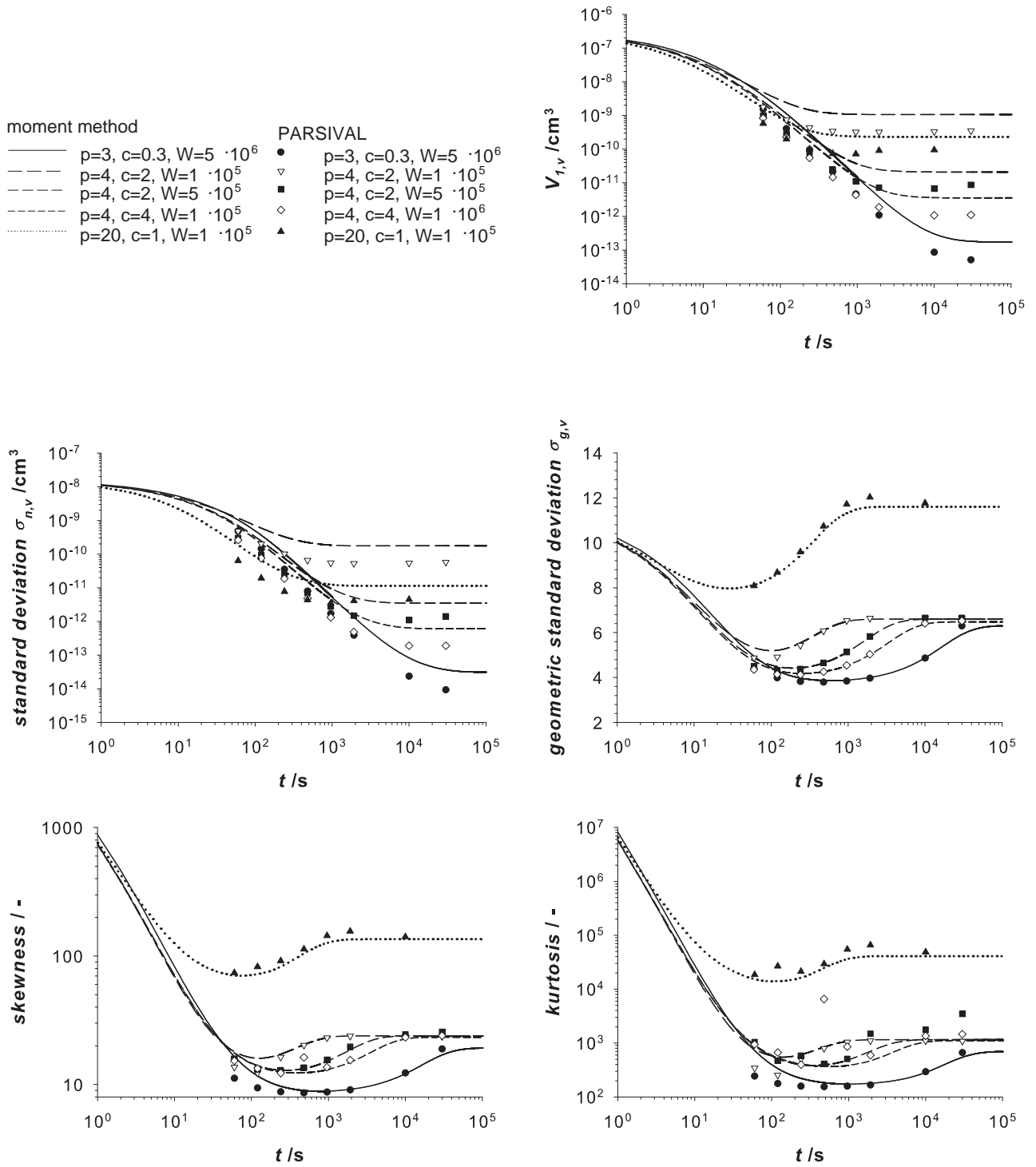
FIGURE 8.7. Comparison of PARSIVAL and the moment method (Parameters of initial distribution: $\sigma = 0.8$, $x_{50} = 3 \cdot 10^5$ m).

8.4.3. Comparison between Batch and Circuit Mode. The batch mode model considered so far was extended to a circuit mode model. In circuit mode breakage and turbulent agglomeration are considered in the mill and Brownian agglomeration in the stirred tank. The flows between the mill and the stirred tank are implemented as plug flows. The parameters used for the calculations are summarized in table 8.2. The initial distribution and the material parameters are for the silica Mikrosil LS500, which is described in section 6.1.1.2. The volume of the mill considered here is equal to the stirred media mill for aqueous suspensions.

TABLE 8.2. Parameters used for simulation.

classification	parameter	value	unit
material	c_m	0.05	–
	ρ_p	2650	kg/m^3
	ρ_f	1000	kg/m^3
	η	0.0014	Pa·s
geometry	V_{mill}	1	l
	V_{tank}	0.6	l
	flow rate	0 - 100	l/h
breakage	p	4	–
	c	30	–
	μ	0.41	–
	$\hat{\Gamma}$	500 - 1000	s^{-1}m$^{3\mu}$
agglomeration	$\bar{E}$	100 - 400	W/kg
	W	$3 \cdot 10^5 - 9 \cdot 10^6$	–

Figure 8.8 shows the influence of the flow rate on the median particle size. The continuous line is the calculated median particle size over the milling time for a batch process. Furthermore, calculations for the circuit mode are presented for the same set of parameters and a variable flow rate. The particle size for the circuit mode process is generally higher than for the batch process, because the particles pass in addition the stirred tank, where only Brownian agglomeration occurs. The higher the flow rate the larger is the particle size. In figure 8.9 the geometric standard deviation of the particle size is shown. The geometric standard deviation is defined as:

$$\sigma_{g,3} = ln\frac{x_{84,3}}{x_{50,3}}. \tag{8.24}$$

The geometric standard deviation increases strongly at the beginning of the milling process and reaches a steady state value, which is for the batch process

0.52. In circuit mode the width of the distribution also increases rapidly. However, the steady state value of the standard deviation is much lower than for the batch mode. The geometric standard deviation depends, according to Stenger [1], on the agglomeration mechanism. He showed that for a turbulent shear mechanism the geometric standard deviation is much larger than for Brownian motion. In the circuit mode breakage, turbulent and Brownian agglomeration are considered while in batch mode only breakage and turbulent shear agglomeration are superposed. Consequently, the Brownian agglomeration in the stirred tank narrows the width of the distribution in circuit mode. However, the flow rate does not influence the geometric standard deviation.
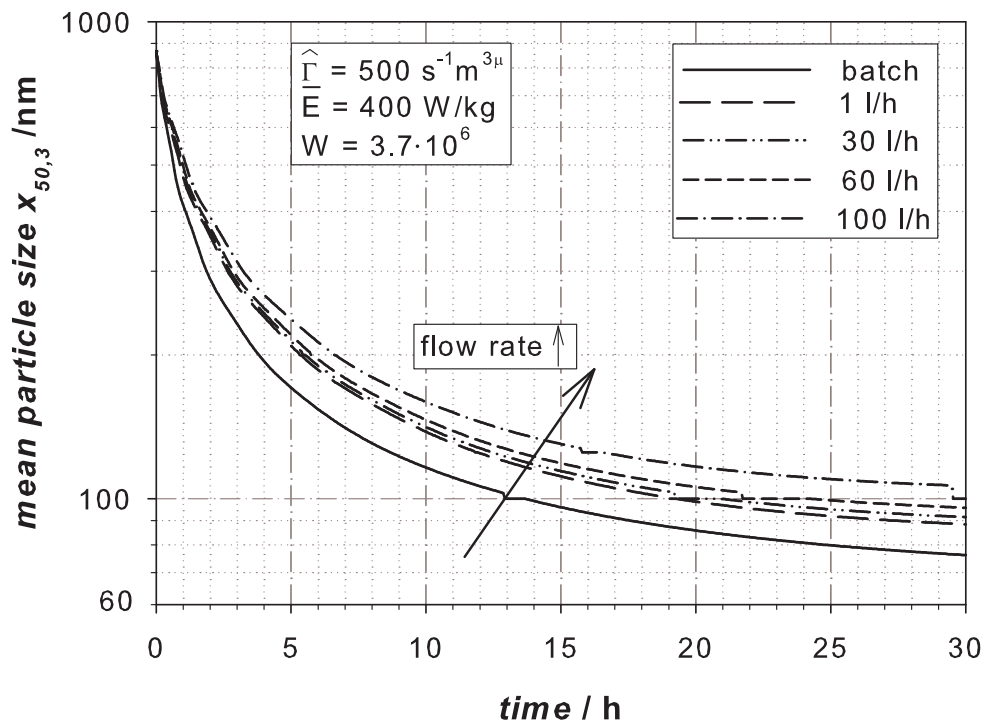
FIGURE 8.8. Influence of the flow rate on the median particle size.

The influence of the mass specific energy input on the median particle size over time is shown in figure 8.10. The lower the mass specific energy input the lower is the archived particle size. This is reasonable, because with lower mass specific energy input the collision kernel β decreases and the breakage side becomes more significant.

Figure 8.11 shows the influence of the size independent part of the breakage kernel on the median particle size. The higher the values of the breakage kernel the smaller are the achieved particle sizes.

Figure 8.12 shows the influence of the stability factor W on the mean particle size. The higher the stability factor W the lower are the steady state values of the mean particle size. This is reasonable because a higher stability factor inhibits agglomeration and breakage gets more emphasized.
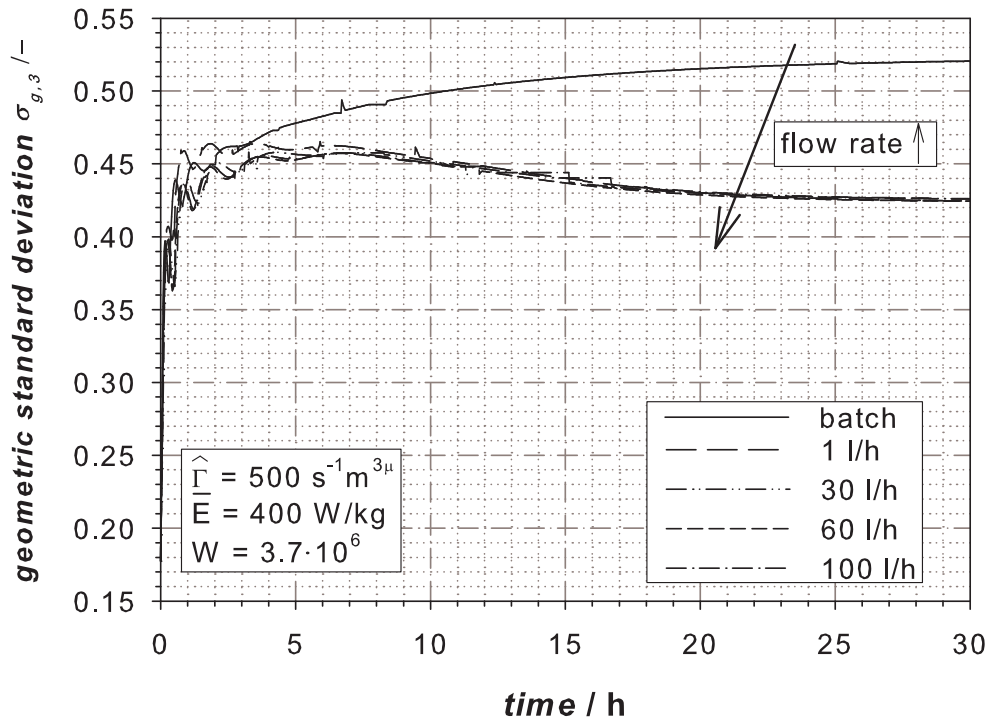
FIGURE 8.9. Influence of the flow rate on the geometric standard deviation.
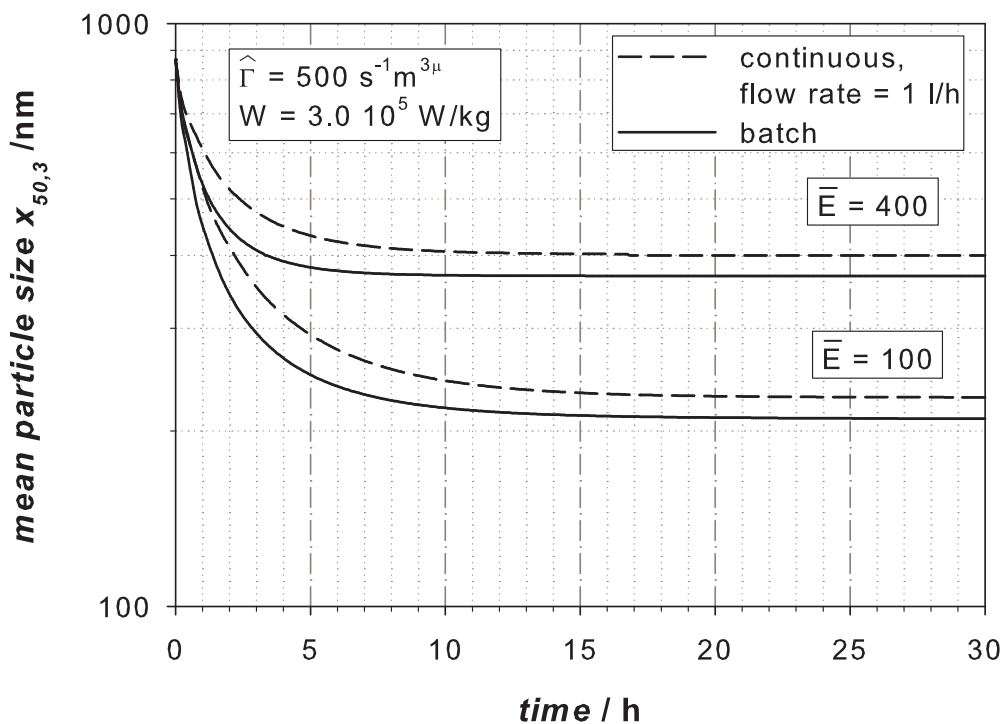
FIGURE 8.10. Comparison of the continuous and the circuit mode - influence of the mass specific energy input.
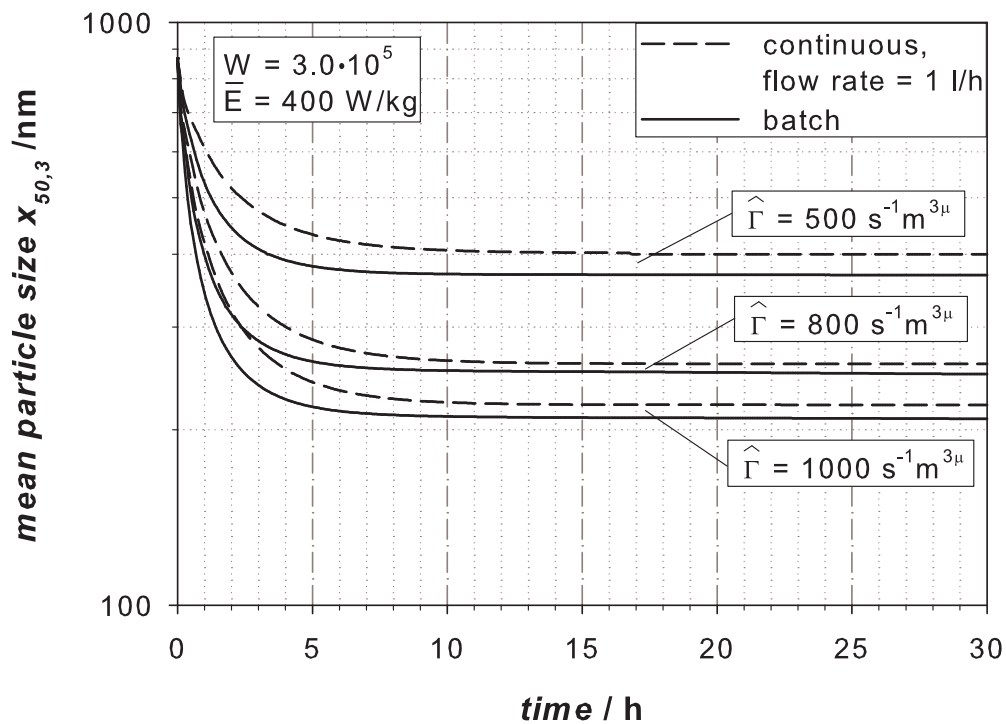
FIGURE 8.11. Comparison of the continuous and the circuit mode - influence of the size independent part of the breakage kernel.
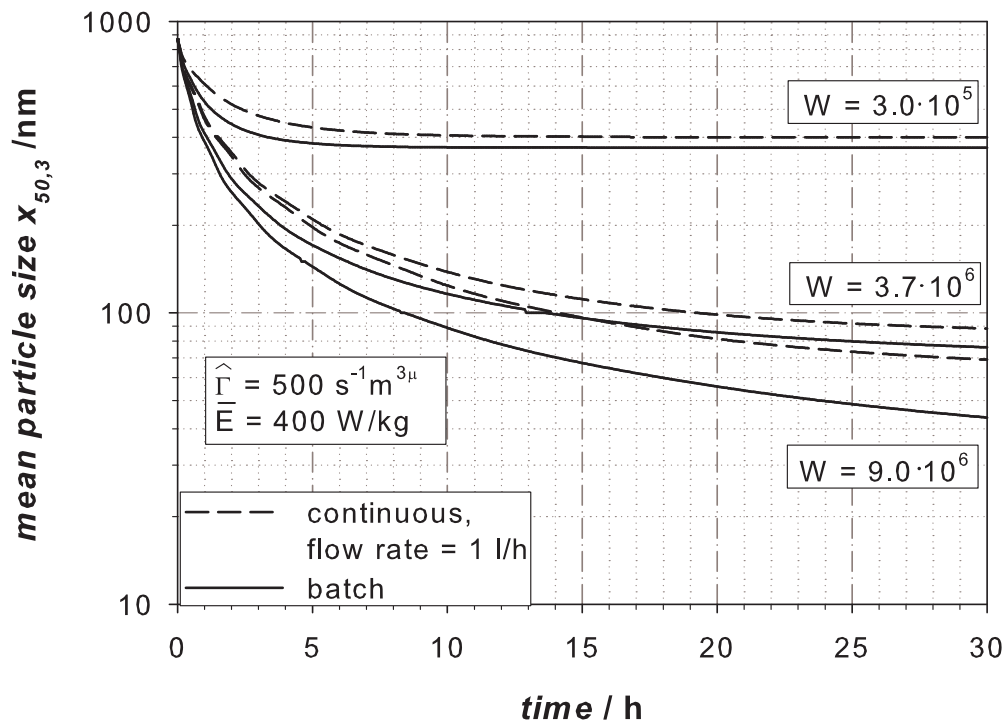
FIGURE 8.12. Comparison of the continuous and the circuit mode - influence of the stability factor.

8.4.4. Comparison of Simulation Results with Experimental Data.
In this chapter a comparison between simulation results that are derived with
the software PARSIVAL with experimental data is drawn. The experimental
results were already presented and discussed in chapter 7.2.2. For the simulation
the circuit mode model was used. The parameters used for the simulation are
summarized in table 8.3.

TABLE 8.3. Parameters used for simulation of experimental data.

classification	parameter	SiO$_2$	Ludox
material	ρ_p	2650 kg/m^3	2100 kg/m^3
	ρ_f	1000 kg/m^3	1000 kg/m^3
	c$_m$	0.05	0.05
geometry	V$_{mill}$	1 l	1 l
	V$_{tank}$	0.6 l	0.6 l
breakage	p	4	4
	c	30	30
	μ	0.41	0.41
	$\hat{\Gamma}$	500 s^{-1}m$^{3\mu}$	700 s^{-1} m$^{3\mu}$
flow rate		30 l/h	30 l/h

In figure 8.13 the hydrodynamic diameter is plotted over the milling time
for a 5 wt% Ludox suspension with 0.6 M KNO$_3$ under perikinetic and under
milling conditions. The experimental data can be modeled with the population
balance model in circuit mode very well. In figure 8.13 it can be see that the
agglomeration is accelerated until the steady state between agglomeration and
breakage is reached. This steady state is strongly dependent on the energy
input. The energy input influences the mass specific energy dissipation as well
as the breakage rate. At a tip speed of 4 m/s and 8 m/s a mass specific
power input $\bar{E}$ of 400 W/kg and 150 W/kg was determined with a torque
meter, respectively. By using these values in the population balance excellent
agreement between the simulation results and the experimental data was found,
if the stability factor and the size independent part of the breakage rate kernel
were kept constant.

In the next figure the influence of the stability conditions on the milling result
is shown by varying the salt concentration, which influences the stability factor.
The size independent part of the breakage rate and the mass specific power
input was kept constant in the calculations, while the stability factor was varied
to fit the data. By doing so good agreement between simulation results and
experimental data was observed. However, differences between the numerically
derived stability factor W and W-factors derived from DLVO theory could be
observed for several reasons. The main reason is the assumption that the Stern-
potential is equal to the ζ-potential. Small fluctuations in the measured value of
the the ζ-potential of about ± 2 mV lead to huge errors in the calculation of the
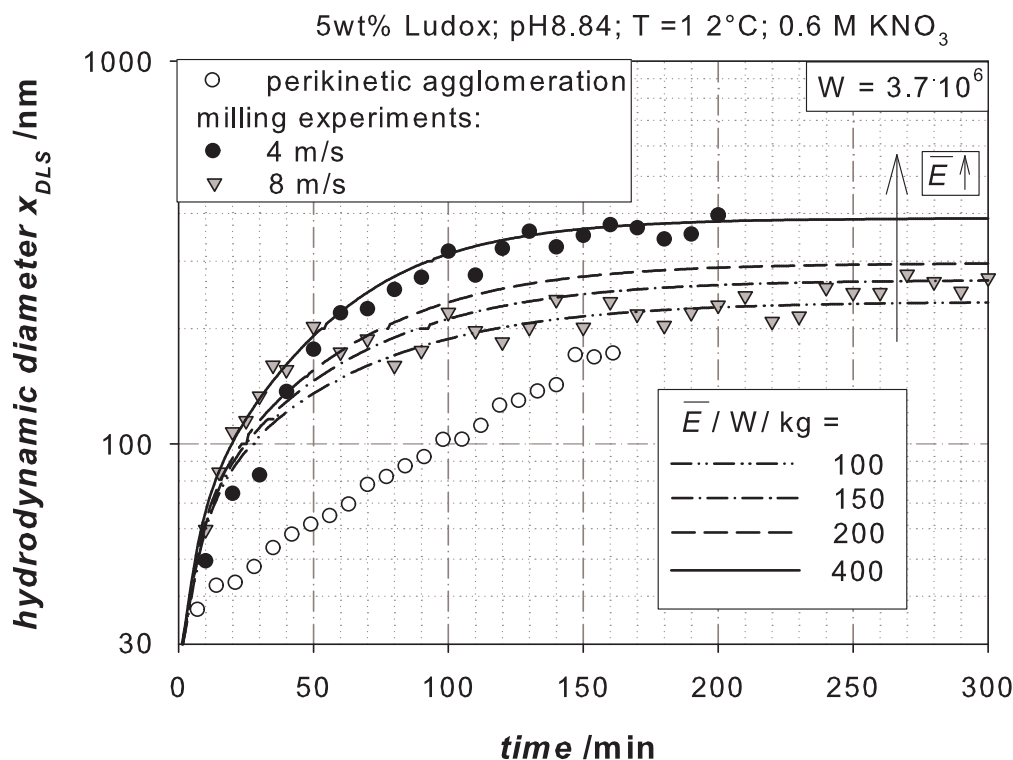
FIGURE 8.13. Comparison of the median particle size from numerical and experimental results.

stability factor. Furthermore, uncertainties in the determination in the value for the Hamaker constant especially for high salt concentrations lead to errors. Moreover the influences of particle shape and the different particle sizes are not incorporated in the calculation of the stability factor. For the correct description of the agglomeration under turbulent conditions also hydrodynamic interactions have to be accounted for. Due to these uncertainties only qualitative consistency in the stability factors could be observed.

In figure 8.15 the experimental data, which were already presented and discussed in chapter 7.2.2 are simulated with the population balance model. The experimental results can be modeled very well. All parameters in the population balance were kept constant and the size independent part of the breakage rate kernel $\hat{\Gamma}$ was used to fit the data. In the salt destabilized suspensions $\hat{\Gamma}$ was found to be 700 $s^{-1}m^{3\mu}$ for the case of Ludox particles. By milling large SiO_2 particles a lower value of $\hat{\Gamma}$ namely 500 $s^{-1}m^{3\mu}$ was used to fit the data. This is reasonable because by milling Ludox only agglomerates were deagglomerated while by milling large SiO_2 particles real breakage of solid particles occurs. This means the breakage rate is much lower as by dispersing agglomerates.
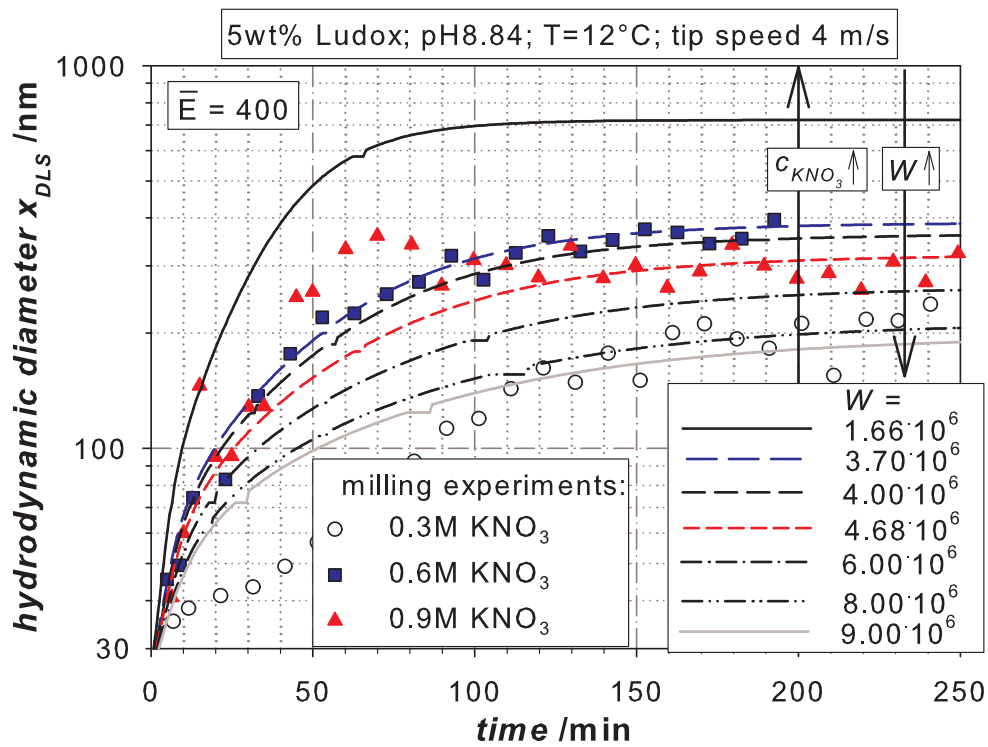
FIGURE 8.14. Comparison of the median particle size from numerical and experimental results.
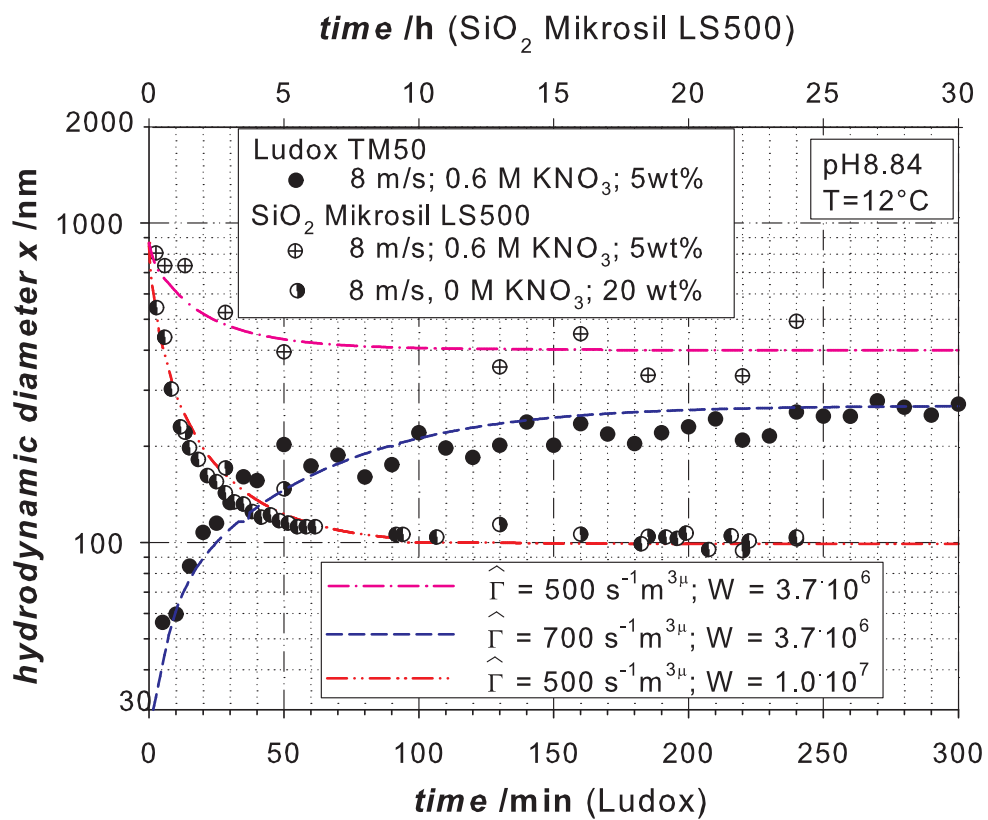
FIGURE 8.15. Comparison of the median particle size from numerical and experimental results.

Degradation of Polymers in Stirred Media Mills

The study of degradation of polymers is an important aspect of polymer science and engineering, with industrial applications such as plastic recycling and fundamental applications like characterization of polymer structures [217, 218]. The degradation of dispersant during milling can have an effect on the dispersion stability. Impacts between particles and media can affect the polymer structure and possibly lead to desorption from the particle surface [219]. However, besides the negative effects as the deterioration of the polymer and destabilization of the suspension the mechanical degradation of polymer chains can be used to determine the stress a particle sees in a stirred media mill. This will be shown in this chapter.

9.1. Theoretical Background

Stress induced scission of polymers in solution has been well studied in the last 50 years. It is well known that polymer chains can be severed by purely mechanical forces encountered in high shear situations. In general, scission of macromolecules in solution is possible under extremely high shear rates up to $10^{10} s^{-1}$ [44]. Some authors [220] believe that simple laminar shear flow is not adequate to induce scission of the polymer chains and that degradation is only encountered when the flow contains an appreciable elongational component, commonly arising as result of flow instabilities or turbulence. The molecular degradation in turbulent flow is affected by a variety of factors, including the molecular weight distribution of the polymer, temperature, polymer concentration, solubility of the polymer in the solvent, turbulent intensity and flow geometry. Several theories have postulated that scission is caused by extremely large extensions of polymer chains. Isolated flexible-chain molecules are stretched out so well in good solvent that the larger molecules receives strong enough shear stress to break main chains into shorter segments. In an good solvent the rate of scission of polymer chains is higher and the final chain length is shorter than in a poor solvent, because the polymer chains are more stretched out and thus have larger intrinsic viscosities in good solvents. At low concentrations the interactions between the polymer chains are smaller and the rate of scission is higher. It has been found theoretically and experimentally that chain scission occurs around the chain midpoint for polymers degradated in extensional flows [44, 221, 222]. This indicates that macromolecules are highly stretched out when they break. At a critical strain rate $\dot{\epsilon}_c$ the molecule chain is expected to

undergo a coil-stretch transition. This critical strain rate is, according to Odell [220], related to the longest relaxation time of the molecule τ_r as:

$$\dot{\epsilon}_c \cdot \tau_r \approx 1. \tag{9.1}$$

As the strain rate is increased beyond $\dot{\epsilon}_c$, the already stretched out chains become increasingly stressed until they rupture. Odell and Keller [223] found that no critical rapture occurs until a critical fracture strain rate $\dot{\epsilon}_f$ is reached ($\dot{\epsilon}_f > \dot{\epsilon}_c$).

Hydrodynamic theory suggests that the critical fracture rate is proportional to the inverse of polymer weight M_n:

$$\dot{\epsilon}_f \propto \frac{1}{M_n^b}. \tag{9.2}$$

where $b = 2$ for steady extensional flow and $b \approx 1$ for transient extensional flow [44]. Midpoint scission was also found in experiments with shear degradation of polymers by turbulent flows [222], [224]. A couple of different devices have been investigated, for example high-speed stirring [225], capillary flow at very high flow rates and high-shear concentric cylinder viscometers [226, 224]. Karis et al. [44] investigated chain scission in a stirred media mill.

9.2. Experimental Part

9.2.1. Material. Poly(ethylene oxide) (PEO) is a simple and representative linear polymer which dissolves not only in a large number of organic solvents but also in water. Polymer grades with different molecular weights were purchased from Dow chemicals. The different polymer grades and the molecular weights denoted by the company are listed in table 9.1. These molecular weights are based on rheological measurements and are not comparable with molecular weights obtained from light scattering and gel permeation chromatography. The table further shows the mean molecular weights for the different polymer grades measured with GPC. The samples have been dissolved in purified water at room temperature. This was done by gently stirring over night. The milling experiments have been accomplished at a polymer concentration of 0.1 wt%.

TABLE 9.1. PEO from Dow chemicals.

PEO grade	molecular weight (Dow) /g/mol	molecular weight (GPC) /g/mol
WSR 301	4 000 000	1 000 000
Ultrafloc 309	8 000 000	2 000 000

9.2.2. Milling Experiments. The milling experiments were carried out at an annular gap mill at DuPont. The volumetric capacity of the mill chamber is 0.21 l. The fluid was recirculated over a stirred vessel with a flow rate of 250 g/min. This is leading to a measured mean single pass residence time

of 0.44 min. The rotor of the annular gap mill is made out of nylon. The annular gap mill has a gap width of 5 mm. The refiner gap was set to 0.25 mm. The milling media loading in these experiments was 80%. Yttrium stabilized zirconia milling beads with an average size of 0.6 - 0.9 mm were used. The mill jacket was cooled with water to 25 °C to prevent frictional heating. In case of the single pass experiments the feed was pumped with the same flow rate of 250 g/min from a 8 l bucket in the mill. The outlet tube was connected to a waste bucket. Three different mill speeds were realized 4, 6 and 8 m/s. Samples were drawn 3 min after the mill speed was adjusted.

9.2.3. Characterization of Products. Gel permeation chromatography (GPC) was used to determine the molecular weight distribution of the polymer in solution before and after being exposed to the turbulent flow field in the stirred media mill.

9.2.4. Results and Discussion. Figure 9.1 shows the influence of the milling time on the molecular weight distribution of PEO. The feed distribution has a mean molecular weight of 10^6 g/mol. After stressing the polymer chains in a single pass experiment with a tip speed of 8 m/s the polymer chains are broken in half. If the polymer chains are further stressed in the mill with the same tip speed no further scission of the polymers is observed. Even after a milling time of 40 min the mean molar mass of the polymer chains is 500 000 g/mol, which is half of the mean molar mass of the feed polymer chains. This means the shear stress in the mill is not sufficient to break chains smaller than 500 000 g/mol. The fluctuations in the date at a molar mass between 10^4 and 10^5 g/mol can be addressed to measurement errors. There is no trend in the data for the fines. The lowest amount of fines was found for the single pass experiment and the highest amount of fines for the 10 nm experiment. The other data are fluctuating between these extremes. With equation 9.2 and the assumption that a steady extensional flow exists in the mill a critical fracture strain rate $\dot{\epsilon}_f$ can be estimated. The proportional constant is according to Odell et al. [220] $1.832 \cdot 10^{18} \frac{g^b}{mol^b} s$. In table 9.2 the estimated critical fracture strain rates are listed.

TABLE 9.2. Estimated critical strain rates.

molecular weight /g/mol	estimated critical strain $\dot{\epsilon}_f$ /s^{-1}
2 000 000	$4.58 \cdot 10^5$
1 000 000	$1.83 \cdot 10^6$
500 000	$7.33 \cdot 10^6$

Consequently, the maximal critical strain rate in the mill is between $1.83 \cdot 10^6$ and $7.33 \cdot 10^6$ s^{-1}. Figure 9.2 shows that this maximal critical fracture rate is also reached at a tip speed of 6 m/s and 4 m/s. However, a single pass is not sufficient to break all polymer chains in half at a tip speed of 4 m/s. Consequently, the

mean of the distribution lays between the mean of the feed distribution and the completely broken polymers which were reached at tip speeds of 6 and 8 m/s.
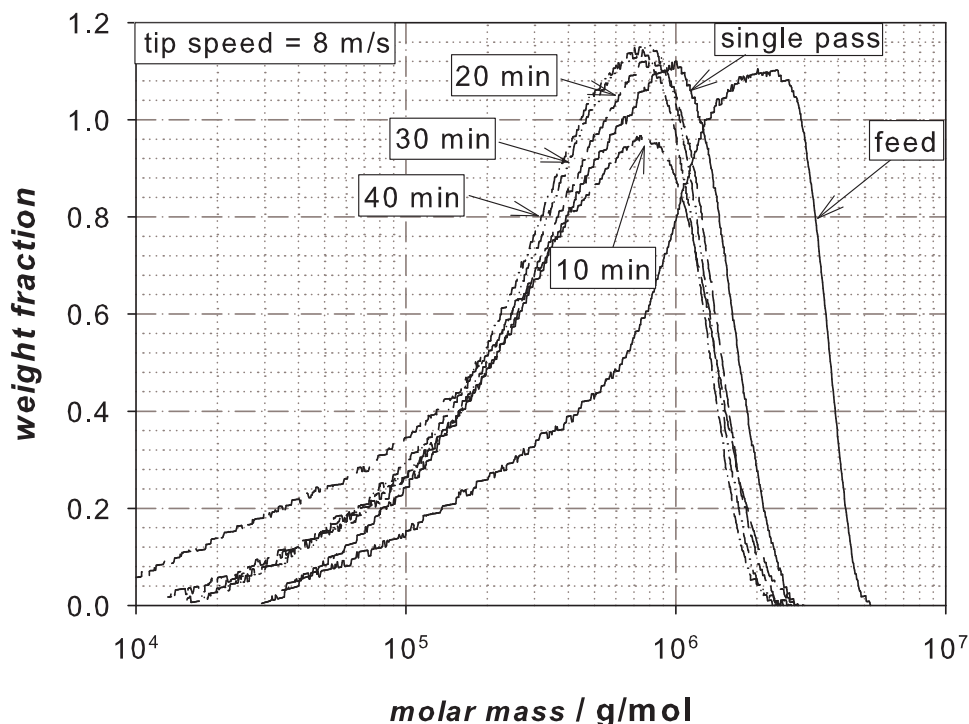
FIGURE 9.1. Mechanical degradation of PEO WSR 301 in a stirred media mill - influence of the milling time.

In figure 9.3 mechanical degradation results of PEO with a molecular weight of 2 000 000 g/mol and the comparison with theoretical results from the population balance model are shown. In the upper left corner of the figure the experimental results before and after milling are presented. The polymer chains are twice as large as the polymer chains used before. After milling the mean molar mass of the polymer is in the order of 500 0000 g/mol. Thus the polymer breaks in average into four pieces with the same final size.

Figure 9.3 also shows model predictions of the mechanical degradation and its comparison to the experimental results. For the calculation the moment method was used as described in chapter 8.3.2. Because in the degradation experiments only breakage occurs the agglomeration terms were neglected and the internal coordinate was changed from volume to molecular mass M_n. Furthermore, a dimensionless time was specified such that:

$$d\tau = \frac{\hat{\Gamma} \cdot (p-1)}{\rho^{\mu}} \cdot \left(M_1^0\right)^{\mu} \cdot dt. \tag{9.3}$$

The final differential system which has to be solved reads as follows:

$$\frac{dln\,(m_k)}{d\tau} = \frac{b_k - 1}{p - 1} \cdot m_{k+\mu}. \tag{9.4}$$
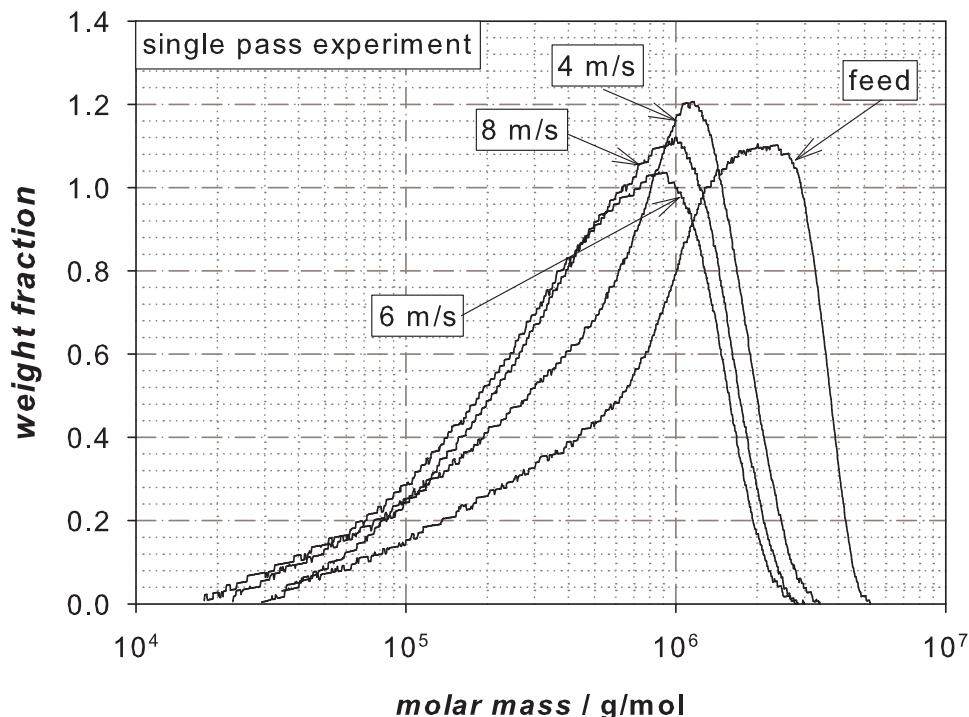
FIGURE 9.2. Mechanical degradation of PEO WSR 301 in a stirred media mill - influence of the tip speed.

All parameters used in the model could be determined experimentally only the dimensionless time was used as fit parameter. For midpoint scission the molecular chain breaks into half. The parameter p, which stands for the number of fragments per breakage event, is for binary breakage equal to 2. Because the pieces broken in half are in this experiment large enough to break again the parameter p used for calculation is equal to 4. In the case of midpoint scission the molecule breaks into daughter molecules of equal size. From this it follows that the daughter distribution is a sharp peaked function. A sharp peak is modeled with high values of c (see figure 8.1). However, it was noticed that the parameter c has only little influence on the result [208]. The power law breakage rate kernel order μ is related to the intrinsic viscosity by:

$$\Gamma(M_n) = \hat{\Gamma} \cdot M_n^{\mu} = [\eta]. \tag{9.5}$$

where M_r is the relative molecular mass. The intrinsic viscosity can be calculated with the Mark-Houwink-Sakurada equation for PEO in water:

$$[\eta] = 5.2 \cdot 10^{-4} \cdot M_n^{0.665} \frac{m^3}{kg}. \tag{9.6}$$

As it can be seen in figure 9.3 the model prediction agree with the experimental results quite well for mean molecular mass, standard deviation, variance and skewness (for definition of these statistical values see appendix A.8). The graph for the kurtosis of the distribution shows that a power law parameter of the order of 0.75 fits the data better. However, the skewness and kurtosis are

calculated from higher moments and are more error afflicted. In addition to this the residence time in the mill smears the breakage results. This can also be a reason why the theoretical predictions differ from the measurements.

The degradation experiments with straight PEO polymer chains show that the chains must be larger than 500 000 g/mol to be broken in the mill. This is much larger than the molecular weight of DAPRAL (50 000 g/mol), which was used for steric stabilization in the milling experiments. Thus, degradation of the polymer used for stabilization is very unlikely. However, degradation experiments with DAPRAL should be performed in future to confirm this assumption.
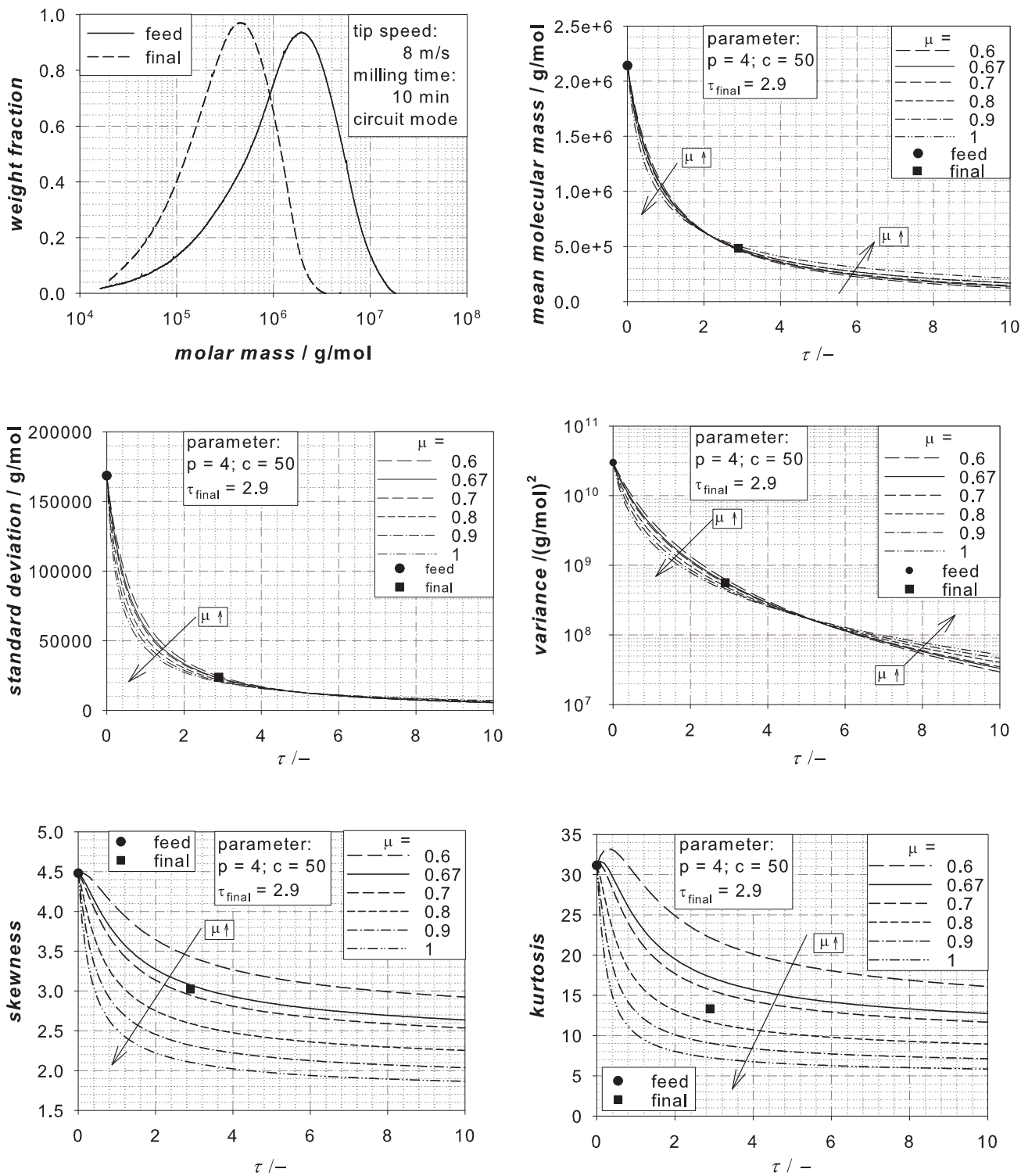
FIGURE 9.3. Mechanical degradation of PEO Ultrafloc 309 in a stirred media mill and comparison of the experimental results with the population balance model (tip speed 8 m/s, milling time 10 min, circuit mode).

Conclusion and Outlook

10.1. Conclusion

Nanotechnology applications in the pharmaceutical, materials, and chemical industries has renewed interest in the use of wet grinding in stirred media mills for the production of nanoparticles with controlled microstructure. However, challenges arise in the production of sub-micron particles that are, in part, due to colloidal surface forces influencing slurry stability and rheology.

In this work experiments were performed on a well characterized model system of monodisperse primary nanoparticles that are salt destabilized and aggregated under various milling conditions. Perikinetic and orthokinetic aggregation rates were measured, with the latter in a laminar shear flow as well as in a stirred media mill, to examine the effects of colloidal stability and flow on the aggregation process. The agglomeration kinetics are measured using dynamic light scattering (DLS) as a function of electrolyte concentrations. Further information on the agglomeration process and the structure of the agglomerates were also obtained from small angle neutron scattering (SANS) and rheo-optical light scattering (ROA) experiments both at rest and under flow. The primary findings of this study are that the aggregation rate under flow (orthokinetic rate) is much higher than perikinetic rate at comparable physicochemical conditions, and the aggregate structure obtained under flow is much denser and more compact than the reaction limited cluster cluster aggregation (RLCCA) structures observed under perikinetic conditions. Samples that undergo perikinetic aggregation followed by shearing show evidence of densification. The fractal dimension evolves from the perikinetic value towards the value obtained under orthokinetic aggregation. These results have important consequences for the production of nanoparticles by stirred media milling by showing that shearing can lead to enhanced aggregation rates and dense aggregate formation. This work also suggests mechanisms to control particle aggregate topology through media milling. Milling studies of Ludox TM50 particles confirmed that agglomeration plays a significant role in stirred media mills. The steady state between agglomeration and deagglomeration depends on agglomeration kinetics and the shear stress provided by the stirred media mill. With increasing stirrer tip speed the agglomeration kinetics is accelerated and the particle size is increasing faster. However, the steady state size between agglomeration and dispersing is smaller for higher tip speeds because the steady state is shifted in favor of breakage. Another handle to control the steady state particle size is the salt concentration. With increasing salt concentration the median steady

state particle size is larger and the agglomeration kinetics is faster. Furthermore, milling experiments with large SiO_2 particles were performed to confirm that this steady state can also be reached by real breakage of large particles. It could be shown that the steady state particle size is independent of the feed particle size and can be reached from small as well as from large particle sizes.

Because of the high industrial demand for nanoparticles in organic media this work was extended to non-aqueous systems. The state and the properties of particle surfaces in the liquid phase are discussed. Based on this, possibilities to influence the interparticle interactions and with it the stabilization of the particles are described. Milling studies with electrostatic and steric stabilization mechanisms in organic solvents were conducted and compared to the milling behavior in water.

For steric stabilization a co-block polymer with lipophilic and lipophobic side chains was chosen, which can be adsorbed on oxide surfaces from various solvents of different polarity in various conformations. Adsorption isotherm measurements showed that a complete coverage of the particle surface with polymer chains is reached at a dimensionless concentration of 0.02 - 0.025 independent of the kind of the used solvent. However, the amount of adsorbed polymer depends on the quality of the solvent. A hydroxide layer around alumina particles has no influence on the amount of adsorbed polymer. The layer thickness of the polymer on the particles was measured with rheological methods. A layer thickness of 42 nm in water and 53 nm in ethanol was estimated with rheological measurements of the shift factor as well as with frequency measurements. These results were additionally verified with gel permeation chromatography measurements. Furthermore, the frequency measurements may also serve as a first estimate of the maximal achievable mass concentration of the particles in the suspension, because the crossing-point of the elastic and the viscous modulus in dependence of the weight-fraction of particles can be taken as an indication of the volume fraction at which the polymer chains just overlap. Thus, the position of the crossing-point determines the economics of the process.

Electrostatic stabilization requires a sufficiently high surface charge leading to a steeply decaying surface potential. These conditions can be met by solvents of medium dielectric constant (i.e. values larger than about 15-20), e.g. alcohols. In these media the particles may carry a high surface charge and the solubility of salts will be sufficiently low to enable a high repulsive barrier. It is shown that stable suspensions with high ζ-potentials can be achieved for alumina in ethanol with elecrostatic stabilization. Alumina particles in ethanol develop a high positive surface charge. The alumina surface acts as a Lewis base, an electron donor. When salt is added to the suspension the concentration of the ethoxide ions in the bulk solvent is reduced due to reaction with the added ions, leading to a rise in surface charge and in the ζ-potential. Simultaneously there is an adsorption of negative salt ions on the surface by substitution of the salt ions for the ethoxide ions at the surface. The surface charge becomes now

a function of the equilibrium dissolution of the salt ions from the surface. The magnitude of the ζ-potential depends of the kind of the added ions, namely their charge density, polarizability, oxidation state, electro negativity and the structure of the solvent cover around the ion.

Milling experiments with steric stabilization in organic solvents produced particle sizes comparable with particle sizes achieved by milling in the aqueous phase at pH3. For both experiments a final particle size of $x_{1,2} = 60$ nm measured by DLS was reached after 24 h (120 000 kJ/kg). In contrast to this the particle size increases up to 400 nm for the electrostatic stabilized suspensions at higher energy inputs. The media wear has a negative influence on the stability of the suspension since the ionic strengths in organic solvents are much lower than in water. However, the particle size determined by BET analysis decreases for electrostatically stabilized suspensions continuously down to 25 nm. The continuous decrease of the particle size measured by BET indicates an increasing fines of primary particles. The slope of the curve for electrostatic stabilized suspensions measured with BET is steeper than the corresponding BET curve for sterically stabilized suspensions. The reason for this could be that the polymer layer around the particles adsorbs part of the grinding energy during the impact of two grinding beads and cushions the comminution. The final particle size for the sterically stabilized suspension is 40 nm measured with BET. The slopes of the curves determined with BET and dynamic light scattering are equal for the sterically stabilized suspension. The narrow difference between the particle size measured with BET and dynamic light scattering shows that the particles are dispersed and sufficiently stabilized.

An important question is whether the mechano-chemical activation which was observed in aqueous media is crucial to obtain nanoparticles. Differential Scanning Calorimetry (DSC), thermogravimetric measurements, X-ray diffraction (XRD) as well as FT-IR measurements showed no mechano-chemical changes during milling of alumina particles in ethanol and toluene. However, during milling with electrostatic stabilization in ethanol physical adsorbed solvent could be detected. In the aqueous phase the stabilization mechanism has no influence on the amount of hydroxide phase. A protecting polymer cover around the particles does not prohibit the mechano-chemical changes.

Milling experiments with hematite show that the obtained median particle sizes are strongly dependent on the stability conditions. The isoelectric point of the used hematite was found to be at pH3. In order to stabilize the suspension at a low pH value Fe^{3+} ions were specifically adsorbed to the hematite surface. By doing so a clear shift of the iep was observed and a sufficiently high ζ-potential was reached. In the milling experiments at pH3 a median particle size $x_{1,2}$ of 60 nm could be determined by means of dynamic light scattering. This result is clearly smaller than the reached median particle size at pH7 (136 nm) and pH10 (85 Nm). In all milling experiments in aqueous phase as well as in

organic solvents the hematite structure remained unchanged and no mechano-
chemical changes could be detected with XRD. However, a color change of
the suspensions during milling was observed in all experiments. This color
change appeared in particular during milling in ethanol and in the aqueous
phase at pH3. The original color of the hematite suspension was bright red.
During milling in ethanol and in the aqueous phase at pH3 the suspensions
changed their color to deep black. This color change could be attributed to the
decreasing particle size during the experiment.

Furthermore, degradation experiments with straight PEO polymer chains
were performed. In these experiments it was observed that midpoint scission of
the polymer chains occurs. The physics of stressed induced scission of polymers
in solution was successfully used to determine the critical fracture strain rate
in the mill. The mechanical degradation results could be described with a pop-
ulation balance model. All parameters used in the model could be determined
experimentally only the dimensionless time was used as fit parameter.

A simulation of the nanomilling process in stirred media mills by a popu-
lation balance model is completing this work. The modeling includes a super-
position of grinding and agglomeration. It could be shown that the calculated
final mean values and the standard deviation of the distribution are the same
for both a wide and a narrow daughter distribution. Skewness, kurtosis and
geometric standard distribution are slightly lower for higher narrower daughter
distributions. The parameter p, which stands for the number of fragments per
breakage event, has a large influence on the mean values as well as on the shape
of the distribution. A higher p value leads to smaller mean values and to a
smaller standard deviation while geometric standard deviation, skewness and
kurtosis all increase. The higher the stability factor W the lower the steady
state values of the arithmetic number mean and the volume mean. This is rea-
sonable because a higher stability factor inhibits agglomeration and breakage
is more dominant. The stability factor has no influence on the shape of the fi-
nal distribution. However, the final distribution is reached later if the stability
factor W is larger.

Furthermore, the influence of different initial distributions on the simulation
results was investigated. It could be shown, that the steady state distributions
are the same regardless the initial distribution. In addition to a wide and
narrow monomodal distribution a bimodal distribution was investigated. Also
with a bimodal distribution as initial conditions the same steady state values
were reached.

A comparison of the two different methods to solve the population balance
showed reasonable agreement between them. Furthermore, the batch mode
model was extended to a circuit model, which includes breakage and turbulent
agglomeration in the mill and Brownian agglomeration in the stirred tank.
Numerically derived results from the population balance model that accounts

for agglomeration and breakage in circuit mode are in reasonable agreement with experimental observations.

10.2. Outlook

Although it could be shown that nano-particles can be produced in stirred media mills in organic media with steric stabilization, were are still open questions. For example the effect of different chain lengths of the polymers on the stability and breakage behavior should be studied. Furthermore, degradation experiments with the polymer DAPRAL, which was used in this work, should be performed. In this study not only the effect of different chain length of the polymers but also the effect of polymer branching should be included. Unclear is further the possibility of desorption of polymer chains due to the high shear forces in the mill. Moreover, little is known on the adsorption kinetics of the polymers. For the selection of polymers, which is still carried out mostly empirically, it is desirable to know the adsorption kinetics. It has to be assured that the stabilization process of newly formed particles is fast enough to certainly stabilize the suspension.

In this work only polar organic solvents with medium electric constants were investigated. This work should be extended to non-polar solvents. Furthermore, nano-milling of organic particles should be investigated, because a widespread knowledge about the comminution of organic solids to the nanometer size range is missing in the existing research literature. Eidelman et al. [227] showed that a stable colloidal suspension of nanodiamond particles can be achieved by stirred media milling. However, the mean core particle size of 4 nm they could achieve is mostly an effect of deagglomeration rather than real breakage.

Besides the investigated parameters the temperature plays a significant role on the agglomeration and grinding process in stirred media mills. With decreasing temperature the breakage rate should be increased due to embrittlement of the particles. Furthermore, the stability of the particles should be increased with decreasing temperature. The effect of temperature on the milling process has been disregarded in the past and milling experiments were only performed at a fixed temperature. A detailed study of the temperature could show if the efficiency of the milling process can be increased by controlling this parameter.

So far the repulsive forces between the particles were increased in order to stabilize the suspensions against agglomeration. A different strategy would be to reduce the attractive forces between the particles. This can be done for example by index matching of the refractive index of the particles and the solvent, because the Hamaker constant will be reduced if the refractive index of the particles and the solvent is the same.

CHAPTER 11

Nomenclature

11.1. Latin Symbols

a	[m]	radius of primary particles
A	[J]	Hamaker constant
$\underline{\underline{A}}$	[–]	matrix with $a_{m,k} = m^k$
A_{123}	[J]	non retarded Hamaker constant for media 1 and 2 interacting across media 3
A'	[m^{-1} s^{y-1}]	proportionality constant
$b(\phi, V)$	[m^{-3}]	daughter distribution function
b_k	[–]	k^{th} moment of the daughter distribution function
B	[m^{-6}s^{-1}]	birth term
B	[–]	shift factor
c	[–]	parameter describing the shape of the daugther distribution
c	[M]	concentration
c_0	[M]	concentration of ions in the bulk phase
c_m	[–]	mass concentration
c_v	[–]	volume concentration
$c_{v,eff}$	[–]	effective volume concentration
d	[m]	pressure wave decay parameter for acoustophoresis
d_F	[–]	fractal dimension
d_{GM}	[m]	diameter of the grinding media
D	[m^{-6}s^{-1}]	death term
D_{DLS}	[m^2/s]	diffusion coefficient
DN	[kcal/ mol]	donor number
e	[C]	elementary charge ($e = 1.6602 \cdot 10^{-19} C$)
$\bar{E}$	[W/kg]	mean mass specific power input
E_{GM}	[Pa]	Jung's modulus of the grinding media
E_m	[J/kg]	mass specific energy
E_p	[Pa]	Jung's modulus of the particles
F	[C/mol]	Faraday constant ($F = 9.6485 \cdot 10^7$ C/kmol)
F	[N]	force

g	[m^2/s]	acceleration of gravity
G'	[Pa]	elastic modulus
G''	[Pa]	viscous modulus
$G(r)$	[–]	correction accounting for the effect of hydrodynamic interaction
h	[m]	sphere surface to surface separation
I	[mol/l]	ionic strength
$I(q)$	[m^{-1}]	scattering intensity
$\vec{j}$	[–]	diffuse exchange stream over the surface
k	[J/K]	Boltzmann constant ($k = 1{,}38066 \cdot 10^{-23}$ J/K)
k	[m^{-1}]	wavenumber
k_{agg}	[s^{-1}]	aggregation rate including inter-particle interactions
$k_{hardsphere}$	[s^{-1}]	aggregation rate without inter-particle interactions (hard spheres)
K	[Pa s$^{1/n}$]	constant
K	[mol^2 l^{-2}]	dissociation constant
K_W	[mol^2 l^{-2}]	dissociation constant of water
l	[m]	segment length
L	[mol^4/l^4]	solubility constant
m	[–]	number of observed properties
m	[kg]	mass
m	[–]	complex refractive index
m_k	[–]	normalized moments
m_{MG}	[g]	milling charge mass
M_d	[Nm]	torque
$M_{d,0}$	[Nm]	idle torque
M_k	[m$^{3(k-1)}$]	kth moment
M_n	[g/mol]	molar weight
M_r	[–]	relative molecular mass
$M_{k,r}$	[m^{k-1}]	moment
n	[m^{-6}]	number concentration distribution
n	[–]	exponent
n	[–]	real part of the refractive index
n_r	[s^{-1}]	rotary speed
n_s	[–]	number of segments in a polymer chain
N	[l^{-1}]	particle concentration
N_0	[l^{-1}]	initial particle concentration
N_A	[mol^{-1}]	Avogadro constant ($N_A = 6.0221415 \cdot 10^{23}$ mol^{-1})
p	[–]	parameter describing the number of fragments
p	[N/m^2]	pressure
p_{max}	[–]	maximal packing density
P	[W]	power input
Pe	[–]	Peclet-number

q	[m^{-1}]	scattering vector
q	[C]	charge
$q_r(x)$	[m^{-1}]	density distribution
$Q_r(x)$	[–]	cumulative distribution
r	[m]	particle center to center distance
r_H	[m]	hydrodynamic radius
$\left\langle r^2 \right\rangle^{1/2}$	[m]	quadratic averaged end to end distance of the polymer chains
R_g	[m]	radius of gyration
R_{DLS}	[m]	particle radius measured with DLS
S	[–]	geometric constant
S_m	[m^2/g]	mass specific BET surface area
S_q	[–]	structure factor
S_t	[m^2/g]	total specific BET surface area
S_{MP}	[m^2/g]	BET surface area of micro pores
SE	[Nm]	stress energy
SN	[–]	stress number
t	[s]	time
t	[Å]	statistical thickness
t_{cryst}	[m]	crystallite size
T	[K]	temperature
T_M	[K]	Morin temperature
T_N	[K]	Néel temperature
v_t	[m/s]	tip speed
V	[m^3]	volume of parent particle
V	[m^3]	volume
$V_{1,n}$	[m^3]	arithmetic mean number particle size
$V_{1,V}$	[m^3]	arithmetic mean volume particle size
V_g	[m^3]	geometric mean particle size
V_{tot}	[m^3]	total volume
$V_{p,tot}$	[m^3]	total volume of particles
V^{STP}	[m^3]	adsorbed gas volume
W	[–]	stability ratio
W_∞	[–]	stability ratio for rapid coagulation
$W(\lambda')$	[–]	wavelength profile
x	[m]	distance from particle surface
x	[m]	particle diameter
x_{DLS}	[m]	mean diameter measured with DLS
x_{SANS}	[m]	mean diameter measured with SANS
$x_{1,2}$	[m]	Sauter mean diameter
$x_{50,3}$	[m]	mean value of the Q$_3$ distribution
y	[–]	constant inversely proportional to the floc strength
z	[–]	electrolyte valence
z	[–]	ratio of daughter to mother particles

11.2. Greek Symbols

α	[–]	expansion factor
α	[–]	length parameter
α_c	[–]	collision efficiency
β	[s^{-1}]	agglomeration kernel with interparticle interactions
β_0	[s^{-1}]	agglomeration kernel without interparticle interactions
χ	[–]	Flory-Huggins parameter
χ_s	[–]	adsorption energy parameter
δ	[m]	thickness of the polymer layer
δ_0	[m]	normalized distance between two particles
δ_s	[m]	Stern layer thickness
Δ	[m]	Stern layer thickness
Δm_{GM}	[g]	grinding media wear
ϵ_{GM}	[–]	porosity of resting milling bead bulk
$\dot{\epsilon}_c$	[s^{-1}]	critical strain rate
$\dot{\epsilon}_f$	[s^{-1}]	critical fracture rate
ε	[s^{-1}]	absorption frequency
ε_0	[AsV^{-1}m^{-1}]	permittivity of the vacuum (ε_0 = $8.854 \cdot 10^{-12}$AsV^{-1}m^{-1})
ε_r	[–]	dielectric constant
ϕ	[m^3]	volume of daughter particle
ϕ_{GM}	[–]	filling degree of grinding media
$\bar{\phi}_2^a$	[–]	median volume fraction of the segments on the adsorbed layer
φ	[V]	electrostatic potential
φ_0	[V]	surface potential
φ_s	[V]	Stern potential
$\Phi(z)$	[–]	self similar daughter distribution function
Φ_B	[J]	Born energy
Φ_{el}	[J]	electrostatic repulsion energy
Φ_{steric}	[J]	steric interaction energy
Φ_{steric}^{osm}	[J]	osmotic steric interaction energy
Φ_{tot}	[J]	total interaction energy
$\Phi_{tot,min1}$	[J]	primary minimum of the total interaction energy
$\Phi_{tot,min2}$	[J]	secondary minimum of the total interaction energy
$\Phi_{tot,max}$	[J]	maximum of the total interaction energy
Φ_{vdW}	[J]	van der Waals energy

$\dot{\gamma}$	[1/s]	shear rate
$\dot{\gamma}_m$	[1/s]	shear rate of the matrix
$\dot{\gamma}_{susp}$	[1/s]	shear rate of the suspension
$\tilde{\Gamma}$	[1/s]	breakage kernel
$\hat{\Gamma}$	[$s^{-1}m^{3\mu}$]	size independent part of the breakage kernel
η	[kg/(ms)]	dynamic viscosity
η_0	[kg/(ms)]	dynamic viscosity $\dot{\gamma} \to 0$
$[\eta]$	[m^3/kg]	intrinsic viscosity
η_r	[–]	relative viscosity
κ	[m^{-1}]	inverse Dybe screening length
λ	[m]	wavelength
λ'	[m]	median reference wavelength
μ	[–]	power-law breakage rate kernel order
μ	[$m^2 \cdot s^{-1}V^{-1}$]	electrophoretic mobility
ν	[m^2/s]	kinematic viscosity
ν_1	[–]	molar volume of the solvent
ν_e	[s^{-1}]	mean electronic absorption frequency in the UV
$\vec{\nu_e}$		displacement vector of the external variables
$\vec{\nu_i}$		displacement vector of the internal variables
ν_p	[m^{-2}]	polymer density at the particle surface
ϖ	[s^{-1}]	measurement frequency in acoustophoresis
θ	[°]	diffraction angle
ρ	[m^{-2}]	scattering length density
ρ_f	[kg/m^3]	density of the fluid
ρ_{GM}	[kg/m^3]	density of the grinding media
ρ_p	[kg/m^3]	density of the particles
$\Re$	[J/(kmol· K)]	gas constant ($\Re = 8.3144 \cdot 10^3$ J/(kmol· K))
σ	[–]	mean deviation
$\sigma_{g,V}$	[–]	geometric volume based standard deviation
$\sigma_{n,V}^2$	[m^6]	variance about the number mean particle size
τ	[–]	delay time
τ	[Pa]	shear stress
τ_0	[Pa]	yield stress
τ_r	[–]	relaxation time
υ_e	[s^{-1}]	main electronic absorption frequency in the UV
ω	[s^{-1}]	frequency
ξ	[m]	aggregate radius
Ψ	[V]	particle potential at stern layer
ζ	[V]	ζ-potential
$\tilde{\zeta}$	[–]	redused potential

CHAPTER 12

Bibliography

[1] F. Stenger. *Grenzflächeneffekte bei der Nanozerkleinerung in Rührwerkskugelmühlen.* PhD thesis, Erlangen-Nuremberg, 2005.

[2] S. Mende. *Mechanische Erzeugung von Nanopartikeln in Rührwerkskugelmühlen.* PhD thesis, TU Braunschweig, 2004.

[3] G. Jimbo. Chamical engineering analysis of fine grinding phenomenon of process. *Journal of Chemical Engineering of Japan*, 25(2):117–127, 1992.

[4] K. Schönert and K. Steier. Die Grenze der Zerkleinerung bei kleinen Korngrößen. *Chemie Ingenieur Technik*, 43(13):773–777, 1971.

[5] J. Theuerkauf and J. Schwedes. Investigation of motion in stirred media mills. *Chemical Engineering and Technology*, 23(3):203–209, 2000.

[6] L. Blecher. *Strömungsvorgänge in Rührwerkmühlen.* PhD thesis, TU Braunschweig, 1993.

[7] N. Stehr. *Zerkleinerung und Materialtransport in einer Rührwerkskugelmühle.* PhD thesis, TU Braunschweig, 1982.

[8] J. Winkler and L. Dulug. Dispergieren von Pigmenten in Lacken mit einer Rührwerkskugelmühle. *Farbe und Lack*, 90:4–5, 1984.

[9] N. Stehr. Naßfeinstmahlung mit Rührwerksmühlen in der Keramik - Grundlagen und technische Ausführungen. *Keramische Zeitschrift*, 42(3):162–167, 1990.

[10] F. Vock. Wet-grinding technologies with grinding media and visions of solutions for centrifuge mills for the production of nanoparticles. *Chemie Ingenieur Technik*, 75(12):1810–1827, 2003.

[11] J. Schwedes and A. Kwade. *Zerkleinern und Dispergieren in Rührwerkskugelmühlen.* Umdruck zum Hochschulkurs vom Institut für Mechanische Verfahrenstechnik und Kwade + Schwedes Zerleinerungstechnik. Braunschweig, 2004.

[12] H. Weit. *Betriebsverhalten und Maßstabsvergrößerung von Rührwerkskugelmühlen.* PhD thesis, TU Braunschweig, 1987.

[13] H.H. Stender, A. Kwade, and J. Schwedes. New results of grinding media wear analysis in stirred media mills under changing operating conditions. *PARTEC*, 2001.

[14] Bühler. Bühler modifiziert individuell Partikel-Oberflächen. *Farbe und Lack*, 110(8), 2004.

[15] B. Joost. *Zerkleinerung von Schmelzkorund und Mahlkörperverschleiß in Rührwerkskugelmühlen.* PhD thesis, TU Braunschweig, 1994.

[16] M. Becker. *Zerkleinerung keramischer Werkstoffe und Simulation der Zerkleinerung in Rührwerkskugelmühlen.* PhD thesis, TU Braunschweig, 1999.

[17] J. Theuerkauf. *Numerische und experimentelle Untersuchungen von Fluid- und Mahlkörperbewegungen in Rührwerkskugelmühlen.* PhD thesis, TU Braunschweig, 2000.

[18] F. Bunge. *Mechanischer Zellaufschluß in Rührwerkskugelmühlen.* PhD thesis, TU Braunschweig, 1991.

[19] J.-P. Thiel. *Energiebedarf und Durchsatzverhalten der Kohlenaßzerkleinerung in einer Rührwerkskugelmühle.* PhD thesis, TU Braunschweig, 1992.

[20] R. Stadler, R. Polke, J. Schwedes, and F. Vock. Naßmahlung in Rührwerkskugelmühlen. *Chemie Ingenieur Technik*, 62(11):907–915, 1990.

[21] M.J. Mankosa, G.T. Adel, and R.H. Yoon. Effect of media size in stirred ball mill grinding of coal. *Powder Technology*, 49:75–82, 1986.

[22] A. Kwade. *Autogenzerkleinerung von Kalkstein in Rührwerkskugelmühlen.* PhD thesis, TU Braunschweig, 1996.

[23] D. Gross, W. Hauger, W. Schnell, and J. Schröder. *Technische Mechanik 2*, volume 8. Springer, Berlin, 1998.

[24] T. Y. Zhang, X. N. Fei, S. R. Wang, and C. L. Zhou. Pigmentation of Vat Blue RS by ball milling in solvents. *Dyes and Pigments*, 45(1):15–21, 2000.

[25] S. F. Lomayeva, E. P. Yelsukov, G. N. Konygin, G. A. Dorofeev, V. I. Povstugar, S. S. Mikhailova, A. V. Zagainov, and A. N. Maratkanova. The influence of a surfactant on the characteristics of the iron powders obtained by mechanical milling in organic media. *Colloids and Surfaces A-Physicochemical and Engineering Aspects*, 162(1-3):279–284, 2000.

[26] R. B. Schwarz. Microscopic model for mechanical alloying. *Mechanically Alloyed, Metastable and Nanocrystalline Materials, Part 2*, 269-2:665–674, 1998.

[27] W. A. Kaczmarek, B. W. Ninham, and I. Onyszkiewicz. Synthesis of Fe_{3n} by mechanochemical reactions between iron and organic H-X(Cn)(6) ring compounds. *Journal of Materials Science*, 30(21):5514–5521, 1995.

[28] W. A. Kaczmarek and B. W. Ninham. Surfactant-assisted ball-milling of $BaFe_{12}o_{19}$ ferrite dispersion. *Materials Chemistry and Physics*, 40(1):21–29, 1995.

[29] W. Kaczmarek and B. W. Ninham. Preparation of Fe_3O_4 and -Fe_2O_3 powders by magnetomechanical activation of hematite. *IEEE Transactions on Magnetics (T-MAG)*, 30:732, 1994.

[30] E. Papirer and P. Martz. Ball milling of muscovite in organic media. *Materials Science and Engineering*, 95:L5–L8, 1987.

[31] R.R. Klimpel. The selection of wet grinding chemical additives based on slurry rheology control. *Powder Technology*, 105(1-3):430–435, 1999.

[32] D. W. Fuerstenau. Grinding aids. *KONA*, 13:5–17, 1995.

[33] P.A. Rehbinder. Verminderung der Ritzhärte bei der Adsorption grenzflächenaktiver Stoffe. *Zeitschrift der Physik*, 72:191–205, 1931.

[34] E. Reinsch. *Der Einfluss von Zusatzstoffen auf die nasse Feinstzerkleinerung in Rührwerkskugelmühlen.* PhD thesis, TU Bergakademie Freiberg, 2003.

[35] K. Greichen, H. Müller, and H. Schubert. Zur Wirkungsweise von Tensiden als Mahlhilfsmittel. *Silikattechnik*, 25(5):169–172, 1974.

[36] H. El-Shall and P. Somasundaran. Physico- chemical aspects of grinding: a review of use of additives. *Powder Technology*, 38:275–293, 1984.

[37] E. Wang and E. Forssberg. Dispersants in stirred ball mill grinding. *Kona*, 13:237–244, 1995.

[38] F. Stenger, S. Mende, J. Schwedes, and W. Peukert. Nanomilling in stirred media mills. *Chemical Engineering Science*, 60(16):4557–4565, 2005.

[39] F. Stenger, S. Mende, J. Schwedes, and W. Peukert. The influence of suspension properties on the grinding behavior of alumina particles in the submicron size range in stirred media mills. *Powder Technology*, 156(2-3):103–110, 2005.

[40] F. Stenger and W. Peukert. Nanomilling - the influence of suspension stability. *IFPRI Conference*, 2002.

[41] F. Stenger and W. Peukert. The role of particle interactions on suspension rheology - application to submicron grinding in stirred ball mills. *Chemical Engineering and Technology*, 26(2):177–183, 2003.

[42] J. Zheng, C. C. Harris, and P. Somasundaran. The effect of additives on stirred media milling of limestone. *Powder Technology*, 91(3):173–179, 1997.

[43] S. Haas, H. W. Hasslin, and C. Schlatter. Influence of polymeric surfactants on pesticidal suspension concentrates: dispersing ability, milling efficiency and stabilization power. *Colloids and Surfaces A-Physicochemical and Engineering Aspects*, 183:785–793, 2001.

[44] T.E. Karis, V.J. Novotny, and R.D. Johnson. Mechanical scission of perfluoropolyethers. *Journal of Applied Polymer Science*, 50:1357–1368, 1993.

[45] F. Stenger, M. Götzinger, P. Jakob, and W. Peukert. Mechano-chemical changes of nano sized α-Al$_2$O$_3$ during wet dispersion in stirred ball mills. *Particle and Particle Systems Characterization*, 21:31–38, 2004.

[46] E. Kostic, S. J. Kiss, S. Zec, and S. Boskovic. Transition of γ-Al$_2$O$_3$ into α-Al$_2$O$_3$ during vibro milling. *Powder Technology*, 107(1-2):48–53, 2000.

[47] E. Kostic, S. Kiss, S. Boskovic, and S. Zec. Mechanical activation of the gamma to alpha transition in Al$_2$O$_3$. *Powder Technology*, 91(1):49–54, 1997.

[48] E. Papirer, J.M. Perrin, B. Siffert, and G. Philipponneau. The influence of grinding on the surface properties of α-aluminias. *Journal of Colloid and Interface Science*, 156:104–108, 1993.

[49] T. Shione, S. Okumura, H. Shiomi, T. Nishida, M. Kitamura, and M. Kamitani. Preparation of inorganic consolidated body using aluminium hydroxide mechanically activated by dry milling. *Journal of Materials Synthesis and Processing*, 8:351–357, 2000.

[50] S. Indris, D. Bork, and P. Heitjans. Nanocrystalline oxide ceramics prepared by high-energy ball milling. *Journal of Materials Synthesis and Processing*, 8(3-4):245–250, 2000.

[51] V. V. Boldyrev. Hydrothermal reactions under mechanochemical action. *Powder Technology*, 122(2-3):247–254, 2002.

[52] Q. W. Zhang, J. F. Lu, J. Wang, and F. Saito. Dependency of mechanochemical reactions forming complex oxides on the crystal structures of starting oxides. *Journal of Materials Science*, 39(16-17):5527–5530, 2004.

[53] M. Senna. Incipient chemical interaction between fine particles under mechanical stress - a feasibility of producing advanced materials via mechanochemical routes. *Solid States Ionics*, 63-65:3–9, 1993.

[54] A. N. Streletskii, I. V. Kolbanev, A. B. Borunova, and P. Yu. Butyagin. Mechanochemical activation of aluminum: 3. inetics of interaction between aluminum and water. *Colloid Journal*, 67(5):631637, 2005.

[55] B. Fritsch. Die Hydratation von α-Aluminiumoxid. *Deutsche Keramische Gesellschaft*, 42:149–160, 1963.

[56] R. Oberacker, S. Poehnitzsch, and H. Hofius. The effect of different milling methods applied in the production of Al$_2$O$_3$ ceramics. *Cfi-Ceramic Forum International*, 78(11-12):E45–E51, 2001.

[57] S. Kikuchi, T. Ban, K. Okada, and N. Otsuka. Mechanochemical effect for some Al$_2$O$_3$ powders by wet grinding. *Journals of materials science letters*, 11:471–474, 1992.

[58] M. Hofmann, S. J. Campbell, W. A. Kaczmarek, and S. Welzel. Mechanochemical transformation of α-Fe$_2$O$_3$ to Fe$_{3-x}$O$_4$-microstructural investigation. *Journal of Alloys and Compounds*, 348(1-2):278–284, 2003.

[59] R. A. Borzi, S. J. Stewart, G. Punte, R. C. Mercader, M. Vasquez-Mansilla, R. D. Zysler, and E. D. Cabanillas. Magnetic interactions in hematite small particles obtained by ball milling. *Journal of Magnetism and Magnetic Materials*, 205(2-3):234–240, 1999.

[60] M. Zdujic, C. Jovalekic, L. Karanovic, M. Mitric, D. Poleti, and D. Skala. Mechanochemical treatment of α-Fe$_2$O$_3$ powder in air atmosphere. *Materials Science and Engineering A-Structural Materials Properties Microstructure and Processing*, 245(1):109–117, 1998.

[61] S. Linderoth, J. Z. Jiang, and S. Morup. Reversible α-Fe$_2$O$_3$ to Fe$_3$O$_4$ transformation during ball milling. *Materials Science Forum*, 235-238:205–210, 1997.

[62] S. Meillon, H. Dammak, E. Flavin, and H. Pascard. Existence of a direct phase-transformation from hematite to maghemite. *Philosophical Magazine Letters*, 72(2):105–110, 1995.

[63] N. Randrianantoandro, A. M. Mercier, M. Hervieu, and J. M. Greneche. Direct phase transformation from hematite to maghemite during high energy ball milling. *Materials Letters*, 47(3):150–158, 2001.

[64] J. D. Betancur, J. Restrepo, C. A. Palacio, A. L. Morales, J. Mazo-Zuluaga, J. J. Fernandez, O. Perez, J. F. Valderruten, and A. Bohorquez. Thermally driven and ball-milled hematite to magnetite transformation. *Hyperfine Interactions*, 148(1-4):163–175, 2003.

[65] Y. Uehera. Structural changes of iron oxides by ball milling in different media. *Bulletin of the chemical society of Japan*, 48(11):3383–3384, 1975.

[66] M. Sorescu. Mechanochemical activation of magnetite nanoparticles. *Journal of Nanoparticle Research*, 2:305–308, 2000.

[67] S. Dutta, S. K. Manik, M. Pal, S. K. Pradhan, P. Brahma, and D. Chakravorty. Electrical conductivity in nanostructured magnetite-hematite composites produced by mechanical milling. *Journal of Magnetism and Magnetic Materials*, 288:301–306, 2005.

[68] M. Sorescu, D. Tarabasanu-Mihaila, and L. Diamandescu. The role of particle morphology in the mechanochemical activation of hematite. *Journal of Materials Synthesis and Processing*, 7(3):167–173, 1999.

[69] M. Sorescu, L. Diamandescu, and A. Grabias. Evolution of phases during mechanochemical activation in magnetite-containing systems. *Materials Chemistry and Physics*, 83(2-3):354–360, 2004.

[70] E. Petrovsky, M. D. Alcala, J. M. Criado, T. Grygar, A. Kapicka, and J. Subrt. Magnetic properties of magnetite prepared by ball-milling of hematite with iron. *Journal of Magnetism and Magnetic Materials*, 210(1-3):257–273, 2000.

[71] E. Clauß. *Gefährdungspotential pyrit- und schwermetallhaltiger Kiesabbrände aus der Schwefelsäureproduktion. Eine mineralogische Analyse am Beispiel des Standorts Kehlheim an der Donau.* PhD thesis, Universität Heidelberg, 2001.

[72] L.H. Bowen. Mössbauer spectroscopy of ferric oxides and hydroxides. *Mössbauer effect reference and data journal*, 2(1):76–95, 1979.

[73] I.E. Dzialoshinskii. Thermodynamic theory of "weak" ferromagnetism in antiferromagnetic substances. *Soviet Physics JETP*, 5(6):1259–1272, 1957.

[74] F.J. Morin. Magnetic susceptibility of α-Fe_2O_3 with added titanium. *In: Phys. Rev.*, 78:819–820, 1950.

[75] J. Svoboda. *Magnetic methods for the treatment of minerals.* Elsevier, New York, 1987.

[76] C. J. Chin, S. Yiacoumi, and C. Tsouris. Agglomeration of magnetic particles and breakup of magnetic chains in surfactant solutions. *Colloids and Surfaces A-Physicochemical and Engineering Aspects*, 204(1-3):63–72, 2002.

[77] A.S. Russell, D.A. Saville, and W.R. Schowalter. *Colloidal dispersions.* Cambridge University Press, Cambridge, 1989.

[78] R.J. Hunter. *Foundations of colloid science.* Oxford University Press, New York, 1986.

[79] J. Israelachvilli. *Intermolecular and surface forces.* Academic Press, 1991.

[80] G. Lagaly, O. Schulz, and R. Zimehl. *Dispersionen und Emulsionen.* Steinkopff, Darmstadt, 1997.

[81] S. Mende, F. Stenger, W. Peukert, and J. Schwedes. Mechanical production and stabilization of submicron particles in stirred media mills. *Powder Technology*, 132(1):64–73, 2003.

[82] H.C. Hamaker. The London-van der Waals attraction between spherical particles. *Physica*, 4:1058–1072, 1937.

[83] W. Peukert, C. Mehler, and M. Götzinger. Surface characterisation of particles by adsorption and adhesion measurements. *PARTEC*, 2001.

[84] S. Maurer, A. Mersmann, and W. Peukert. in adsorption science and technology (ed. do d.d.). Brisbane, Australia, 2000. World Scientific.

[85] W. Peukert, C. Mehler, and M. Götzinger. Application of adsorption and adhesion measurements for particle surface characterization. *Particle and Particle Systems Characterization*, 18(5-6):229–234, 2002.

[86] W. Peukert, C. Mehler, and M. Götzinger. Novel concepts for characterisation of heterogeneous particulate surfaces. *Applied Surface Science*, 196(1-4):30–40, 2002.

[87] D.B. Hough and L.R. White. The calculation of Hamaker constants from Liftshitz theory with applications to wetting phenomena. *Advances in Colloid and Interface Science*, 14(1):3–41, 1980.

[88] D.C. Prieve and W.B. Russel. Simplified predictions of Hamaker constants from Lifshitz theory. *Journal of Colloid and Interface Science*, 125(1):1–13, 1988.

[89] D. Tabor and R.H.S. Winterton. Surface forces: direct measurement of normal and retarded van der Waals forces. *Nature*, 219(5159):1120–1, 1969.

[90] J. Gregory. Calculation of Hamaker constants. *Advances in Colloid and Interface Science*, 2(4):396–417, 1970.

[91] M. Götzinger. *Zur Charakterisierung von Wechselwirkungen partikulärer Feststoffoberflächen.* PhD thesis, TU München, 2004.

[92] H.D. Ackler, R.H. French, and Y.M. Chiang. Comparisons of Hamaker constants for ceramic systems with intervening vacuum or water: From force laws and physical properties. *Journal of Colloid and Interface Science*, 179(2):460–469, 1996.

[93] P.C. Hiemenz and R. Rajagopalan. *Principles of colloid and surface chemestry.* Marcel Dekker, 1997.

[94] J. Lyklema. *Fundamentals of interface and colloid science*, volume 1. Academic Press, London, 1993.

[95] M.E. Labib. The origin of the surface charge on particles suspended in organic liquids. *Colloids and Surfaces*, 29:293–304, 1988.

[96] E.J.W. Verwey. The charge distribution in the water molecule and calculation of the intermolecular forces. *Recl. Trav. Chim. Pays-Bas*, 60:625, 1941.

[97] M.E. Labib and D.R.M. Williams. An experimental comparison between the aqueous pH scale and the electron donicity scale. *Colloid and Polymer Science*, 264:533–541, 1986.

[98] V. Gutmann. *The Donor-Acceptor-Approach to molecular interactions.* Plenum, New York, 1978.

[99] J. Huheey, E. Keiter, and R. Keiter. *Anorganische Chemie, Prinzipien von Struktur und Reaktivität*, volume 2. Walter de Gruyter, Berlin, 1995.

[100] R. Schmid. Re-interpretation of the solvent dielectric constant in coordination chemical terms. *J. Solution Chem.*, 12:135, 1983.

[101] E.C.Y. Yan, Y. Liu, and K.B. Eisenthal. New method for determination of surface potential of microscopic particles by second harmonic generation. *Journal of Physical Chemistry B*, 102(33):6331–6336, 1998.

[102] L. Schneider, H.J. Schmid, and W. Peukert. Concentration dependency of the secound harmonic signal generated at colloidal surfaces. *Langmuir*, submitted, 2006.

[103] B. Derjaguin. Friction and adhesion. IV the theory of adhesion of small particles. *Kolloid-Zeitschrift*, 69:155–164, 1934.

[104] G.M. Bell, S. Levine, and L.N. McCartney. Approximate methods of determining the double-layer free energy of interaction between two charged colloidal spheres. *Journal of Colloid and Interface Science*, 43:335–359, 1970.

[105] B.W. Ninham. On progress in forces since the DLVO theory. *Advances in Colloid and Interface Science*, 83(1-3):1–17, 1999.

[106] L. Günther and W. Peukert. Control of coating properties by tailored particle interactions: relation between suspension rheology and film structure. *Colloids and Surfaces A-Physicochemical and Engineering Aspects*, 225(1-3):49–61, 2003.

[107] J.P. Chapel. Electrolyte species dependent hydration forces between silica surfaces. *Langmuir*, 10(11):4237–4243, 1994.

[108] B. Derjaguin and L. Landau. A theory of the stability of strongly charged lyophobic sols and the coalescence of strongly charged particles in electrolyte solution. *Acta Phys. Chim. USSR*, 14:633–658, 1941.

[109] E.J.W. Verwey and J.T.G. Overbeek. *Theory of the stability of lyophobic colloids: The interaction of sol particles having an electrical double layer.* Elsevier, New York, 1948.

[110] D.H. Napper. Steric stabilization. *Journal of Colloid and Interface Science*, 58(2):390–407, 1977.

[111] G.J. Fleer, J. Lyklema, G.D. Parfitt, and C.H. Rochester. *In Adsorption from solution at the solid/liquid interface.* Academic Press, London, 1938.

[112] J. Davies and J.G.P. Binner. Coagulation of electrosterically dispersed concentrated alumina suspensions for paste production. *Journal of the European Ceramic Society*, 20(10):1555–1567, 2000.

[113] R. Evans, D.H. Napper, and Z.Z. Knoll. Steric stabilization I. Comparison of theories with experiment. *Polymer*, 251:409–414, 1973.

[114] B. Vincent, J. Edwards, S. Emmett, and A. Johns. Depletion flocculation in dispersions of sterically-stabilized particles ("soft particles"). *Colloids and Surfaces*, 18:261–281, 1986.

[115] J.C. Dijt, C.M.A. Stuart, J.E. Hofman, and G.J. Fleer. Kinetics of polymer adsorption in stagnation point flow. *Colloids and Surfaces A-Physicochemical and Engineering Aspects*, 51:141, 1990.

[116] M.R. Rosen. *Surfactants and interfacial phenomena.* Wiley, New York, 1989.

[117] M. von Smoluchowski. Versuch einer mathematischen Theorie der Koagulationskinetik kolloidaler Lösungen. *Zeitschrift der physikalischen Chemie*, 92:129–181, 1917.

[118] P.G. Saffman and J.S. Turner. On the collision of drops in turbulent clouds. *Journal of Fluid Mechanics*, 1:16–30, 1956.

[119] M.Y. Lin, H.M. Lindsay, D.A. Weitz, R. Klein, R. C. Ball, and P. Meakin. Universal diffusion-limited colloid aggregation. *Journal of Physics: Condensed Matter*, 2:3093–3113, 1990.

[120] M.Y. Lin, H.M. Lindsay, D.A. Weitz, R.C. Ball, R. Klein, and P. Meakin. Universal reaction-limited collid aggregation. *Physical Review A*, 41(4):2005–2019, 1990.

[121] M. Lattuada, P. Sandkuhler, H. Wu, J. Sefcik, and M. Morbidelli. Aggregation kinetics of polymer colloids in reaction limited regime: experiments and simulations. *Advances in Colloid and Interface Science*, 103(1):33–56, 2003.

[122] L.H. Hanus, R.U. Hartzler, and N.J. Wagner. Electrolyte-induced aggregation of acrylic latex. 1. dilute particle concentrations. *Langmuir*, 17(11):3136–3147, 2001.

[123] C. Cametti, P. Codastefano, and P. Tartaglia. Light scattering measurements of slow aggregation in colloids: Deviations from asymptotic time scaling. *Physical Review A*, 36(10):4916–4921, 1987.

[124] G. Odriozola, M. Tirado-Miranda, A. Schmitt, M. Martinez, F. Lopez, J. Callejas-Fernandez, R. Martinez-Garcia, and R. Hidalgo-Alvarez. A light scattering study of the transition region between diffusion- and reaction-limited cluster aggregation. *Journal of Colloid and Interface Science*, 240:9096, 2001.

[125] I.K. Yudin, G.L. Nikolaenko, E.E. Gorodetskii, E.L. Markhashov, V.A. Agayan, M.A. Anisimov, and J.V. Sengers. Crossover kinetics of asphaltene aggregation in hydrocarbon solutions. *Physica A-Statistical Mechanics and Its Applications*, 251(1-2):235–244, 1998.

[126] M. Carpineti and M. Giglio. Spinodal type dynamics in fractal aggregation of coloidal clusters. *Physical Review Letters*, 68:3327–3330, 1992.

[127] V.A. Tolpekin, M.H.G. Duits, D. van den Ende, and J. Mellema. Aggregation and breakup of colloidal particle aggregates in shear flow, studied with video microscopy. *Langmuir*, 20(7):2614–2627, 2004.

[128] F. Le Berre, G. Chauveteau, and E. Pefferkorn. Perikinetic and orthokinetic aggregation of hydrated colloids. *Journal of Colloid and Interface Science*, 199(1):1–12, 1998.

[129] N. Fuchs. Über die Stabilität und Aufladung der Aerosole. *Zeitschrift der Physik*, 89:736–743, 1934.

[130] L.A. Spielman. Viscous interactions in brownian coagulation. *Journal of Colloid and Interface Science*, 33(4):562–571, 1970.

[131] E.P. Honig, G.J. Roebersen, and P.H. Wiersema. Effect of hydrodynamic interaction on the coagulation rate of hydrophobic colloids. *Journal of Colloid and Interface Science*, 36(1):97–109, 1971.

[132] Q. Wang. On colloidal suspension Brownian stability ratios: Theoretical approaches. *Journal of Colloid and Interface Science*, 145(1):99–107, 1991.

[133] D.C. Prieve and E. Ruckenstein. Role of surface chemistry in primary and secondary coagulation and heterocoagulation. *Journal of Colloid and Interface Science*, 73(2):539–555, 1980.

[134] J.W. Virden and J.C. Berg. The use of photon correlation spectroscopy for estimation the rate constant for doublet formation in an aggregating colloidal dispersion. *Journal of Colloid and Interface Science*, 149(2):528–535, 1991.

[135] H. Holthoff, M. Borkovec, and P. Schurtenberger. Determination of light-scattering form factors of latex particle dimers with simultaneous static and dynamic light scattering in an aggregating suspension. *Physical Review E*, 56(6):6945–6953, 1997.

[136] S. Melis, M. Verduyn, G. Storti, M. Morbidelli, and J. Baldyga. Effect of fluid motion on the aggregation of small particles subject to interaction forces. *AIChE Journal*, 45(7):1383–1393, 1999.

[137] A. Einstein. Eine neue Bestimmung der Moleküldimension. *Annalen der Physik*, 19:289–306, 1906.

[138] H.A. Barnes. Shear-thickening ("dilantancy") in suspensions of nonaggregating solid particles dispersed in newtonian liquids. *Journal of Rheology*, 33(2):329–366, 1989.

[139] M.K. Chow and C.F. Zukoski. Gap size and shear history dependencies in shear thickening of a suspension ordered at rest. *Journal of Rheology*, 39:15 – 32, 1995.

[140] M.K. Chow and C.F. Zukoski. Nonequilibrium behavior of dense suspensions of uniform particles: Volume fraction and size dependence of rheology and microstructure. *Journal of Rheology*, 39:33 – 59, 1995.

[141] J. Bender and N.J. Wagner. Reversible shear thickening in monodisperse and bidisperse colloidal dispersions. *Journal of Rheology*, 40(5):899–916, 1996.

[142] D. Ramkrishna. The status of population balances. *Chemical Engineering Communications*, 3:49 – 95., 1985.

[143] D. Gouvea and B.B.S. Murad. Influence of acid-basic characteristic of Al_2O_3 or SnO_2 surfaces on the stability of ceramic suspensions with commercial dispersants. *Ceramica*, 47:51 – 56, 2001.

[144] C.W. Macosco. *Rheology: Principles, measurements and applications*. VCH Publishers, New York, 1994.

[145] G.K. Batchelor. The effect of brownian motion on the bulk stress in a suspension of spherical particles. *Journal of Fluid Mechanics*, 83(1):97–117, 1977.

[146] I.M. Krieger and T.J. Dougherty. A mechanism for non-newtonian flow of rigid spheres. *Transactions of the Society of Rheology*, pages 137–152, 1959.

[147] W. Gleißle and M.K. Baloch. Advances in rheology. In *IXth International congress on rheology*, Acapulco, 1983.

[148] R. Finsy. Particle sizing by quasi-elastic light scattering. *Advances in Colloid and Interface Science*, 52:79–143, 1994.

[149] B.J. Berne and R. Pecora. *Dynamic light scattering*. Wiley, New York, 1976.

[150] H.C. van de Hulst. *Light scattering by small particles*. Reprinted by Dover Puplication, New York, (1981), 1957.

[151] C.F. Bohren and D.R. Huffman. *Absorption and scattering of light by small particles*. John Wiley, New York, 1983.

[152] Malvern Instruments Ltd. *Operators guide MAN 0247*, volume 1,1. Malvern Instruments, Worcestershire, 1998.

[153] C. J. Glinka, J. G. Barker, B. Hammouda, S. Krueger, J. J. Moyer, and W. J. Orts. The 30 m small-angle neutron scattering instruments at the national institute of standards and technology. *Journal of Applied Crystallography*, 31:430–445, 1998.

[154] J. Van Tassel and C.A. Randall. Surface chemistry and surface charge formation for an alumina powder in ethanol with the addition of HCl and KOH. *Journal of Colloid and Interface Science*, 241(2):302–316, 2001.

[155] D.R. Lide. *Handbook of Chemestry and Physics*, volume 77. CRC Press Inc., New York, 1996.

[156] KMF Laborchemie Handels GmbH. analysis certificate. 2005.

[157] Chemdat, the merck chemical databases, http://www.chemdat.info.

[158] L. Cromieres, V. Moulin, B. Fourest, and E. Giffaut. Physico-chemical characterization of the colloidal hematite/water interface: experimentation and modelling. *Colloids and Surfaces A-Physicochemical and Engineering Aspects*, 202(1):101–115, 2002.

[159] D.C. Prieve and W.B. Russel. Simplified procedure of Hamaker constants from Lifshitz theory. *Journal of Colloid and Interface Science*, 125:1–13, 1988.

[160] Y.V. Tanchuk. *Kataliz i neftekhimiya*, 1(3), 1995.

[161] G. Kostorz. *Neutron Scattering, in Treatise on materials science and technology*, volume 15. Academic Press, 1982.

[162] A. Guinier. *X-ray diffraction in crystalls, imperfect crystals and amorphous bodies.* Dover Puplications Inc., New York, 1994.

[163] J. Teixeira. Small-angle scattering by fractal systems. *Journal of Applied Crystallography*, 21:781–785, 1988.

[164] I.R. Collins and S.E. Taylor. The microstructural properties of coagulated nonaqueous carbon black dispersions. *Journal of Colloid and Interface Science*, 155:471–481, 1993.

[165] F.E. Torres, W.B. Russel, and W.R. Schowalter. Floc structure and growth kinetics for rapid shear coagulation of polystyrene colloids. *Journal of Colloid and Interface Science*, 142(2):554–574, 1991.

[166] F.E. Torres, E. Russell, and W.R. Schowalter. Simulation of coagulation in viscous flows. *Journal of Colloid and Interface Science*, 145(1):51–73, 1991.

[167] H. Hoekstra, J. Vermant, and J. Mewis. Flow-induced anisotropy and reversible aggregation in two-dimensional suspensions. *Langmuir*, 19(22):9134–9141, 2003.

[168] J. Vermant and M. J. Solomon. Flow-induced structure in colloidal suspensions. *Journal of Physics-Condensed Matter*, 17(4):R187–R216, 2005.

[169] P.D.A. Mills, J.W. Goodwin, and B.W. Grover. Shear field modification of strongly flocculated suspensions aggregate morphology. *Colloid and Polymer Science*, 269:949–963, 1991.

[170] P. Varadan and M. J. Solomon. Shear-induced microstructural evolution of a thermoreversible colloidal gel. *Langmuir*, 17(10):2918–2929, 2001.

[171] C. J. Rueb and C. F. Zukoski. Viscoelastic properties of colloidal gels. *Journal of Rheology*, 41(2):197–218, 1997.

[172] J.V. DeGroot, C.W. Macosko, T. Kume, and K. Hashimoto. Flow-induced anisotropic SALS in silica-filled PDMS liquids. *Journal of Colloid and Interface Science*, 166:404, 1994.

[173] H. Verduin, B.J. deGans, and J.K.G. Dhont. Shear induced structural changes in a gel-forming suspension studied by light scattering and rheology. *Langmuir*, 12(12):2947–2955, 1996.

[174] F. Pignon, A. Magnin, and J.M. Piau. Butterfly light scattering pattern and rheology of a sheared thixotropic clay gel. *Physical Review Letters*, 79(23):4689–4692, 1997.

[175] V. Oles. Shear induced aggregation and breakup of polystyrene latex particles. *Journal of Colloid and Interface Science*, 154(2):351–358, 1992.

[176] P.T. Spicer, S.E. Pratsinis, M.D. Trennepohl, and G.H.M. Meesters. Coagulation and fragmentation: The variation of shear rate and the time lag for attainment of steady state. *Industrial and Engineering Chemistry Research*, 35(9):3074–3080, 1996.

[177] P.T. Spicer and S.E. Pratsinis. Shear-induced flocculation: The evolution of floc structure and the shape of the size distribution at steady state. *Water Research*, 30(5):1049–1056, 1996.

[178] P.T. Spicer and S.E. Pratsinis. Coagulation and fragmentation: Universal steady-state particle-size distribution. *AIChE Journal*, 42(6):1612–1620, 1996.

[179] P.T. Spicer, S.E. Pratsinis, A.W. Willemse, H.G. Merkus, and B. Scarlett. Monitoring the dynamics of concentrated suspensions by enhanced backward light scattering. *Particle and Particle Systems Characterization*, 16(5):201–206, 1999.

[180] P. Somasundaran, X. Yu, and S. Krishnakumar. Role of conformation and orientation of surfactants and polymers in controlling flocculation and dispersion of aqueous and non-aqueous suspensions. *Colloids and Surfaces A-Physicochemical and Engineering Aspects*, 133(1-2):125–133, 1998.

[181] S.H. Ehrman. Effect of particle size on rate of coalescence of silica nanoparticles. *Journal of Colloid and Interface Science*, 213(1):258–261, 1999.

[182] W. Liang, G. Bognolo, and T.F. Tadros. Stability of dispersions in the presence of graft copolymer (II) adsorption of graft copolymers on titanium dioxide and the stability and rheology of the resulting dispersions. *Langmuir*, 16(3):1306–1310, 2000.

[183] R.P. Sawatzky and A.J. Babchin. Hydrodynamics of electrophoretic motion in an alternating electric field. *Journal of Fluid Mechanics*, 246:321–334, 1992.

[184] D.C. Henry. Cataphoresis of suspended particles. Part I the equation of cataphoresis. *Proceedings of the Royal Society of London, Series A*, 133(106):106–129, 1931.

[185] H. Hofmeister. Zur Lehre von der Wirkung der Salze: Zweite Mitteilung. Über Regelmäßigkeiten in der eiweißfällenden Wirkung der Salze und ihre Beziehung zum physiologischen Verhalten derselben. *Arch Exp Pathol u Pharmakol*, 24:247–260, 1888.

[186] T.G.M. van de Ven. On the role of ion size in coagulation. *Journal of Colloid and Interface Science*, 124:138–145, 1988.

[187] T.G.M. van de Ven and S.G. Mason. The microrheology of colloidal dispersions. VII orthokinetic doublet formation of spheres. *Colloid and Polymer Science*, 255:468–479, 1977.

[188] M. Kosmulski. *Chemical Properties of Material Surfaces*. Marcel Dekker, Inc, 2001.

[189] N. Wiberg. *Lehrbuch der anorganischen Chemie*, volume 91-100. Walter de Gruyter, Berlin, 1985.

[190] J.H. de Boer, B.G. Linsen, T. van der Plas, and G. J. Zondervan. Studies on pore systems in catalysis. 7. Description of pore dimensions of carbon blacks by t method. *Journal of Catalysis*, 4:649 – 656, 1965.

[191] D.H. Lee and R.A. Condrate. An FTIR spectral investigation of the structural species found on alumina surfaces. *Materials Letters*, 23(4-6):241–246, 1995.

[192] A.L. Loeb, J.T.G. Overbeek, and P.H. Wiersema. *The electrical double layer around a spherical colloidal particle*. MIT Press, Cambridge, MA, 1961.

[193] S.E. O'Reilly and M.F. Hochella. Lead sorption efficiencies of natural and synthetic Mn and Fe-oxides. *Geochimica Et Cosmochimica Acta*, 67(23):4471–4487, 2003.

[194] K. Subramaniam, V. Vithayaveroj, S. Yiacoumi, and C. Tsouris. Copper uptake by silica and iron oxide under high surface coverage conditions: surface charge and sorption equilibrium modeling. *Journal of Colloid and Interface Science*, 268(1):12–22, 2003.

[195] I. Puigdomenech. Chemical equilibrium software, www.kemi.kth.se/medusa.

[196] A.F. Holleman and N. Wiberg. *Lehrbuch der Anorganischen Chemie*. Walter de Gruyter, Berlin, 1995.

[197] R. Greenwood and K. Kendall. Acoustophoretic studies of aqueous suspensions of alumina and 8 molyttria stabilised zirconia powders. *Journal of the European Ceramic Society*, 20(1):77–84, 2000.

[198] C. Mätzler. Matlab functions for Mie scattering and absorption. Institut für Angewandte Physik, Universität Bern, Bern, research report no. 2002-08 edition, 202.

[199] http://irina.eas.gatech.edu/lectures/lec26.html.

[200] P.C. Kapur, P.J. Scales, D.V. Boger, and T.W. Healy. Yield stress of suspensions loaded with size distributed particles. *AIChE Journal*, 43(5):1171–1179, 1997.

[201] J.D. Boadway. Dynamics of growth and breakage of alum floc in presence of fluid shear. *Journal of Environmental Engineering Division*, 104:901–991, 1978.

[202] P.J. Hill and K.M. Ng. Statistics of multiple particle breakage. *AIChE Journal*, 42(6):1600–1611, 1996.

[203] R.B. Diemer and J.H. Olson. A moment methodology for coagulation and breakage problems: Part 3 - generalized daughter distribution functions. *Chemical Engineering Science*, 57(19):4187–4198, 2002.

[204] R.B. Diemer and J.H. Olson. A moment methodology for coagulation and breakage problems: Part 1 - analytical solution of the steady-state population balance. *Chemical Engineering Science*, 57(12):2193–2209, 2002.

[205] R.B. Diemer and J.H. Olson. A moment methodology for coagulation and breakage problems: Part 2 - moment models and distribution reconstruction. *Chemical Engineering Science*, 57(12):2211–2228, 2002.

[206] E. Schaer, R. Ravetti, and E. Plasari. Study of silica particle aggregation in a batch agitated vessel. *Chemical Engineering and Processing*, 40(3):277–293, 2001.

[207] M. Vanni. Approximate population balance equations for aggregation-breakage processes. *Journal of Colloid and Interface Science*, 221(2):143–160, 2000.

[208] M. Sommer, F. Stenger, W. Peukert, and N.J. Wagner. Agglomeration and breakage of nanoparticles in stirred media mills - a comparison of different methods and models. *Chemical Engineering Science*, 61(1):135–148, 2006.

[209] D. Ramkrishna. *Population Balances - Theory and Applications to Particulate Systems in Engineering*. Academic Press, San Diego, 2000.

[210] M.J. Hounslow, V.R. Marshall, and R.L. Ryall. A discretized population balance for nucleation, groth, and aggregation. *AIChE Journal*, 34(11), 1988.

[211] J. Litster. Process modelling in particulate systems. 2000.

[212] S. Kumar and D. Ramkrishna. On the solution of population balance equations by discrettization. 1. A fixed pivot technique. *Chemical Engineering Science*, 51(8):1311–1332, 1996.

[213] M. Wulkow. The simulation of molecular weight distributions in polyreation kinetics by discrete galerkin methods. *Macromolecular Theory Simulations*, 5:393 – 416, 1996.

[214] M. Wulkow, A. Gerstlauer, and U. Nieken. Modeling and simulation of crystallization processes using PARSIVAL. *Chemical Engineering Science*, 56(7):2575–2588, 2001.

[215] M. Frenklach and S. J. Harris. Aerosol dynamics modelling using the method of moments. *Journal of Colloid and Interface Science*, 118(1):252–261, 1987.

[216] T. Roths, M. Marth, J. Weese, and J. Honerkamp. A generalized regularization method for nonlinear ill-posed problems enhanced for nonlinear regularization terms. *Computer Physics Communications*, 139(3):279–296, 2001.

[217] G. Madras, G.Y. Chung, J.M. Smith, and B.J. McCoy. Molecular weight effect on the dynamics of polystyrene degradation. *Industrial and Engineering Chemistry Research*, 36(6):2019–2024, 1997.

[218] M. Kostoglou. Mathematical analysis of polymer degradation with chain-end scission. *Chemical Engineering Science*, 55(13):2507–2513, 2000.

[219] T. Chartier, S. Souchard, J.F. Baumard, and H. Vesteghem. Degradation of dispersant during milling. *Journal of the European Ceramic Society*, 16(12):1283–1291, 1996.

[220] J.A. Odell, A.J. Müller, K.A. Narh, and Keller A. Degradation of polymer solutions in extensional flows. *Macromolecules*, 23:3092–3103, 1990.

[221] S.P. Carrington and J.A. Odell. How do polymers stretch in stagnation point extensional flow-fields? *Journal of Non-Newtonian Fluid Mechanics*, 67:269–283, 1996.

[222] M. Netopilik, M. Kubin, G. Schultz, J. Vohlidal, I. Kössler, and P. Kratochvil. Degradation of polystyrene by shear stress in isopropylphenyl phosphate solution. *Journal of Applied Polymer Science*, 40:1115–1130, 1990.

[223] A. Keller and J.A. Odell. Flow induced chain fracture of isolated linear macromolecules in solution. *Journal of polymer science part B-polymer physics*, 24(1889-1916), 1986.

[224] C.A. Kim, J.T. Kim, K. Lee, H.J. Choi, and M.S. Jhon. Mechanical degradation of dilute polymer solutions under turbulent flow. *Polymer*, 41(21):7611–7615, 2000.

[225] A. Nakano and Y. Minoura. Relationship between hydrodynamic volume and the scission of polymer chains by high-speed stirring in several solvents. *Macromolecules*, 8(5), 1975.

[226] K. Lee, C.A. Kim, S.T. Lim, D.H. Kwon, H.J. Choi, and M.S. Jhon. Mechanical degradation of polyisobutylene under turbulent flow. *Colloid and Polymer Science*, 280(8):779–782, 2002.

[227] E. D. Eidelman, V. I. Siklitsky, L. V. Sharonova, M. A. Yagovkina, A. Y. Vul', M. Takahashi, M. Inakuma, M. Ozawa, and E. Osawa. A stable suspension of single ultrananocrystalline diamond particles. *Diamond and Related Materials*, 14(11-12):1765–1769, 2005.

[228] M. Piwonski. *Keramische Membranen auf Basis von LPS-SiC: Schlickerentwicklung und Beschichtungsverfahren.* PhD thesis, Technischen Universität Dresden, 2005.

[229] E. Liden, P. Persson, E. Carlström, and R. Carlson. Electrostatic adsorption of a colloidal sintering agent on silicon nitirde particles. *Journal of the American Ceramic Society*, 74(6):1335–1339, 1991.

[230] Y. Hirata, S. Tabata, and J. Ideue. Interactions in the silicon carbide-polyacrylic acid-yttrium ion system. *Journal of the American Ceramic Society*, 86(1):5–11, 2003.

[231] www.netzsch.de.

[232] http://www.itl.nist.gov/div898/handbook/eda/section3/eda35b.htm.

Appendix

A.1. Influence of Particle Concentration on the Aggregation Rate

Figure A.1 shows the influence of the particle concentration on the aggregation kinetic. The aggregation rate increases with increasing solid concentration as expected.
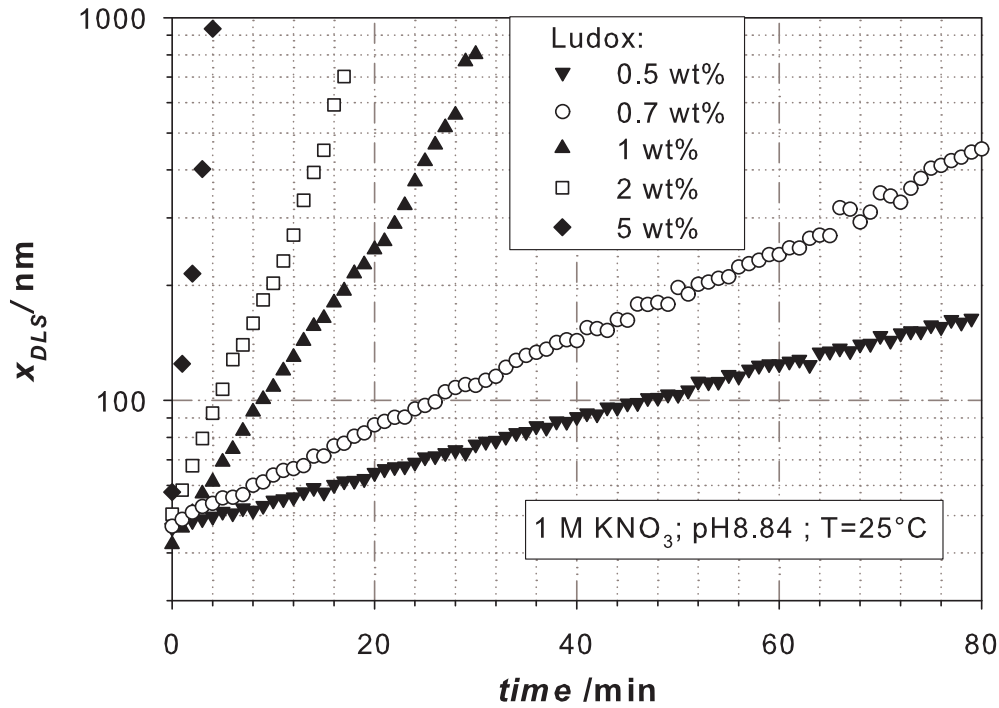
FIGURE A.1. Influence of the particle concentration on the aggregation kinetic.

A.2. Micro Pore Analysis by means of V-T-method

The V-t method according to de Boer [190] is applied to determine micro pores in the milled particles. In this method the adsorption isotherm at low relative pressures is analyzed. The volume of the adsorbed gas V^{STP} referred to standard conditions is plotted against the thickness of the adsorbed film. This statistical thickness t can be calculated from the relative pressures p/p_0 according to de Boer [39]:

$$t(\mathring{A}) = 6.0533 \cdot \left[\frac{1}{ln\left(\frac{p}{p_o}\right)} \right]^{1/3}. \qquad (A.1)$$

For non porous material this plot contains a straight line which passes through the origin. The total surface area S_t can be calculated for this case from the adsorbed gas volume V^{STP} and the statistical thickness t as follows:

$$S_t = \frac{15.47 \cdot V^{STP}}{t(\mathring{A})}. \qquad (A.2)$$

For non porous material the calculated total surface area S_t is equal to the surface area S_m determined with the BET-method. In the case of micro pores the slope of the the V-t curve has a steeper gradient at low relative pressures because the effective surface available for adsorption is larger. At higher relative pressures the slope flattens because the micropores are filled with gas and the available surface for adsorption is reduced. From the steep part of the curve the total surface area S_t can be determined. The flat part of the curve is equivalent to the surface area S_m calculated from the 4 point BET-method. The surface area resulting from micro pores S_{MP} can be calculated as follows:

$$S_{MP} = S_t - S_m. \qquad (A.3)$$

Further more the mean radius of the micro pores can be estimated from the intersection of both straight lines. A typical V-t plot of a microporous sample is shown in figure A.2. The median radius of the micro pores is in this case 0.4 nm.
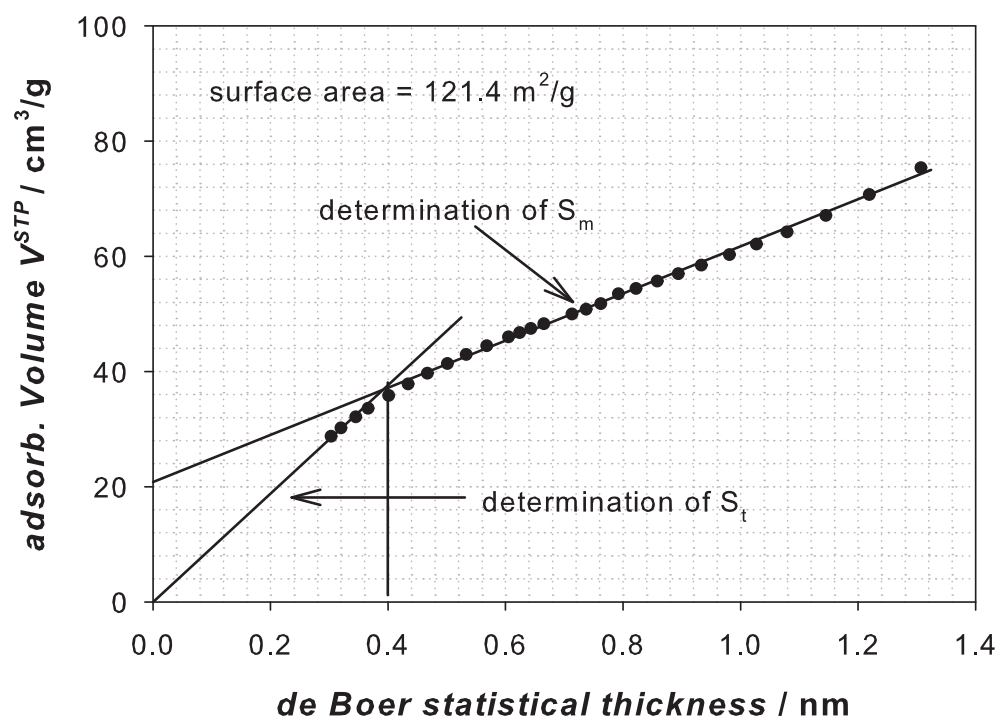
FIGURE A.2. Typical V-t-Plot milled alumina sample containing micro pores.

A.3. FT-IR

Figure A.3 shows infrared spectra for alumina milled in ethanol with 0.04 mM NaAOT as background salt. The spectrum labeled with two was measured on a sample milled with the LabStar mill for 24 h with yttrium stabilized zirconia milling beads (120 000 kJ/kg, $v_t = 8.5$ m/s, $d_{GM} = 0.5$ - 0.6 mm, $c_m = 0.2$). In contrast to the milling experiment in water no additional bands are generated during milling in ethanol. This means no hydroxide phases are being built during milling in ethanol. However, a wide band between 3600 and 3000 cm^{-1} could be detected, which can be associated with physically combined solvent at the surface. After heating the samples up to 900 °C with a heating rate of 10 K/min in nitrogen atmosphere (see spectrum 3), these bands are still present. However, the intensity of the bands is reduced. The intensity of the infrared bands of the heated samples is still higher than the intensity of the infrared band of the feed material, which can be explained with a higher surface area of the milled particles in comparison to the feed particles.
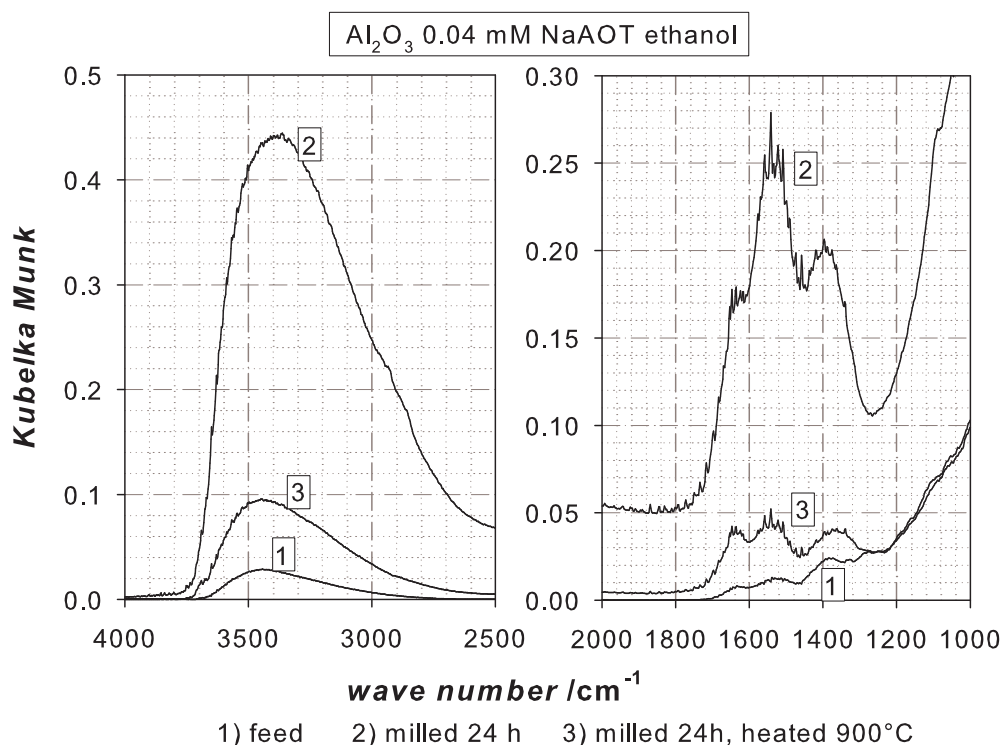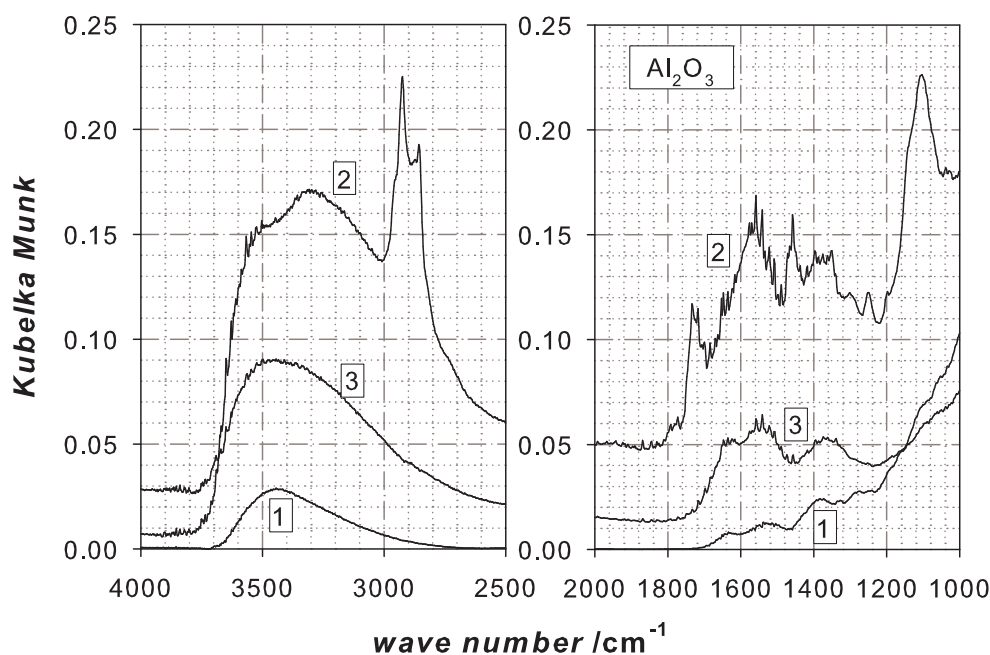

FIGURE A.3. FT-IR measurements of α-Al$_2$O$_3$ milled in ethanol and 0.04 mM NaAOT (LabStar, 120 000 kJ/kg, $v_t = 8.5$ m/s, $d_{GM} = 0.5$ - 0.6 mm, $c_m = 0.2$).

Figure A.4 shows infrared spectra for alumina milled in ethanol with steric stabilization. The spectrum labeled with two was measured on a sample milled with the LabStar mill for 24 h with yttrium stabilized zirconia milling beads (120 000 kJ/kg, $v_t = 8.5$ m/s, $d_{GM} = 0.5$ - 0.6 mm, $c_m = 0.2$). The peak around 3000 cm^{-1} can be attributed to the adsorbed polymer chains. After heating the samples up to 900 °C with a heating rate of 10 K/min in nitrogen atmosphere (see spectrum 3), this peak vanishes. The polymer cover is completely destroyed due to heating the sample up to 900°.

1) feed   2) DAPRAL, milled 24h   3) DAPRAL, milled 24h, heated 900°C

FIGURE A.4. FT-IR measurements of sterically stabilized α-Al$_2$O$_3$ milled in ethanol (LabStar, 120 000 kJ/kg, $v_t = 8.5$ m/s, $d_{GM} = 0.5$ - 0.6 mm, $c_m = 0.2$).

A.4. Electrostatically Stabilized Fe$_2$O$_3$ Particles in Water

Figure A.5 shows the influence of different ions on the ζ-potential for electrostatically stabilized Fe$_2$O$_3$ particles in water. Additionally to figure 7.45 the effect of Y^{3+} and Ni^{2+} ions is shown. At low pH values the ζ-potential behaves as if Na$^+$ or Li$^+$ ions are added. However, with increasing pH value a strong increase of the ζ-potential values is observed. The reason for this increase is that Y(OH)$_{3(s)}$ and Ni(OH)$_{3(s)}$ is formed at higher pH values. These hydroxide complexes are present in colloidal form. According to [228] the hydroxide particles are charged highly positive. These charged particles attach preferable on the negatively charged iron oxide particles. Piwonski [228] observed this phenomena on alumina particles and Liden et al. [229] and Hirata et al. [230] on silicon carbide particles.
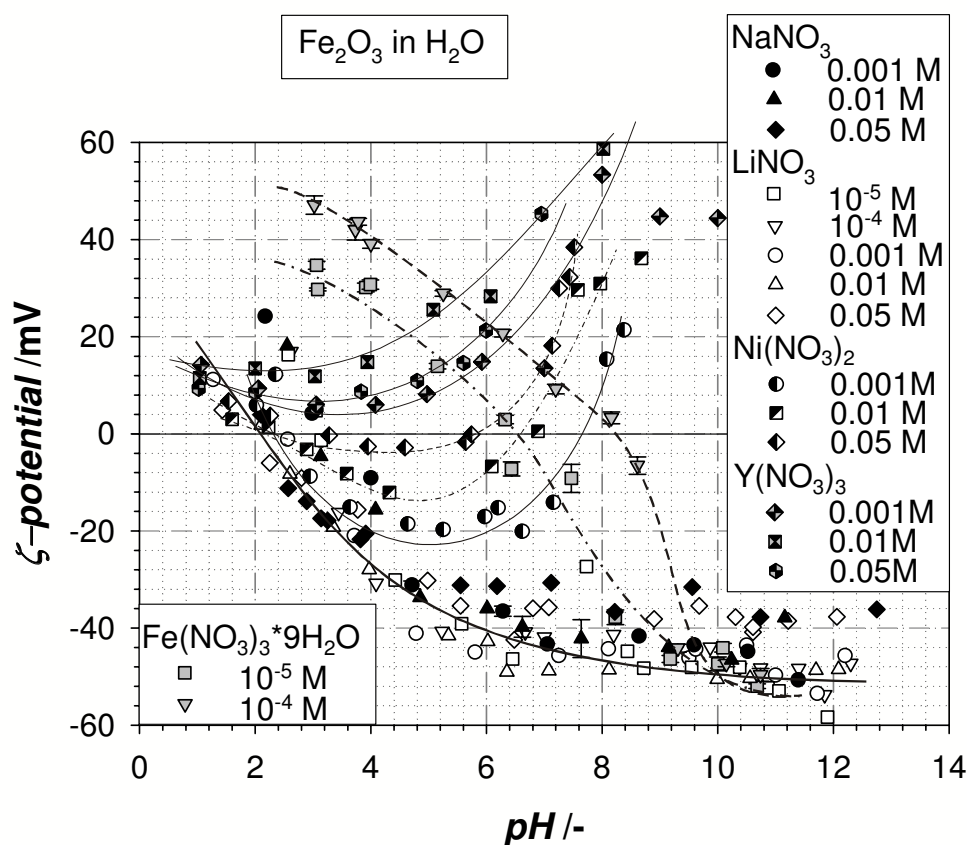

FIGURE A.5. Influence of different ions on the ζ-potential for electrostatic stabilized Fe$_2$O$_3$ in water.

A.5. Centrifugal Separating Systems of the LabStar Mill

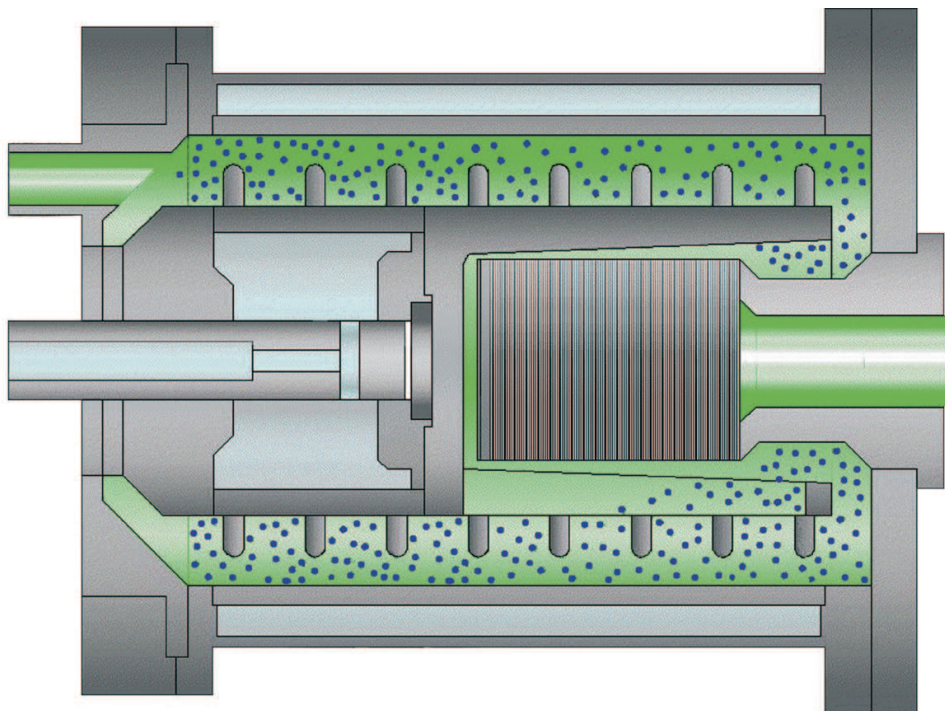Figure A.6 shows the centrifugal separating systems for the milling beads of the LabStar mill.

FIGURE A.6. Centrifugal separating systems of the LabStar mill [**231**].

A.6. Mini Bead Beater

Figure A.7 shows the design of the mini bead beater from BIOSPEC Products.

The mini bead beater violently agitates a sealed vial of 2 ml volume containing the suspension and milling beads. It is driven by a motor (115 V A/C, 60 Hz, 0.6 A) and can be adjust to four different speeds: 2500, 4200, 4600, and 4800 rpm. The vials are standard 2.0 ml microvials with screw-caps containing neoprene O-rings.

FIGURE A.7. The design of the mini bead beater.

A.7. Simulation

A.7.1. Model Validation. The model was validated for an initially monodisperse, dilute ($c_v = 5 \cdot 10^{-5}$) suspension of spherical polystyrene latex particles with a diameter of 2.17 μm. Oles [175] studied the shear induced aggregation and breakup of these particles. His experimental data and the model predictions for the evolution of the dimensionless mass mean floc diameter are shown in figure A.8. The filled symbols in this graph are the data of Oles, the unfilled symbols are model predictions from Spicer and Pratsinis [178], who employed the same kernels and a sectional method, and the lines are simulation results achieved with PARSIVAL and with the moment method.

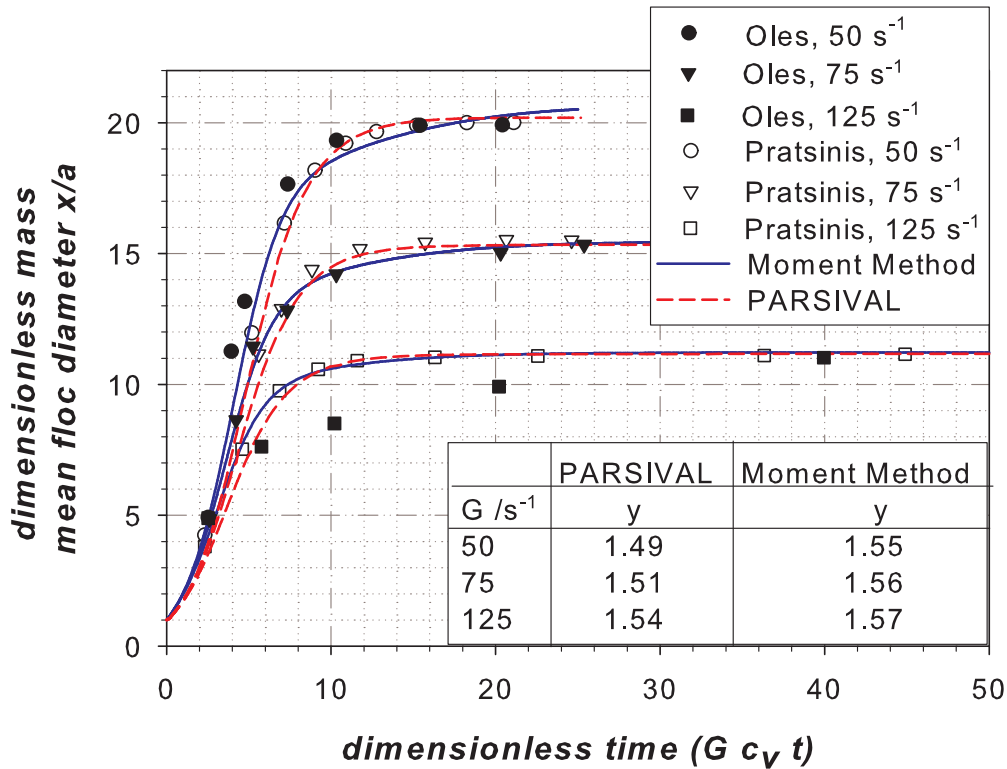|	PARSIVAL	Moment Method
G /s^{-1}	y	y
50	1.49	1.55
75	1.51	1.56
125	1.54	1.57

FIGURE A.8. Model predictions versus experimental data of Oles for the evolution of the dimensionless mass mean floc diameter.

In the calculations binary ($p = 2$), uniform ($c = 30$) breakage of aggregates are assumed. All parameters used for the calculations are summarized in table A.1. The size independent part of the collision frequency is according to Spicer and Pratsinis equal to $0.31 \cdot G$. This is true for a stability factor W of unity. Spicer and Pratsinis [178] determined the constants A' and y in the breakage rate coefficient for shear induced fragmentation (see equation 8.3) by fitting the data, finding $A' = 0.0047 \pm 0.0002$ cm$^{-1}s^{y-1}$ and $y = 1.6 \pm 0.18$. The same parameters were used in our simulations. A constant $A' = 0.0047$ was used and the parameter y was varied to fit the data. Both methods showed very good agreement with the data of Oles. The parameters found for the moment method as well as for PARSIVAL are within the error range Spicer and Pratsinis are

TABLE A.1. Parameters used in A.8.

parameter	value	unit	comments
d_g	2.17	μm	size of primary particles
p	2	-	number of particles per breakage event
c	30	-	uniform breakage
μ	1/3	-	
ρ_p	1050	mg/m^3	polystyrene latex
ρ_F	997	mg/m^3	water
η	$1.067 \cdot 10^{-3}$	Pa $\cdot$s	
W	1	-	
c_v	$5 \cdot 10^{-5}$	-	
A'	0.0047	-	

reporting. The parameters found for the moment method are in general a little higher than the parameters used with PARSIVAL but they are still below y = 1.6 used by Spicer and Pratsinis.

A.8. Definition of statistical measures

For a particle population with distribution $n(\phi)$ the kth moment is defined as:

$$M_k = \int_\infty^0 \phi^k \cdot n(\phi) \cdot d\phi. \tag{A.4}$$

M_0 is the total number of particles in the system, usually expressed as number concentration.

$$M_0 = \frac{N_{tot}}{V_{susp}}. \tag{A.5}$$

M_1 is the total particle volume per unit suspension volume:

$$M_1 = \frac{V_{p,tot}}{V_{susp}}. \tag{A.6}$$

The arithmetic number mean particle size in volume units is defined as [232]:

$$V_{1,n} = \frac{M_1}{M_0} = \frac{V_{p,tot}}{N_{tot}}. \tag{A.7}$$

The variance about this mean is [232]:

$$\sigma_{n,v}^2 = \frac{M_2}{M_0} - V_{1,n}^2. \tag{A.8}$$

The arithmetic volume mean particle size in volume units is defined as [232]:

$$V_{1,v} = \frac{M_2}{M_1}. \tag{A.9}$$

The geometric volume mean particle size in volume units is [232]:

$$V_g = \frac{M_1^2}{M_0^{3/2} M_2^{1/2}}. \tag{A.10}$$

The geometric standard deviation is given by [232]:

$$\sigma_{g,v} = exp\left[\left(ln\left(\frac{M_0 M_2}{M_1^2}\right)\right)^{1/2}\right]. \tag{A.11}$$

The skewness characterizes the degree of asymmetry of a distribution around its mean. While the mean, the standard deviation and the variance are dimensional quantities the skewness is non-dimensional. It is a pure number, which characterizes the shape of the distribution. The skewness for a normal distribution is zero, and any symmetric data should have a skewness near zero. Negative values for the skewness indicate the distribution is skewed to small sizes and positive values for the skewness indicate data that are skewed to large sizes [232].

$$skewness = \frac{1}{M_0 \sigma_{n,v}^3}\left(M_3 - 3\frac{M_1 M_2}{M_0} + 3\frac{M_1^3}{M_0^2} - \frac{M_1^3}{M_0^3}\right). \tag{A.12}$$

The kurtosis is also a non-dimensional quantity [232]. It measures the peakedness or flatness of a distribution relative to the standard normal distribution. The kurtosis for a standard normal distribution is zero. The conventional definition of the kurtosis is:

$$kurtosis = \frac{1}{M_0 \sigma_{n,v}^4}\left(M_4 - 4\frac{M_1 M_3}{M_0} + 6\frac{M_1^2 M_2}{M_0^2} - 4\frac{M_1^4}{M_0^3} + \frac{M_1^4}{M_0^4}\right) - 3. \tag{A.13}$$

Positive kurtosis indicates a peaked distribution and negative kurtosis indicates a flat distribution.

Curriculum Vitae

Personal Data:

Name: Marc Sommer
Date of Birth: 20 September 1975
Place of Birth: Frankfurt (Main)
Marital Status: single
Citizenship   German

Education:

08/1982-02/1986   Kelkheim Elementary School
02/1986-07/1992   Kelkheim Comprehensive School
07/1992-06/1995   Kelkheim Grammar School, with graduation Abitur

Military Service:

10/1995-7/96   Military service in the Air Force as aircraft turbine engine mechanic

Studies:

WS/1996-WS/2001   Mechanical Engineering at the TU Munich
6/2001-12/2001   Diploma thesis in the USA with DuPont.

Promotion:

01/2002 - 03/2002   Research Associate at the Institute of Particle Technology, TU Munich
03/2002 - 12/2003   Visiting Scientist, University of Delaware
01/2004 - 04/2004   Research Associate at the Institute of Particle Technology, TU Munich
05/2004 - 08/2006   Research Associate at the Institute of Particle Technology, University of Erlangen